
**Search for Astronomical Neutrinos
from Blazar TXS0506+056
in Super-Kamiokande**

2020, MARCH
HAGIWARA KAITO

Graduate School of
Natural Science and Technology
(Doctor's Course)
OKAYAMA UNIVERSITY

Abstract

The IceCube Neutrino Observatory detected a high-energy neutrino event with an estimated energy 290 TeV on 22 September 2017 at 20:54:30:43 Coordinated Universal Time. The arrival direction of the neutrino coincides with the location of the blazar named TXS0506+056, which is located at right ascension= 77.3582° and declination= $+5.6931^\circ$ (redshift $z = 0.3364 \pm 0.0010$). Within a minute of detection, the information of this event shared via the Gamma-ray Coordinate Network and follow-up observations over a wide range of energies were carried out by several observatories. According to the Fermi All-sky Variability Analysis, TXS0506+056 brightened in the GeV band starting in April 2017. Subsequently, the IceCube collaboration additionally reported a possible neutrino event excess from this blazar in older data between September 2014 and March 2015. However, about the average from 2014 to 2015, neither excessive gamma-rays nor significant changes in the gamma ray spectrum are observed. The coincidence between the neutrino arrival direction and the blazar location as well as timing correlated with the associated gamma-ray flare suggest that the observed neutrinos originated from the blazar and strongly motivate searches for neutrinos in the other energy regions by Super-Kamiokande.

Super-Kamiokande is a large water Cherenkov detector located 1,000 m underground in the Kamioka-mine, Gifu Prefecture, Japan. It is a cylindrical detector, 39.3 m in diameter and 41.4 m in height and contains 50 kilotons of ultra-pure water as neutrino target. The experiment has been operated since April 1996 and has made observations in four distinct phases known as SK-I, SK-II, SK-III, and SK-IV. In this study neutrino data from SK-I to SK-IV through February 2018 corresponding to 5,924.4 live days are used for analysis. To estimate the atmospheric neutrino background for this study, a 500-year-equivalent Monte Carlo simulation of each phase has been used.

The present analysis utilizes the Super-Kamiokande neutrino data with more than 100 MeV of visible energy, divided into three classes depending upon the event topology. In the fully-contained and partially-contained event samples, the neutrino interaction is reconstructed within the inner-detector using Cherenkov rings produced by its daughter particles. An event where all daughter particles stop inside the detector is classified as fully-contained and those where at least one particle exits the detector is classified partially-contained. Upward-going muon events are observed when energetic muons produced by muon-neutrino interactions with the rock surrounding the detector penetrate the detector from below its horizon.

To use events with sufficient angular resolution for association with the blazar direction, cut on the observed energy is applied. For these criteria, fully-contained and partially-contained samples are ensured that the angular deviation of the reconstructed direction from the truth is within 10 degrees for more than 68% of these events. Since upward-going muon events originate from neutrinos with higher energy than other categories, their arrival direction is estimated with higher accuracy. Therefore, no additional restriction on the upward-going muon energy is used

as more than 77% of events are reconstructed within 5 degrees of the true arrival direction.

By comparing to the expected backgrounds, no significance excess was observed at greater than the 1.2σ level in the blazar direction. The average and variance of the number of observed events in these off-source are compared with those in the on-source region around the blazar and showed consistency within 1.6σ . And the event rate in the on-source and the off-source are also consistent, indicating no excess of neutrino events in the direction of the blazar. No significant temporal increase of neutrino flux was found in the blazar direction by examining the change of the event rate using the Kolmogorov-Smirnov-test.

Based on no signal assumption, upper limits of the neutrino fluence, the energy-dependent neutrino flux, and the neutrino luminosity are given for both electron-neutrinos and muon-neutrinos. We prepared four types of the neutrino energy spectrum for the calculation, which are three power-law types and one log-parabola type. The averaged fluence upper limits are placed on the electron-neutrino fluence of $1.9 \times 10^4 \text{ cm}^{-2}$ below 10 GeV and the muon-neutrino fluence of 8.0×10^4 to $3.1 \times 10^{-1} \text{ cm}^{-2}$ in the range 1 GeV to 10 TeV. The averaged upper limits of the energy-flux are $6.1 \times 10^{-7} \text{ erg cm}^{-2} \text{ sec}^{-1}$ for electron-neutrinos and 4.8×10^{-7} to $1.1 \times 10^{-9} \text{ erg cm}^{-2} \text{ sec}^{-1}$ for muon-neutrinos. The luminosity is 1.9×10^{50} to $4.3 \times 10^{47} \text{ erg sec}^{-1}$ in the range 1 GeV to 10 TeV.

The upper limit obtained in this study was compared with the numerical calculation by simulation. As a result, it was shown that neutrinos from the blazar is possible to be detected by SK. By using neutrinos in the GeV to TeV region that can be observed by SK, it is possible to limit the model parameters of blazar's jet mechanism. From limiting the parameters, the origin of high-energy CRs and the mechanism of acceleration of CRs will be elucidated.

Acknowledgement

I want to show the expression of my deep gratitude to my supervisor Prof. Yusuke Koshio for his enormous support. The discussion of physics with him has greatly helped my research. He taught me many important and useful things not only physics but also career, private life and so on. This thesis would never exist without his kind comments and detailed suggestions. He also gave me the opportunity to study in Italy and I had a wonderful experience. I am very happy that I decided to join his group.

I would like to appreciate all SK collaborators and all the staffs at Kamioka Observatory. This study could not be done without their studies and various advice. Especially, Prof. Kimihiro Okumura and Prof. Roger Wendell in the ATMPD group gave me a lot of advice on the analytical method, from basic to detailed things. Without their great guidance, my research could not be accomplished.

I am grateful to Prof. Makoto Sakuda and Prof. Hirokazu Ishino for their kind guidance in the physics lecture in Okayama University. I also would like to thank to laboratory members and secretary in Okayama University; Dr. Shintaro Ito, Atsushi Nakamura, Nishtha Piplani, Masayuki Harada, Toshiaki Horai, Seiya Sakai, Ryo Okada, Wenjie Ma, Hussain Kitagawa, Shoya Tanaka, Nahoko Koeda, and Kayoko Nagatsuna. Discussing and drinking with them was an integral part of my research life. I wish them a greater success in every situations.

Finally, I want to thank to my family and all friends. They have been supported me for everything. I was able to enjoy student life thanks to them.

Thank you everyone for everything !

Contents

1	Introduction	15
1.1	Neutrinos	15
1.1.1	History	15
1.1.2	Neutrino Oscillation	16
1.1.3	Oscillation Parameters	20
1.2	Multi-messenger Astronomy	20
1.2.1	CR	21
1.2.2	Gamma Rays	22
1.2.3	Neutrinos	23
1.3	Active Galactic Nucleus (AGN)	24
1.3.1	Blazar	25
1.3.2	Neutrinos from Blazars	26
2	Super-Kamiokande (SK)	28
2.1	Cherenkov Radiation	29
2.2	SK Detector	31
2.2.1	History of SK	31
2.2.2	ID PMT	34
2.2.3	OD PMT	36
2.3	Water and Air System	37
2.3.1	Water Purification System	37
2.3.2	Air Purification System	38
2.4	Electronics and Data Acquisition (DAQ) System	38
2.4.1	ID Electronics and DAQ: SK-I to SK-III	38
2.4.2	OD Electronics and DAQ: SK-I to SK-III	41
2.4.3	Hardware Trigger: SK-I to SK-III	42
2.4.4	Electronics and DAQ for ID & OD: SK-IV and SK-V	43
2.4.5	Online System for ID & OD: SK-IV and SK-V	44
2.4.6	Software Trigger: SK-IV and SK-V	46
3	Simulation	47
3.1	Atmospheric Neutrino Flux	47
3.1.1	Primary Cosmic Ray	47
3.1.2	Hadronic Interaction	48
3.1.3	3D Flux Calculation	50
3.1.4	Neutrino Flux at SK	52
3.2	Neutrino Interaction	53
3.2.1	Elastic and Quasi-Elastic Scattering	54
3.2.2	Meson Exchange Current	56
3.2.3	Single Meson Production	57
3.2.4	Deep Inelastic Scattering	60
3.2.5	Coherent Pion Production	61

3.2.6	Nuclear Effects	63
3.3	Detector Simulation	64
3.3.1	SK Detector Simulation	65
3.3.2	SK Geant4 based Simulation	67
4	Calibration	71
4.1	ID PMT Calibration	71
4.1.1	High-Voltage (HV)	71
4.1.2	Relative Gain	71
4.1.3	Absolute Gain	73
4.1.4	QE	73
4.1.5	Timing Response	74
4.2	Water Transparency in the ID	75
4.2.1	Light Absorption and Scattering	76
4.2.2	Light Reflection at the PMT and Black Sheet	76
4.3	OD PMT Calibration	76
4.3.1	Charge Response	77
4.3.2	Timing Response	77
4.4	Optical Properties of the OD	79
4.5	Energy Calibration	79
4.5.1	High Energy Stopping Muons	79
4.5.2	Low Energy Stopping Muons	80
4.5.3	Neutrino Induced π^0 Events	80
4.5.4	Decay Electrons	81
4.5.5	Summary of Energy Calibration	82
5	Event Reduction	84
5.1	FC	85
5.1.1	First Reduction	85
5.1.2	Second Reduction	86
5.1.3	Third Reduction	86
5.1.4	Fourth Reduction	90
5.1.5	Fifth Reduction	90
5.1.6	Final FC Selection	93
5.1.7	Summary of FC Reduction	94
5.2	Partially Contained	96
5.2.1	First Reduction	96
5.2.2	Second Reduction	97
5.2.3	Third Reduction	98
5.2.4	Fourth Reduction	99
5.2.5	Fifth Reduction	101
5.2.6	Final PC Reduction	109
5.2.7	Summary of PC Reduction	109
5.3	UPMU	113
5.3.1	First Reduction	113

5.3.2	Second Reduction	113
5.3.3	Third Reduction	114
5.3.4	Final UPMU Reduction	114
5.3.5	Summary of UPMU Reduction	114
6	Event Reconstruction	116
6.1	Vertex Fitting	116
6.2	Ring Counting	117
6.3	Particle Identification	119
6.4	Momentum Determination	123
6.5	Improvements in Reconstruction	123
6.5.1	Ring number Correction	123
6.5.2	Decay electron Finding	123
6.5.3	π^0 Reconstruction	124
6.6	Event Reconstruction for UPMU Sample	124
7	Search for Astronomical Neutrino from Blazar	125
7.1	Angular Resolution	125
7.2	Expected Background	126
7.3	On-source vs. Off-source	128
7.4	Kolmogorov–Smirnov (KS) Test	130
7.5	Summary	133
8	Limit Calculation	134
8.1	90% Confidence Level (C.L.)	134
8.2	FC and PC Fluence	135
8.3	UPMU Fluence	136
8.3.1	Effective Area	137
8.3.2	Probability of a Neutrino Creating a Muon	138
8.3.3	Shadow Effect	139
8.4	Results	140
8.4.1	Fluence Limit	143
8.4.2	Energy-flux Limit	144
8.4.3	Luminosity Limit	144
8.5	Discussion	146
A	Table of the Upper Limit	150
B	Gamma-ray Spectrum from Gadolinium	153

List of Figures

1.1	Energy flux spectra of CRs for all particles.	22
1.2	Schematic of AGN.	24
1.3	Spectral-energy distribution of Markarian 421.	25
1.4	Time-dependent multi-wavelength observations of TXS0506+056. . .	27
1.5	Broadband spectral-energy distribution of the blazar TXS0506+056.	27
2.1	Schematic of the SK detector (cutaway view).	28
2.2	The image of the Cherenkov radiation.	29
2.3	Schematic of the module structure of the PMT support frame. . . .	32
2.4	20-inch ID PMT.	34
2.5	FRP case and acrylic cover of the ID PMT.	34
2.6	Quantum efficiency of the 20-inch ID PMT.	35
2.7	Single-p.e. pulse height distribution expressed in light-intensity-dependent ADC count.	35
2.8	Schematic of a module of ID and OD PMTs.	36
2.9	Logic diagram of the electronics system for the ID used with SK-I to SK-III.	39
2.10	Block diagram of the circuit in the ATM.	40
2.11	Timing chart for signal and trigger in an ATM.	40
2.12	Data accusation system for OD.	41
2.13	Block diagram of the QTC and its surroundings.	43
2.14	Timing chart for signal and trigger in a QTC.	44
2.15	Block diagram of the new online system.	45
3.1	Measured primary CR flux and the model used for the HKKM calcu- lation.	48
3.2	Comparison between HARP data and theoretical models.	49
3.3	Comparison of CR muon flux between experimental data and modified flux.	50
3.4	Interaction areas of primary CRs, and atmosphere for 1D and 3D flux calculation.	51
3.5	Atmospheric neutrino flux in three energy bins.	52
3.6	Comparison of calculated atmospheric neutrino fluxes averaged over all directions (left panel). Comparison of flavor ratio and neutrino anti-neutrino ratios (right panel).	53
3.7	Cross-section for the CCQE scattering of muon neutrino (left panel) and muon anti-neutrino (right panel).	56
3.8	Cross-section for single pion production of the muon neutrino.	58
3.9	Comparison between experimental and calculated data of the total cross-section of the CC interaction for ν and $\bar{\nu}$	61
3.10	Cross-section of coherent pion production from the carbon nucleus via CC interaction (left panel) and NC interaction (right panel). . .	62
3.11	Interaction probabilities of a nucleon in ^{16}O as a function of the nu- cleon momentum.	64

3.12 Distributions of the wavelength of Cherenkov photon.	67
3.13 Comparison between SKDETSIM and SKG4 to confirm the effect of absorption.	68
3.14 Distributions of neutron capture time and distance from emission location to capture location.	69
3.15 The energy spectra of gamma-rays emitted from the thermal neutron capture on Gd.	70
3.16 SKG4 Logo	70
4.1 The location of standard PMTs and the schematic view of grouping for the PMTs.	72
4.2 Distribution of the observed charge for the single p.e. signal.	74
4.3 Typical TQ distribution for one PMT.	75
4.4 Fitted water coefficient functions.	77
4.5 Global timing offset.	78
4.6 Summary of absolute energy scale measurements for each SK phase.	82
4.7 Energy scale stability as a function of date since the start of SK operations.	83
5.1 Three types of high-energy neutrino events at SK	84
5.2 Expected energy distributions from atmospheric neutrino simulation for each event classification.	84
5.3 FC first reduction	85
5.4 FC second reduction	86
5.5 FC third reduction for through-going muon	87
5.6 FC third reduction for stopping muon	88
5.7 Cable hole and veto counter.	88
5.8 FC third reduction for flasher events	89
5.9 FC fifth reduction for stopping noise event	91
5.10 FC fifth reduction for invisible muon	92
5.11 FC fifth reduction for coincidence muon	92
5.12 FC fifth reduction for electric noise	93
5.13 PC first reduction	97
5.14 Algorithm for finding hit clusters in OD.	98
5.15 PC second reduction	99
5.16 PC third reduction	99
5.17 PC fourth reduction	101
5.18 PC fifth reduction for through-going muon cut B	102
5.19 PC fifth reduction for through-going muon cut C	103
5.20 PC fifth reduction for through-going muon cut D	104
5.21 PC fifth reduction for stopping muon cut A	104
5.22 PC fifth reduction for stopping muon cut B	105
5.23 PC fifth reduction for stopping muon cut C	106
5.24 PC fifth reduction for corner clipping muon cut A	107
5.25 PC fifth reduction for corner clipping muon cut B	108
6.1 Illustration of the basic idea of finding ring candidates.	118
6.2 Ring-counting likelihood distributions.	120

6.3	PID likelihood distributions of single-ring events.	121
6.4	PID likelihood distributions of multi-ring events.	122
7.1	Resolution of angle between reconstructed direction and true neutrino direction by MC.	126
7.2	A sky map of the reconstructed arrival direction if selected neutrino events around the blazar direction for all samples.	127
7.3	Area ratio (blue circle/green area and blue circle/yellow area).	128
7.4	Number of detected events in each search region and expected background.	128
7.5	The number of event in the on-source and off-source.	129
7.6	Event rate of the on-source and off-source.	130
7.7	Kolmogorov-Smirnov test for FC, PC, and UPMU.	131
7.8	Distribution of maximum distance calculated by the toy-MC with the result of experimental data.	132
8.1	Poisson distribution with expected background and 90% C.L. upper limit	134
8.2	Neutrino-nucleon interaction cross-section.	135
8.3	Detection efficiency for FC and PC.	136
8.4	Effective area of UPMU.	137
8.5	Effective area as a function of zenith angle.	138
8.6	Probability that a neutrino creates a muon via neutrino interaction and that the muons reach the detector.	139
8.7	Earth's shadow effect	140
8.8	Relationship between the reconstructed momentum and neutrino energy.	141
8.9	Fluence upper limits at 90% C.L.	143
8.10	The energy-flux upper limit at 90% C.L. compared with IceCube event.	145
8.11	Energy-flux upper limit at 90% C.L. compared with gamma-ray spectrum.	146
8.12	Spectral energy distributions and muon neutrino fluxes.	147
8.13	Time evolution of the muon neutrino emission from the jet of AGN.	149
B.1	The energy spectrum from $^{157}\text{Gd}(n, \gamma)$ reaction with different multiplicity values and hit values	154
B.2	The energy spectrum of single gamma-rays from $^{157}\text{Gd}(n, \gamma)$ reaction.	155
B.3	The Ratio of data by MC for the single gamma-ray from $^{155}\text{Gd}(n, \gamma)$, $^{157}\text{Gd}(n, \gamma)$, and $^{\text{natural}}\text{Gd}(n, \gamma)$ reaction.	155

List of Tables

1.1	Best fit values of the neutrino oscillation parameters.	21
2.1	Cherenkov threshold of various particles.	30
2.2	Summary of characteristics of each SK phase.	34
2.3	Water Purification System.	37
2.4	Trigger threshold for each SK-I to SK-III phase.	42
2.5	Trigger threshold of SK-IV phase.	46
3.1	List of resonances and background terms used in the NEUT simulation.	59
3.2	Simulated process for each particle in SKDETSIM.	66
5.1	Reduction efficiency after each FC reduction step	94
6.1	Vertex resolution.	117
6.2	Angular resolution.	118
7.1	The number of expected events at each SK phase.	130
7.2	Summary of analysis of neutrino search from the blazar TXS0506+056.	133
8.1	Parameters of the neutrino energy spectrum.	142
8.2	Summary of upper limits of luminosity	146
A.1	Summary of upper limits at 90% C.L. (Parameter1)	150
A.2	Summary of upper limits at 90% C.L. (Parameter2).	151
A.3	Summary of upper limits at 90% C.L. (Parameter3).	151
A.4	Summary of upper limits at 90% C.L. (Parameter4).	152

Acronym

- 3FGL:** *The third Fermi-LAT source catalog*
- ADC:** *Analog Digital Converter*
- AFT:** *After Trigger*
- AGN:** *Active Galactic Nuclei*
- AMS:** *Alpha Magnetic Spectrometer experiment*
- ANNRI:** *Accurate Neutron-Nucleus Reaction measurement Instrument detector*
- ASAS-SN:** *All-Sky Automated Survey for Supernovae*
- ASIC:** *Application Specific Integrated Circuits*
- ATM:** *Analog Timing Module*
- BEBC:** *Big European Bubble Chamber experiment*
- BESS:** *Balloon-borne Experiment with Superconducting Spectrometer experiment*
- C.L.:** *Confidence Level*
- CAPRICE:** *Cosmic Antiparticle Ring Imaging Cherenkov Experiment*
- CC:** *Charged-Current interaction*
- CCQE:** *Charged-Current Quasi-Elastic scattering*
- CMB:** *Cosmic Microwave Background*
- CP:** *charge-parity*
- CR:** *Cosmic Ray*
- DAQ:** *Data Acquisition system*
- DIS:** *Deep Inelastic Scattering*
- DONuT:** *Direct Observation of the Nu Tau experiment*
- DPM:** *Dual Parton Model*
- DSM:** *Data Sort Mapping*
- Dec.:** *Declination*

-
- FAVA:** *Fermi All-Sky Variability Analysis*
- FC:** *Fully-Contained event*
- FIFO:** *First-in First-out memory*
- FKM:** *Feynman-Kislinger-Ravndal baryon model*
- FPGA:** *Field Programmable Gate Array*
- FSCC:** *Fastbus Smart Crate Controller*
- FSRQ:** *Flat-Spectrum Radio Quasar*
- FV:** *Fiducial Volume*
- Fermi-ASP:** *Fermi's Automated Science Processing*
- Fermi-LAT:** *Fermi Large Area Telescope*
- GCN:** *Gamma-ray Coordinate Network*
- GEANT:** *Geometry and Tracking*
- GONG:** *Go/NoGo module*
- GRV:** *Gluck-Reya-Vogt parton distribution*
- HARP:** *Hadron Production experiment*
- HE:** *High Energy*
- HKKM:** *Honda-Kajita-Kasahara-Midorikawa neutrino flux model*
- HV:** *High-Voltage*
- ID:** *Inner Detector*
- IMAX:** *Isotope Matter-Antimatter Experimen*
- IMB:** *Irvine-Michigan-Brookhaven experiment*
- J-PARC:** *Japan Proton Accelerator Research Complex*
- JACEE:** *Japanese-American Cooperative Emulsion Experiment*
- JSNS:** *Japan Spallation Neutron Source*
- K2K:** *KEK-to-Kamioka experiment*
- KEK:** *The High Energy Accelerator Research Organization (in Japanese :
Ko Enerugi Kasokuki Kenkyu Kiko)*
- KNO:** *Koba-Nielsen-Olsen scaling factor*

-
- KS-test:** *Kolmogorov-Smirnov Test*
- KamLAND:** *Kamioka Liquid scintillator Anti-Neutrino Detector experiment*
- LE:** *Low Energy*
- LEAP:** *Low Energy Antiproton balloon flight experiment*
- LPF:** *Low-Pass Filter*
- LVDS:** *Low Voltage Differential Signaling drivers*
- MC:** *Monte Carlo*
- MEC:** *Meson Exchange Current*
- MINOS:** *Main Injector Neutrino Oscillation Search*
- MLF:** *Material and Life Science Experimental Facility*
- MSW:** *Mikheev-Smirnov-Wolfenstein effect (matter effect of neutrino oscillation)*
- MiniBooNE:** *Mini Booster Neutrino Experiment*
- NC:** *Neutral-Current interaction*
- OD:** *Outer Detector*
- PC:** *Partially-Contained event*
- PDF:** *Parton Distribution Function*
- PHITS:** *Particle and Heavy-Ion Transport code System*
- PID:** *Particle Identification*
- PMT:** *Photomultiplier Tube*
- QAC:** *Charge to Analog Converter*
- QBEE:** *QTC based Electronics with Ethernet*
- QE:** *Quantum efficiency*
- QTC:** *Charge to Time Converter*
- R.A.:** *Right Ascension*
- RENO:** *Reactor Experiment for Neutrino Oscillation*
- RMS:** *Root Mean Square*
- RUNJOB:** *Russian-Nippon Joint Balloon experiment*

-
- SCH:** *Super Control Header module*
- SF:** *Spontaneous Fission*
- SHE:** *Special High Energy*
- SIC:** *System Interface Control*
- SK:** *Super-Kamiokande experiment*
- SKAT:** *Sequential Kernel Association Test experiment*
- SKDETSIM:** *Super-Kamiokande Detector Simulation*
- SKG4:** *Super-Kamiokande Geant4 based simulation*
- SLE:** *Super Low Energy*
- SMP:** *Super Memory Partner*
- SNO:** *Sudbury Neutrino Observatory*
- T2K:** *Tokai-to-Kamioka experiment*
- TAC:** *Time to Analog Converter*
- TDC:** *Time to Digital Converter*
- TKO:** *Tristan KEK Online system*
- TOF:** *Time-of-Flight*
- TRG:** *Trigger module*
- UPMU:** *Upward-going Muon event*
- UTC:** *Coordinated Universal Time*
- V/I:** *Voltage-to-Current converter*
- VME:** *Versa Module Europa*
- WS:** *Wavelength Shifting plate*
- p.e.:** *photoelectron*

1 Introduction

Neutrinos emitted from cosmic bodies play an important role in understanding celestial phenomena. Owing to their small cross-sections, neutrino observations are limited only by detector volume. Currently, neutrino detectors have extremely large volumes are operating worldwide. This chapter introduces the general properties of neutrinos, followed by those originated from high energy celestial objects, and then by the current status of astronomical neutrino observations.

1.1 Neutrinos

Neutrinos are elementary particles possessing a half-integer spin of the lepton sector. They interact only via the weak subatomic force and gravity¹. There have been, thus far, many theoretical and experimental achievements of neutrino physics.

1.1.1 History

The existence of neutrinos was first postulated by Pauli [1] in 1930 to explain the continuous energy spectrum of β decay. About 20 years after Pauli's proposal, (1956), the electron-anti-neutrino was discovered by Reines and Cowan [2, 3] at a nuclear reactor. In 1962, the existence of the muon-neutrino was confirmed by Danby et al. [4] using a neutrino beam produced created by the decay of charged pions shot into a beam of muon neutrinos. The third type neutrino, the tau neutrino, was discovered in 2001 via the Direct Observation of the Nu Tau (DONuT) Experiment [5] and the detection of tau leptons in neutrino interactions.

The first measurement of an electron-neutrino flux from the core of the sun was made in the 1960s via the Homestake Experiment [6]. The measured value of the flux was between one third and one-half the number predicted by the standard solar model [7]. A similar difference was observed at the Kamioka Observatory [8] and at the Sudbury Neutrino Observatory (SNO) [9]. Another indication that the neutrino flux differed between simulation and observation was found using the atmospheric neutrino of Kamiokande [10] in 1988 and the Irvine-Michigan-Brookhaven experiment (IMB) [11] in 1992.

The problem was solved after gaining an improved understanding of the properties of neutrinos. It was first believed that neutrinos did not have mass. However, in practice, the mass was found to be nonzero. Furthermore, the masses of individual states differ. Allowing the interacting flavor state to differ from the mass state appears as an oscillation. Evidence of neutrino oscillations was reported via the Super-Kamiokande Experiment (SK) in 1998 using the asymmetry of upward and downward atmospheric neutrinos [12]. Furthermore, by comparing solar neutrinos measured at the SK [13] and at the SNO [14] concerning neutrino oscillations, the problem of solar neutrinos was completely solved. Later, in 2015, the Nobel

¹The effect of gravity is negligible because of the neutrino's tiny mass.

Prize was awarded to Takaaki Kajita (SK) and Arthur B. McDonald (SNO) for the discovery of neutrino oscillations, which proved that neutrinos had mass.

More astronomical neutrinos were observed in 1987. The neutrinos emitted from a supernova explosion (SN1987A), located in the Large Magellanic Cloud, was detected at Kamiokande [15], IMB [16], and Baksan [17] observatories. On 23 February 1987 at 07:35 Coordinated Universal Time (UTC), the Kamiokande detected 11 neutrino events. The IMB detected eight, and Baksan detected five. Although only 24 events were detected, the observations were consistent with theoretical supernova models, in which 99% of the decay energy was emitted in the form of neutrinos [18]. This was the first time neutrinos were known to have been emitted from a supernova and were directly observed. This further demarked the beginning of neutrino astronomy. For pioneering contributions to astrophysics for the detection of cosmic neutrinos, Masatoshi Koshiba and Raymond Davis were awarded the Nobel Prize in 2002.

The IceCube neutrino observatory detected a high-energy neutrino event on 22 September 2017 [19]. The origin of the event was found to have been the blazar TXS0506+056, and it became the third astronomical neutrino event. This neutrino event attracted attention for three reasons. First, the event produced high-energy neutrinos of several-hundred PeV. Second, an automated alert was distributed to telescopes around the world 43 sec later, and follow-up observations were quickly conducted. Finally, a gamma-ray flare was found in the GeV band in April 2017. From these discoveries, the blazar TXS0506+056 was the first known source of a multi-messenger between a high-energy astronomical neutrino and gamma rays.

1.1.2 Neutrino Oscillation

Neutrino oscillations reflect transitions between the different types of neutrinos, because neutrino flavor eigenstates are not identical to mass eigenstates. A theory was proposed by Pontecorvo [20, 21] for neutrino and anti-neutrino oscillations. The idea for the quantitative theory of neutrino oscillation was first developed by Maki et al. [22] in 1962 and further expanded on by Pontecorvo [23] in 1968.

In vacuum

The neutrino flavor state, $|\nu_\alpha\rangle$ ($\alpha = e, \mu, \tau$), can be described as a linear combination of different mass eigenstates $|\nu_i\rangle$ having masses $i = 1, 2$, and 3 ,

$$|\nu_\alpha\rangle = \sum_{i=1}^3 U_{\alpha i}^* |\nu_i\rangle, \quad (1.1)$$

where U is a 3×3 matrix between these states, called the Pontecorvo–Maki–Nakagawa–Sakata (PMNS) matrix,

$$U = \begin{pmatrix} 1 & 0 & 0 \\ 0 & c_{23} & s_{23} \\ 0 & -s_{23} & c_{23} \end{pmatrix} \begin{pmatrix} c_{13} & 0 & s_{13}e^{-i\delta_{CP}} \\ 0 & 1 & 0 \\ -s_{13}e^{-i\delta_{CP}} & 0 & c_{13} \end{pmatrix} \begin{pmatrix} c_{12} & s_{12} & 0 \\ -s_{12} & c_{12} & 0 \\ 0 & 0 & 1 \end{pmatrix}, \quad (1.2)$$

where $s_{ij} = \sin(\theta_{ij})$ and $c_{ij} = \cos(\theta_{ij})$. The angle θ_{ij} represents the mixing between states i and j . The δ is the charge-parity (CP) violating phase for the lepton sector. The time evolution of the flavor eigenstate is

$$|\nu_\alpha\rangle = \sum_{i=1}^3 U_{\alpha i}^* e^{-iE_i t} |\nu_i(t=0)\rangle, \quad (1.3)$$

where E_i is the energy of the eigenstate of ν_i . The probability amplitude of detecting a neutrino in the flavor eigenstate, $|\nu_\beta\rangle$, at time t from one created as $|\nu_\alpha\rangle$ at time $t=0$ is

$$\begin{aligned} A_{\nu_\alpha \rightarrow \nu_\beta}(t) &\equiv \langle \nu_\beta | \nu_\alpha \rangle \\ &= \sum_i \langle \nu_\beta | U_{\alpha i}^* e^{-iE_i t} | \nu_i \rangle \\ &= \sum_i \sum_{\gamma=e,\mu,\tau} \langle \nu_\beta | U_{\alpha i}^* e^{-iE_i t} U_{\gamma i} | \nu_\gamma \rangle \\ &= \sum_i \sum_{\gamma=e,\mu,\tau} U_{\alpha i}^* U_{\gamma i} e^{-iE_i t} \langle \nu_\beta | \nu_\gamma \rangle \\ &= \sum_i U_{\alpha i}^* U_{\beta i} e^{-iE_i t}. \end{aligned} \quad (1.4)$$

The probability of the flavor transition is then given by

$$\begin{aligned} P_{\nu_\alpha \rightarrow \nu_\beta}(t) &= |A_{\nu_\alpha \rightarrow \nu_\beta}(t)|^2 \\ &= \left(\sum_i U_{\alpha i}^* U_{\beta i} e^{-iE_i t} \right) \left(\sum_j U_{\alpha j} U_{\beta j} e^{-iE_j t} \right)^* \\ &= \sum_i \sum_j U_{\alpha i}^* U_{\beta i} U_{\alpha j} U_{\beta j}^* e^{-i(E_i - E_j)t} \\ &= \sum_i U_{\alpha i}^* U_{\beta i} U_{\alpha i} U_{\beta i} + \sum_{i \neq j} U_{\alpha i}^* U_{\beta i} U_{\alpha j} U_{\beta j}^* e^{-i(E_i - E_j)t} \end{aligned} \quad (1.5)$$

When the neutrinos are relativistic ($\mathbf{p}^2 \gg m^2$), the relationship between the energy and the mass can be approximated as follows, using natural units ($c = \hbar = 1$):

$$\begin{aligned} E_i - E_j &= \sqrt{\mathbf{p}_i^2 + m_i^2} - \sqrt{\mathbf{p}_j^2 + m_j^2} \\ &\simeq \mathbf{p}_i \left(1 + \frac{m_i^2}{2\mathbf{p}_i^2} \right) - \mathbf{p}_j \left(1 + \frac{m_j^2}{2\mathbf{p}_j^2} \right) \\ &= \frac{\Delta m_{ij}^2}{2E} \end{aligned} \quad (1.6)$$

where $\Delta m_{ij}^2 = m_i^2 - m_j^2$ is the mass-squared difference between two mass eigenstates and the relativistic neutrino energy, expressed as $E \simeq |\mathbf{p}_i| = |\mathbf{p}_j|$. Furthermore,

considering the distance traveled by neutrino $L = ct$, Equation 1.5 can be expressed as follows:

$$\begin{aligned}
P_{\nu_\alpha \rightarrow \nu_\beta}(t) &= \sum_i U_{\alpha i}^* U_{\beta i} U_{\alpha i} U_{\beta i}^* + \sum_{i \neq j} U_{\alpha i}^* U_{\beta i} U_{\alpha j} U_{\beta j}^* \exp\left(-i \frac{\Delta m_{ij}^2 L}{2E}\right) \\
&= \sum_i U_{\alpha i}^* U_{\beta i} U_{\alpha i} U_{\beta i}^* + \sum_{i \neq j} U_{\alpha i}^* U_{\beta i} U_{\alpha j} U_{\beta j}^* \\
&\quad - 2 \sum_{i \neq j} U_{\alpha i}^* U_{\beta i} U_{\alpha j} U_{\beta j}^* \sin^2\left(\frac{\Delta m_{ij}^2 L}{4E}\right) \\
&\quad + i \sum_{i \neq j} U_{\alpha i}^* U_{\beta i} U_{\alpha j} U_{\beta j}^* \sin\left(\frac{\Delta m_{ij}^2 L}{2E}\right) \\
&= P_1 + P_2 - 2P_3 + iP_4
\end{aligned} \tag{1.7}$$

P_1 and P_2 are evaluated jointly:

$$\begin{aligned}
P_1 + P_2 &= \sum_i \sum_j U_{\alpha i}^* U_{\beta i} U_{\alpha j} U_{\beta j}^* \\
&= \sum_i (U_{\alpha i}^* U_{\beta i}) \sum_j (U_{\alpha j} U_{\beta j}^*) \\
&= \left| \sum_i U_{\alpha i}^* U_{\beta i} \right|^2 \\
&= \delta_{\alpha\beta},
\end{aligned} \tag{1.8}$$

where δ is the Kronecker delta function. We proceed similarly for P_3 :

$$\begin{aligned}
P_3 &= \sum_{i>j} (U_{\alpha i}^* U_{\beta i} U_{\alpha j} U_{\beta j}^* + U_{\alpha j}^* U_{\beta j} U_{\alpha i} U_{\beta i}^*) \sin^2\left(\frac{\Delta m_{ij}^2 L}{4E}\right) \\
&= \sum_{i>j} (U_{\alpha i}^* U_{\beta i} U_{\alpha j} U_{\beta j}^* + (U_{\alpha j}^* U_{\beta j} U_{\alpha i} U_{\beta i}^*)^*) \sin^2\left(\frac{\Delta m_{ij}^2 L}{4E}\right) \\
&= 2 \sum_{i>j} \text{Re}\{U_{\alpha i}^* U_{\beta i} U_{\alpha j} U_{\beta j}^*\} \sin^2\left(\frac{\Delta m_{ij}^2 L}{4E}\right).
\end{aligned} \tag{1.9}$$

Finally, P_4 is expressed as follows:

$$\begin{aligned}
P_4 &= \sum_{i>j} (U_{\alpha i}^* U_{\beta i} U_{\alpha j} U_{\beta j}^* - U_{\alpha j}^* U_{\beta j} U_{\alpha i} U_{\beta i}^*) \sin\left(\frac{\Delta m_{ij}^2 L}{2E}\right) \\
&= -2i \sum_{i>j} \text{Im}\{U_{\alpha i}^* U_{\beta i} U_{\alpha j} U_{\beta j}^*\} \sin\left(\frac{\Delta m_{ij}^2 L}{2E}\right).
\end{aligned} \tag{1.10}$$

Net, putting Equation 1.8, 1.9, and 1.10 in Equation 1.7, we get

$$\begin{aligned}
P_{\nu_\alpha \rightarrow \nu_\beta}(t) &= \delta_{\alpha\beta} - 4 \sum_{i>j} \operatorname{Re}\{U_{\alpha i}^* U_{\beta i} U_{\alpha j} U_{\beta j}^*\} \sin^2\left(\frac{\Delta m_{ij}^2 L}{4E}\right) \\
&\quad + 2 \sum_{i>j} \operatorname{Im}\{U_{\alpha i}^* U_{\beta i} U_{\alpha j} U_{\beta j}^*\} \sin\left(\frac{\Delta m_{ij}^2 L}{2E}\right). \quad (1.11)
\end{aligned}$$

Matter effect

When neutrinos propagate through matter, the neutrino oscillation changes because of the interactions between the neutrino and matter. The effect is known as the Mikheev–Smirnov–Wolfenstein (MSW) [24–26] effect or the matter effect of neutrino oscillation.

All three flavors of neutrinos undergo neutral-current coherent scattering with protons, neutrons, and electrons. For only the electron neutrinos, coherent charged current scattering also occurs, because ordinary matter contains electrons. The effective potentials of neutral current, V_{NC} , and charged current, V_{CC} , are expressed as

$$V_{CC} = \sqrt{2} G_F N_e, \quad (1.12)$$

$$V_{NC} = -\frac{\sqrt{2}}{2} G_F N_n, \quad (1.13)$$

where G_F is the weak-coupling constant, and $N_{e,n}$ are the number densities of electrons or neutrons in the matter. In the case of an anti-neutrino, the potentials are negative. After subtracting the universal neutral current contribution, the time evolution of the mass eigenstates for the two-flavor-mixing case is expressed as

$$i \frac{d}{dt} \begin{pmatrix} \nu_1 \\ \nu_2 \end{pmatrix} = \begin{pmatrix} E_1 & 0 \\ 0 & E_2 \end{pmatrix} \begin{pmatrix} \nu_1 \\ \nu_2 \end{pmatrix}. \quad (1.14)$$

It is then converted into the flavor basis, as

$$\begin{aligned}
i \frac{d}{dt} \begin{pmatrix} \nu_e \\ \nu_\mu \end{pmatrix} &= U \begin{pmatrix} E_1 & 0 \\ 0 & E_2 \end{pmatrix} U^\dagger \begin{pmatrix} \nu_e \\ \nu_\mu \end{pmatrix} \\
&= \frac{\Delta m_M^2}{4E} \begin{pmatrix} -\cos 2\theta_M & \sin 2\theta_M \\ \sin 2\theta_M & \cos 2\theta_M \end{pmatrix} \begin{pmatrix} \nu_e \\ \nu_\mu \end{pmatrix} \quad (1.15)
\end{aligned}$$

where Δm_M^2 is the effective mass-squared difference, and θ_M is the effective mixing angle. These effective parameters are defined by

$$\Delta m_M^2 = \Delta m^2 \sqrt{\sin^2 2\theta + (\cos 2\theta - x)^2}, \quad (1.16)$$

$$\sin^2 2\theta_M = \frac{\sin^2 2\theta}{\sin^2 2\theta + (\cos 2\theta - x)^2}, \quad (1.17)$$

where x quantifies the degree of the effect and is defined as

$$x \equiv \frac{2\sqrt{2}G_F N_e E}{\Delta m^2} \quad (1.18)$$

The survival probabilities of ν_e propagating and the two neutrino oscillation through a matter of constant electron density, N_e , can be written as

$$P_{\nu_e \rightarrow \nu_e} = 1 - \sin^2 2\theta_M \sin^2 \left(\frac{\Delta m_M^2 L}{4E} \right), \quad (1.19)$$

$$P_{\nu_e \rightarrow \nu_\mu} = \sin^2 2\theta_M \sin^2 \left(\frac{\Delta m_M^2 L}{4E} \right). \quad (1.20)$$

1.1.3 Oscillation Parameters

Neutrino oscillations in a vacuum are fully characterized by six parameters: three mixing angles (θ_{13} , θ_{12} , θ_{23}), two mass-splittings (Δm_{21}^2 , Δm_{31}^2), and one CP-violating phase (δ_{CP}). Most are determined by reactor, atmospheric, solar, and long-baseline neutrino experiments.

The solar neutrino analysis of SK [27], SNO [28], and the Kamioka Liquid scintillator Anti-Neutrino Detector (KamLAND) experiment [29] measured parameters θ_{12} and Δm_{21}^2 . Parameters θ_{23} and Δm_{32}^2 are measured by the atmospheric neutrino and log-baseline neutrino experiments: SK [30]; KEK to Kamioka (K2K) [31]; Main Injector Neutrino Oscillation Search (MINOS) [32]; and Tokai to Kamioka (T2K) [33] experiments. Measurements at reactor experiments (the Daya Bay [34], the Reactor Experiment for Neutrino Oscillation (RENO) [35], and the Double Chooz [36]) and T2K [37] established that the mixing angle, θ_{13} , was small but nonzero. The precise value of δ_{CP} is still unknown, but long-baseline experiments (T2K [38] and NOvA [39]) have begun to constrain it.

The values of these parameters are derived from a global fit of current neutrino oscillation data [40], as listed in Table 1.1. There are two possibilities of mass hierarchy, which depend upon the ordering of the neutrino mass eigenstates. The normal hierarchy (inverted hierarchy) corresponds to the order, $m_1 < m_2 < m_3$ ($m_3 < m_1 < m_2$).

1.2 Multi-messenger Astronomy

Cosmic rays (CR), electromagnetic radiation, neutrinos, and gravitational waves are the most important messengers that deliver information from celestial bodies to us. They are created by different processes, and they reveal varying knowledge about their sources. Therefore, observing these messengers is useful, but more comprehensive information can be obtained by observing their combinations.

Table 1.1: Best fit values of the neutrino oscillation parameters. The definition of Δm^2 is $\Delta m^2 = m_3^2 - (m_2^2 + m_1^2)/2$. The errors stated are at the 3σ level.

Parameter	Best Fit	
	Normal Hierarchy	Inverted Hierarchy
Δm_{12}^2 [10^{-5} eV 2]		$7.37^{+0.60}_{-0.44}$
$\sin^2 \theta_{12}$ [10^{-1}]		$2.97^{+0.57}_{-0.47}$
Δm^2 [10^{-3} eV 2]	2.50 ± 0.13	$2.46^{+0.14}_{-0.13}$
$\sin^2 \theta_{13}$ [10^{-2}]	$2.14^{+0.32}_{-0.29}$	$2.18^{+0.30}_{-0.32}$
$\sin^2 \theta_{23}$ [10^{-1}]	$4.37^{+1.79}_{-0.58}$	$5.69^{+0.68}_{-1.86}$
δ_{CP} [π]	$1.35^{+0.65}_{-1.35}$	$1.32^{+0.68}_{-1.32}$

1.2.1 CR

CRs are particles produced and accelerated by astrophysical sources. About 90% are protons; 9% are atoms, such as helium; and electrons compose less than 1% [41]. The origin of CRs and their processes of acceleration remain a mystery of astroparticle physics.

The magnitude of the kinetic energy of a nucleus is often measured with units of GeV and EeV. Figure 1.1 shows the flux of high-energy CRs for all particles, providing a good approximation of the power-law: $E^{-\gamma}$. The power-law index changes at two different points, creating a "knee" (around 3×10^{15} eV) and "ankle" (around 10^{19} eV). Although less certain, the most recent experiments revealed an extra feature around 10^{17} eV called the "2nd knee." The spectral indices are observed as:

- $\gamma \approx 2.7$ for about 10^{10} to 3×10^{15} eV
- $\gamma \approx 3.1$ for about 3×10^{15} to 3×10^{18} eV
- $\gamma \approx 2.6$ for about 3×10^{18} to 10^{20} eV

If high-energy CR fluxes are cosmological in origin, there should be a rapid steepening of the spectrum around 5×10^{19} eV. This is called the Greisen–Zatsepin–Kuzmin (GZK) limit [42, 43], which results from inelastic interactions of CRs with the cosmic microwave background (CMB).

Because CR particles arrive at the Earth at energies much larger than the thermal energies of typical astrophysical objects, specific acceleration mechanisms apart from blackbody radiation are needed to explain the spectra observed. It is known that CRs from the sun arrive at upwards of 10^8 to 10^{10} eV [45]. Therefore, the mechanism of acceleration of high-energy CRs probably differs from one energy region to another.

The acceleration process of CRs could be generated within our galaxies or at point-like sources of extreme extragalactic energy densities. In 1949, Fermi proposed a mechanism whereby particles could gain energy from collisions with moving

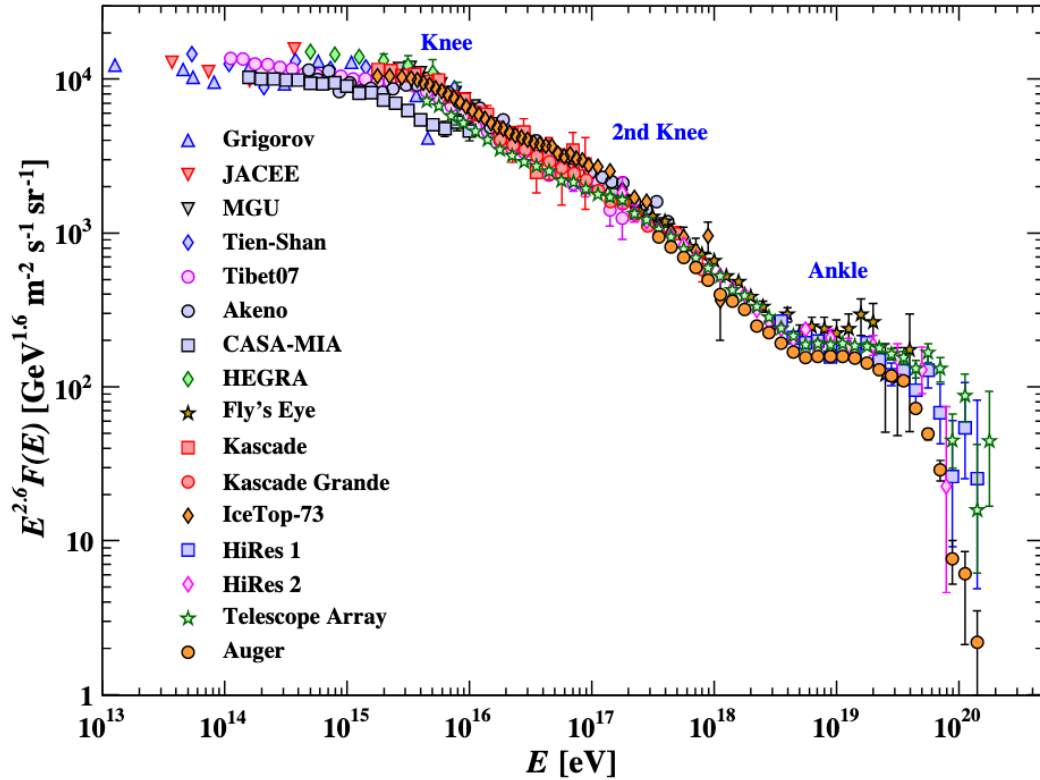


Figure 1.1: Energy flux spectra of CRs for all particles as a function of energy per nucleus obtained from air-shower measurements [44].

interstellar ionized gas clouds [46]. That mechanisms provided an estimate of achievable energies for particles trapped in the magnetic field of our galaxy. However, pure galactic acceleration is insufficient to produce CRs in the high-energy tail of the spectrum. The highest energetic CRs are probably created by extragalactic source (e.g., neutron stars, gamma-ray bursts, active galactic nuclei). Hillas reported that the maximum energy of a CR was a correlation between the magnitude of the magnetic field and the radius of the object [47]. However, if the magnetic field becomes too large, the protons lose more energy because of synchrotron radiation. Neutron stars and active galactic nuclei may not reach the GZK limit because of this synchrotron loss.

1.2.2 Gamma Rays

Gamma rays are produced by accelerated electrons and possibly protons; they have been measured at very high energies in the CR spectrum. Contrary to charged particles, photons are not deflected by magnetic fields, and they point straight to the objects from which they originated. Gamma rays, on the other hand, are produced by radiation or decay by both leptonic and hadronic processes.

Proton acceleration is always accompanied by photons and neutrinos generated by charged and neutral meson decays. These mesons are mostly pions and are generated by proton–proton collisions (pp) or photo–hadronic (p γ) interactions:

$$p + p \rightarrow \pi^\pm, \pi^0, K^\pm, K^0, p, n, \dots \quad \text{or} \quad , \quad (1.21)$$

$$p + \gamma \rightarrow \Delta^+ \rightarrow \pi^+ + n \quad \text{or} \quad , \quad (1.22)$$

$$p + \gamma \rightarrow \Delta^+ \rightarrow \pi^0 + p. \quad (1.23)$$

In both scenarios, the decays of the neutral pions, $\pi^0 \rightarrow 2\gamma$, give rise to a flux of high-energy gamma rays. The two gamma rays per meson produced by this decay are emitted isotropically in the rest frame but are boosted similar to the mesons from the laboratory frame. As a result, the original proton spectrum is reproduced after the gamma-ray spectrum rises above the production threshold energy.

The energy window of gamma-rays from radio to soft X-rays is dominated by radiation emitted by accelerated electrons propagating through a strong magnetic field. The radiation pattern of the relativistic electron in a magnetic field is beamed in the direction of the motion of the electron itself, which turns proportionally to the magnetic field. The synchrotron flux from its source having a power-law energy distribution of $dN/dE \propto E^{-\gamma}$ is shown to be

$$F \propto \frac{R^3}{d^2} B^{1+\alpha} f^{-\alpha}, \quad (1.24)$$

where the source having radius R at a distance d emits a population of particles. B is the magnetic field, f is the synchrotron frequency, and $\alpha = (\gamma - 1)/2$. Charged particles having masses greater than electrons suppress synchrotron radiation in proportion to their mass.

1.2.3 Neutrinos

It is important to search for neutrinos at CR sources to elucidate acceleration mechanisms. Because neutrinos do not interact with surrounding materials, owing to their very small cross-sections, it is possible to study the hadron processes that occur at CR sources.

The interaction of proton–proton collisions explains not only the production of gamma rays, but also the production of high-energy neutrinos. Together with π^0 , π^+ , and π^- are produced in approximately the same number. Although the neutral pion decays into two photons, the processes connected to charged pion decay are

$$\pi^+ \rightarrow \mu^+ + \nu_\mu \rightarrow e^+ + \nu_e + \bar{\nu}_\mu + \nu_\mu \quad \text{and} \quad , \quad (1.25)$$

$$\pi^- \rightarrow \mu^- + \bar{\nu}_\mu \rightarrow e^- + \bar{\nu}_e + \nu_\mu + \bar{\nu}_\mu. \quad (1.26)$$

The injected neutrino flavor ratios for neutrinos and anti-neutrinos depend on the details of energy loss mechanisms at the source. However, the neutrino oscillations over astrophysical distances will alter the injected flavor ratio, from which one expects to observe a nearly equal admixture of neutrino flavors in the measured flux, $(\bar{\nu}_e : \bar{\nu}_\mu : \bar{\nu}_\tau) = (\nu_e : \nu_\mu : \nu_\tau) \approx (1 : 1 : 1)$, at the Earth.

1.3 Active Galactic Nucleus (AGN)

AGNs are extreme extragalactic objects and candidates for CR accelerations at the highest energies. They are observable across a wide range of wavelengths up to 10^{27} Hz, and the most distant detected AGNs are at a redshift of $z = 7.1$ [48]. An AGN consists of a supermassive black hole (about 10^6 to 10^{10} solar masses) with an accretion disk at its gravitational potential.

From the unified view of AGNs [49], the black hole and accretion disk appear surrounded by a dusty torus and a cloud obscuring the AGN center, and a fraction of the AGN emits jets orthogonal to the rotating disk. For a 10^8 solar-mass black hole, the radius is about 3×10^{13} cm; the accretion disk emits between 1×10^{14} to 30×10^{14} cm; the clouds are located within about 2×10^{16} to 20×10^{16} cm; and the inner radius of the dusty torus is perhaps 10^{17} cm. Jets have been detected on scales from 10^{17} to several-times 10^{24} cm.

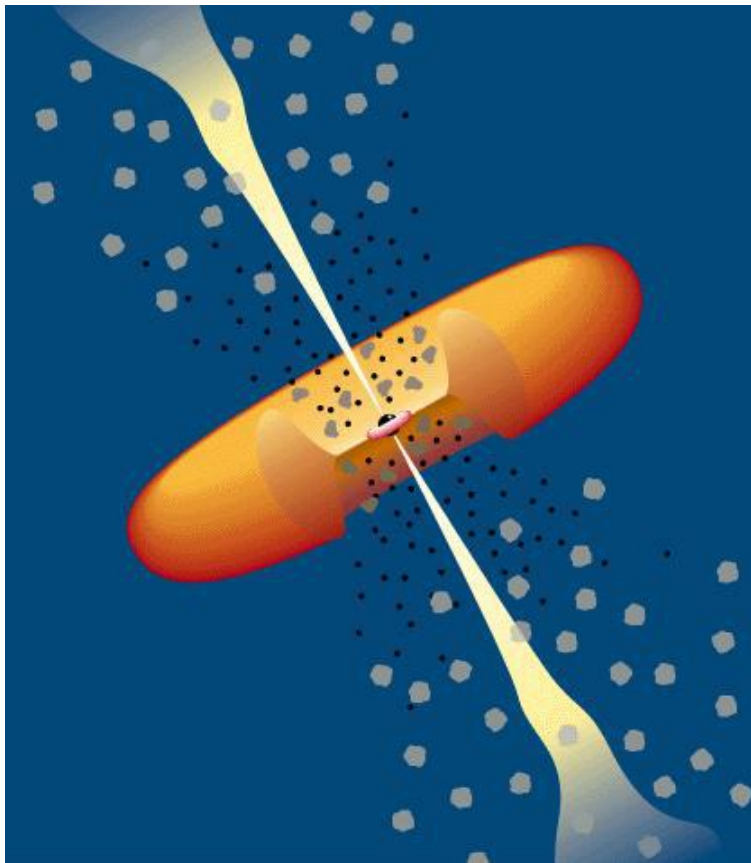


Figure 1.2: Schematic of AGN (not to scale) [49]. Surrounding the central black hole is a luminous accretion disk and a dusty torus. The clouds of gas move rapidly in the potential of the black hole. Beyond the torus, the clouds of gas move slower. The jets emanate from the region near the black hole.

1.3.1 Blazar

AGNs having jets aligned with the line of sight of the observer are classified as the blazars. These emit non-thermal radiation mainly from jets at all observed wavelengths and have broad absorption characteristics or no absorption at all.

The spectrum of a blazar is Doppler-boosted and blue-shifted because of the emission of light emitted at a small angle from a very relativistic jet [49]. It forms a characteristic shape having two wide humps (10 MeV to 100 GeV and 50 GeV to 10 TeV). Low-energy humps are assumed to originate from synchrotron radiation, but high-energy humps are not fully understood.

Blazars comprise two types of objects: BL Lac and flat-spectrum radio quasar (FSRQ). FSRQs show broad absorption lines, and BL Lac type objects display these lines only very weakly or not at all. The spectrum from a BL Lac usually extends to higher energies. Furthermore, blazars can be subdivided into classes based on the peak position of their first hump. If the first hump peaks above 10^{15} Hz (below 10^{14} Hz), the object is called a high- (low-) synchrotron-peak HSP (LSP) or high- (low-) synchrotron-peaked BL Lac HBL (LBL) for BL Lac blazars [50, 51]. The intermediate objects are called ISP or IBL.

Figure 1.3 shows the spectral-energy distribution of Markarian 421 (MRK421), resulting from the 4.5-month-long multifrequency campaign. MRK421 is one of the closest (redshift $z = 0.031$ [52]) and the most prominent BL Lac blazar. It clearly distinguishes the two hump characteristic. The first is a tracer of synchrotron emission, and the second can be attributed to hadronic processes.

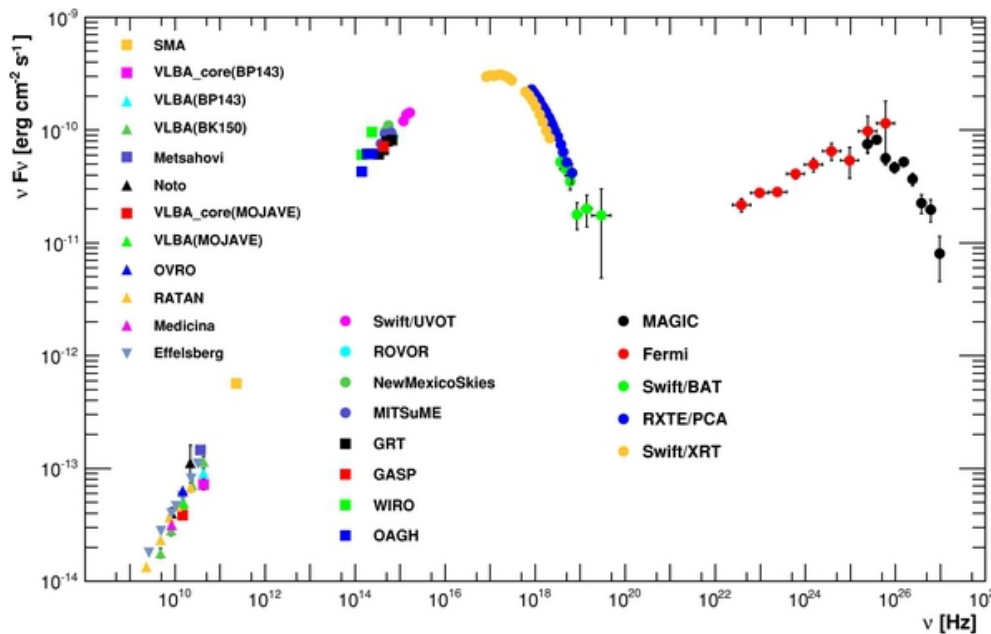


Figure 1.3: Spectral-energy distribution of Markarian 421 averaged over all observations taken during the multifrequency from January 19 to June 1, 2019 [53, 54].

1.3.2 Neutrinos from Blazars

Neutrino detection from blazars help probe hadronic interactions in the jets. Furthermore, it helps clarify the structure of relativistic jets, jet content, and acceleration processes.

The IceCube Neutrino Observatory [55] detected a high-energy neutrino event having an estimated energy of 290 TeV on 22 September 2017 at 20:54:30:43 UTC [19, 56]. The event was called IceCube-170922A. The arrival direction of the neutrino event coincided with the location of a blazar named TXS0506+056, assuming a BL Lac type blazar (redshift $z = 0.3364 \pm 0.0010$ [57]) and located at a right ascension (R.A.) of 77.3582° and declination (Dec.) of $+5.6931^\circ$ (J2000 equinox) [58]. Within a minute of detection, the information of this event was shared via the Gamma-ray Coordinate Network (GCN)² and follow-up observations over a wide range of energies have been carried out at several observatories. According to the Fermi All-sky Variability Analysis (FAVA) [59], TXS0506+056 brightened in the GeV band starting in April 2017 [60]. Independently, Fermi's Automated Science Processing (ASP) [61] found a gamma-ray flare. The coincidence between the neutrino arrival direction and the blazar location and timing correlated with the associated gamma-ray flare suggesting that the observed neutrinos originated from the blazar.

Figure 1.4 and 1.5 summarize the multi-wavelength light curves and the changes in the broadband spectral-energy distribution. To calculate the energy flux, the IceCube collaboration considered two neutrino-emission periods. In the first scenario, neutrinos were assumed to have been emitted only during the 6-month period corresponding to the duration of the gamma-ray flare. The second scenario presumes that neutrinos are emitted over the entire IceCube observation (7.5 years).

Furthermore, time-dependent analysis was performed at the coordinates of TXS-0506+056 [56]. As a result of the analysis, one data period contained a significant signal, identified by both time window shapes (gaussian-shaped and box-shaped windows). The excess consists of 13 ± 5 events above the expectation from the atmospheric background. However, there was no excess gamma-ray flare nor a significant gamma-ray spectral change with respect to the average during the time of 2014 to 2015 (Figure 1.4).

²The GCN/AMON : <https://gcn.gsfc.nasa.gov/amon.html>

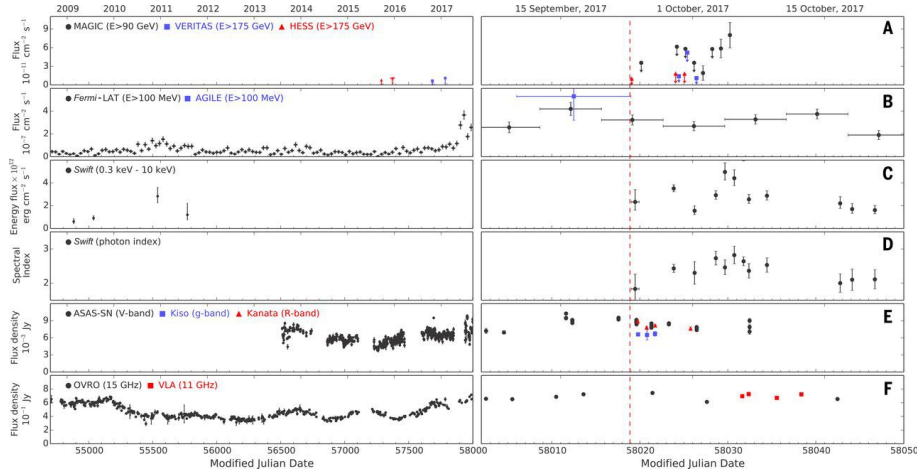


Figure 1.4: Time-dependent multi-wavelength observations of TXS0506+056 [19]. From top to bottom, the panels show differences in observed energy. The left panels show measurements between 22 August 2008 and 6 September 2017. The right panels show an expanded scale for times ranging from 6 September to 24 October 2017. The red dashed-line marks the detection time of the neutrino IceCube-170922A.

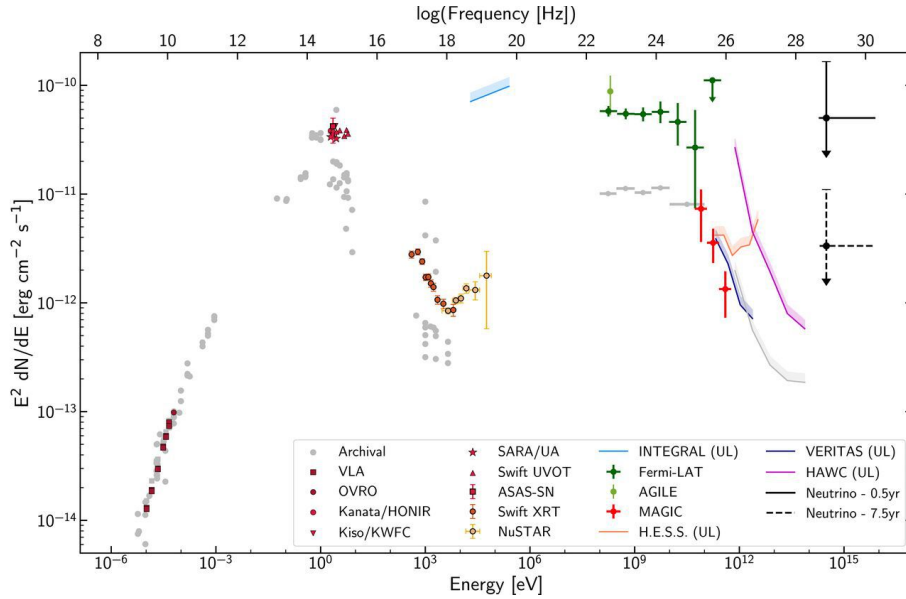


Figure 1.5: Broadband spectral-energy distribution of the blazar TXS0506+056 with neutrino flux [19]. The distribution based on observations obtained within 14 days of the detection of the IceCube-170922A event. The neutrino flux upper limits produced on average per detection over a period of 6 months and 7.5 years are shown. The neutrino energy assumes the most probable energy (311 TeV).

2 Super-Kamiokande (SK)

SK is a large water Cherenkov detector build in the Kamioka mine at a depth of about 1,000 m underground (2,700 m water equivalent) [62]. It is located at latitude $36^{\circ}25'N$ and longitude $137^{\circ}18'E$ in Mt. Ikenoyama, Gifu Prefecture, Japan. Owing to the overburden of the mountain above the detector, the cosmic muon background is reduced by a factor of $\sim 10^{-5}$, compared to that at the mountain's surface.

The detector is a cylindrical tank, and it is optically separated into inner and outer detectors. The tank contains a total of 50 kilotons of ultra-pure water as the neutrino target. The layout of the detector is shown in Figure 2.1³.

The primary purpose of this experiment was to search for proton decay and study neutrinos from atmospheric, solar, and astrophysical sources, including supernovae, gamma-ray bursts, and active galactic nuclei. SK also serves as the far detector for the Tokai-to-Kamioka (T2K) long-baseline neutrino experiment [63].

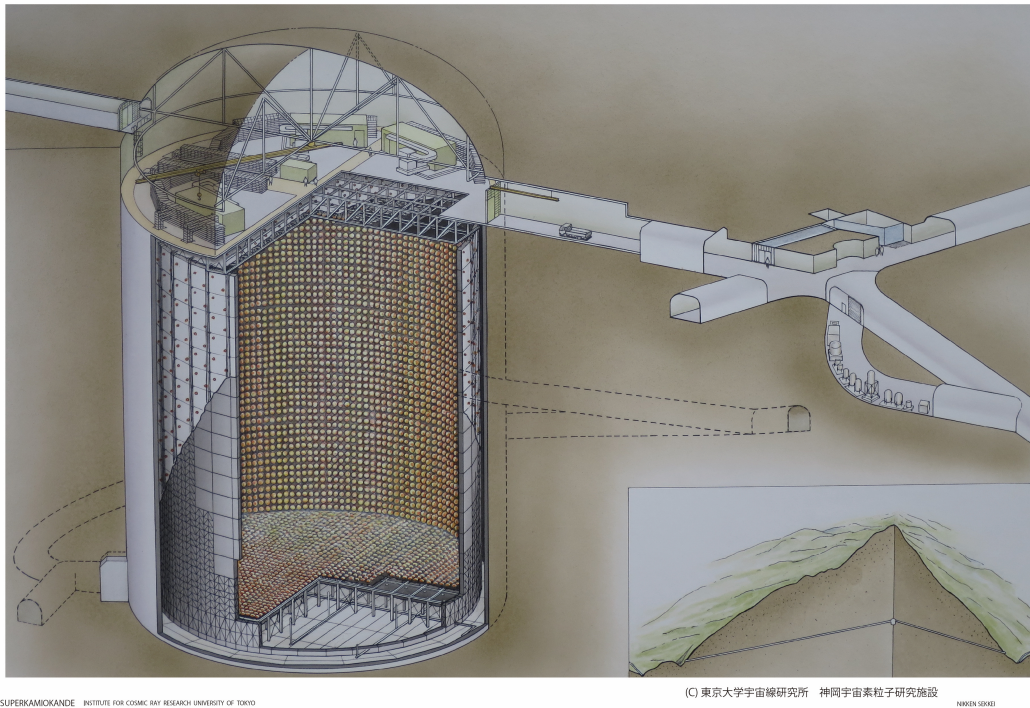


Figure 2.1: Schematic of the SK detector (cutaway view).

³The figure taken from the web page of Super-Kamiokande <http://www-sk.icrr.u-tokyo.ac.jp/sk/index.html>

2.1 Cherenkov Radiation

In dielectrics, having a refractive index greater than 1, an electromagnetic shock called Cherenkov radiation occurs when the velocity of charged particles is greater than the speed of light passing through the medium.

$$v > \frac{c}{n}, \quad (2.1)$$

where v is the velocity of the charged particle, c is the speed of light in a vacuum, and n is the refractive index of the medium. This phenomenon was first discovered by Cherenkov [64], and a theory of this effect was later developed by Frank and Tamm [65]. The direction of the emitted light can be calculated using classical physics, the Huygens–Fresnel principle. The effect is caused by coherent radiation from atoms and molecules excited along the charged-particle trajectory. Figure 2.2 shows a schematic of Cherenkov radiation, comprising the movement of a relativistic and non-relativistic charged particle.

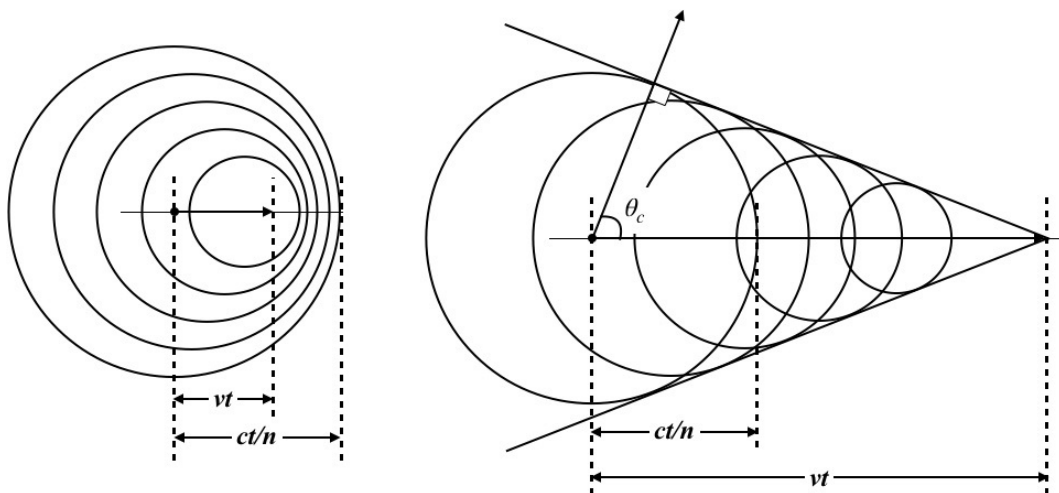


Figure 2.2: Cherenkov radiation. A particle moves along the projection of the left to the right during time t in the medium. The case of $\beta < c/n$ (left) and $\beta > c/n$ (right) are shown .

The relativistic charged particle can cross a distance of $x_p = vt$. However, the Cherenkov radiation travels radially at a distance $x_c = ct/n$. Thus, the angle between the direction of Cherenkov light and the direction of the charged particle is defined as the Cherenkov angle θ_C ,

$$\cos \theta_C = \frac{x_p}{x_c} = \frac{1}{n\beta}, \quad (2.2)$$

where n is the refractive index of the medium, and β is the ratio of the velocity of the particle to the speed of light in a vacuum, $\beta = v/c$. The refractive index of the ultra-pure water of SK is about 1.33 for 580 nm photons. Thus, the maximum

emission angle of Cherenkov light is about 42° at $\beta = 1$. Assuming that a particle's charge is equal to 1, the energy of emitted photon is given by the Frank–Tamm formula [66, Chap. 6]:

$$\frac{d^2E}{dx d\omega} = \frac{\hbar\alpha}{c} \omega \left(1 - \frac{1}{\beta^2 n^2}\right), \quad (2.3)$$

where α is the fine-structure constant, x is the per-unit path length, and ω is the frequency. There exists a relationship between frequency and wavelength, $\omega = 2\pi c/\lambda$, and between the energy and the number of photons, $E = Nh\nu = Nhc/\lambda$. It is easy to convert this to an expression regarding the number of Cherenkov photons generated:

$$\frac{d^2N}{dx d\lambda} = \frac{2\pi\alpha}{\lambda^2} \left(1 - \frac{1}{\beta^2 n^2}\right). \quad (2.4)$$

With SK, Cherenkov radiation is estimated to emit hundreds of photons per centimeter. From this relation, the minimum energy needed to emit at least one photon can be calculated as the Cherenkov threshold. The threshold is thus reached when the expression is exactly equal to zero, or

$$\beta_{\text{thr}} = \frac{1}{n}. \quad (2.5)$$

Because there exists relationships, $E = \gamma mc^2$ and $\gamma = (1 - \beta^2)^{-1/2}$, the energy threshold can be written as

$$E_{\text{thr}} = \frac{mc^2}{\sqrt{1 - \frac{1}{n^2}}}, \quad (2.6)$$

where m is the mass of the charged particle. The Cherenkov threshold of each charged particle detected with SK (refractive index $n = 1.33$) is shown in Table 2.1.

Table 2.1: Cherenkov threshold of various particles.

Particle	Rest Mass [MeV/c ²]	Cherenkov Threshold [MeV]
e^\pm	0.511	0.775
μ^\pm	105.7	160.3
π^\pm	139.6	211.7
K^\pm	493.7	748.8

With SK, neutrinos are indirectly observed when they interact with the water and produce charged particles above the Cherenkov threshold. The ring-image of Cherenkov light is detected by the PMTs on the detector wall. For each event, the information of the photon arrival time and the integrated charge at each PMT is recorded. Thus, it is possible to identify the vertex position of the neutrino interaction, the number of Cherenkov rings, the momentum of the charged particle, and the particle type of the daughter particle. The details are described later.

2.2 SK Detector

The detector shape is cylindrical: 39.3 m diameter and 41.4 m tall. It contains 50 kilotons of ultra-pure water. The inside of the tank is optically separated into an inner detector (ID) and an outer detector (OD). Between the ID and OD, there is a steel support structure having a width of about 60 cm to accommodate the PMTs (Figure 2.3). The surface of the SK dome cavity above the tank houses five electronic huts, a linear accelerator for detector calibration, and storage for various equipment. Additionally, to avoid disturbing the photoelectrons (p.e.) in the PMTs with the Earth's magnetic field (about 450 mG), 26 Helmholtz coils are lined up along the wall of the SK tank, reducing it to 50 mG.

The ID wall exists about 2.7 m inward from the wall of the SK tank and about 2.6 m from the top and bottom, comprising a total water mass of about 32 kilotons. It consists of 20-inch PMTs facing inward, and the space between the ID PMTs is covered with a black sheet to reduce unnecessary photon reflection. ID PMTs are arranged in modules, each consisting of 3×4 PMTs spaced about 70 cm from each other. A fiducial volume (FV) of the ID is defined as the cylindrical volume 2 m inward from the ID wall and has a mass of 22.5 kilotons.

The OD region has a width of about 2.2 m along the wall of the SK tank and is about 2.1 m thick at the top and bottom with a total water mass of about 18 kilotons. It tags outgoing charged particles, and can also be used as a veto detector for cosmic rays and the gamma rays from surrounding rocks. It detects photons with 1,885 8-inch PMTs facing outward from the support structure, and the space between the OD PMTs is covered with a white Tyvek sheet to maximize the light detection efficiency.

2.2.1 History of SK

The Kamioka Nucleon Decay Experiment (KamiokaNDE) detector, the predecessor of SK, has a tank 15.6 m in diameter and 16 m in height. It contains about 3 kilotons of pure water and 948 PMTs in the ID with 123 PMTs in the OD [67]. Its observation was carried out from July 1983 to April 1996, during which it observed the neutrinos from a supernova (SN1987A) [15].

The construction of the SK detector started in 1991 as a successor to the KamiokaNDE experiment. For the SK tank, the cavity in the mine was excavated until the middle of 1994. Afterwards, water-tank construction started, and PMTs were installed until the end of 1995. Water-filling started in January 1996. Experimental data were collected starting 1 April 1996 after a 1-month test run. From the start of the operation to the present, SK has five phases (i.e., SK-I, SK-II, SK-III, SK-IV, and SK-V). Furthermore, the SK-Gd phase, in which gadolinium is loaded to ultra-pure water to improve neutron identification accuracy, is scheduled to start.

SK-I

The SK-I phase started 1 April 1996 continually operated until July 2001. At the ID, 11,146 PMTs were placed at intervals of about 70 cm, and the photo coverage

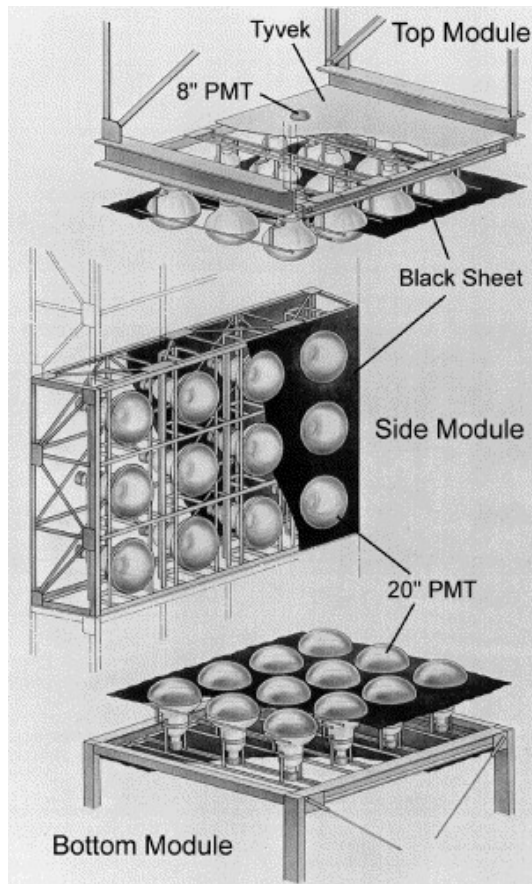


Figure 2.3: Schematic of the module structure of the PMT support frame [62]. The inward-facing ID PMTs and the outward-facing OD PMT can be seen. The region of ID and OD are optically separated by a black sheet inside the support structure and a Tyvek sheet outside the support structure.

was 40%. During this period, in 1998, the SK collaboration released the first highly significant experimental evidence for neutrino oscillations [68]. Furthermore, the K2K experiment [31, 69, 70] started during that phase. The experiment was the first accelerator neutrino long-baseline experiment, which sent a nearly pure ν_μ beam 250 km from the Japanese accelerator facility KEK to the SK. The main data was taken from June 1999 to November 2004 and 112 beam-originated neutrino events were observed. From this observation, the probability of the expectation for no neutrino oscillation was estimated to be 0.0015% (4.5σ) [31].

SK-II

On 12 November 2001, one of the bottom PMTs imploded during a post-maintenance tank refill. A total of 7,796 PMTs were damaged (6,779 ID PMTs and 1,017 OD PMTs) because of the subsequent chain reaction.⁴ Since this accident, each ID PMT has been covered with an acrylic and fiberglass reinforced plastic (FRP) case to protect from shock waves. The remaining ID PMTs were relocated, and the new OD PMTs were prepared to resume observations. The observation period from

⁴The details of the accident were reported at <http://www-sk.icrr.u-tokyo.ac.jp/cause-committee/index-e.html>.

October 2002 to October 2005, called SK-II, was operated with 5,182 covered ID PMTs and 1,885 OD PMTs, and the photo coverage of ID was 19%.

SK-III

In October 2005, work began to reinstall PMTs. This work was completed in July 2006, and full operation with 11,129 ID PMTs was given. 17 ID PMTs were removed, compared with SK-I, owing to the size of the acrylic cover. However, the photo coverage of ID was 40%. Moreover, the barrel and end-cap regions of OD were optically separated by the Tyvek sheet directory upward and downward from the barrel region. Via optical partitioning, it was possible to distinguish between neutrino events with leptons exiting from ID and muon events, both activating the top/bottom and barrel regions of the OD. This helped improve the reduction of background. The data period from July 2006 to August 2008 is called SK-III.

SK-IV

Since September 2008, the detector was shut down once because all of the front-end electronics were upgraded. SK-IV then was continued from September 2008 to June 2018. During this period, the T2K experiment using SK as a far detector started, and on 24 February 2010, the first event of the T2K experiment was successfully observed at SK.

SK-V

Repair work started in June 2018 for the next SK phase, known as SK-Gd. The main purpose was to repair a leak in the SK tank, install new plumbing to smooth-out the water flow in the tank, replace dead ID and OD PMTs, and clean up the detector. SK-V has been running since January 2019. It represents the final phase of using ultra-pure water as a neutrino target at SK. A summary of the differences between each of the SK phases can be found in Table 2.2.

SK-Gd

The SK-Gd phase is the next project, which will dissolve gadolinium in ultra-pure water at SK [71]. Gadolinium has the largest cross-section of thermal neutron capture among natural elements, and a total of about 8 MeV gamma rays are emitted. Therefore, it is possible to distinguish between neutrino reactions with neutrons and those without. This new phase, SK-Gd, is scheduled to start March 2020.

the PMT to the p.e.. The average collection efficiency at the first dynode is 70%, which is uniform within $\pm 7\%$ across the whole PMT surface. The gain of the PMT is 1×10^7 at a high voltage around 2,000 V. The single-p.e. peak can be clearly seen in the charge distribution shown in Figure 2.7. The relative transit time spread for the single p.e. signal is about 2.2 nsec (1σ), which was got from the test with 410 nm wavelength light using a typical ID PMT. The average dark-noise rate at the 0.25 p.e. threshold is about 3 kHz.

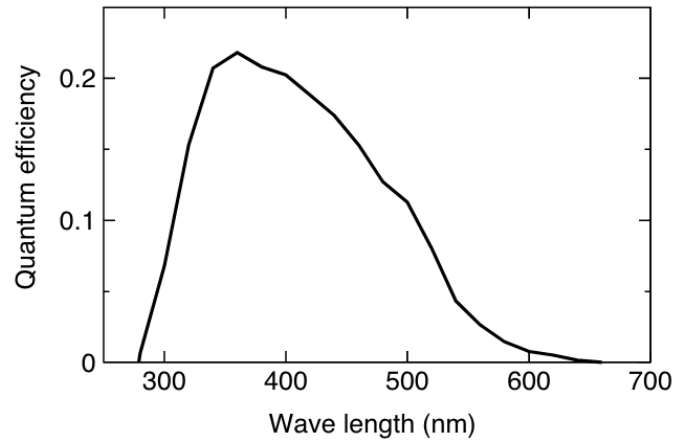


Figure 2.6: Quantum efficiency of the 20-inch ID PMT as a function of the light wavelength [nm] [62].

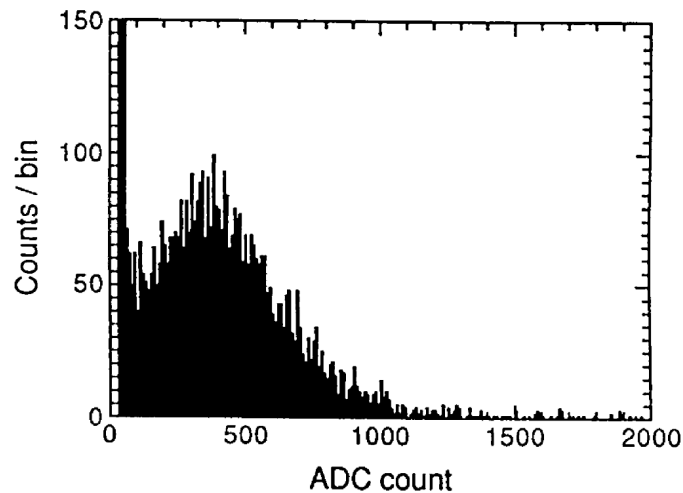


Figure 2.7: Single-p.e. pulse height distribution expressed as a light-intensity-dependent analog-to-digital-converter (ADC) count. The peak nearest zero ADC count is caused by the PMT dark current [62].

2.2.3 OD PMT

The OD has 1,885 PMTs with a diameter of 8-inch (22 cm). During the SK-I phase, OD PMTs were reused from the IMB experiment [75] after it was decommissioned in 1991. However, after the accident in 2001, most OD PMTs were replaced. The new OD PMT, Hamamatsu R5912 PMT, is the same size and has similar characteristics as the older IMB PMT. Each OD PMT is attached to a 60 cm×60 cm×1.3 cm wavelength-shifting (WS) plate to compensate for the relatively few numbers of PMTs, also taken from the IMB detector. The WS plates are acrylic-doped panels with a 50 mg/L scintillator, bis-MSB ($C_{24}H_{22}$). It absorbs light in the ultraviolet region and emits blue green light closer to the sensitivity peak of the OD PMTs. The light collection efficiency thus increased by 60%, but the timing resolution slightly decreased from 13 to 15 nsec for the single-p.e. signal. Because the OD functions primarily as a veto, observing the extra photons is of much more importance than better timing resolution.

The OD PMTs are uniformly distributed using 1,275 tubes on the barrel, 302 tubes at the top, and 308 tubes at the bottom. The OD is lined with a layer of Tyvek between the OD PMTs and is over 80% reflective to enhance the OD light collection. The relationship between ID PMT and OD PMT is shown in Figure 2.8.

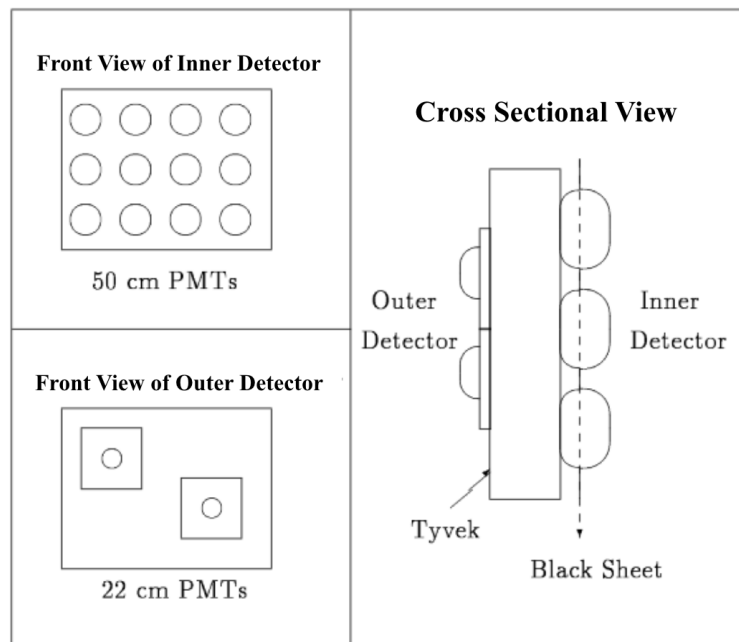


Figure 2.8: Schematic of a module of ID and OD PMTs [76]. Each OD PMT is housed in an inner structure that holds 12 ID PMTs facing inward for every 2 OD PMTs facing outward.

2.3 Water and Air System

2.3.1 Water Purification System

The original SK water was produced from the mine, and it was thus very important to keep the water transparency as high as possible. It is also important to remove radioactive materials, especially radon and radium. Gamma rays emitted from such radioactive nuclides become the background for observation in the MeV-energy range. The water is constantly circulated through a purification system at a flow rate of about 50 tons/h. The system is summarized in Table 2.3.

Table 2.3: Water Purification System: the components and their purpose and result.

Component	Purpose & Results
1 μm Mesh Filter	Removes dust and larger particles
Heat Exchanger	Cools water to suppress the growth of bacteria. Typical water temperatures before the first heat exchanger and after the second heat exchanger are 14.2 $^{\circ}\text{C}$ and 12.9 $^{\circ}\text{C}$, respectively
Cartridge Polisher	Eliminates heavy ions which also reduce water transparency. It is able to remove ions such as Na^+ , Cl^- , Ca^{2+} , and others
Ultraviolet Sterilizer	Kills bacteria that could not be killed with a heater exchanger
Radon-reduced Air Dissolving	Dissolves radon-reduction air into the water to increase radon removal efficiency at the vacuum degasifier stage
Reverse Osmosis Filter	Further removal of contaminations heavier than 1,000 molecular weight. This is newly added when the SK-III phase
Vacuum Degasifier	Removes dissolved gases in water, such as the oxygen and radon. Radon gas is removed about 96% and oxygen gas is also removed about 99%
Ultra Filter	Removes minute particles of the order of 10 nm
Membrane Degasifier	Removes radon dissolved in water with about 83% efficiency. After going through the system, the radon concentration is reduced to less than $0.4 \pm 0.2 \text{ mBq/m}^3$

The typical resistivity of water entering the purification system from the detector is about $11 \text{ M}\Omega \cdot \text{cm}$. After purification, the water has an average resistivity of $18.20 \text{ M}\Omega \cdot \text{cm}$, approaching the chemical limit. Thanks to this water system, the

transparent of ultra-pure water reaches about 90 m.

2.3.2 Air Purification System

The air in the mine is richer in radon gas than is the outside of the mine, because the rocks of mine contain radon. The concentration of radon gas inside the mine is about 1,000 to 2,000 Bq/m³ during summer and about 100 to 300 Bq/m³ during winter because of the changing air-flow patterns. To reduce the radon level in the air, an air purification system is used. It consists of three compressors, a buffer tank, dryers, filters, and activated charcoal filters. The resulting radon concentration is less than 3 mBq/m³, which is supplied between the water surface and the top of the SK tank.

2.4 Electronics and Data Acquisition (DAQ) System

The DAQ system for SK-I and SK-III (1996–2008) phases used the analog timing module (ATM) of the Tristan KEK Online (TKO) standard [77, 78]. During those phases, the DAQ system did not undergo any major upgrades. During the SK-IV phase, the ATM was replaced with new electronics, QBEE [79], short for a charge-to-time converter (QTC) based electronics with ethernet. Owing to the QBEE, the dead time associated with the DAQ system was reduced, the dynamic range was expanded, and the energy threshold was lowered.

The data analyzed in this work spans SK-I through SK-IV phases. The detailed description of the original DAQ system and the new DAQ system are provided.

2.4.1 ID Electronics and DAQ: SK-I to SK-III

Each ID PMT signal is connected to an ATM, and each ATM accepts 12 input channels. 20 ATMs are included in each TKO crate with a super control header (SCH) module and go/nogo (GONG) module. The SCH module is a bus-interface module between TKO and Versa Module Europa (VME). The GONG module distributes control signals as a master module to its slave module. In the VME crate, there are six data-buffer modules (i.e., super-memory partner (SMP) and an Sbus-VME interface). There are four separate electronics huts atop of the SK tank, each having 12 TKO system crates and two VME crates. The schematic of the electronics system is shown in Figure 2.9.

Figure 2.10 shows a schematic of the analog input block of the ATM. The signal from each PMT has two switching pairs of charge-to-analog converter (QAC) and time-to-analog converter (TAC) to measure the charge of the input pulse and the time. The QAC provides 550 pC full range with 0.2 pC resolution, and the TAC provides 1.2 μsec full range in time with 0.3 nsec resolution. Each PMT signal is divided by four after amplification at a factor of 100.

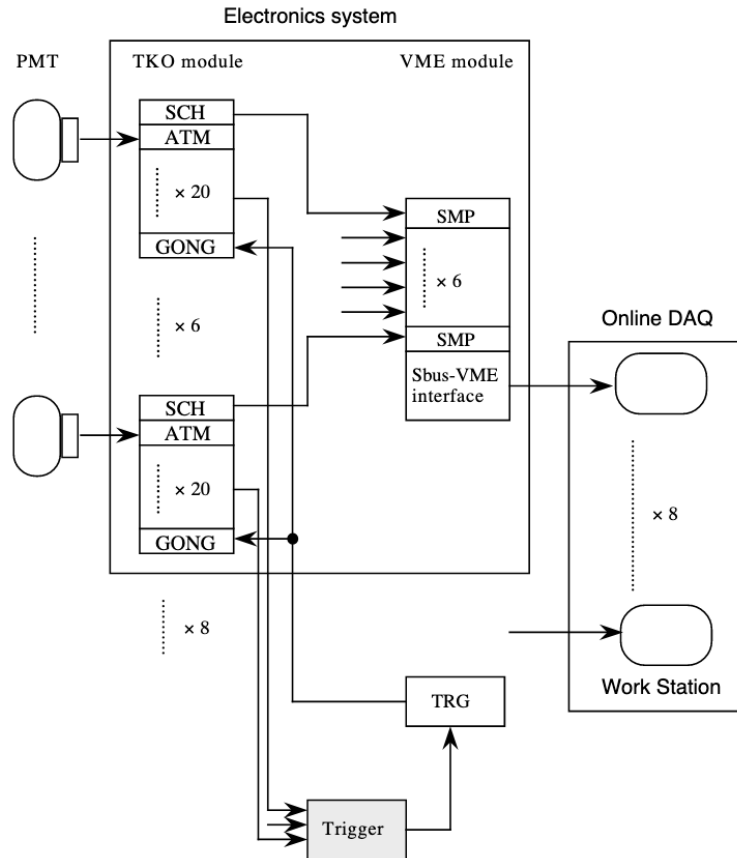


Figure 2.9: Logic diagram of the electronics system for the ID used with SK-I to SK-III [80].

One PMT signal travels through a discriminator threshold that is set to about 0.25 p.e.. When the pulse height of a signal exceeds the threshold, a 900 nsec gate signal as a HIT signal, a 400 nsec gate signal for QAC, and a start signal for the TAC are generated. For the HIT signal, any subsequent PMT signal is rejected. Simultaneously, a rectangular signal (200 nsec wide and 15 mV pulse height) is generated. The rectangular signal from every 12 PMTs are summed and output as the ID-HITSUM signal.

The other two PMT signals are fed to the QAC and TAC. If the global trigger arrives within 1.3 μ sec after the HIT signal, the charge/timing information from the QAC/TAC are digitized by an ADC. Otherwise, the readouts of QAC/TAC are cleared. The ADC outputs are stored in the 1,024 word first-in first-out (FIFO) memory with an event number. It takes 5.5 μ sec to convert from analog to digital and store it in memory, during which time the signal is not processed. Therefore, the QAC/TAC has two channels to minimize the electronics dead time during data collection for two successive events, such as a muon followed by its decay electron.

The final signal from the PMT is an output signal without a discriminator threshold (i.e., PMTSUM). The timing chart of the signal in the ATM is shown in Fig-

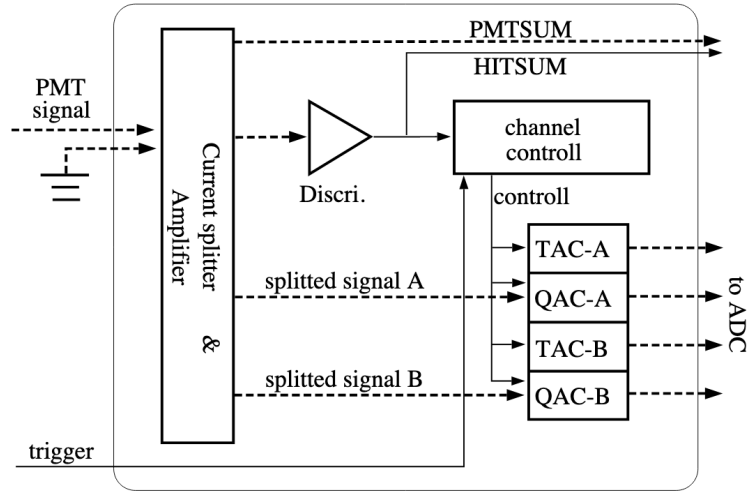


Figure 2.10: Block diagram of the circuit in the ATM [81].

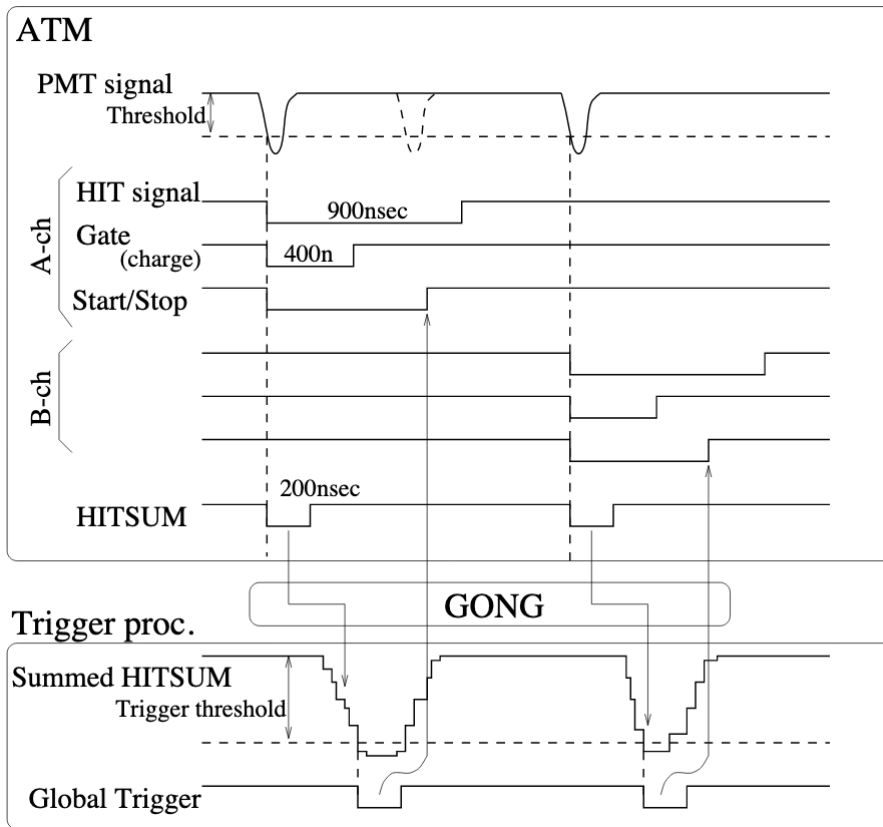


Figure 2.11: Timing chart for signal and trigger in an ATM [80].

ure 2.11

2.4.2 OD Electronics and DAQ: SK-I to SK-III

The schematic of the electronics system for OD is shown in Figure 2.12. The OD PMT signal is connected to the paddle cards, and each paddle card handles 12 OD PMTs. The signals from four paddle cards are sent to the QTC module. The QTC output signals are digitized using a LeCroy 1877 multi-hit time-to-digital converter (TDC), which can record up to two QTC pulses. The fastbus crate holds four modules: five TDCs, an event-number latch, a fastbus smart-crate controller (FSCC), which reads out the signals recorded by the TDCs, and a custom-built interface board. The fastbus crate is placed in each electronics hut with ID electronics. The paddle cards fan-out high voltage from one of the mainframe channels into the OD PMT output. Thus, it plays a role in picking off the PMT signals through a high voltage capacitor, allowing the disconnection of the channel. All 12 outputs have jumpers.

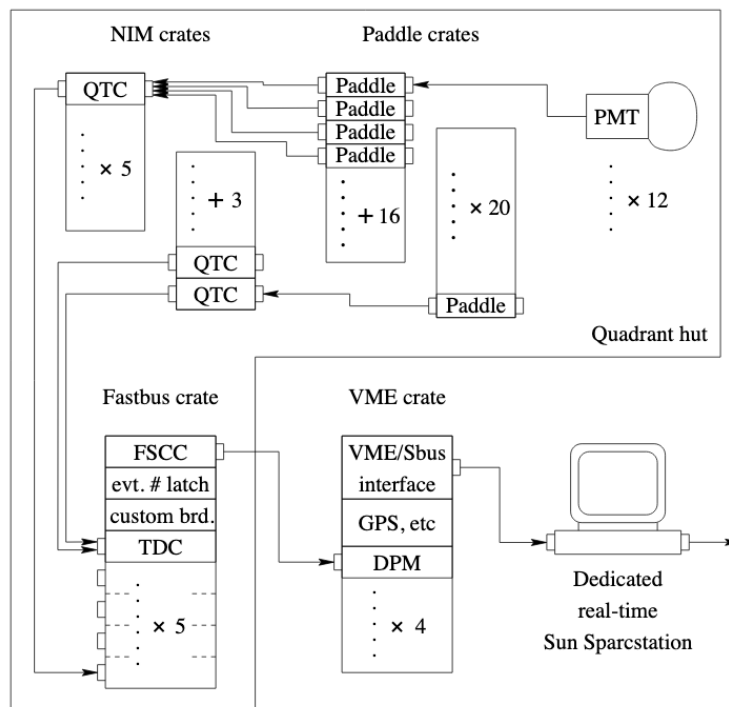


Figure 2.12: Data acquisition system for OD [82].

The purpose of the QTC modules is to measure the hit time and charge of the OD PMT signal. The output of the QTC module is a logic pulse. The leading edge of the pulse represents the hit-arrival time, and the width is proportional to the integrated charge of the OD PMT pulse. The QTC modules also provide an OD-HITSUM signal of 200 nsec width and 20 mV pulse, as does the ID.

Each TDC module behaves as a circular buffer that can store pulses with a resolution of 0.5 nsec. The dynamic range was originally set to 32 μ sec, centered around the trigger time. However, after September 1996, the width is set to 16 μ sec

which starts from 10 μ sec prior to trigger timing to reduce the data size. The TDC signal is then read by the FSCC, and the stored data are sent to the online computer via the VME bus.

2.4.3 Hardware Trigger: SK-I to SK-III

There are three types of ID triggers: the high energy (HE) trigger, the low energy (LE) trigger, and the super low energy (SLE) trigger. Trigger thresholds are defined by the level of the ID-HITSUM signal. The HE trigger is used to identify CR muon, atmospheric neutrinos, and proton decay. The LE is used for solar neutrino analysis, and SLE was implemented in May 1997 to perform solar neutrino analysis at lower energy.

During the SK-I phase, the HE trigger requires the pulse height of the ID-HITSUM signal to exceed a threshold of -340 mV within a 200 nsec time window. The HE trigger rate is about 5 Hz with an energy threshold of 10 MeV. The threshold of LE trigger is set to -320 mV, equivalent to a signal expected from a 5.7 MeV electron with 50% trigger efficiency. The LE trigger rate is about 11 Hz with an energy threshold of 8 MeV. The threshold level of the SLE gradually decreases as the trigger central processing unit (CPU) power increases. The threshold is set to -186 mV in July 2000, which is equivalent to signal expected from a 4.6 MeV electron, and the trigger rate is about 1 kHz. In the SK-II and SK-III, the same trigger scheme having different thresholds for each phase is used. The trigger conditions in each phase are summarized in Table 2.4.

Table 2.4: Trigger threshold for each SK phase. The SLE threshold is sometimes lowered during SK-I phase, and here is the final value.

Trigger Type	SK-I	SK-II	SK-III
High Energy (HE)	-340 mV	-180 mV	-320 mV
Low Energy (LE)	-320 mV	-152 mV	-302 mV
Super Low Energy (SLE)	-186 mV	-110 mV	-186 mV
Outer Detector (OD)	19 hits	19 hits	19 hits

The OD trigger is generated using a similar procedure as the one for ID. The threshold for the OD trigger corresponds to 19 hits of the OD PMTs in a 200 nsec time window. If the ID does not trigger on its own within 100 nsec, the OD alone will trigger the readout of the full detector.

These four trigger signals (i.e., HE, LE, SLE, and OD) are fed to the hardware trigger (TRG) module. When any of the trigger types is asserted, the TRG module generates a global trigger signal and a 16-bit event number. These are sent to all electronics huts to initiate DAQ for the current event.

2.4.4 Electronics and DAQ for ID & OD: SK-IV and SK-V

To improve detector sensitivity, new front-end electronics were installed in September 2008. The existing ATMs were replaced with QBEE boards, which are housed in the same TKO crates used to house the ATMs. However, the readout scheme was completely changed. The output signal from QBEE is now transmitted to the on-line computers via ethernet cables using TCP/IP. This greatly improves the transfer time for data and eliminates bottlenecks, which were sometimes caused by the TKO readouts in the original DAQ. The same QBEE is also used for the OD PMTs.

Each QBEE board is equipped with eight QTCs, which are custom application-specific integrated circuits (ASIC) [83, 84]. Because each QTC has three inputs, one QBEE board processes the signal from 24 PMTs. As shown in Figure 2.13, the output signal of the QTC is sent to the multi-hit TDC.

The digitized information of the TDC is sent to a field-programmable gate array (FPGA) for data-sort mapping (DSM). There are four DSM chips in each QBEE board, and each DSM chip deals with data from six input channels. The DSM outputs are sent to another FPGA, called the system-interface controller (SIC). SIC sorts the data from the DSM and stores them into FIFO memory.

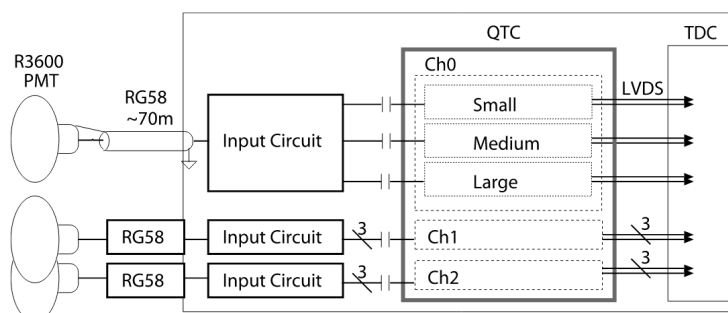


Figure 2.13: Block diagram of the QTC and its surroundings. PMT signals are sent to the QTC using an RG58 coaxial cable and are divided among three gain ranges. Output signals are generated with low-voltage differential signaling (LVDS) drivers. The figure was taken from [84].

Each QTC channel has three gain ranges (i.e., small, medium, and large), which can be adjusted using an external resistor network. When the relative gain ratio is $1: \frac{1}{7}: \frac{1}{49}$, the charge dynamic ranges from 0.2 to 2,500 pC. Following the gain stage, the signal from PMTs is amplified using a low-noise amplifier (LNA), delayed by a low-pass filter (LPF), processed by a voltage-to-current (V/I) converter, and integrated using a capacitor. One of the output waveforms of the V/I converter is saved as the analog sum (i.e., PMTSUM).

The other output signal is sent to the charge integration stage. When the amplified signal crosses the discriminator threshold, the leading edge of the output signal represents this timing, and a trigger-flag signal (HIT) is generated. Starting

with the HIT-trigger flag, three gates are created: charging, discharging, and veto (see Figure 2.14). The charging gate operates for 400 nsec, the switch between the V/I converter and charging capacitor closes, and charge accumulates in the capacitor. After operation of the charge gate, the discharging gate operates for 350 nsec. During this phase, the switch between the discharging current source and capacitor closes, and arriving signals are ignored. Then, the reset and the veto gate are issued. The width of the veto gate is 150 nsec, and all input signals are ignored. In total, the processing time for one input signal is 900 nsec.

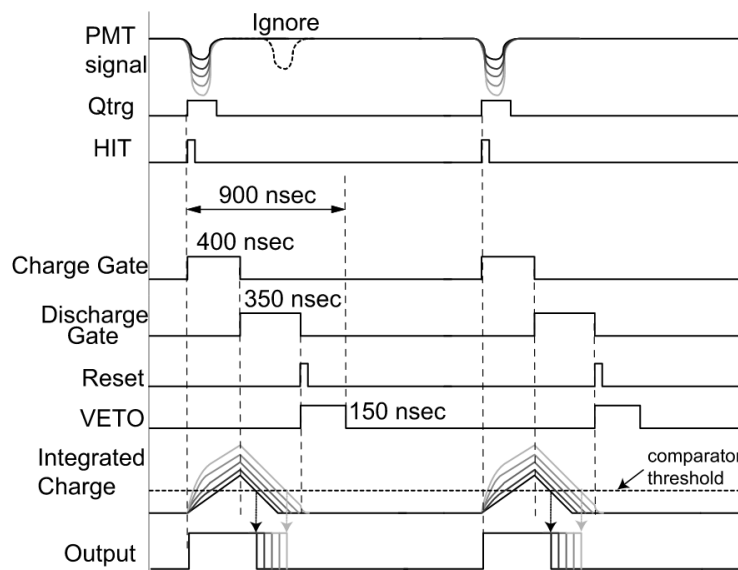


Figure 2.14: Timing chart for signal and trigger in a QTC. The gradation of PMT signal corresponds to that of the integrated charge and output. The figure was taken from [84].

2.4.5 Online System for ID & OD: SK-IV and SK-V

Figure 2.15 shows the schematic of the new online system. The signal from about 13,000 PMTs (ID and OD PMTs) are transferred to 20 front-end PCs via about 550 QBEEs. One front-end PC receives the data from 30 QBEE boards. The data are then sent to 10 merger PCs for event building. The front-end PCs and the merger PCs are linked by 10-Gigabit ethernet. In the merger PCs, the data from all the front-end PCs are merged. At that time, a software trigger is applied to select candidates for physics analyses. The data from the merger PCs are sent to an organizer PC via ethernet, where they are merged and written onto a disk for offline analysis.

The front-end PC system comprises three components: collector (receives data from QBEEs), sorter (sorts data in time order), and sender (sends data to merger PCs). These components run as threads during the same process.

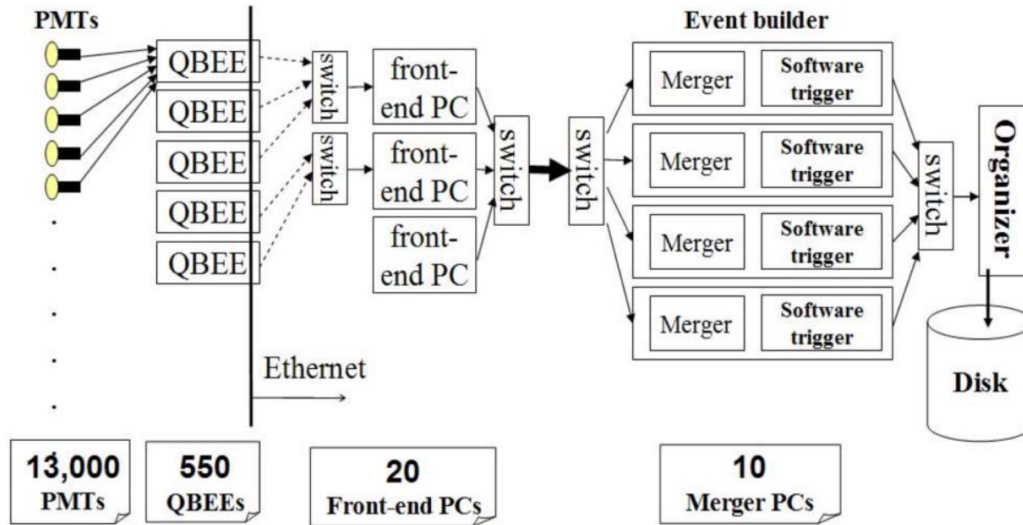


Figure 2.15: Block diagram of the new online system. Data are transferred from QBEEs to the organizer PC via 100 Base-T (broken line), gigabit ethernet (solid line), and 10-Gigabit Ethernet (bold solid line). The figure was taken from [79].

The data from the front-end PCs are merged onto the merger PC, and all merged events are again sorted by time order. At that time, because the data were already sorted by each front-end PC, the heap-sort technique is used for sorting to reduce the CPU costs. Another component of a merger PC is its software trigger management system. One merged block contains hit data within a 22 msec time window and is sent to the software trigger.

The final component of the online data system is the organizer, which sorts the data blocks from the merger PCs in time order. A 22 msec data block has an adjacent block and a 1 msec overlap area, so that no events are missed at the boundary. The organizer checks for this duplicate area and removes the double-count event. The data are then written to disk, and further data reduction and physics analysis are performed by the offline system. The offline system has 700 TB disk storage and a 1,080 CPU cluster.

The capability of data transfer was greatly improved in QBEE by adopting ethernet data transfer to online PCs. As a result of measuring the throughput of the QBEE by feeding analog pulses to the QBEE and receiving output data in a PC, 11.8 MB/sec per QBEE board was achieved, which nearly reaches the 100 Base-T theoretical limit.

The data flow of the new online system is much larger than that of the previous system, because the new system receives all hit data from the front-end electronics. Assuming a hit-rate per 4.5 kHz PMT, the data flow rate can reach 18.5 MB/sec in the front-end PC and 37 MB/sec in the merger PC. Adding the size of headers, trailers, and other information, the total data rate for all the merger PCs is about 470 MB/sec.

2.4.6 Software Trigger: SK-IV and SK-V

The hardware trigger used for SK-I to SK-III was replaced with a software trigger for SK-IV. With the achievement of high-speed signal digitization, all PMT hits are now collected on merger PCs. With the previous hardware trigger, the event width was always set to $1.3\mu\text{sec}$. This event width can now be selected according to the trigger type per software trigger. There are five main triggers: special high energy (SHE), high energy (HE), low energy (LE), super low energy (SLE), and outer detector (OD).

The software trigger scans the data block and searches for events that satisfy the trigger condition. The base trigger is set to replicate the previous hardware trigger condition. When the number of hits within a 200 nsec time frame (sliding time window) exceeds the threshold, the data for the time window around the triggered timing are sent downstream. The SHE, HE, LE, and OD triggers have a wider event width of $40\mu\text{sec}$, and the SLE trigger is set to $1.5\mu\text{sec}$ because of its high rate and radioactive background. The software trigger threshold and gate window are summarized in Table 2.5.

The SHE trigger is installed at the SK-IV phase as a new trigger. If a SHE triggered event is not accompanied by an OD trigger, an additional after-trigger (AFT) is issued. AFT stores an additional 500 μsec of data, which can be used to analyze neutron capture.

Table 2.5: Trigger threshold of SK-IV phase. SHE, HE, LE, and SLE triggers are based on ID hits, and the OD trigger is calculated using the hits in the OD PMTs only. The SHE and SLE triggers were lowered in September 2011 and May 2015 respectively.

Trigger Type	Hit Threshold (hits/200 nsec)	Gate Window [μsec]
Special High Energy (SHE)	70 \rightarrow 58	[-5, +35]
High Energy (HE)	50	[-5, +35]
Low Energy (LE)	47	[-5, +35]
Super Low Energy (SLE)	34 \rightarrow 31	[-0.5, +1.0]
Outer Detector (OD)	22 (only in OD)	[-5, +35]

3 Simulation

Physics analysis at SK is performed by comparing the observed data with predictions from Monte Carlo (MC) simulations. MC comprises neutrino flux, neutrino interaction, and SK detector simulation. In the search for astronomical neutrinos from a blazar, signals originating from atmospheric neutrinos are the primary background. The atmospheric neutrino flux at the SK is calculated by considering the flux of primary CRs, interactions that produce neutrinos, and the propagation to the SK. Neutrino interactions simulate different modes of interaction between water and neutrinos at various energy ranges. From the relationship between the neutrino flux and interaction in the detector, the events observed by the detector are calculated. The detector simulates particles, Cherenkov photon emissions, photon propagation, and detector hardware responses using the information of produced particles, such as vertex, direction, momentum, etc.

3.1 Atmospheric Neutrino Flux

The atmospheric neutrino flux model was calculated by Honda et al. [85, 86, 87, 88, 89]. It is called the Honda–Kajita–Kasahara–Midorikawa (HKKM) flux model, and there are several versions. The SK uses the flux model announced in February 2011 (HKKM2011), and this model has three components: a CR flux, hadron interaction models, and a virtual detector.

3.1.1 Primary Cosmic Ray

Many experiments have attempted to determine the flux of primary CRs, as summarized with the HKKM flux model in Figure 3.1. As the input of the neutrino flux calculation, the primary CR flux (up to 100 GeV) can be precisely measured using balloon-borne experiment with superconducting spectrometer (BESS) [90, 91] and the alpha magnetic spectrometer (AMS) [92] experiments. Above 100 GeV, the curve is adjusted slightly to agree with emulsion-chamber data [93, 94].

The flux of primary CRs is affected by solar activity and the geomagnetic field. The solar wind drives back the low energy CRs that enter into the solar sphere of influence. Because solar activities change periodically, the CR flux during periods of intense and mild solar activity is defined as solar maximum and solar minimum, respectively. The difference at solar maximum and solar minimum is more than a factor of two for 1 GeV CRs, whereas it decreases to about 10% for 10 GeV CRs. The geomagnetic field determines the minimum energy (rigidity cutoff) with which CRs can arrive at the Earth. The rigidity cutoff is expressed as a function of the entering position at the Earth and the arrival direction. This information can be obtained using the IGRF2005 model⁵.

⁵<https://www.ngdc.noaa.gov/IAGA/vmod/igrf.html>

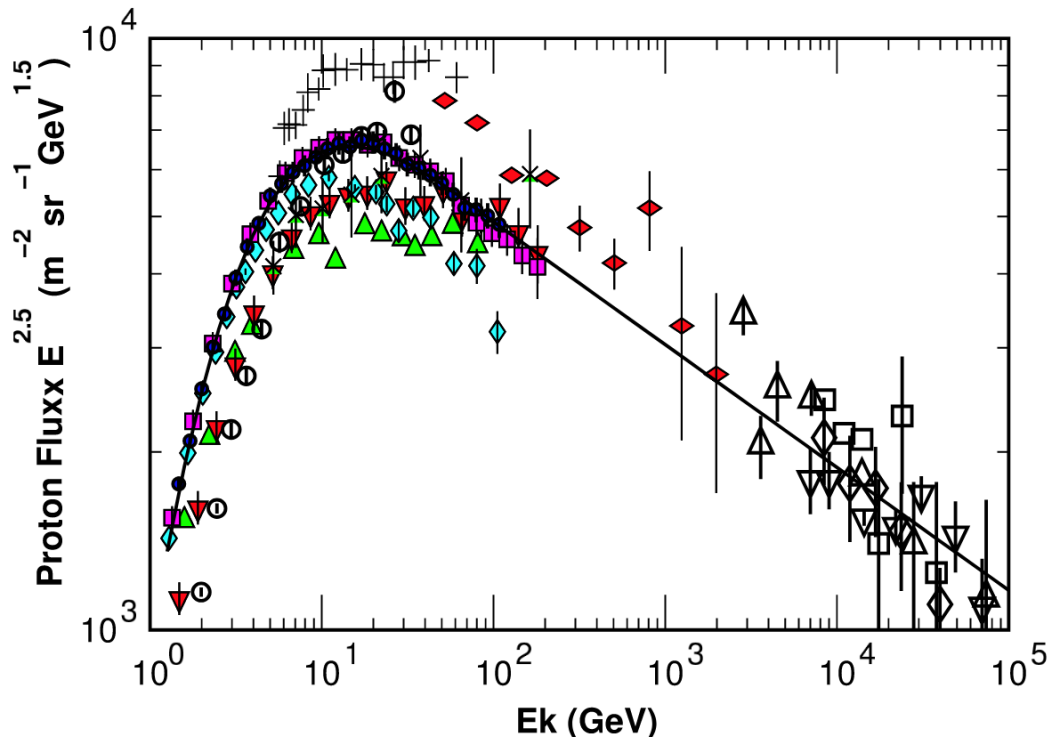


Figure 3.1: Measured primary CR flux and the model used for the HKKM calculation (solid line). The x-axis shows the kinetic energy of the proton, and the y-axis shows the proton flux multiplied by the energy spectrum having an index of 2.5. The data were taken from Webber et al. [95] (crosses), MASS [96] (open circles), LEAP [97] (upward triangles), IMAX [98] (downward triangles), CAPRICE [99] (vertical diamonds), AMS [92] (squares), BESS98 [90] (circles), Ryan et al. [100] (horizontal diamonds), JACEE [101] (downward open triangles), RUNJOB [102] (open diamonds), Ivanenko et al. [103] (upward open triangles), and Kawamura et al. [104] (open large squares). The figure was taken from Mclachlan Fukuei [105].

The U.S. standard atmosphere 1976 model⁶ is used to treat atmospheric information, such as the pressure, temperature, density, and viscosity, and it covers a wide range of altitudes and elevations worldwide.

3.1.2 Hadronic Interaction

Two theoretical models are used to measure interactions between the air molecules and the CRs. The JAM [106] model is used below 32 GeV, and The DPMJET-III [107] model is used above it. The JAM is used in the Particle and Heavy-Ion Transport code System (PHITS) [108]. It is a hadron cascade model that handles

⁶<https://ntrs.nasa.gov/search.jsp?R=19770009539>

the established hadron states, including resonances with explicit spins and isospins. The DPMJET-III is a code system based on the dual-parton model (DPM) [109], and it treats interactions between hadrons, nuclei, and photons above a few GeV.

Figure 3.2 shows a comparison of the JAM, DPMJET-III, and the hadron production (HARP) experiment [110, 111]. The HARP experiment investigated details of hadronic interactions of protons on thin N_2 and O_2 targets at low energy. In the figure, the JAM model shows slightly better agreement with the HARP experiment than did the DPMJET-III model.

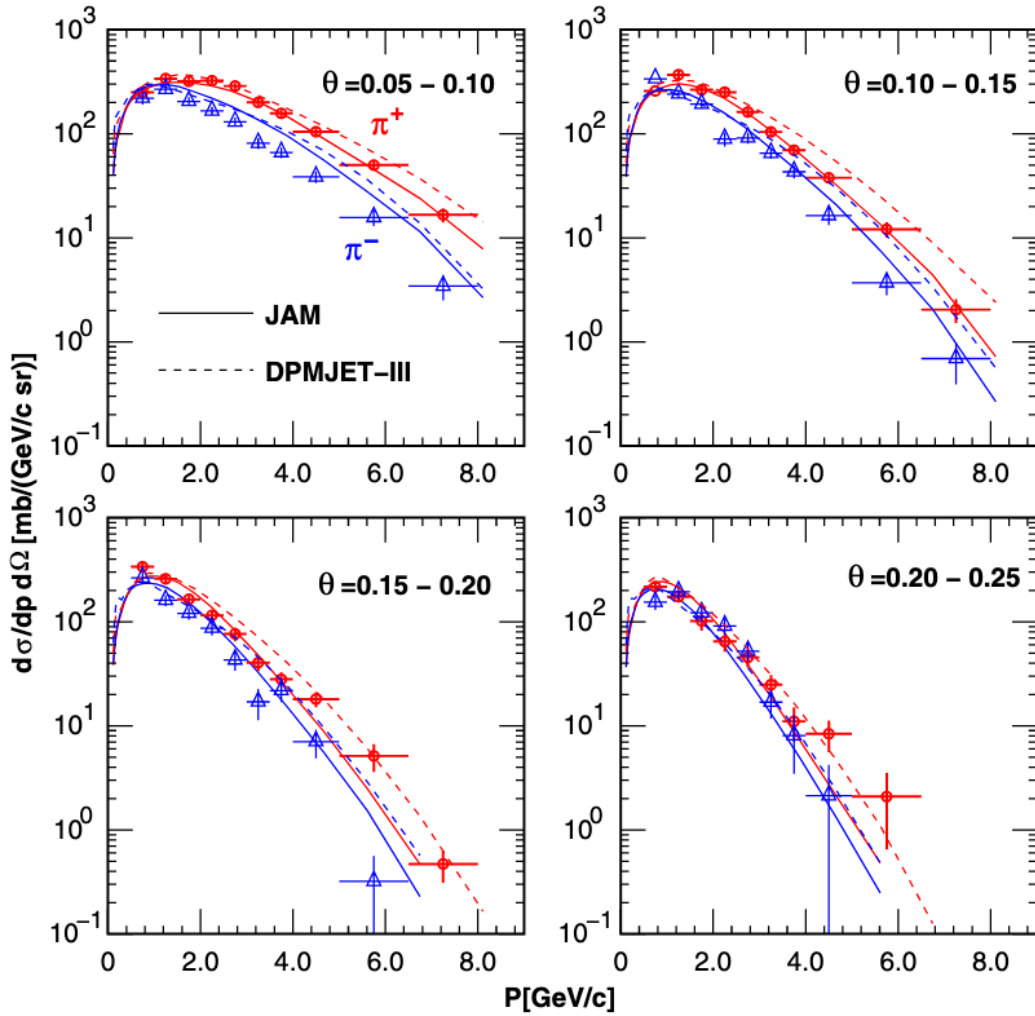


Figure 3.2: Comparison between HARP data (cross-section of forwarding pion production by low energy hadron interactions) and theoretical models: JAM (solid line) and DPMJET-III (dashed line). The HARP data on N_2 and O_2 targets were combined into a ratio of 78.5% and 21.5%, respectively, to simulate an air target. The red (blue) lines and points indicate the cross-section for producing π^+ (π^-). The figure was taken from Honda et al. [89].

In the high energy region, to confirm that the hadron interactions are correct and to fine-tune interactions in the simulation, the flux of CR muons from the simulation is compared with external experimental data. CR muons are produced in the decay chain, and their flux has been measured by BESS [91, 112] and L3+C [113]. The DPMJET-III model was modified using the results of these experiments. The ratio between the CR muon spectrum and the modified model is shown in Figure 3.3. After modification, the hadronic interaction model agrees with the data within $\lesssim 10\%$ in the 1 to 100 GeV muon energy range.

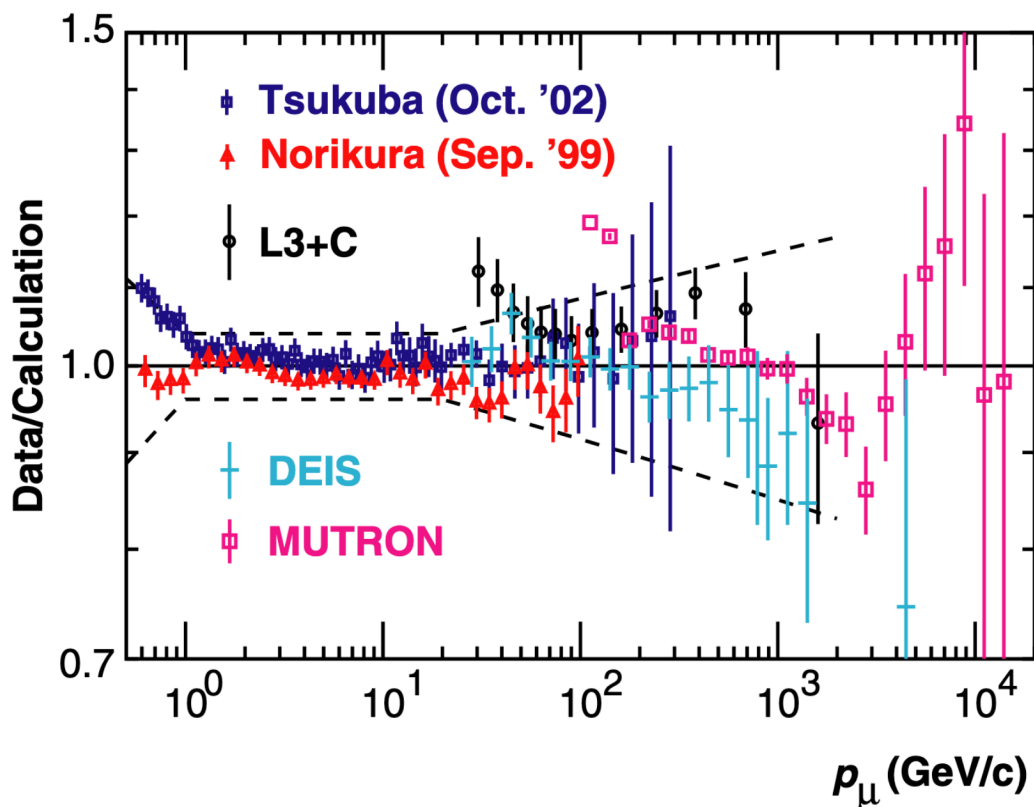


Figure 3.3: Comparison of cosmic ray muon flux between experimental data and modified flux [88]. The data were observed at Mt. Tsukuba (squares) and Mt. Norikura (triangles) using the BESS detector, and at CERN (circles) using the L3 detector. The results of the DEIS [114] and MURTON [115] experiments are also plotted, but they are not included in the calculation of error bars. The dashed line is the sum of the errors in data and calculation. The figure was taken from Sanuki et al. [116].

3.1.3 3D Flux Calculation

When primary CRs hit the atmosphere, mainly pions and kaons are generated as secondary particles. The decay of secondary mesons creates mostly muons and neu-

trinos. The calculation of neutrino flux treats the interactions and the propagation of particles in a 3D manner. In the 3D calculation, the point of entry into the Earth and the point of emergence from the Earth are calculated. The neutrinos that do not enter the Earth are discarded. In the 1-dimensional (1D) calculation, all particles are treated using COSMOS simulation [117]. All secondary particles are produced in the direction of primary CRs. The features of 3D calculation compared to the 1D calculation are the enhancement of neutrino flux near the horizontal direction and the neutrino generation at low altitude near the horizontal. Figure 3.4 shows a schematic of the 1D- and 3D-flux calculation methods.

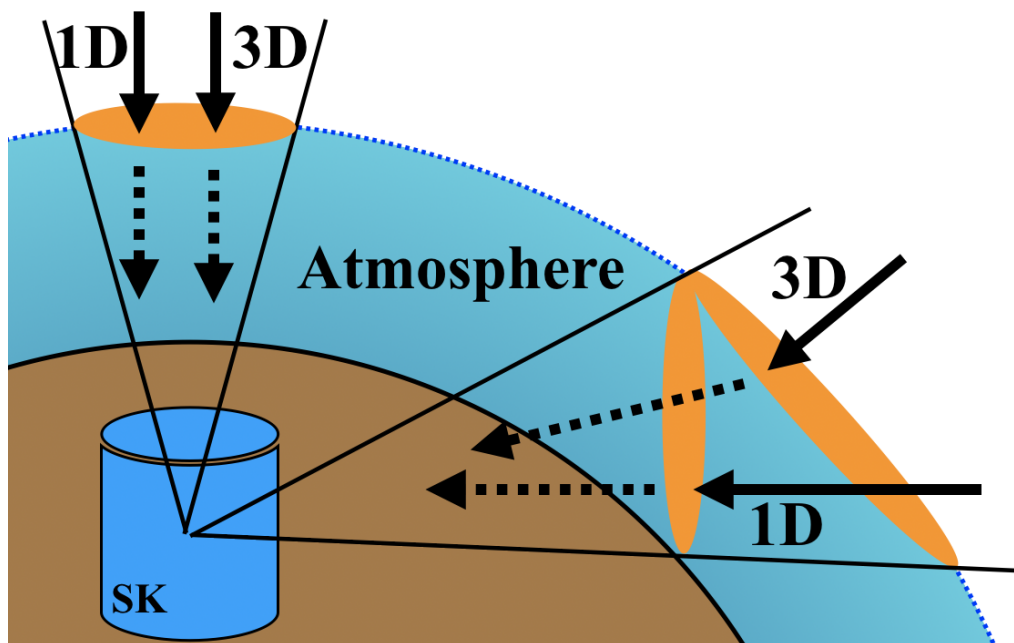


Figure 3.4: Interaction areas of primary CRs, and atmosphere for 1D and 3D flux calculation.

The enhancement of neutrino flux coming from near horizontal is explained as the difference in the effective area of primary CRs interacting with Earth's atmosphere. As seen in Figure 3.4, because the effective area is always perpendicular to the horizontal direction in the case of 1D calculation, the effective area is smaller than the case of 3D calculation. This effect does not affect the neutrinos coming from the vertical. Furthermore, the increase in neutrino flux is also related to the low energy charged particles affected by the geomagnetic field [86]. Figure 3.5 provides a comparison of the neutrino flux of the two calculations (1D and 3D) and two simulation models (FLUKA [118] and DIPOLE [86]).

The neutrino generation at low altitude near the horizontal can be explained using the difference in the path length of the primary CRs. In the case of the 1D calculation, the primary CRs from the horizontal direction travel a longer distance through the atmosphere than vertical rays to reach the same altitude. In the 3D calculation, a primary CR that has a more vertical incident angle and then curves

to the horizontal direction has a shorter path length than the equivalent horizontal 1D case. Therefore, the neutrinos reach low altitudes in 3D calculations before interacting. This effect is also prominent at lower energies.

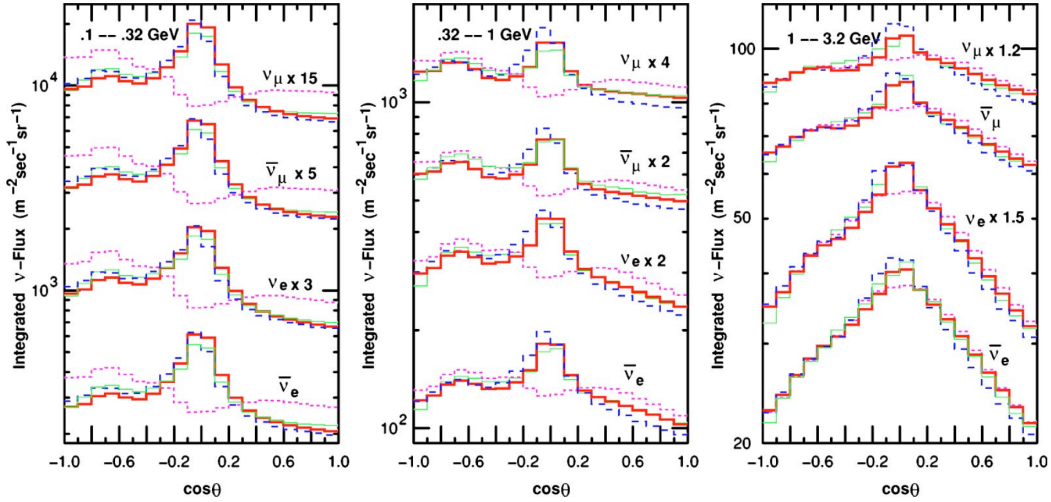


Figure 3.5: Atmospheric neutrino flux in three energy bins (Left: 0.1 to 0.32 GeV, Center: 0.32 to 1.0 GeV, Right: 1.0 to 3.2 GeV). The x-axis shows the zenith angle from which the averages are taken. The y-axis shows the neutrino flux with histograms for each neutrino flavor multiplied by a constant to avoid overlapping. The red solid lines are for 3D, magenta dotted lines for 1D, blue dashed lines for FLUKA, and green thin solid lines for DIPOLE. The figure was taken from Honda et al. [87].

3.1.4 Neutrino Flux at SK

Figure 3.6 shows the energy spectrum of atmospheric neutrinos at the SK site, which is compared among HKKM06, HKKM11, FLUKA, and Bartol [119] models. The calculated spectra and ratio of neutrino fluxes are shown averaged over all directions from 0.1 to 32 GeV.

The flux of the electron neutrinos drops at a faster rate than the muon neutrinos with increasing energy. This is explained by the higher energy muons reaching the surface of the Earth before they can decay and produce electron neutrinos. The ratio between muon neutrino and electron neutrino is around two up until few GeV with increasing energy.

The MC events are generated using the predicted flux at the SK without considering neutrino oscillations. All neutrinos reach the detector with production flavors from the atmosphere. The neutrino oscillations are applied at the time of performing an analysis by re-weighting each MC event according to its oscillation probability based on the neutrino energy and direction.

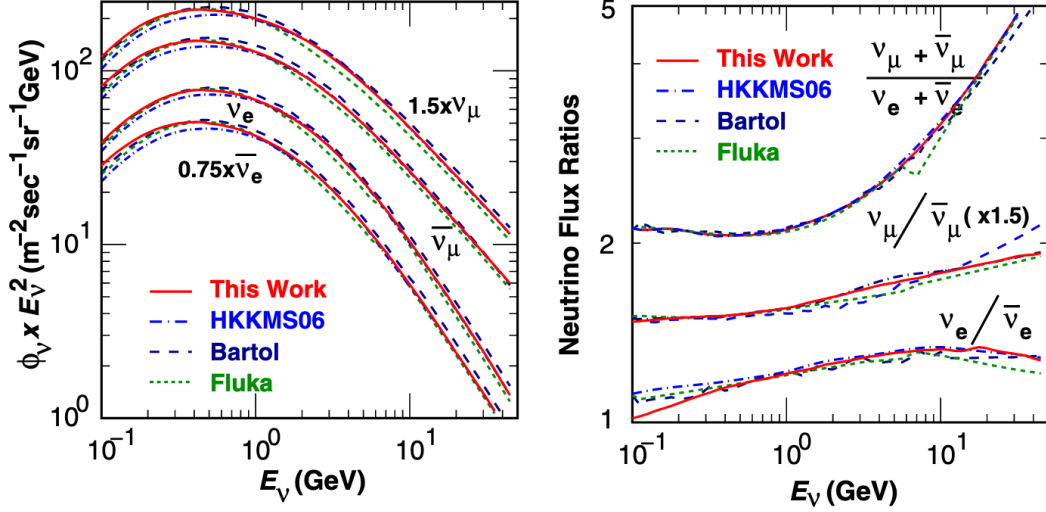


Figure 3.6: Comparison of calculated atmospheric neutrino fluxes averaged over all directions (left panel). Comparison of flavor ratio and neutrino anti-neutrino ratios (right panel). The solid line shows the HKKM11 flux model, and the previous version of the HKKM model is shown with a dot-dashed line. For comparison, the FLUKA model (dotted line) and Bartol model (dashed line) are also shown. The figure was taken from Honda et al. [89].

3.2 Neutrino Interaction

The interaction of neutrinos at the SK is handled using an interaction generator called NEUT [120, 121]. NEUT handles a wide energy range of neutrinos from a few tens of MeV to hundreds of TeV, and the primary target materials are hydrogen and oxygen inside the water and the rock (SiO_2) surrounding the detector.

Neutrino interaction can be classified into charged current (CC) and neutral current (NC) interactions determined by the type of weak bosons exchanged (W^\pm and Z bosons for CC and NC reactions, respectively). The incoming neutrino in a CC event can be identified by distinguishing the flavor of the charged lepton. However, an NC event does not have a signal about the neutrino flavor remaining in the detector because the outgoing lepton is also a neutrino. In NEUT, the following CC and NC interactions are simulated:

CC/NC (Quasi-) Elastic Scattering	$\nu_\ell + N \rightarrow \ell/\nu_\ell + N'/N$
CC Meson Exchange Current	$\nu_\ell + NN' \rightarrow \ell + N''N'''$
CC/NC Single Meson Production	$\nu_\ell + N \rightarrow \ell/\nu_\ell + N'/N + \text{Meson}$
CC/NC Deep Inelastic Scattering	$\nu_\ell + N \rightarrow \ell/\nu_\ell + N'/N + \text{Hadron}$
CC/NC Coherent Pion Production	$\nu_\ell + {}^{16}\text{O} \rightarrow \ell/\nu_\ell + {}^{16}\text{O} + \pi$

where N and N' represent nucleon (proton or neutron) states before and after interaction, and ℓ is a lepton.

The cross-section of neutrino–electron elastic scattering is about three orders of magnitude smaller than the neutrino–nucleon interaction at neutrino energies of about 1 GeV. Therefore, the interaction between atmospheric neutrinos and electrons are neglected in the simulation.

Although the original neutrino flux produced in the atmosphere only contains electron and muon neutrinos, tau neutrinos are also detected at the SK because of oscillations. Because the tau lepton has a large mass value ($1.78 \text{ GeV}/c^2$), their CC interaction can only occur at energies above several GeV. For that reason, the number of events caused by tau neutrino interactions is significantly smaller compared with electron and muon neutrino interactions. Nevertheless, tau neutrino interactions are simulated in the same manner as electron and muon neutrino interactions by NEUT, and the produced tau leptons are simulated by TAUOLA [122].

3.2.1 Elastic and Quasi-Elastic Scattering

There is a way to classify neutrino interactions based on the final state of the nucleon. NC elastic scattering is a process in which a neutrino simply scatters off of a nucleon target by transferring some momentum without producing any new particles. This is CC quasi-elastic scattering (CCQE), in which the nucleon changes but does not break up. For example, NC and CCQE interactions are shown as follows:

$$\text{NC elastic : } \nu_\ell(\bar{\nu}_\ell) + \text{p} \rightarrow \nu_\ell(\bar{\nu}_\ell) + \text{p}, \quad (3.1)$$

$$\text{NC elastic : } \nu_\ell(\bar{\nu}_\ell) + \text{n} \rightarrow \nu_\ell(\bar{\nu}_\ell) + \text{n}, \quad (3.2)$$

$$\text{CCQE : } \nu_\ell(\bar{\nu}_\ell) + \text{p} \rightarrow \ell(\bar{\ell}) + \text{n}, \quad (3.3)$$

$$\text{CCQE : } \nu_\ell(\bar{\nu}_\ell) + \text{n} \rightarrow \ell(\bar{\ell}) + \text{p}, \quad (3.4)$$

where the neutrons are assumed to be present in the oxygen nuclei. It is also assumed that protons are present in the oxygen nuclei and with a free nucleon (free proton in water). The cross-section of the CCQE interaction is calculated from two types of reactions ($\nu - \text{p}$ and $\nu - \text{O}$). The cross-section of the NC elastic is estimated from the cross-section of the CCQE interaction.

For the CCQE interaction in NEUT, the interactions on a free nucleon target were first simulated by Llewellyn Smith [123]. The differential cross-section is written as:

$$\frac{d\sigma^{\text{CCQE}}}{dq^2} = \frac{M^2 G_F^2 \cos^2(\theta_C)}{8\pi E_\nu^2} \left[A(q^2) \mp B(q^2) \frac{s-u}{M^2} + C(q^2) \frac{(s-u)^2}{M^4} \right] \quad (3.5)$$

where E_ν is the neutrino energy, $M = 0.938 \text{ GeV}$ is the nucleon mass, $G_F = 1.1663787 \times 10^{-5} \text{ GeV}^{-2}$ is the Fermi coupling constant, θ_C is the Cabibbo angle, $q = q_\nu - q_\ell$ is the transferred four-momentum, s and u are Mandelstam variables,

m is the mass of outgoing lepton, and factors A , B , and C are expressed as

$$A(q^2) = \frac{m^2 - q^2}{4M^2} \left[\left(4 - \frac{q^2}{M^2} \right) |F_A|^2 - \left(4 + \frac{q^2}{M^2} \right) |F_V^1|^2 - \frac{q^2}{M^2} |\xi F_V^2|^2 \left(1 + \frac{q^2}{4M^2} \right) - \frac{4q^2 F_V^2 \xi F_V^2}{M^2} - \frac{m^2}{M^2} \left(|F_V^1 + \xi F_V^2|^2 + |F_A|^2 \right) \right] \quad (3.6)$$

$$B(q^2) = \frac{q^2}{M^2} F_A (F_V^1 + \xi F_V^2) \quad (3.7)$$

$$C(q^2) = \frac{1}{4} \left(|F_A|^2 + |F_V^1|^2 - \frac{q^2}{4M^2} |\xi F_V^2|^2 \right) \quad (3.8)$$

where ξ is defined by anomalous magnetic moment, $\xi \equiv \mu_p - \mu_n = 3.71$, $F_A(q^2)$ is the axial-vector form factor, and $F_V^1(q^2)$ and $F_V^2(q^2)$ are the vector form factor. They are expressed as

$$F_A(q^2) = -g_A \left(1 - \frac{q^2}{M_A^2} \right)^{-2} \quad (3.9)$$

$$F_V^1(q^2) = \left(1 - \frac{q^2}{4M^2} \right)^{-1} \left[G_E(q^2) - \frac{q^2}{4M^2} G_M(q^2) \right] \quad (3.10)$$

$$\xi F_V^2(q^2) = \left(1 - \frac{q^2}{4M^2} \right)^{-1} \left[G_M(q^2) - G_E(q^2) \right] \quad (3.11)$$

$$G_E(q^2) = \left(1 - \frac{q^2}{M_V^2} \right)^{-2}, \quad G_M(q^2) = (1 + \xi) \left(1 - \frac{q^2}{M_V^2} \right)^{-2} \quad (3.12)$$

where g_A is the axial-vector coupling constant, M_V and M_A are the masses of vector and axial-vector, respectively, and G_E and G_M are the electric and magnetic form factors, respectively. At NEUT, M_V is set to be 0.84 GeV, and M_A is set to be 1.21 GeV. Both values were obtained from the experimental measurement at K2K [124] and the Mini Booster Neutrino Experiment (MiniBooNE) [125]. This M_A value is also used for single meson production. The g_A is measured by polarized nucleon beta decay [126, 127] and set to be 1.232 in the NEUT simulation. The world average g_A value is 1.2673 ± 0.0035 [128], although the change of cross section-caused by the difference g_A value is less than 5%. In addition to the dipole form factor, several types have been proposed [129–131]. The difference of the cross-section between their models and the dipole form factors is estimated to be less than 10% [132].

The interactions for a nucleon bound in an oxygen nucleus were used for the relativistic Fermi gas model by Smith and Moniz [133] to account for Fermi motion

and Pauli blocking of the nucleon. The outgoing momentum of the nucleons in the interactions is required to be larger than the Fermi surface momentum to allow quasi-elastic scattering to occur. The Fermi surface momentum is set to 225 MeV/c, which is required to reproduce the quasi-elastic peak in electron scattering. The NEUT model was compared with other models [134, 135] to estimate systematic uncertainties of neutrino interactions and nuclear effects. Figure 3.7 shows the cross-section of the quasi-elastic scattering from the experimental data and the calculations from the NEUT library.

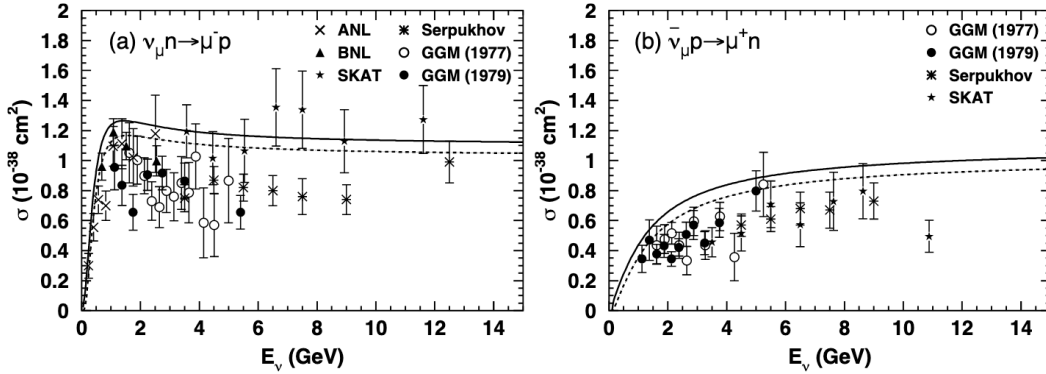


Figure 3.7: Cross-section for the CCQE scattering of muon neutrino (left panel) and muon anti-neutrino (right panel). Solid lines show the calculated free targets, and the dashed lines show the calculated bound targets. Data points are taken from ANL [136] (crosses), BNL [137] (triangles), Gargamelle [138–140] (circles), Serpukhov [141] (asterisks), and SKAT [142] (stars). The figure was taken from Hayato [121].

The NC elastic scattering cross-sections were estimated from the CC cross-section by the following relations [143, 144]:

$$\sigma^{\text{NC}}(\nu p \rightarrow \nu p) = 0.153 \times \sigma^{\text{CCQE}}(\nu n \rightarrow e^- p) \quad (3.13)$$

$$\sigma^{\text{NC}}(\bar{\nu} p \rightarrow \bar{\nu} p) = 0.218 \times \sigma^{\text{CCQE}}(\bar{\nu} p \rightarrow e^+ n) \quad (3.14)$$

$$\sigma^{\text{NC}}(\nu n \rightarrow \nu n) = 1.5 \times \sigma^{\text{NC}}(\nu p \rightarrow \nu p) \quad (3.15)$$

$$\sigma^{\text{NC}}(\bar{\nu} n \rightarrow \bar{\nu} n) = 1.0 \times \sigma^{\text{NC}}(\bar{\nu} p \rightarrow \bar{\nu} p) \quad (3.16)$$

3.2.2 Meson Exchange Current

The CCQE interaction is approximated so that the neutrino interacts with a single nucleon only if it ignores the direct correlation between the nucleons in the nucleus. In reality, however, the interaction between nucleons must introduce some direct correlation, such that the incident neutrino interacts simultaneously with multiple

nucleons. The difference between the existing CCQE and the result of the Mini-BooNE experiment [145] suggests the existence of this process.

The meson exchange current (MEC) model by Nieves et al. [146] was introduced for NEUT. It is a prominent model that attempts to extend the preexisting simplistic model of CCQE. The incident neutrino interacts with a pair of two nucleons as opposed to a single nucleon target, as follows:

$$\nu_\ell + NN' \rightarrow \ell + N''N''' \quad (3.17)$$

where NN' and $N''N'''$ represent the nucleon pair before and after the interaction, respectively. Although multi-nucleon correlations should be present in any neutrino interaction on a bound nucleon, the CC MEC interaction is the only process that is considered in NEUT.

3.2.3 Single Meson Production

The interactions that produce a single meson occurs via baryon resonance. When the invariant mass of the hadron system, W , is less than about $2.0 \text{ GeV}/c^2$, the interactions are dominant hadron production processes. In NEUT simulation, their method is extended with some modification to simulate single η and K productions. For W larger than $2.0 \text{ GeV}/c^2$, the interactions are simulated as deep inelastic scatterings. An example of single meson production is shown as follows:

$$\begin{aligned} \nu_\mu + p &\rightarrow \mu^- + \Delta(1232) P_{33} \\ \Delta(1232) P_{33} &\rightarrow p + \pi^+ \end{aligned} \quad (3.18)$$

The process in NEUT is based on a previous model [147, 148], originally developed for single pion production. The amplitudes of each resonance production multiplied by the decay probability of resonance into one pion and one nucleon are calculated to obtain the cross-section. When the differential cross-section is calculated ignoring the width, it can be expressed as follows:

$$\frac{d^2 \sigma^{\text{single } \pi}}{dq^2 dE_\nu} = \frac{1}{32\pi M E_\nu^2} \cdot \frac{1}{2} \sum_{j, \text{spin}} |T(\nu N \rightarrow \ell N_j^*)|^2 \cdot \frac{1}{2\pi} \frac{\Gamma}{(W - M_j)^2 + \Gamma^2/4} \quad (3.19)$$

where M is the mass of the target nucleon, E_ν is the neutrino energy, $T(\nu N \rightarrow \ell N_j^*)$ is the amplitude of a baryon excitation, N is the nucleon, N^* is a baryon resonance, W is the invariant mass of the hadronic system, M_j is the mass of the baryon resonance, and Γ the finite decay width. The matrix elements of the hadron current are calculated using the Feynman–Kislinger–Ravndal (FKR) baryon model [149]. The resonance width is considered using the Breit–Wigner factor [150]. The lepton mass effects and the pion-pole term are adopted to the CC interactions [151, 152], resulting in the suppression of the cross-section at lower q^2 .

The calculated cross-sections of the single pion productions and the experimental results are shown in Figure 3.8. When calculating the cross-section for these interactions, 18 resonances and three background terms are considered, as listed in Table 3.1.

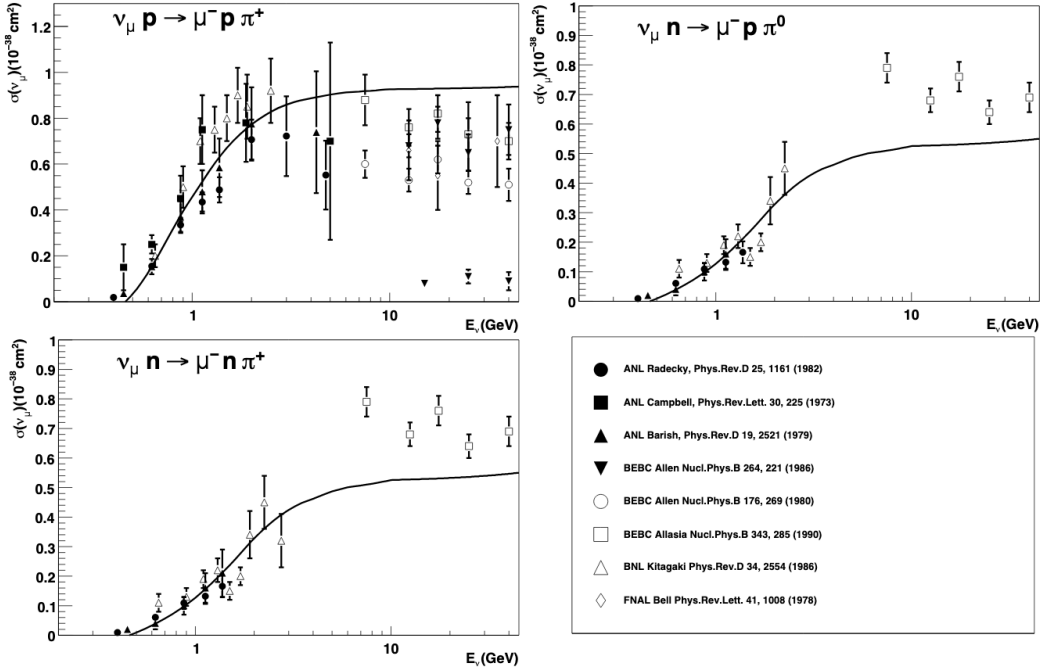


Figure 3.8: Cross-section for single pion production of the muon neutrino. The solid lines show the calculated cross-section. The experimental data are summarized in the bottom right panel. The figure is taken from Hayato [121]

To determine the angular distribution of a pion in the final state for $\Delta(1232) P_{33}$ resonance, the model of Rein and Sehgal [147] is used. For the other resonances, the isotropic feature of the resonance rest frame is used as the directional distribution of the generated pion. The Pauli blocking effect in the decay of resonances is also considered, which suppresses the interaction cross-section by the fewest percent. The pion-less delta decay is also considered, and 20% of the resonance decay is assumed to disappear without meson emission.

Table 3.1: List of resonances and background terms used in the NEUT simulation.

Resonances (Background)	Mass (W) [GeV/c]	Width (Γ) [GeV/c]
$S_{11}(1540)$	1.535	0.150
$S_{31}(1620)$	1.620	0.140
$S_{11}(1640)$	1.650	0.150
$P_{33}(1232)$	1.232	0.115
$P_{11}(1450)$	1.440	0.200
$P_{33}(1640)$	1.600	0.370
$P_{11}(1710)$	1.710	0.110
$P_{13}(1740)$	1.720	0.200
$P_{31}(1920)$	1.910	0.220
$P_{33}(1960)$	1.920	0.250
$D_{13}(1525)$	1.520	0.125
$D_{13}(1670)$	1.700	0.100
$D_{15}(1680)$	1.675	0.155
$D_{33}(1730)$	1.700	0.250
$F_{15}(1680)$	1.680	0.125
$F_{35}(1920)$	1.905	0.300
$F_{37}(1950)$	1.950	0.240
$F_{17}(1970)$	1.990	0.325
(Proton)	0.940	3.000
(Neutron)	0.940	3.000
($J = 3/2$)	0.940	3.000

3.2.4 Deep Inelastic Scattering

The interaction of incident neutrinos with the constituent quarks of the target nucleon often generates multiple hadrons via CC deep inelastic scattering (DIS). When the hadronic invariant mass, W , is greater than $1.3 \text{ GeV}/c^2$, this process is dominant in NEUT. The differential cross-section of DIS is calculated as follows.

$$\frac{d^2\sigma^{\text{CC DIS}}}{dx dy} = \frac{G_F M_N E_\nu}{\pi} \times \left[\left(1 - y + \frac{y^2}{2} + C_1 \right) F_2(x, q^2) \pm y \left(1 - \frac{y}{2} + C_2 \right) x F_3(x, q^2) \right] \quad (3.20)$$

$$C_1 = \frac{y M_\ell^2}{4 M_N E_\nu x} - \frac{xy M_N}{2 E_\nu} - \frac{m_\ell^2}{4 E_\nu^2} - \frac{m_\ell^2}{2 M_N E_\nu x} \quad (3.21)$$

$$C_2 = -\frac{m_\ell^2}{4 M_N E_\nu x} \quad (3.22)$$

where the Bjorken parameters, x and y , are defined as $x = -q^2/(2M(E_\nu - E_\ell))$ and $y = (E_\nu - E_\ell)/E_\nu$, M_N is the nucleon mass, m_ℓ is the outgoing lepton mass, E_ν and E_ℓ represent the energies of the incoming neutrino and the outgoing lepton, respectively, in the laboratory frame. The nucleon structure functions, F_2 and $x F_3$, are taken from the Parton distribution function (PDF) GRV98 [153]. The correction function given by Bodek and Yang [154] is adopted to improve agreement with experiments in the low q^2 region.

The cross-section of DIS via NC reactions is assumed to have the following relations, which are estimated from the experimental results [155, 156].

$$\frac{\sigma^{\text{NC DIS}}(\nu N \rightarrow \nu X)}{\sigma^{\text{CC DIS}}(\nu N \rightarrow \mu^- X)} = \begin{cases} 0.26 & (E_\nu < 3 \text{ GeV}) \\ 0.26 + 0.04(E_\nu/3 - 1) & (3 \text{ GeV} \leq E_\nu < 6 \text{ GeV}) \\ 0.30 & (E_\nu \leq 6 \text{ GeV}) \end{cases} \quad (3.23)$$

$$\frac{\sigma^{\text{NC DIS}}(\bar{\nu} N \rightarrow \bar{\nu} X)}{\sigma^{\text{CC DIS}}(\bar{\nu} N \rightarrow \mu^+ X)} = \begin{cases} 0.39 & (E_\nu < 3 \text{ GeV}) \\ 0.39 - 0.02(E_\nu/3 - 1) & (3 \text{ GeV} \leq E_\nu < 6 \text{ GeV}) \\ 0.37 & (E_\nu \leq 6 \text{ GeV}) \end{cases} \quad (3.24)$$

The kinematics of the hadronic system is treated by two methods according to the ranges of invariant mass. For the interaction in the range, 1.3 to 2.0 GeV/c, only pions are considered as outgoing mesons. The mean multiplicity of pions is estimated from the result of an experiment at Fermilab [157].

$$\langle n_\pi \rangle = 0.09 + 1.83 \ln(W^2) \quad (3.25)$$

The number of pions is determined using the Koba–Nielsen–Olsen (KNO) scaling factor [158]. NEUT requires $n_\pi > 2$ to avoid overlapping with the W region for single pion production. The forward-backward asymmetry of pion multiplicity in

the hadronic center of mass system is obtained from the result of the Big European Bubble Chamber (BEBC) experiment [159].

$$\frac{n_{\pi}^F}{n_{\pi}^B} = \frac{0.35 + 0.41 \ln(W^2)}{0.50 + 0.09 \ln(W^2)} \quad (3.26)$$

For the region of W greater than 2.0 GeV, the kinematics of the hadronic system are calculated using the PYTHIA/JETSET package [160], which treats K , η , ρ , and π .

The total CC cross-section, including CCQE, single meson productions, and DIS for ν and $\bar{\nu}$, are shown in Figure 3.9.

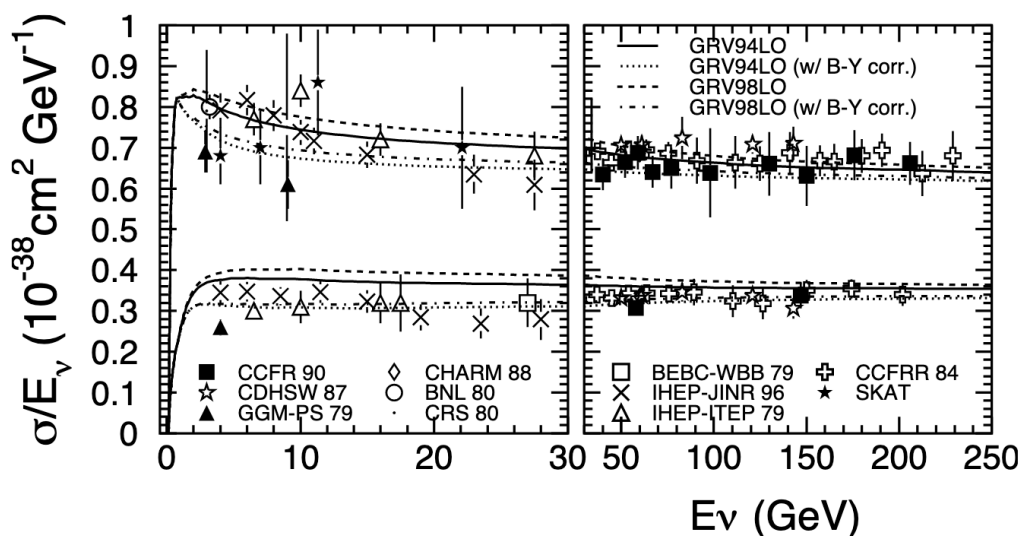


Figure 3.9: Comparison between experimental and calculated data of the total cross-section of the CC interaction for ν and $\bar{\nu}$. The upper 4 lines correspond to neutrino and the lower 4 lines correspond to the anti-neutrino. The experimental data were taken from CCFR [161], CDHSW [162], GGM-PS [163], CHARM [164], BNL [165], CRS [166], BEBC-WBB [167], IHEP-JINR [168], IHEP-ITEP [137], CCFRR [169], and SKAT [170]. The figure was taken from Hayato [121].

3.2.5 Coherent Pion Production

The reaction in which a single pion having the same charge as the incoming weak current can be generated by the interaction between an oxygen nucleus and the neutrino and is called the coherent pion production.



Because the momentum transmitted to the oxygen nucleus is very small, the angular distribution of the outgoing leptons and pions are peaked in the forward

direction. The formalism developed by Rein and Sehgal [171] is adopted to simulate these interactions, and the differential cross-section is given by

$$\frac{d^3\sigma^{\text{coherent}}}{dQ^2 dy dt} = \beta \frac{G_F^2 M_N}{2\pi^2} f_\pi^2 A^2 E_\nu (1-y) \frac{1}{16\pi} [\sigma_{\text{tot}}^{\pi N}]^2 \times (1+r^2) \left(\frac{M_A^2}{M_A^2 + Q^2} \right)^2 |F(t)| \quad (3.28)$$

$$r = \frac{\text{Re}\{f_{\pi N}(0)\}}{\text{Im}\{f_{\pi N}(0)\}} \quad (3.29)$$

where Q^2 is the square of the 4-momentum transfer of the lepton, y is the lepton fractional energy loss, t is the momentum transferred to the nucleus, β is the axial-vector coupling constant, which is 1 (2) for NC (CC) interactions, M is the nucleon mass, $f_\pi = 0.93m_\pi$ is the pion decay constant, A is the atomic number (=16 for oxygen), $\sigma_{\text{tot}}^{\pi N}$ is the averaged pion-nucleon cross-section, and $F(t)$ is the nuclear form factor. $f_{\pi N}(0)$ in r is the $\pi - N$ scattering amplitude.

The cross-section of the CC coherent pion production is measured using the K2K experiment, and the upper limit is set [172] as shown in Figure 3.10. The experimental upper limit is significantly lower than the calculated cross-section, according to Rein and Sehgal [171]. NEUT modifies the results of Rein and Sehgal [173] to account for the non-vanishing leptonic mass of CC interactions. In the case of ν_μ , the cross-section at about 25% is suppressed at 1.3 GeV because of the interference of the axial vector and the pseudoscalar amplitudes.

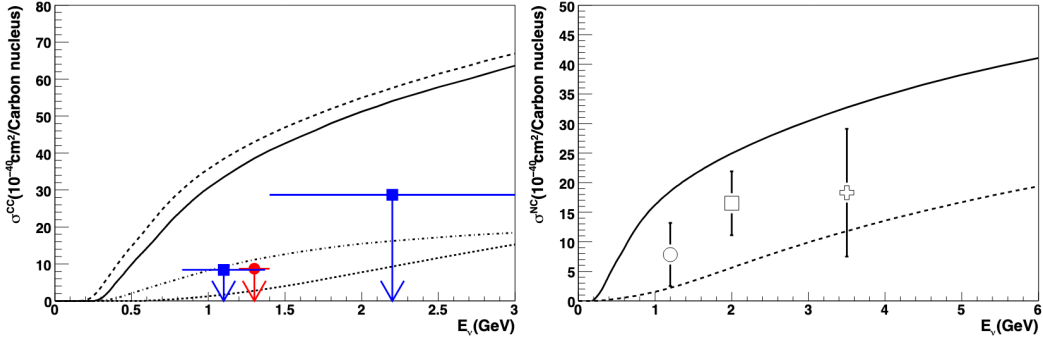


Figure 3.10: Cross-section of coherent pion production from the carbon nucleus via CC interaction (left panel) and NC interaction (right panel). The solid and dashed lines represent the Rein and Sehgal [171] model with and without modification, respectively. The dotted and dash-dotted lines correspond to the model of Kartavtsev et al. [174] and Alvarez-Ruso et al. [175], respectively. The experimental data were taken from K2K [172] (filled squares), SciBooNE [176] (filled circle), MiniBooNE [177] (open circle), Aachen-Padova [178] (open square), and Gargamelle [179] (open cross).

3.2.6 Nuclear Effects

The interaction of mesons produced in neutrino interactions with nucleons inside the ^{16}O nuclei is also simulated at NEUT. These are secondary interactions of the outgoing mesons, although they are still inside the nucleus. All the mesons generated in the ^{16}O nuclei are tracked until they exit or are absorbed by the nucleus. To propagate the π , K , and η , the cascade model is used at NEUT, which considers the interactions, the inelastic scattering, the charge exchange, and absorption.

At $E_\nu > 1$ GeV, the cross-sections for pion production from neutrino interactions are large. Moreover, the cross-section of pion-nucleon interaction is also large. Thus, the secondary interactions of pions are especially important. The initial pion production point in the nucleus where neutrino-nucleon interactions occur is determined using the Wood–Saxon density distribution [180].

$$\rho(r) = \frac{Z}{A} \rho_0 \frac{1}{1 + \exp\left(\frac{r-c}{a}\right)} \quad (3.30)$$

where ρ_0 is the average density of the nucleus, a and c are the density parameters, Z is the atomic number, and A is the mass number. For ^{16}O nucleus : $\rho_0 = 0.48m_\pi^3$, $a = 0.41$ fm, $c = 2.69$ fm, $Z = 8$, and $A = 16$ [181]. The mean free path of the pion interactions is modeled according to Salcedo et al. [182], who depend on their momenta and positions in the nucleus. Fermi motion and Pauli blocking are also considered. The energy of the outgoing nucleon must be greater than the Fermi surface momentum:

$$p_F(r) = \left(\frac{3}{2} \pi^2 \rho(r) \right)^{1/3} \quad (3.31)$$

Using the results of a phase shift analysis from the $\pi - N$ scattering experiment [183], the momentum of the pion after the interaction is determined. We use the medium correction suggested by Seki and Masutani [184]. The pion interaction is tested using experimental data for the three interactions: $\pi - ^{12}\text{C}$ scattering, $\pi - ^{16}\text{O}$ scattering, and the pion photoproduction, $\gamma + ^{12}\text{C} \rightarrow \pi^- + X$ [185, 186].

For the kaons at NEUT, elastic scattering and charge exchange interactions are considered using the results of $K^\pm - N$ scattering experiments [187–189]. For η mesons, the absorption ($\eta N \rightarrow N^* \rightarrow \pi(\pi)N$) is considered [190], where the pions are tracked as previously described.

Nucleons generated in the nucleus often cause secondary interactions with nucleons bound in the nucleus. The nucleon-nucleon elastic scattering was considered using cross-section measurements [191]. The production of delta resonances, which decay to produce pions, comes from those interactions. This effect was considered with the isobar production model proposed by Lindenbaum and Sternheimer [192].

Figure 3.11 shows the probability of the nucleon-nucleon interaction in ^{16}O . The production of nucleons with nucleon momenta below 225 MeV/c is suppressed by the Pauli exclusion principle, and half of the nucleons interact mainly via elastic scattering in the range above 300 MeV/c. Therefore more than one nucleon escapes from the oxygen.

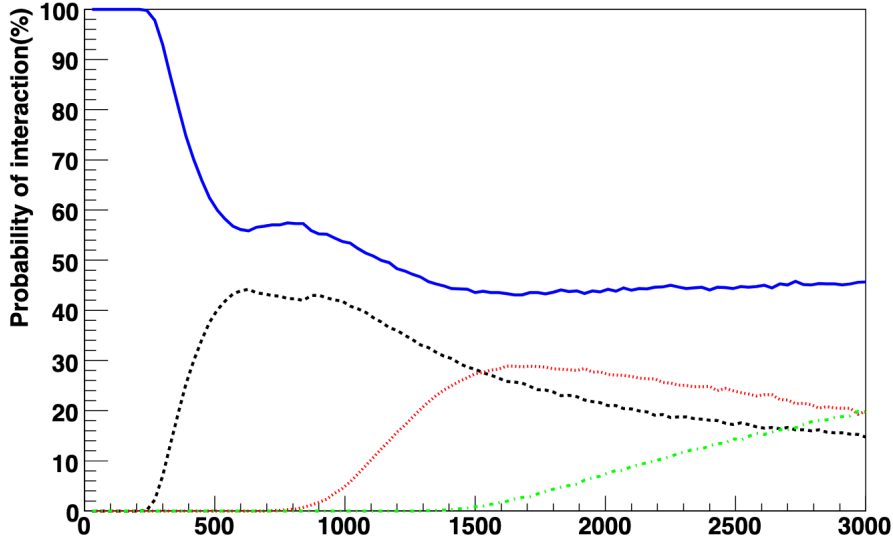


Figure 3.11: Interaction probabilities of a nucleon in ^{16}O as a function of the nucleon momentum [MeV/c]. The curves correspond to no interaction (solid line), the elastic scattering (dashed line), single pion production (dotted line), and double pion production (dash-dotted line), respectively. The figure was taken from Hayato [121].

The distances or times from the interaction points of neutrinos and hadrons are considered for all hadrons produced in the nucleus. The intermediate types are assumed to be non-bound quark states, and the formation length of each hadron is expressed as:

$$L = \frac{p}{\mu^2} \quad (3.32)$$

where p is the momentum of the hadron and $\mu^2 = 0.08 \text{ GeV}^2$ is a fitted constant from the SKAT experiment⁷. The nucleon-nucleon interaction in the nucleus has a grate effect and results in significant distortion of the geometry of particles observed in the detector.

3.3 Detector Simulation

Currently, secondary particles produced by NEUT are propagated in the SK detector simulation (SKDETSIM). SKDETSIM was developed based on the GEANT3 [193, 194] toolkit and is implemented in the FORTRAN programming language. GEANT3 toolkit contains a series of simulation programs for geometry and tracking (GEANT), originally developed by CERN for high energy physics experiments. The first version was created in 1982, and the final version was released in 1994.

⁷V. Ammosov, Talk at NuINT01 workshop at KEK, Tsukuba, Japan (2001). <http://neutrino.kek.jp/nuint01/>

3.3.1 SK Detector Simulation

SKDETSIM simulates the tracking of outgoing particles through the detector, the generation and propagation of Cherenkov photons in water, and PMT responses. It also produces an electronics readout. The structure and electronics system of the SK detector is slightly different for each phase (SK-I to SK-IV), and the environment of measurement also slightly changes for each. These differences are considered in SKDETSIM. Table 3.2 shows the processes for particles in the SKDETSIM.

Particle tracking

In SK water, multiple processes can occur depending on the type of particles. Each particle interaction is calculated using a physics model provided by GEANT3.

Hadronic interactions are simulated using GCALOR [195], except for pions below 500 MeV/c. For low energy pions, a custom program [196] based on experimental data from $\pi - {}^{16}\text{O}$ scattering [197] and $\pi - \text{p}$ scattering [198] is used. To estimate the systematic uncertainty in the hadron simulation, results of the GCALOR package and FULKA model are used. Especially for the ν_μ -enriched samples, the uncertainty affects the contamination of NC interactions.

For the propagation of charged particles, the number of Cherenkov photons and their wavelengths are calculated using Equation 2.4. The opening angle of the Cherenkov ring is calculated using Equation 2.2. Only photons in the 300 to 700 nm range, the sensitive region of PMTs, are generated.

Cherenkov photon tracking

Cherenkov photons produced by the charged particles can be scattered or absorbed in water. The probability of either of these processes occurring is characterized by parameters that depend on the transparency of the water. When the Cherenkov photon is absorbed, tracking of that photon stops. Otherwise, the photon can cause two types of scattering: Rayleigh and Mie.

When the Cherenkov photons arrive at the wall of the tank (i.e., black sheet, acrylic cover, or PMT), reflections on the surface can occur. The calculated reflection value, including the polarization, is used for the SKDETSIM.

PMT response

The charge and timing response of the PMT and the electronics are simulated based on the calibration measurements. Then the detector simulation provides the same data structure as the observed data so that the two can be analyzed in the same manner.

Table 3.2: Simulated process for each particle in SKDETSIM.

	(e^-, e^+) pair production
γ	Compton scattering
	Photoelectric effect

	Multiple scattering
	Ionization and δ -rays production
e^\pm	Bremsstrahlung
	Annihilation of positron
	Generation of Cherenkov radiation

	Decay in flight
	Multiple scattering
	Ionization and δ -rays production
μ^\pm	Bremsstrahlung
	Direct (e^-, e^+) pair production
	Nuclear interactions
	Generations of Cherenkov radiation

	Decay in flight
	Multiple scattering
Hadrons	Ionization and δ -rays production
	Hadronic interactions
	Generations of Cherenkov radiation

	Rayleigh scattering
	Mie scattering
	Absorption on the black sheet
Photon	Absorption on the acrylic case
	Absorption on the PMT surface
	Reflection on the black sheet
	Reflection on the acrylic case
	Reflection on the PMT surface

3.3.2 SK Geant4 based Simulation

The current detector simulation (i.e., SKDETSIM) was built on the GEANT3 toolkit. The simulation toolkit, GEANT3, had its last update in 1994, and it has difficulty using the latest physics models. Instead, GEANT4 [199–201] was released as a successor to GEANT3 in 1998 and has been updated to date. It was created via software engineering and object-oriented technology and implemented in the C++ programming language.

For the upcoming SK-Gd phase, a new simulation is required that can use the latest physics models and can be easily maintained and expanded. The SK GEANT4 based simulation (SKG4 [202, 203]) is being developed to solve this problem. In particular, the physics model of the neutron capture reaction is important in the SK-Gd phase. The gamma-ray emission from thermal neutron capture on Gd was modeled by Das et al. [204], Hagiwara et al. [205, 206]: the ANNRI-Gd model. This model was installed in the SKG4 simulation. The details of the ANNRI-Gd model are described in Appendix B. Various tests were performed for use as a new SK detector simulation.

Electromagnetic physics

The electromagnetic processes adopted the Livermore physics list [207] and compared it with the SKDETSIM. Figure 3.12 shows the distributions of the wavelength of Cherenkov photons calculated by SKG4 and SKDETSIM using 10 MeV electrons. SKDETSIM emits 2.6% more photons than SKG4 and has a slightly different distribution. This difference occurred because SKDETSIM did not consider the wavelength dependence of the refractive index of water.

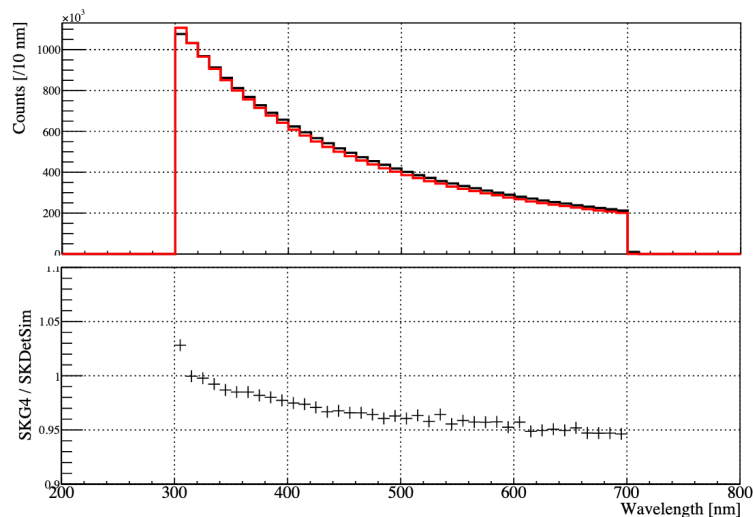


Figure 3.12: Top: distributions of the wavelength of Cherenkov photon emitted from 10 MeV electron in SKG4 (red) and SKDETSIM (black). Bottom: ratio between SKG4 and SKDETSIM.

Optical photon physics

The Cherenkov photons scatter and absorb depending on their wavelengths prior to reaching the PMT. The scattering and absorption factors are defined by the laser calibration described in Chapter 4. Figure 3.13 shows the number of photons reaching the PMTs with and without the absorption effect of water. The number of photons reaching the PMT was reduced 29.8% by SKDETSIM, where SKG4 was reduced by 29.2%. This difference was caused by the slightly different wavelength distribution of the Cherenkov photons.

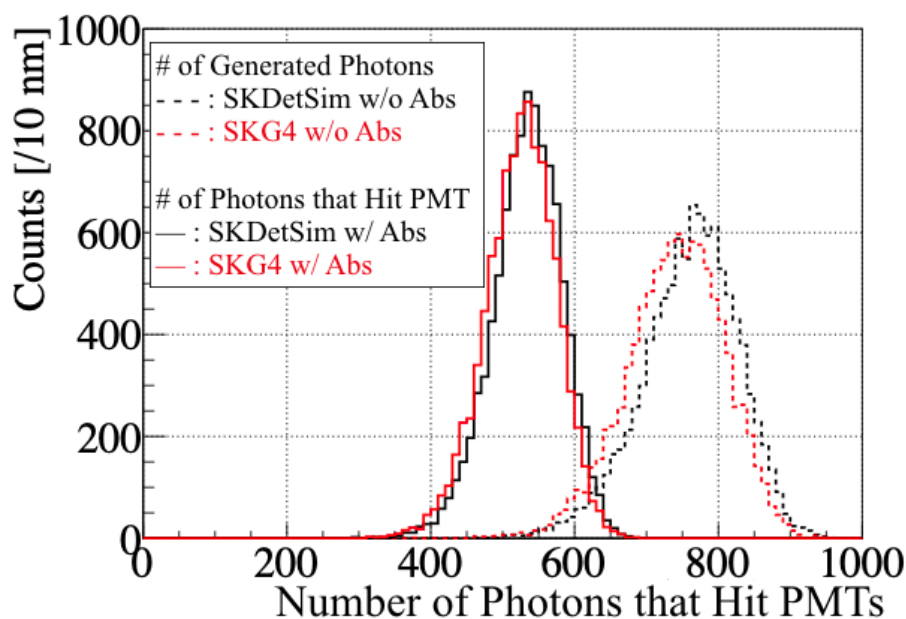


Figure 3.13: Comparison of SKDETSIM and SKG4 to confirm the effect of absorption, as indicated by the number of photons reaching the PMTs. The solid line is a simulation result considering the effect of absorption, and the dashed line is a result of ignoring the effect of absorption. The black line is the result of SKDETSIM and the red line is the result of SKG4.

Photons reaching the inner wall are absorbed or are reflected by the black sheet. Some photons reaching the PMT are absorbed or reflected, but about 20% generate p.e.. The QE of photons to p.e. depends on the wavelength of the photons and is 22% at a wavelength of 390 nm. When the test was performed without the effect of photon wavelength, the behavior of photons on the black sheet and the PMT in SKG4 completely replicates those of SKDETSIM.

We found a few percent difference between SKDETSIM and SKG4 in the electromagnetic and optical processes. These differences can be explained by differences in the wavelength distribution of Cherenkov light between SKDETSIM and SKG4 as shown, in Figure 3.12.

Hadronic physics

The testing of a physics model of the hadron process is ongoing. The neutron capture on Gd is an important process for the SK-Gd phase. To test the behavior of the neutron capture reaction, neutrons were released in an environment where $\text{Gd}_2(\text{SO}_4)_3$ was dissolved in ultra-pure water at a mass concentration of 0.2%. At this concentration, it is estimated that about 90% of the neutrons emitted from inverse beta decay are captured by Gd, and the remaining about 10% are captured by hydrogen. This is the target concentration for the SK-Gd experiment.

An electron antineutrino of a few tens of MeV emits a neutron having the momentum of several hundred keV via inverse beta decay. Therefore, the test was performed using 200 keV neutrons. When the neutrons were emitted downward from the center of the tank, the capture time by Gd was $27 \pm 1 \mu\text{sec}$, and that of the proton was $18 \pm 1 \mu\text{sec}$ (Figure 3.14, left). For ultra-pure water without dissolved Gd, neutrons were captured by a proton in $196 \pm 3 \mu\text{sec}$. The distance from the point where neutrons were generated to the point where Gd (proton) captured the neutrons is $70 \pm 33 \text{ mm}$ ($68 \pm 31 \text{ mm}$) (Figure 3.14, right). In the case of ultra-pure water, neutrons were captured by protons $107 \pm 60 \text{ mm}$ from the center of the tank.

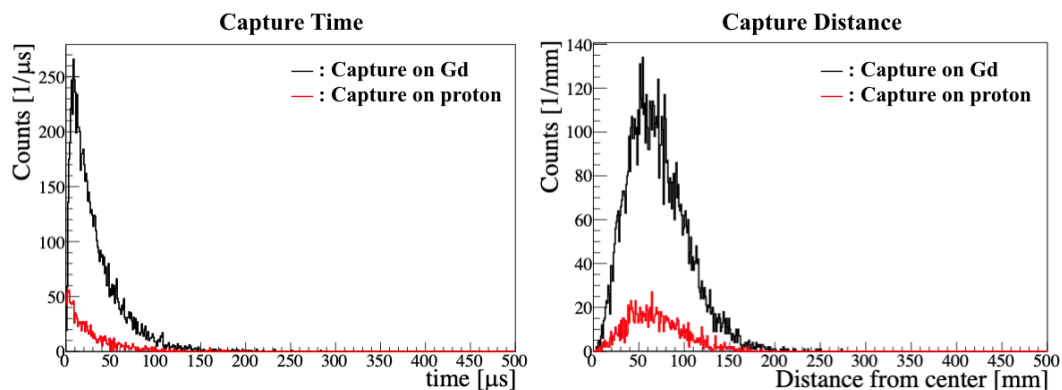


Figure 3.14: Left: time distribution in which neutrons were captured by Gd (black) and captured by proton (red) are shown. Right: distance from the center of the tank to the point where neutrons are captured by Gd (black) and by proton (red).

Figure 3.15 shows the energy spectra of gamma-rays emitted from the thermal neutron captured by Gd. For comparison with our model, the spectrum calculated by the model, FTFP_BERT_HP of Geant4, is drawn. The FTFP_BERT_HP model adds a low energy neutron reaction model to the high energy physics model recommended by Geant4. The feature of the Geant4 model is that many gamma-rays are de-excited at once from the excited state to the ground state. Our model, on the other hand, has a low probability of de-excitation at once and has a characteristic peak at 5 to 8 MeV. Furthermore, the slope of the spectrum in the region below 5 MeV is different.

The neutrons were $86.5 \pm 0.9\%$ captured by Gd and $13.5 \pm 0.4\%$ captured by protons. Oxygen nuclei capture the neutrons with a probability of 1% or less. This is

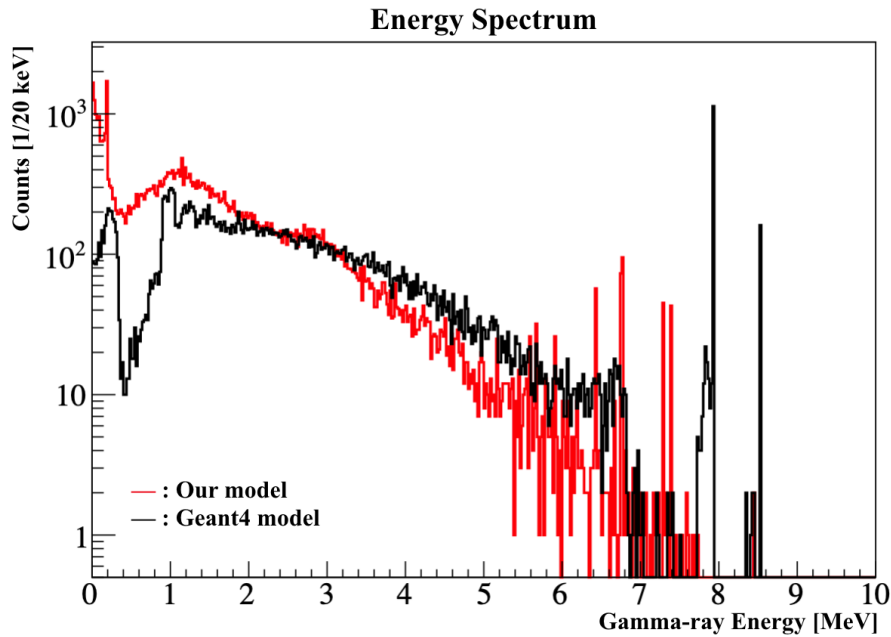


Figure 3.15: The energy spectra of gamma-rays emitted from the thermal neutron capture on Gd is shown. The red line is the gamma-ray spectrum calculated by our model and the black line is the spectrum calculated by the model of Geant4.

in good agreement with the expectation provided by Beacom and Vagins [71]. When protons capture neutrons, they emit 2.2 MeV gamma-rays. Oxygen and neutrons may emit gamma-rays of various energies owing to capture and inelastic reactions.

Current status of SKG4

SKG4 will be an indispensable tool for the physical analysis of the SK-Gd experiment, and our model has been confirmed to well-reproduce gamma rays from the thermal neutron capture reaction of Gd (Appendix B). The current status of SKG4 development includes reproducing the data acquisition process, comparing results with calibration experimental data, and developing a better user interface.



Figure 3.16: SKG4 logo.

4 Calibration

To understand the detector and keep its performance high, calibrations were performed at the SK. Several parameters were measured or calibrated: ID calibration for each PMT and photon tracking; OD calibration for each PMT and photon properties, and the absolute energy scale. Calibration results are used to produce the detector simulation and to analyze the observed data. Details on the calibration methods can be found in Abe et al. [208].

4.1 ID PMT Calibration

There are several PMT calibrations, which directly affect SK performance. In the definition for the PMT charge calibration, “gain” is a conversion factor from the number of p.e. to charge in units of pC. “QE” is the product of the quantum efficiency and collection efficiency of p.e. onto the first dynode of the PMT. The timing behavior of PMTs depends on the charge of the measured pulse.

4.1.1 High-Voltage (HV)

All PMTs are set to match the HV charge of the incident light. For the incident light, the light from a Xe lamp is passed through a UV filter and injected into a scintillator ball: a 5 cm diameter acrylic ball containing a diffuser. The scintillator ball/Xe lamp light source remains permanently centered in the SK tank for real-time and long-term monitoring of the PMT gain.

To control the incident light yields to each PMT at different locations, 420 pre-calibrated PMTs were positioned. They are standard PMTs and serve as a reference for other PMTs that have a similar geometric relationship to the light source at the center of the ID. The HV of the standard PMTs was adjusted in advance using the same light source. The standard PMTs were placed as shown on the left of Figure 4.1, and examples are shown on the right side of Figure 4.1.

The HV setting of the other PMTs was adjusted so that the observed charge from the light source flash matched the average charge of the standard PMTs in the group. After determining the HV setting for all PMTs, reproducibility was checked and confirmed to be within 1.3% in RMS.

4.1.2 Relative Gain

The gain for each PMT is determined to interpret the output charge from the PMTs across several p.e.. To measure the relative gain difference, a stable light source emitting a constant intensity flash (high-intensity and low-intensity) is placed at a specific location in the tank. An average charge, $Q(i)$, for each PMT, i , is created using a high-intensity flash, from which every PMT receives a suitable number of photons. Single-p.e. hits are measured by using a low-intensity flash that hits only a few PMTs during each event. The number of times $N(i)$ that PMT i records a

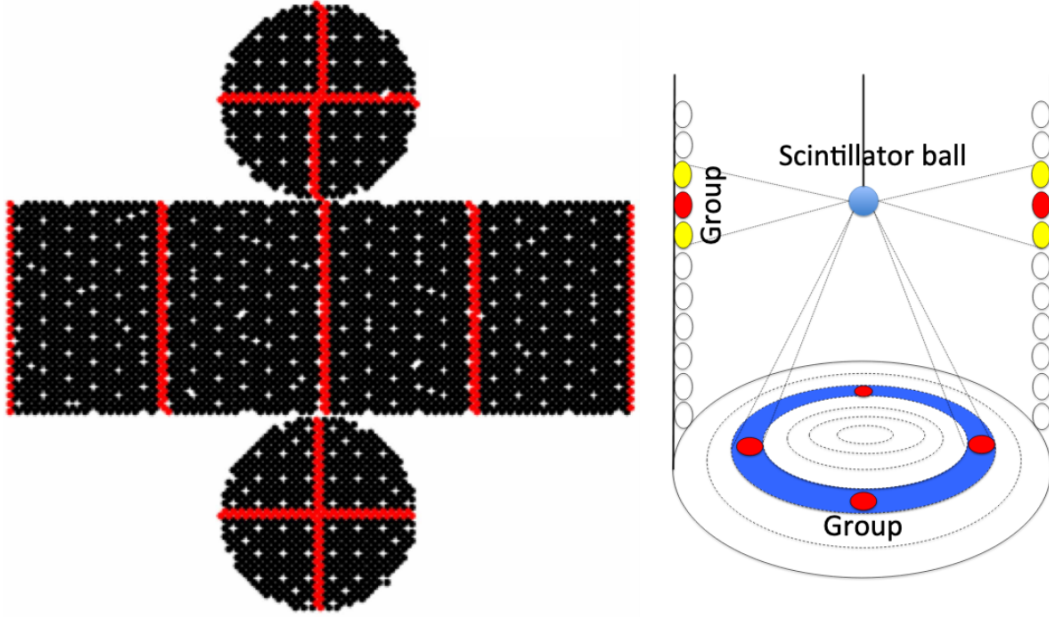


Figure 4.1: Left figure shows the net drawing of the SK tank, and the red points indicate the location of the standard PMTs. The right figure shows the schematic view of PMT groupings. These PMTs serve as references for others belonging to the same group having similar geometrical relationship to the light source. The red point corresponds to the location of standard PMTs. The figure was taken from Abe et al. [208].

charge that is greater than the threshold value are counted. Because the location of the light source does not change between the two measurements, the factors are almost identical:

$$Q(i) \propto I_H \times a(i) \times \varepsilon(i) \times G(i), \quad (4.1)$$

$$N(i) \propto I_L \times a(i) \times \varepsilon(i), \quad (4.2)$$

where I_H and I_L are the average intensities of high- and low-intensity flashes, $a(i)$ is the acceptance of PMT, $\varepsilon(i)$ denotes its QE, and $G(i)$ denotes its gain. The gain of each PMT can then be derived by taking the ratio of $Q(i)$ and $N(i)$ as:

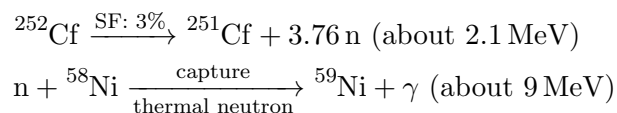
$$G(i) \propto \frac{Q(i)}{N(i)}. \quad (4.3)$$

The relative gain of each PMT can then be obtained via normalization with the average gain over all PMTs. The common factor, I_H/I_L , is also eliminated by this normalization.

The standard deviation of the gain for all PMTs is found to be 5.9%. Because the HV value of each PMT is determined to cause Q to be the same, this deviation is presumed to be caused by the difference in QE among PMTs. Using the relative gain difference of each PMT, the output charge is converted to the number of p.e. observed at each PMT.

4.1.3 Absolute Gain

The absolute gain is used to convert the charge recorded by a PMT in pico Coulombs into the number of incident p.e.. A uniform plus a stable source of single p.e. level light is required for measurement. Therefore about 9 MeV gamma rays emitted from the reaction of thermal neutrons captured on 58-Nickel, $^{58}\text{Ni}(n, \gamma)^{59}\text{Ni}$, were used. The neutrons were produced by the spontaneous fission (SF) of 252-Californium (^{252}Cf), whose the half-life is 2.56 years. Approximately 97% of the time, it decays via an α , whereas the remaining 3% undergoes SF. An average of 3.76 neutrons are produced per fission, and the average neutrino energy is 2.1 MeV. The spectrum extends to about 14 MeV. The neutrons lose energy via elastic scattering off the protons in the water and are thermalized. The gamma rays are delivered 0.004 p.e./event for each PMT, ensuring more than 99% hits are single p.e. hits. The reaction is shown below.



The relative gain correction is applied to measure the cumulative single-p.e. distribution for all PMTs. The result of charge distribution at the SK-III phase is shown in Figure 4.2. A sharp peak near zero is caused by electrons passing through the first dynode, and the second round peak corresponds to a single-p.e. signal. The average pC for the whole distribution is defined as the conversion factor from pC to a single-p.e.: 2.044 pC/p.e. for SK-I, 2.297 pC/p.e. for SK-II, 2.243 pC/p.e. for SK-III, and 2.658 pC/p.e. for SK-IV.

4.1.4 QE

The relative difference in QE is also measured for each PMT. It affects the charge response for a small number of incident photons as can be seen in Equation 4.2. MC simulation was used to predict the number of photons reaching each PMT. From the results, we determine the rate at which photons are converted to p.e..

The Ni-Cf source is used for measurement and for absolute gain calibration. The hit probability depends on the PMT position because of the photon path. The PMT position dependence of the hit probability is calculated using the following correction:

$$N(i) \times \frac{R^2(i)}{a(\theta_i)} \quad (4.4)$$

where i indexes the PMTs, $R(i)$ is the distance from the source position to the PMT position, and $a(\theta_i)$ is the acceptance as a function of incident angle θ [209]. Even after this correction, some position dependence remains owing to reflection, scattering, and absorption by the water or surface of the wall. These further corrections are estimated via MC simulation, which considers the water property and the behavior of the surfaces of the PMTs and black sheet. The remaining difference between calibration data and MC simulation is attributed to the QE of individual PMTs. This quantity is tabulated for use in the MC simulation.

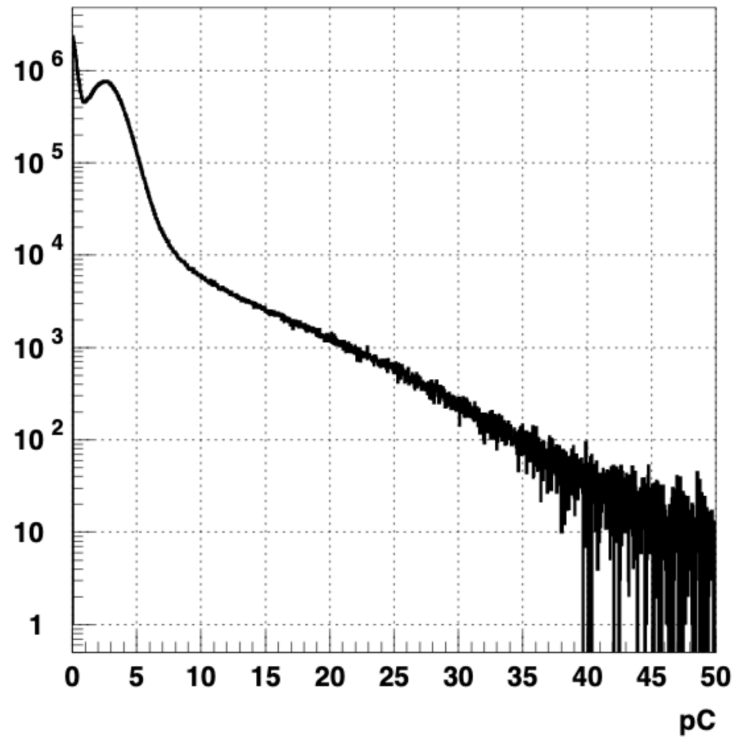


Figure 4.2: Distribution of the observed charge for the single p.e. signal at the SK-III phase. The signals were observed from the calibration using Ni-Cf source. The figure was taken from Abe et al. [208].

4.1.5 Timing Response

The readout response time varies among PMTs because of cable length, the transit times, and the processing time of electronics. Moreover, the response times of readout channels depend on the pulse height of PMTs, known as the “time-walk” effect. The purpose of timing calibration is to make a correction table for the time-walk effect of each PMT, accounting for the overall process time.

A nitrogen laser as a light source was used for timing calibration. It is a gas flow laser that emits fast pulses of light at 0.4 nsec FWHM at a wavelength of 337 nm. Because the light intensity varies per optical filter, the time responses of readouts are measured by various pulse heights. For the selection of laser events, we apply a time of flight (TOF) timing correction. It subtracts the TOF from the diffuser ball to each PMT position, using the group velocity of light at a measurement wavelength of 398 nm.

Timing versus pulse height correlation tables create individual TQ distributions based on the 2D distribution of each PMT. Figure 4.3 shows a typical scatterplot of the TQ distribution. The plot is fitted by the function described below. By multiplying the reciprocal of the fitted function by the TQ distribution, the time correction is found.

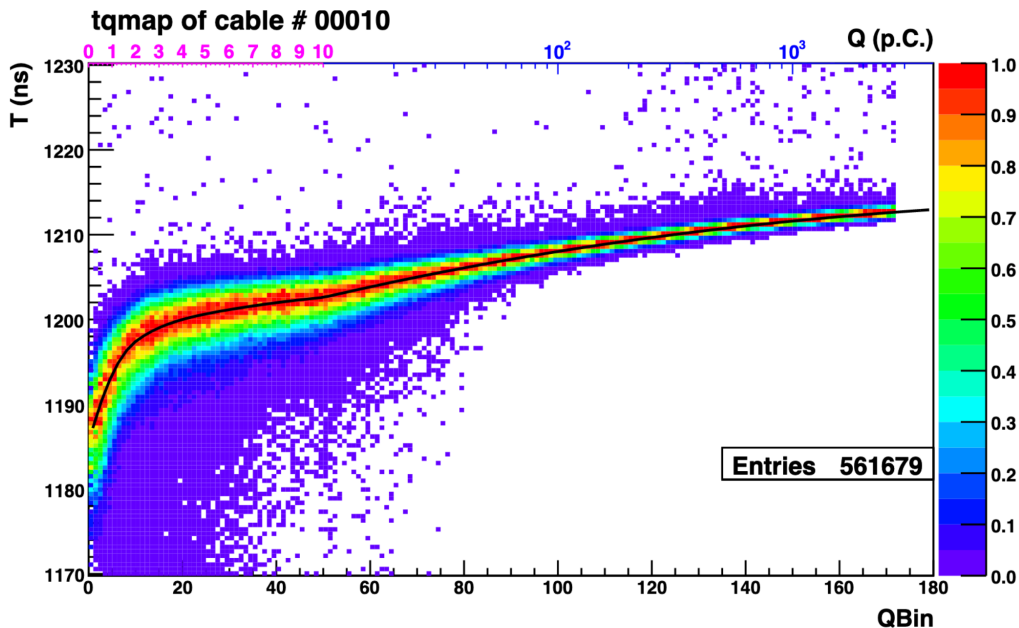


Figure 4.3: Typical TQ distribution for one PMT. The horizontal axis is the charge of each hit, and the vertical axis is the TOF subtracting the timing of the hits. The larger (smaller) TOF timing corresponds to earlier (later) hits in this figure. The figure was taken from Abe et al. [208].

The selected laser-hit events for each readout are divided into 180 bins of charge, (i.e., Qbins). Each Qbin is defined as the amount of charge from the PMT in pC, using a linear scale from 0 to 10 pC and a logarithmic scale from 10 to 3,981 pC. The peak timing and standard deviations for respective charges are fitted to polynomial functions depending on the Qbin:

$$\text{pol}N(x) \equiv p_0 + p_1x + p_2x^2 + \dots + p_Nx^N,$$

$$\text{Qbin} \leq 10 : F_1(x) \equiv \text{pol}3(x), \quad (4.5)$$

$$\text{Qbin} \leq 50 : F_2(x) \equiv F_1(10) + (x - 10)[F_1'(10) + (x - 10)\text{pol}3(x - 10)], \quad (4.6)$$

$$\text{Qbin} > 50 : F_3(x) \equiv F_2(50) + (x - 50)\text{pol}6(x - 50), \quad (4.7)$$

where F_1' is a derivation of F_1 introduced for continuity between $F_1(x)$ and $F_2(x)$ at $\text{Qbin} = 10$. $F_1(x)$ and $F_2(x)$ have four fit parameters each and $F_3(x)$ has seven fit parameters. Thus, the number of the fit parameter is 15 in total. The parameters resulting from the fit are saved in a dataset as the TQ-map and are used to correct the timing response of each PMT.

4.2 Water Transparency in the ID

MC simulations must consider the Cherenkov light effect on photons during propagation. The photons are absorbed or scattered by the water, each of which has

a wavelength dependence. When the photons reach the surface of PMT or black sheet, they are reflected or absorbed.

4.2.1 Light Absorption and Scattering

The attenuation of light in the water is expressed as

$$I(\lambda) = I_0(\lambda) \exp\left(-\frac{\ell}{L(\lambda)}\right), \quad (4.8)$$

where $I_0(\lambda)$ is the initial intensity, ℓ is the distance the light travels, and $L(\lambda)$ is the total attenuation length as a function of wavelength λ . In the SK simulation, $L(\lambda)$ is defined as

$$L(\lambda) = \frac{1}{\alpha_{\text{abs}}(\lambda) + \alpha_{\text{asym}}(\lambda) + \alpha_{\text{sym}}(\lambda)} \quad (4.9)$$

where $\alpha_{\text{abs}}(\lambda)$, $\alpha_{\text{asym}}(\lambda)$, and $\alpha_{\text{sym}}(\lambda)$ are coefficients for absorption, asymmetric scattering, and symmetric scattering, respectively. Note that these are tuning parameters used in the SK simulation, and they are SK-based empirical functions.

To calculate these parameters, a collimated laser beam is injected vertically downward from the top of the SK tank. The laser beams are generated with adjusted wavelengths of 337, 375, 405, 445, and 473 nm. The scattered and reflected light is detected by the PMT, and the detected time distribution is compared with the MC. The inverse transparency depends on the wavelength applied during the MC simulation. Figure 4.4 shows the result based on the data taken in April 2019.

4.2.2 Light Reflection at the PMT and Black Sheet

The same laser data are used to calibrate the light reflection at the PMT surface. Four layers of material from the surface to the inside of the PMT are considered. Each material and refractive index include water (1.33), glass ($1.472 + 3670/\lambda^2$, where λ is the wavelength in nm), bialkali ($n_{\text{real}} + i \cdot n_{\text{img}}$) [210], and vacuum (1.0). Here, n_{real} and n_{img} are the real and imaginary parts of the complex refractive index, respectively. The best fit values from the tuning include the following: n_{img} is 1.677, and n_{real} is 2.31, 2.69, 3.06, and 3.24 at $\lambda = 337, 365, 400,$ and 420 nm, respectively.

The reflectivity of the black sheet is measured using a light injector set in the SK tank. The reflected charge is measured at three incident angles (30° , 45° , and 60°) at three-wavelengths (337, 400, and 420 nm). The adjustment results in agreement between data and MC at better than the $\pm 1\%$ level at each wavelength and position.

4.3 OD PMT Calibration

The primary role of the OD PMTs is identifying incoming CRs and atmospheric neutrino interactions with particles leaving the ID. Charge reconstruction accuracies of about 10% to 20% and the timing accuracy of 5 to 10 nsec are sufficient for physics analysis.

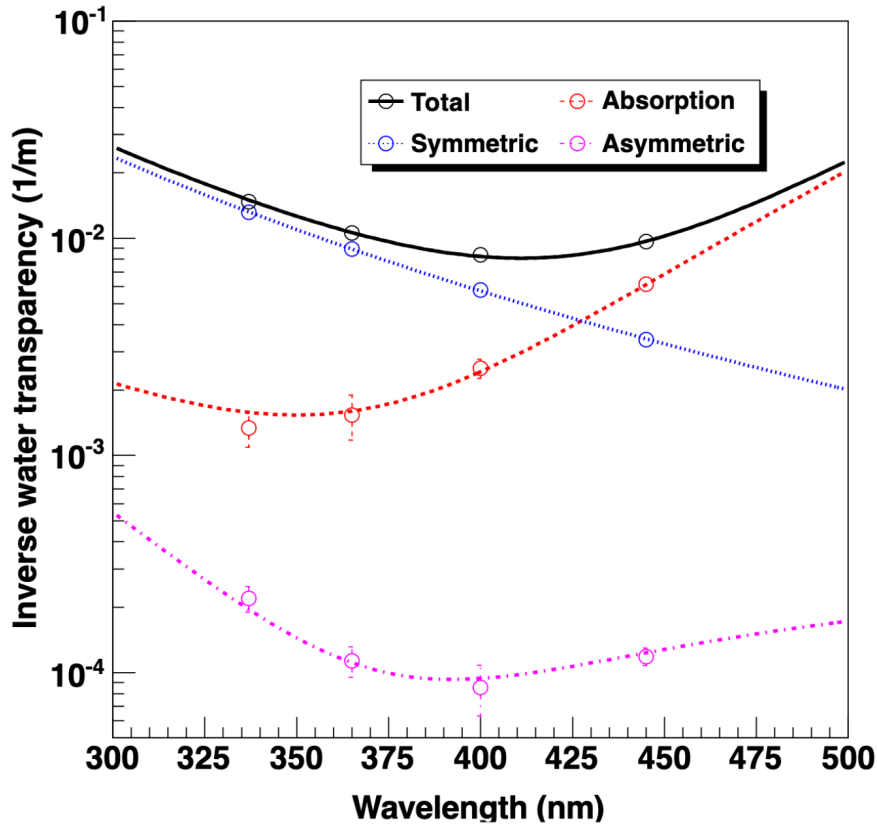


Figure 4.4: Typical fitted water coefficient functions used for the SK simulation. The points represent the average value of data obtained from April 2019. The red, blue, and magenta lines represent tuned $\alpha_{\text{abs}}(\lambda)$, $\alpha_{\text{asym}}(\lambda)$, and $\alpha_{\text{sym}}(\lambda)$, respectively. The black line is the sum of the three, which is the inverse of the attenuation length. The figure was taken from Abe et al. [208].

4.3.1 Charge Response

To determine the charge in pC corresponding to a single-p.e., OD hits leading outside the trigger time window are used (dark rate method). Hits preceding the trigger time have a high probability of being single-p.e. hits because of the noise of PMT. Thus, the mean value is taken as pC per p.e.. To validate the charge response per p.e. at low light levels, the laser is flashed at a low light level. The results from the laser method and the dark rate method are found to be in agreement within 10%. The typical conversion factor is 1 to 6 pC/p.e. for SK-IV. The value of the conversion factor is stable within a maximum of 5% for one tube for 1 year.

4.3.2 Timing Response

The purpose of timing calibration of the OD is to confirm the relative timing offset of each OD PMT and the global timing offset between ID and OD. For the relative

timing offset, cable length differences are considered. About 87% of the cables are 70 m long, and the remaining are 71 to 78 m. For the global timing offset, a laser system and CR muon are used. The laser events are taken by flashing the laser at the ID center and the OD top at the same time. From the results, a global timing offset is determined to be within several nsec. Using CR muon data, the global time offset can be independently confirmed. The OD resolution for determining the time the muon passes through the OD was found to be within about 10 nsec as shown in Figure 4.5.

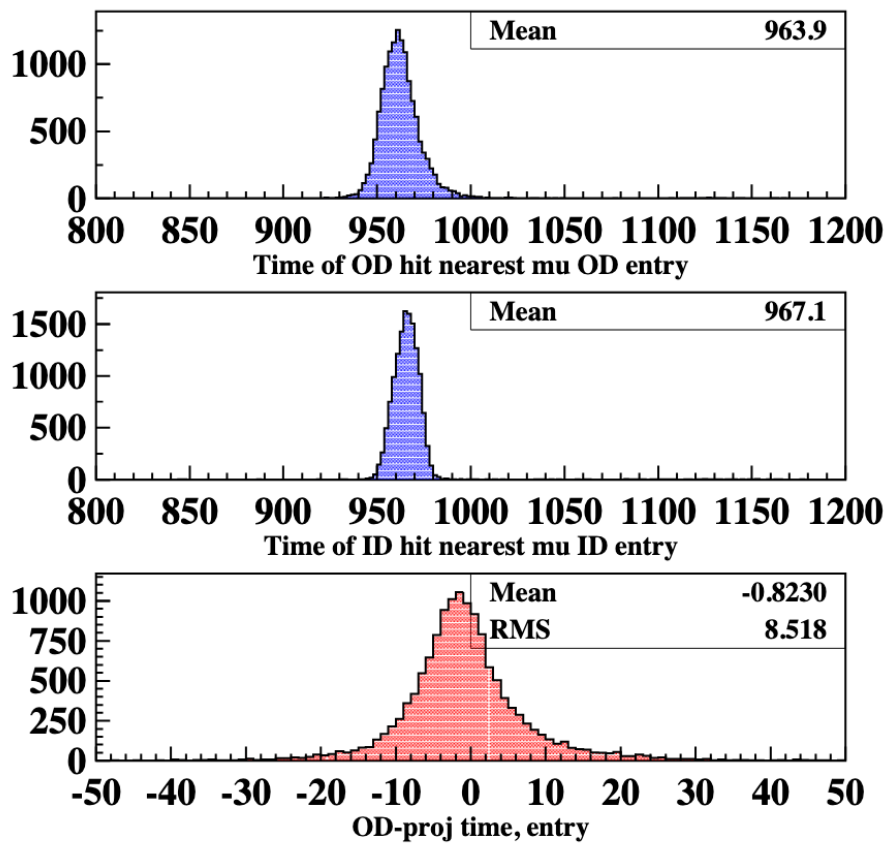


Figure 4.5: Timing distribution of CR muons data used to calculate the global timing offset. Top: distribution of times (nsec) for the nearest hit OD-PMT to the fit tracks of downward CR muons. Center: the same histogram as that of the top with the nearest hit ID-PMT. Bottom: distribution of the difference between ID and OD time after correction for TOF of the muon. The figure was taken from Abe et al. [208].

4.4 Optical Properties of the OD

The optical properties of OD materials are treated as parameters to be tuned in the MC simulation. The reflectivity of the Tyvek sheet is modeled as a combination of Gaussian specular reflections and Lambert diffuse reflections [211]. The contribution of these model varies as a function of the angle. The relative reflectivity of Tyvek on each OD surface and transmissivity of Tyvek for the segmentation barriers are tuned. The OD collection efficiency is also adjusted as an averaged parameter for the three optically separated segments (i.e., top, bottom, and barrel) of the OD. This quantity takes into account both QE and photon collection.

4.5 Energy Calibration

The reconstructed momentum of the neutrino is based on the total charge observed by the PMTs. Determining the systematic uncertainty of the energy scale is also essential. Four sources from highest to lowest energies are used to study this.

- Track length of high energy stopping muons (1 to 10 GeV/c)
- Cherenkov angle of low energy stopping muons (200 to 500 MeV/c)
- The invariant mass of π^0 produced by neutrino interactions (about 130 MeV/c)
- Momentum distribution of decay electron (about 50 MeV/c)

The accuracy of the absolute energy scale is checked by comparing data from all calibration sources from the MC simulation. Time variation, detector uniformity, and uncertainty of energy scale are also estimated.

4.5.1 High Energy Stopping Muons

Because the energy loss (dE/dx) is approximately constant in water, the momentum of CR muon can be determined by track length. Muon events that decay and emit electrons in the detector are used to estimate the track length. This muon events is a “stopping muon event”. The track length is defined by the distance between the entering position at the detector and the vertex position of the subsequent decay electron. Selection criteria for stopping muons are listed follows:

1. The entering the position of the cosmic muon is at the top wall of the detector
2. The direction of the stopping muon is downward
3. Only one decay electron is detected
4. Reconstructed range of the muon track is $7 < L < 30$ m

The first three criteria are used to select vertical downward going muons that have a clear Cherenkov ring. Therefore, it can be well reconstructed. The fourth criterion selects high energy events.

Muon momentum loss is thus calculated. The range of the muon is determined from the distance between the entrance point and the vertex point of the decay electron. The distribution of momentum per range is then compared with the MC simulation. Data and MC agree at 2.1%, 0.4%, 1.7%, and 0.7% for SK-I, SK-II, SK-III, and SK-IV, respectively.

4.5.2 Low Energy Stopping Muons

The momentum of stopping muons having low energy ($<500 \text{ MeV}/c$) can be estimated using the Cherenkov angle. The relationship between the Cherenkov angle and momentum can be expressed as follows:

$$\begin{aligned} \cos \theta_C &= \frac{1}{n\beta} = \frac{1}{n} \sqrt{1 + \frac{m^2}{P^2(\theta_C)}} \\ \therefore P(\theta_C) &= \frac{m}{\sqrt{n^2 \cos^2 \theta_C - 1}} \end{aligned} \quad (4.10)$$

where θ_C is the Cherenkov angle, n is the refraction index of water, $\beta = v/c$, m is mass, and P is momentum, respectively. Selection criteria for the low energy stopping muons are as follows:

1. The entering the position of the cosmic muon is at the top wall of the detector
2. The direction of the stopping muon is downward
3. Only one decay electron is detected
4. Total number of p.e. in the ID is less than 1,500 p.e. (750 p.e. for SK-II)

The first three criteria are the same as those for the high energy muon events. The fourth criterion selects low energy cosmic muons having momenta less than $380 \text{ MeV}/c$. The momentum estimated from the total charge is then compared with the estimation from the Cherenkov opening angle, $P(\text{p.e.})/P(\theta_C)$. The ratio is compared between data and MC. The agreement is within 3.3%, 2.1%, 1.5%, and 2.1% for SK-I, SK-II, SK-III, and SK-IV, respectively.

4.5.3 Neutrino Induced π^0 Events

Single π^0 events are produced by NC interactions of atmospheric neutrinos in the detector. The produced π^0 decays into two photons almost immediately. Therefore the invariant mass of π^0 can be calculated using the reconstructed momentum of two photons.

$$M_{\pi^0} = \sqrt{2P_{\gamma 1}P_{\gamma 2}(1 - \cos \theta)} \quad (4.11)$$

where $P_{\gamma 1}$ and $P_{\gamma 2}$ are the momenta of the two gamma-rays, and θ is the opening angle between them, NC π^0 events are selected from the atmospheric neutrino event sample by the following criteria.

1. Two electron-like rings are detected
2. An electron from muon decay is not detected
3. Vertex position is reconstructed within the FV

The second criterion rejects events in which charged pions are produced with the π^0 or CC events.

The actual π^0 mass is $135 \text{ MeV}/c^2$, and the mean invariant mass reconstructed is about $139 \text{ MeV}/c^2$. This shift to a slightly larger mass can be explained two ways. First, the pion is produced from the interaction with an oxygen nucleus, which is left in an excited state. That oxygen nucleus emits gamma-rays and transitions into its the ground state. Owing to the energy of the de-excitation of the gamma-ray, the reconstruction energy is large. Second, the gamma rays from the pion decay propagate for a short distance before causing an electromagnetic shower. Therefore, the reconstructed vertex is slightly forward, and the opening angle between two gamma rays is reconstructed slightly larger. This provides a larger pion invariant mass. The MC considers the de-excitation of the oxygen nucleus. The peak position of data and MC agree with 0.3%, 2.8%, 0.9%, and 1.0% for SK-I, SK-II, SK-III, and SK-IV, respectively.

4.5.4 Decay Electrons

Stopping CR muons produces many decay electron events. Decay electrons have energy spectra below about 53 MeV (i.e., the Michel spectrum). This energy range is compared between the data and the MC. Selection criteria for decay electron are listed follows:

1. Time interval from a stopping muon is 2.0 to $8.0 \mu\text{sec}$
2. The number of PMT hits in a 50 nsec window is > 60 (30 for SK-II)
3. The goodness of vertex fit is greater than 0.5
4. Vertex position is reconstructed within the FV

The first criterion involves the efficient timing of decay electron tagging. The second criterion rejects gamma rays of 6 MeV or more emitted from muon capture on nucleons.

The observed momentum spectra of the decay electrons have tails extending upwards to around $70 \text{ MeV}/c$. This is because some muons (μ^-) are captured by the K-Shell of an oxygen. The decay electrons are affected by the potential of the oxygen nucleus and muon orbital motion [212]. The MC considers this effect and the measured charge ratio (μ^+/μ^-) of 1.37 [213]. The mean values of the data spectrum agree with MC within 1.0%, 1.5%, 0.2%, and 1.5% for SK-I, SK-II, SK-III, and SK-IV, respectively.

4.5.5 Summary of Energy Calibration

The absolute energy scale is calibrated by various methods for different momentum ranges. To estimate the systematic uncertainty of the energy scale, the ratio of values between data and MC in each calibration method is used as shown in Figure 4.6.

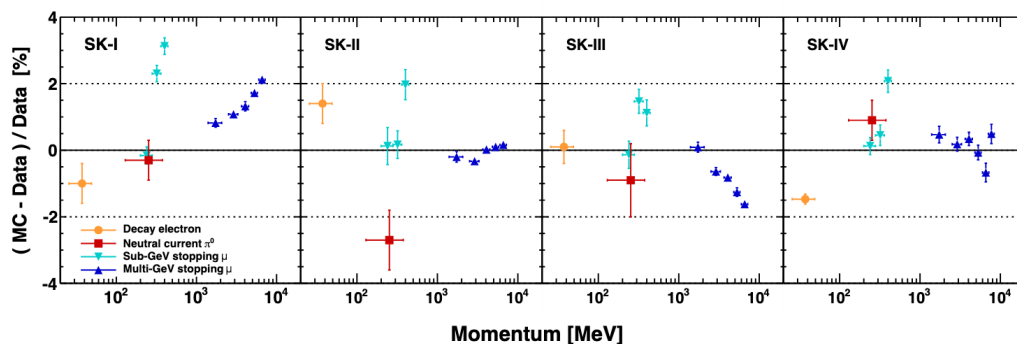


Figure 4.6: Summary of absolute energy scale measurements for each SK phase. The percentage of differences between data and MC are shown. Vertical error bars denote the statistical uncertainty and horizontal error bars denote the momentum range spanned by each analysis. The figure was taken from Abe et al. [214].

Because the distribution of the decay electron vertex and direction is almost uniform, the detector uniformity of the energy scale detector can be estimated using the decay electron sample. Electrons perpendicular to the direction of the parent muon are used for this measurement to take consider muon polarization. This condition is $|\cos \theta_{\mu e}| < 0.25$, where $\theta_{\mu e}$ is the opening angle between the muon and the electron directions. The ratio of averaged momenta of decay electrons between data and MC as a function of the opening angle is checked. The detector gains are uniform within 0.6%, 0.6%, 1.3% and 0.5% for SK-I, SK-II, SK-III, and SK-IV, respectively.

The stability of the energy scale is confirmed by stopping muons and decay electrons. Figure 4.7 shows the time variation of the energy scale, which is the average of the reconstructed momentum divided by range. During the SK-III phase, the transparency of water is poor, resulting in an energy scale with severe time fluctuations. The SK-IV phase is a result of improvements in the water purification system and of corrections for the time variation of the PMT responses. During the SK-IV phase, the energy scale has small time fluctuation caused by the further improvement to the water purification system and the correction of the time fluctuation of the PMT response.

Based on the results thus far, the final energy scale uncertainty in each phase was estimated at 3.3% in SK-I, 2.8% in SK-II, 2.4% in SK-III, and 2.1% in SK-IV.

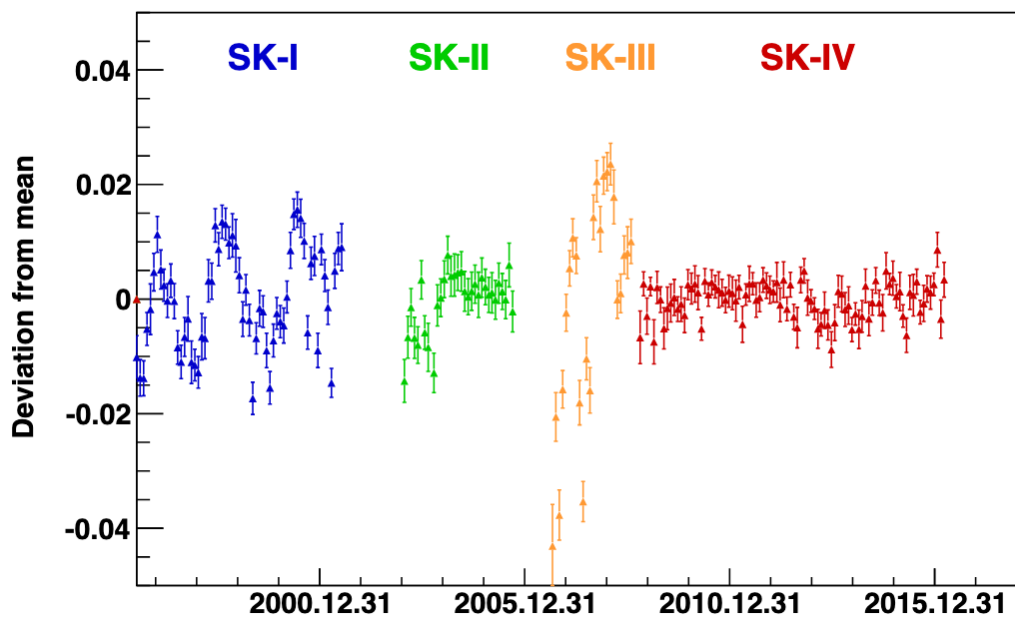


Figure 4.7: Energy scale stability as a function of date since the start of SK operations. The stability parameter was taken from the results of stopping muon. The vertical axis shows the deviation of this parameter from the mean value for each SK phase separately. The figure was taken from Abe et al. [214].

5 Event Reduction

The atmospheric neutrino events observed at SK are classified into three types: fully-contained (FC), partially-contained (PC), and upward-going muon (UPMU), as shown in Figure 5.1. In the FC and PC event samples, neutrino interactions are reconstructed within the ID using Cherenkov rings generated by charged particles.

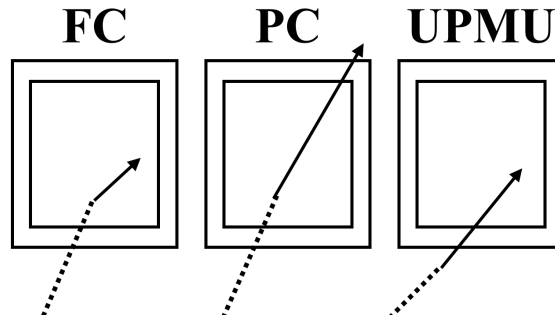


Figure 5.1: Three types of high-energy neutrino events at SK.

Events where all charged particles stop within the ID are classified as FC, and the events where at least one particle exits the ID and deposits energy in the OD is classified as PC. UPMU events are observed when energetic muons, generated by muon neutrino interactions with the rock surrounding the detector, enter the ID from below the horizon. Because a large amount of CR muons are detected as background from the top of the detector, the direction of the UPMU sample is required to be upward. There are no such restrictions for FC and PC events.

The mean energies of these event categories are about 1 GeV for FC, 10 GeV for PC, and 10 to 100 GeV for UPMU. Figure 5.2 shows the atmospheric neutrino energy spectra from the simulation without the effect of neutrino oscillations. The data reduction procedures are different for each of these categories and are described in this chapter.

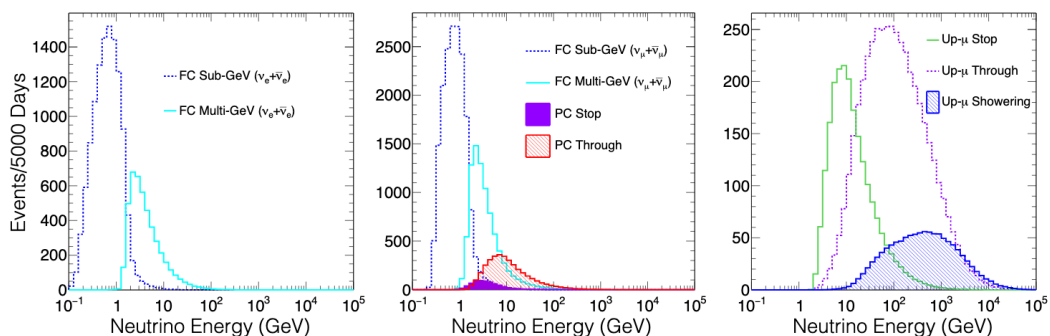


Figure 5.2: Expected energy distributions from atmospheric neutrino simulation for each event classification [214].

5.1 FC

FC reduction consists of five steps. During the SK-II period, the ID PMT coverage was around half that of other SK periods. Thus the values of criteria were individual. Because SK-IV has a different data acquisition system, some values are defined individually. The histograms in the following sections are criteria for a 5-day dataset during SK-IV phase.

5.1.1 First Reduction

The first reduction has two criteria to quickly filter out obvious backgrounds from CR muons, electrical noises, and low energy background, such as those caused by radiation. This reduction is performed for real time analysis.

To remove most of the low energy background, events are selected based on the amount of light incident on the PMTs. Events whose maximum number of total p.e. observed by the total ID PMTs in a sliding 300 nsec time window (PE_{300}) is less than 200 p.e. (100 p.e. for SK-II) are rejected. This threshold corresponds to 22 MeV/c electron momentum. Thus, in the analysis, events having a visible energy below 30 MeV are not used.

To remove the CR muon event that leaves a signal in the OD, events without OD triggers are selected. Furthermore, events whose number of hit OD PMTs in a fixed 800 nsec time window around the trigger timing ($NHITA_{800}$) is greater than 50 (55 for SK-IV) are rejected as shown in Figure 5.3.

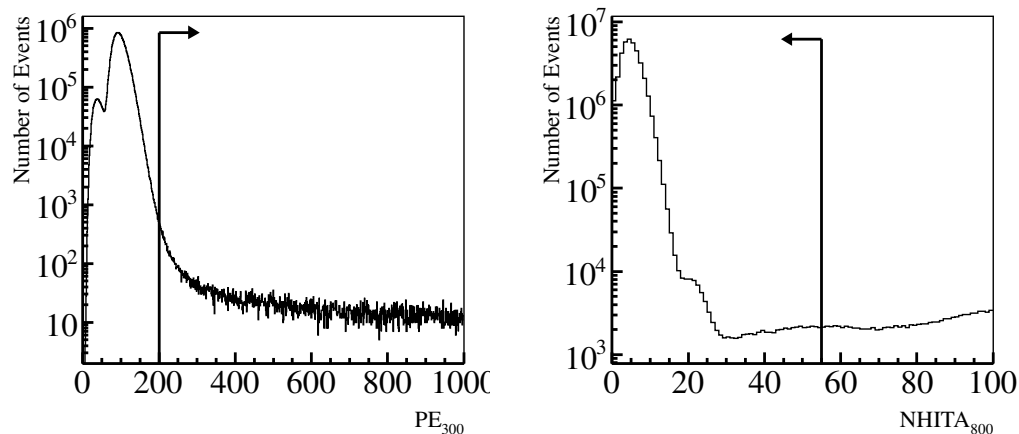


Figure 5.3: FC first reduction; the distribution of the number of p.e. observed by ID (PE_{300}) and OD ($NHITA_{800}$). The arrows mark the selected events. A typical 1-week dataset of the SK-IV phase was used.

5.1.2 Second Reduction

The second reduction comprises two cuts to give additional rejection of CR muons and electric noise events. From this reduction, the analysis is performed offline.

Events are rejected if the maximum number of p.e. observed by an ID PMT (PE_{\max}) is greater than half that of PE_{300} . This criterion rejects low energy electric noise events, to whose signal a single PMT largely contributes. This cut also discards events that record very large charges, called “flasher events”. A flasher event is caused by spontaneous flashing due to a discharge of the dynode structure.

For the reduction of lower energy muons, the criterion is set using a tighter threshold than that of the first reduction. If the $NHITA_{800}$ is greater than 25 (30 for SK-IV), and the PE_{300} is less than 100,000 p.e. (50,000 p.e. for SK-II), the events are rejected as shown in Figure 5.4.

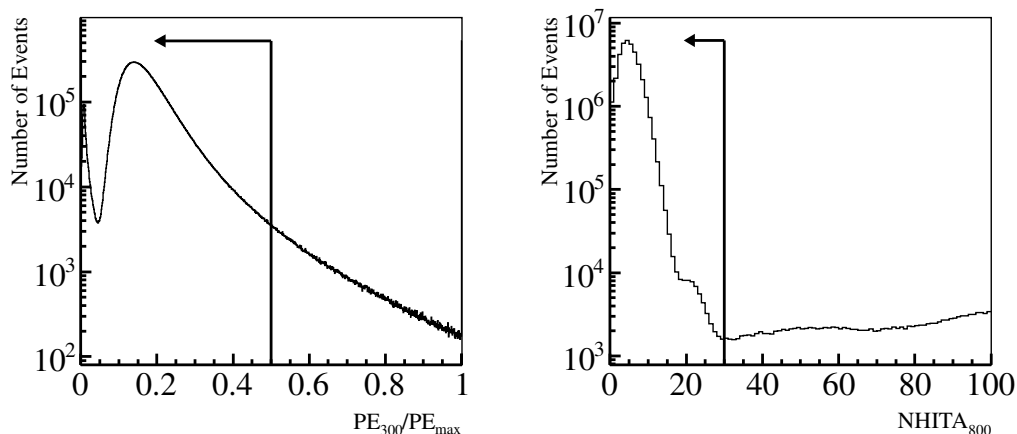


Figure 5.4: FC second reduction; PE_{300}/PE_{\max} and $NHITA_{800}$ distributions. The arrows mark the selected events. A typical 1-week dataset of the SK-IV phase was used.

5.1.3 Third Reduction

After the first and second reductions, a third reduction comprises of several cuts optimized to reduce various types of muons, flasher events, low energy radioactive, and electric noise events.

Through-going muon cut

A high-energy CR muon that passes through the ID is called a through-going muon. To eliminate these events, a through-going muon fitter is applied for events whose PE_{\max} is greater than 231 p.e., and the number of hit ID PMTs (NHIT) is more than 1,000. The fitter first selects the entrance point by locating the earliest hit PMT with some neighboring hit PMTs and selects the exit point by searching for

the center of the hit ID PMTs. The goodness of through-going muon fit is defined as:

$$\text{goodness} = \frac{1}{\sum_i \frac{1}{\sigma_i}} \sum_i \frac{1}{\sigma_i} \exp\left(-\frac{(t_i - T_i)^2}{2(1.5 \times \sigma_i)^2}\right), \quad (5.1)$$

where t_i and σ_i are the observed hit time of i -th PMT and its resolution and T_i is the expected hit time. Events whose values are greater than 0.75 are rejected. Furthermore, the number of hit OD PMTs located within 8 m of the entrance and exit points in a fixed time 800 nsec time window (NHITA_{in} and $\text{NHITA}_{\text{out}}$) are used for reduction. The events having more than 10 hits of NHITA_{in} or $\text{NHITA}_{\text{out}}$ are also rejected, as shown in Figure 5.5.

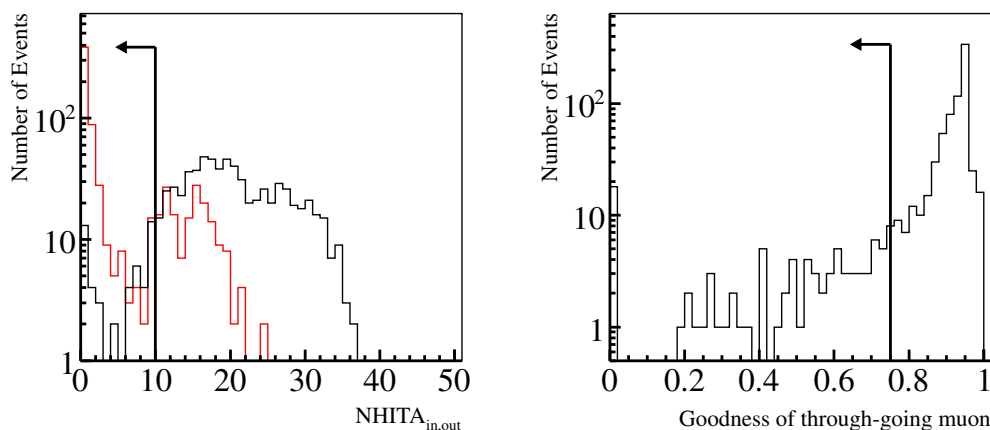


Figure 5.5: FC third reduction for through-going muon: NHITA_{in} (black line), $\text{NHITA}_{\text{out}}$ (red line), and goodness distributions. The arrows mark the selected events. A typical 1-week dataset of the SK-IV phase was used.

Stopping muon cut

CR muons that stop inside the ID detector are called stopping muons and are removed the same way as through-going muons. A stopping muon fitter is applied which finds the entrance point in a similar way as the through-going case. The events whose NHITA_{in} is greater than or equal to 10 are rejected as shown in Figure 5.6. When the goodness of fit is greater than or equal to 0.5 and NHITA_{in} is greater than or equal to 5, the events are rejected for only SK-I.

Cable hole muon cut

There are cable holes on the top of the detector tank to take the signal and HV supply cables out. The CR muons that enter through cable holes are removed using veto counter, as shown in Figure 5.7. When one veto counter hit and the distance

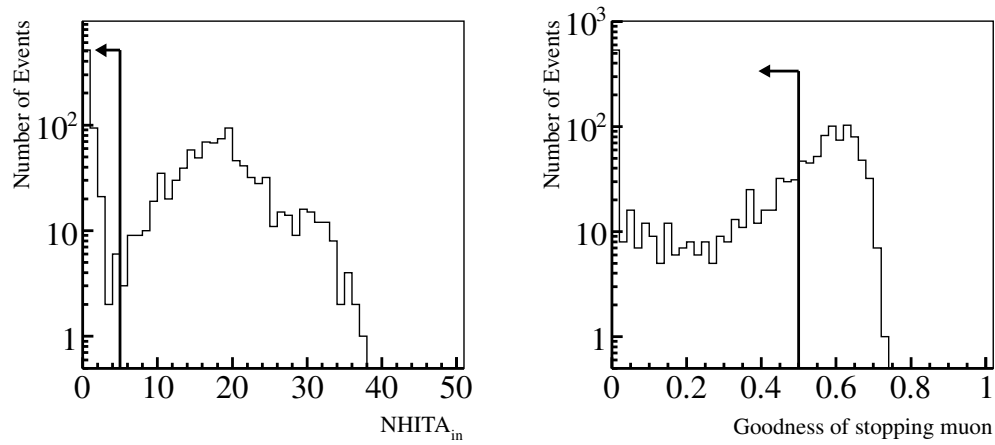


Figure 5.6: FC third reduction for stopping muon: $NHITA_{in}$ and goodness distributions. The arrows mark the selected events. A typical 1-week dataset of the SK-IV phase was used.

from the cable hole to the reconstructed vertex (L_{veto}) is less than 4 m, the events are rejected.

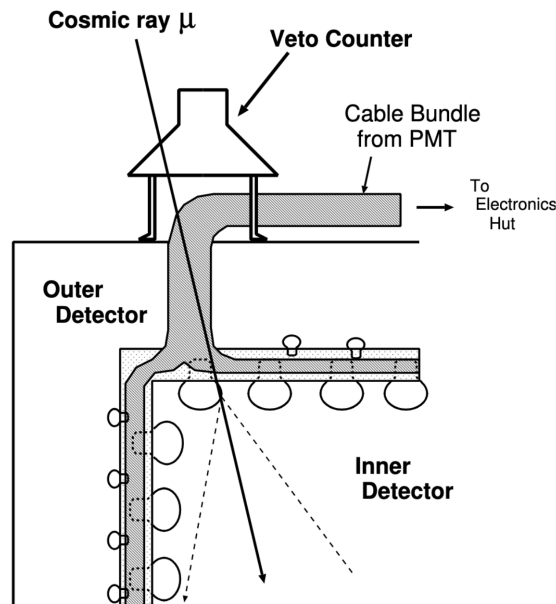


Figure 5.7: Cable hole and veto counter. The veto counter is a 2×2.5 m plastic scintillation counter set as veto for four large cable holes, installed in April 1997.

Flasher event cut

A flasher PMT event is an event caused by an electrical discharge in a PMT. Typical flasher events have broader hit timing distributions than neutrino events. To reduce such background, the events are rejected if the minimum number of hit ID PMTs in a sliding 100 nsec time window from 300 to 800 nsec after the trigger ($N_{MIN_{100}}$) is greater than 19 (14 for SK-I). Furthermore, when the $N_{MIN_{100}}$ is greater than 9, and the number of hit ID PMTs is less than 800, the events are removed for only the SK-I phase. Furthermore, when the goodness of the TOF fitter is less than or equal to 0.4, the events are rejected as shown in Figure 5.8.

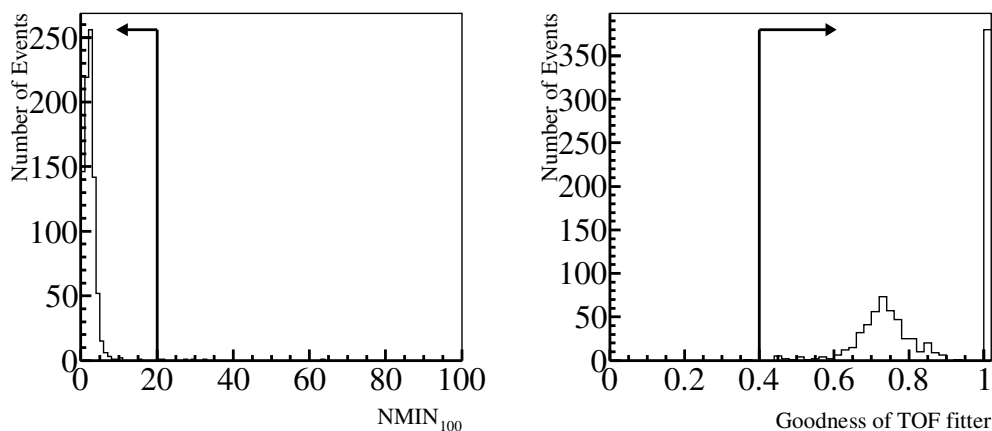


Figure 5.8: FC third reduction for flasher events: $N_{MIN_{100}}$ and goodness of TOF fitter distributions. The arrows mark the selected events. A typical 1-week dataset of the SK-IV phase was used.

Accidental coincidence events cut

Sometimes a CR muon event enters the trigger gate which is activated by a low energy event. These events are rejected to remove such coincidences when the number of hit OD PMTs in a fixed 500 nsec time window from 400 to 900 nsec after the trigger timing ($N_{HITA_{off}}$) is greater than 19, and the number of p.e. observed by ID PMTs in the same time window (PE_{off}) is greater than 5,000 p.e. (2,500 p.e. for SK-II).

Low-energy event cut

The remaining low-energy background events are from electronic noise and radioactive decay. After subtracting the TOF of each observed photon assuming all photons are generated at a point, the number of hit ID PMTs in a sliding 50 nsec time window ($N_{HIT_{50}}$) is counted. When the $N_{HIT_{50}}$ is less than 50 (25 for SK-II), the events are rejected.

5.1.4 Fourth Reduction

To remove the remaining flasher events, an intelligent pattern matching algorithm is used. The flasher events usually repeat with similar hit patterns in the detector, because the flasher events occur when light is emitted from flasher PMTs. It usually takes time before such bad PMTs are identified and turned off. The algorithm of the pattern matching is as follows:

1. Divide the ID wall into 1,450 patches of 2×2 m square.
2. Compute the correlation factor r by comparing the total charge in each patch of two events, A and B . The correlation is defined as:

$$r = \frac{1}{N} \sum_i \frac{(Q_i^A - \langle Q^A \rangle) \times (Q_i^B - \langle Q^B \rangle)}{\sigma^A \times \sigma^B}, \quad (5.2)$$

where N is the number of the patches, $Q_i^{A,B}$ are the charge of i -th PMT for the A and B events, $\langle Q^{A,B} \rangle$ are the averaged charge, and $\sigma^{A,B}$ are the standard deviations of charge distribution.

3. Calculate the distance (DIST_{max}) between the PMTs with the maximum pulse heights in the two compared events.
4. If DIST_{max} less than 75 cm, an offset value is added to r ($r = r + 0.15$).
5. If r exceeds the threshold (r_{thr}), events A and B are recognized as matched events. The r_{thr} is defined as

$$r > r_{\text{thr}} = 0.168 \times \log \left(\frac{\text{PE}_{300}^A + \text{PE}_{300}^B}{2} \right) + 0.13, \quad (5.3)$$

where $\text{PE}_{300}^{A,B}$ are the total number of p.e. observed in the ID.

6. Repeat the above calculation over 10,000 events around the target event and count the number of matched events.
7. Remove the events with large correlation factor, r , or a large number of matched events.

5.1.5 Fifth Reduction

The fifth reduction is designed to reject the remaining CR muons and flasher events. The remaining background events are few and can be removed by criteria specialized for each background event type.

Stopping muon cut

The remaining stopping muons are rejected more tightly than that of the third reduction. The entrance point is computed by extrapolating backward from the fitted track of the event instead of using the earliest hit PMT. $NHITA_{in}$ and goodness are calculated using the reconstructed entry point as the third reduction. Events whose $NHITA_{in}$ is greater than or equal to 10 are rejected. When the goodness of fit is greater than or equal to 0.5 and the $NHITA_{in}$ is greater than 5, the events are also rejected as shown in Figure 5.9.

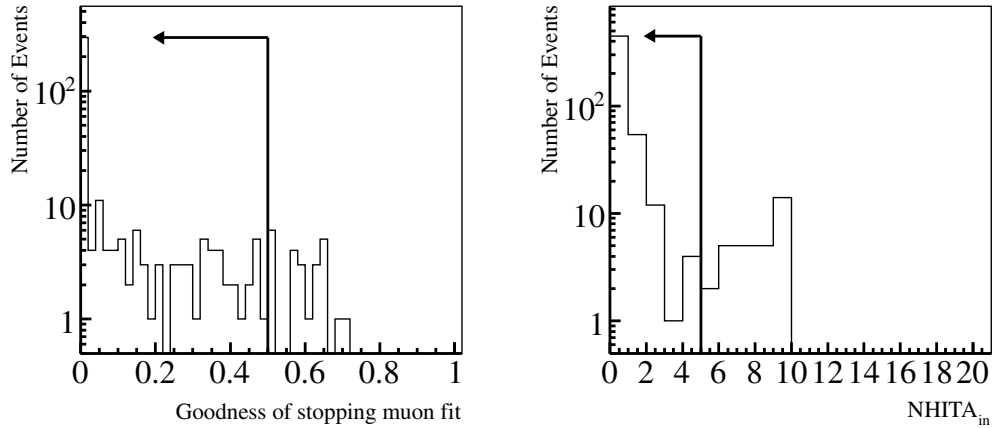


Figure 5.9: FC fifth reduction for stopping muon: Goodness and $NHITA_{in}$ distributions. The arrows mark the selected events. A typical 1-week dataset of the SK-IV phase was used.

Invisible muon cut

If the CR muon has too low a momentum to generate Cherenkov photons, it is called an invisible muon. Events caused by invisible muons are characterized by a low energy signal from a decay electron and a signal in the OD prior to trigger timing. If the PE_{300} is greater than or equal to 1,000 p.e. (500 p.e. for SK-II), this reduction is not performed, because the events are not from a decay electron. To count the hit OD cluster, two methods are used. $NHITAC_{early}$ is the maximum number of hit PMTs in an OD hit cluster in a sliding 200 nsec time window from $-8,000$ to 800 nsec. $NHITAC_{500}$ is the number of OD hits in the cluster in a fixed 500 nsec time window from -100 to 400 nsec around the trigger. If the distance between the OD hit clusters used for the calculation of $NHITAC_{early}$ and $NHITAC_{500}$ is less than 500 cm and $NHITAC_{500}$ is greater than 1, the sum of $NHITAC_{early}$ and $NHITAC_{500}$ is defined as a total number of OD PMT hits in the cluster ($NHITAC_{total}$). Otherwise, $NHITAC_{total}$ is defined as equivalent to $NHITAC_{early}$. The events are rejected when $NHITAC_{early}$ is greater than 5, and $NHITAC_{total}$ is greater than 10, as shown in Figure 5.10.

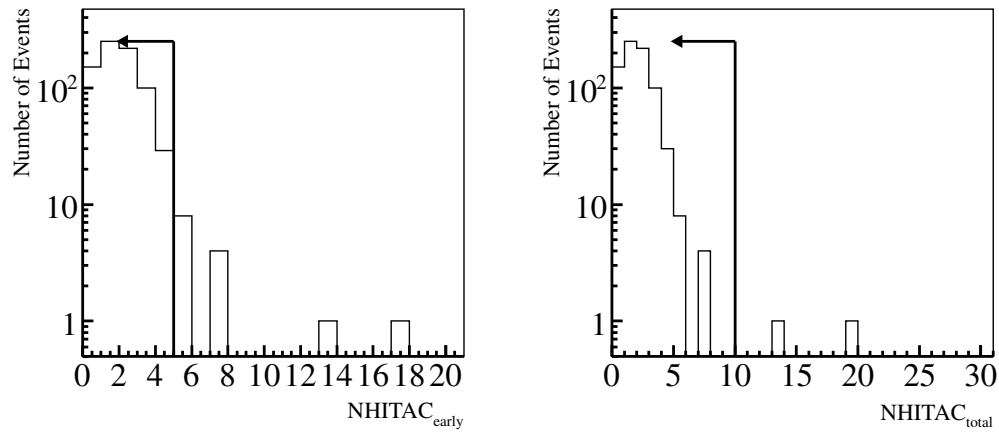


Figure 5.10: FC fifth reduction for invisible muon: $\text{NHITAC}_{\text{early}}$ and $\text{NHITAC}_{\text{total}}$ distributions. The arrows mark the selected events. A typical 1-week dataset of the SK-IV phase was used.

Accidental coincidence muon cut

The remaining accidental events after the third reduction are further removed. When the total number of p.e. observed in the ID in a fixed 500 nsec time window -100 to 400 nsec (PE_{500}) is less than 300 p.e. (150 p.e. for SK-II), and the maximum number of hit OD PMTs in a 200 nsec sliding window from 400 to 1,600 nsec (PE_{late}) is greater than 19 p.e., the events are rejected, as shown in Figure 5.11.

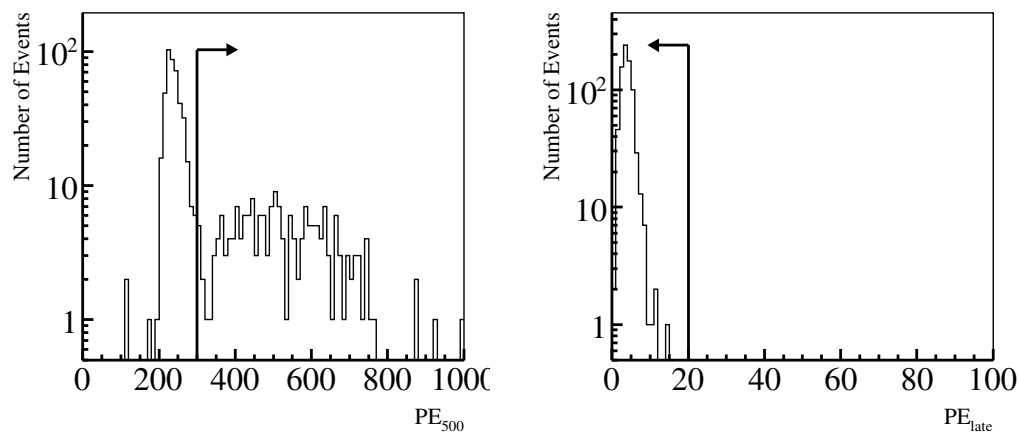


Figure 5.11: FC fifth reduction for coincidence muon: PE_{500} and PE_{late} distributions. The arrows mark the selected events. A typical 1-week dataset of the SK-IV phase was used.

Long-tail flasher cut

The remaining flasher events after the third reduction are further removed. For cut criteria, the goodness-of-vertex fit and the variable described in the third reduction $N_{\text{MIN}_{100}}$ are used. For SK-I, when the goodness-of-vertex fitter is less than 0.4 and $N_{\text{MIN}_{100}}$ is greater than 5, the events are rejected. From SK-II, when the goodness-of-vertex fit is greater than 0.3, and $N_{\text{MIN}_{100}}$ is less than 6, the events are rejected.

Electric noise event cut

The electric noise from HV systems or electronic boards create a lot of hits with a small amount of charge. To reject these as non-physical background events, the number of hits for ID PMTs having less or more than a single p.e., N_0 and N_1 respectively, are counted. When the N_0 is greater than or equal to 250 (125 for SK-II) and $N_0 - N_1$ greater than or equal to 100 (50 for SK-II), the events are rejected.

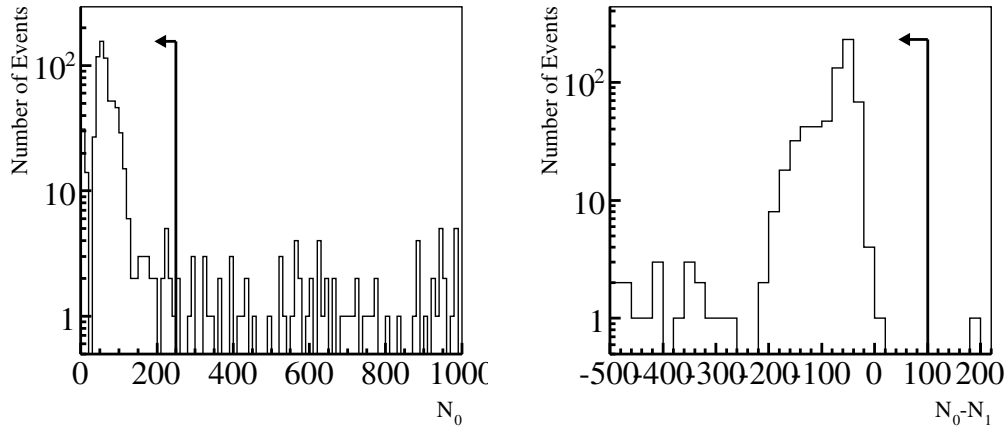


Figure 5.12: FC fifth reduction for electric noise event: N_0 and $N_0 - N_1$ distributions. The arrows mark the selected events. A typical 1-week dataset of the SK-IV phase was used.

5.1.6 Final FC Selection

After five reduction steps, the neutrino events that satisfy the following three criteria are finally selected. First, the number of hit PMTs in the largest OD hit cluster (NHITAC) is less than 16 (10 for SK-I). The OD activity is low enough that it can be classified as an FC event rather than a PC event. Second, the reconstructed vertex (D_{wall}) of neutrino interaction locates more than 200 cm away from the ID wall. This is the FV cut, which defines a 22.5 kilotons FV of the SK detector. Finally, the visible energy (E_{vis}) obtained from the reconstruction algorithm should be greater

than 30 MeV, because the atmospheric neutrino flux falls off at such a low energy. The cut is applied to reject any potential low energy events which are not relevant.

5.1.7 Summary of FC Reduction

The overall efficiency of the FC sample selections for the true neutrino events is estimated by the atmospheric neutrino MC as shown in Table 5.1. The efficiency is greater than 98% during the SK-I to SK-IV phase, and the systematic uncertainty is less than 1%. The average number of events per day in the final sample is about 8 events/day, which is stable through all SK phases.

Table 5.1: Reduction efficiency after each FC reduction step calculated by atmospheric neutrino MC. The selection efficiencies are for events whose FV are cut using true vertex information.

Efficiency [%]	SK-I	SK-II	SK-III	SK-IV
1st Reduction	100.00	99.96	100.00	100.00
2nd Reduction	100.00	99.90	99.98	99.99
3rd Reduction	99.91	99.77	99.81	99.83
4th Reduction	99.51	99.51	99.68	99.00
5th Reduction	99.47	99.43	99.62	98.95

The remaining backgrounds after reductions are CR muons, flasher events, and neutrons from the rock around the detector. The background contamination in the final sample is estimated to be about 0.1% based on the eye-scant of the selected events.

The summary of FC reduction is posted at the end. The definition of variables is described above.

First & Second Reduction

For a rough background estimation: an event is rejected if one of these criteria is satisfied.

1. $PE_{300} < 200$ p.e. (100 p.e. for SK-II)
2. $NHITA_{800} > 50$ (55 for SK-IV)
3. $PE_{\max}/PE_{300} > 0.5$
4. $NHITA_{800} > 25$ (30 for SK-IV) and $PE_{300} < 100,000$ p.e. (50,000 p.e. for SK-II)

Third Reduction

For through-going muons, an event that satisfies all of the following criteria is removed as through-going muon events:

1. $PE_{\max} > 231$ and $NHIT \geq 1,000$

2. goodness of through-going muon fitter > 0.75
3. $\text{NHITA}_{\text{in}} > 10$ or $\text{NHITA}_{\text{out}} > 10$

For stopping muons, an event is rejected if one of these criteria is satisfied:

1. $\text{NHITA}_{\text{in}} \geq 10$
2. goodness of stopping muon fitter ≥ 0.5 and $\text{NHITA}_{\text{in}} \geq 5$ (only for SK-I)

For cable hole muons, an event that satisfies all of the following criteria is removed:

1. One veto counter hit
2. $L_{\text{veto}} \leq 400$ cm

For flasher events, an event is rejected if one of these criteria is satisfied:

1. $\text{NMIN}_{100} \geq 20$ (15 for SK-I)
2. $\text{NMIN}_{100} \geq 10$ and $\text{NHIT} \leq 800$ (only for SK-I)
3. goodness of TOF fitter ≤ 0.4

For accidental coincidence & low energy events, an event is rejected if one of these criteria is satisfied:

1. $\text{NHITA}_{\text{off}} \geq 20$ and $\text{PE}_{\text{off}} > 5,000$ p.e. (2,500 p.e. for SK-II)
2. $\text{NHIT}_{50} < 50$

Fourth Reduction

For flasher events, a pattern matching algorithm is used to evaluate the similarity of the past events that passed the third reduction.

Fifth Reduction

For stopping muons, an event is rejected if one of these criteria is satisfied:

1. $\text{NHITA}_{\text{in}} \geq 10$
2. $\text{NHITA}_{\text{in}} \geq 5$ and goodness of fitter ≥ 0.5

For invisible muons, an event that satisfies all of the following criteria is removed:

1. $\text{PE}_{300} < 1,000$ p.e. (500 p.e. for SK-II)
2. $\text{NHITAC}_{\text{early}} \geq 5$
3. $\text{NHITAC}_{\text{total}} \geq 10$

For accidental coincidence, an event that satisfies all of the following criteria is removed:

1. $\text{PE}_{500} < 300$ p.e. (150 p.e. for SK-II)
2. $\text{PE}_{\text{late}} \geq 20$ p.e.

For long-tail flasher, an event is rejected if one of these criteria is satisfied:

1. $N_{\text{MIN}100} \geq 6$ and goodness of vertex fitter < 0.4 (for SK-I)
2. $N_{\text{MIN}100} < 6$ and goodness of vertex fitter < 0.3 (for SK-II to SK-IV)

For electric noise, an event that satisfies all of the following criteria is removed:

1. $N_0 \geq 250$ (125 for SK-II)
2. $N_0 - N_1 \geq 100$ (50 for SK-II)

Final Reduction

For the FV cut, an event that satisfies all of the following criteria is selected:

1. $\text{NHITAC} < 16$ (10 for SK-I)
2. $D_{\text{wall}} < 200$ cm
3. $E_{\text{vis}} > 30$ MeV

5.2 Partially Contained

PC events are separated from FC events via OD activities. Because OD segmentation was installed during the SK-III phase, the reduction process is modified to adjust. There are five steps for PC reduction. The histograms in the following sections are also criteria for a 5-day dataset of the SK-IV phase.

5.2.1 First Reduction

To reject through-going CR muons and low energy events, the first reduction is done for real time analysis. For all SK phases, the PC sample requires that exiting particles have a track length in the ID of at least 2 m, which corresponds to a momentum loss of 500 MeV/c for muons. Therefore, PE_{300} should be greater than or equal to 1,000 p.e. (500 p.e. for SK-II) conservatively, which corresponds to 310 MeV/c for muons.

For SK-I and SK-II, to remove through-going CR muons, when the width of the hit timing distribution in the OD PMTs (TWIDA) is greater than 260 nsec (170 nsec for SK-II), and the number of hit cluster in the OD (NCLSTA) is greater than 1 (only for SK-I), the events are rejected. Because through-going muon events have a broad hit timing distribution, two hit clusters are found around the entrance and exit point in the OD.

For SK-III and SK-IV phases, a more efficient cut was used because of the segmentation of the OD. PE_{300} should be greater than or equal to 1,000 p.e. as with the SK-I phase. If either the number of OD hits in the top (bottom) ($\text{NHITA}_{\text{top}}$ ($\text{NHITA}_{\text{bottom}}$)) is less than 11 (10), the event is rejected. Moreover, the events are rejected if the total number of OD hits in top and bottom called end-cap region ($\text{NHITA}_{\text{endcap}}$) is less than 29 or the number of OD hits in side ($\text{NHITA}_{\text{side}}$) is less than 84, as shown in Figure 5.13. Because through-going muons are expected to deposit energy in two regions of the OD, the average distance between all hit pairs

(ODR_{mean}) is expected to be larger than PC events. Thus, when ODR_{mean} is greater than or equal to 2,140 cm, the events are rejected, as shown in Figure 5.13. The definition of ODR_{mean} is as follows:

$$\text{ODR}_{\text{mean}} = \frac{1}{N_{\text{pair}}} \sum_{i=i}^{N-1} \sum_{j=i+1}^N |\vec{x}_i - \vec{x}_j|. \quad (5.4)$$

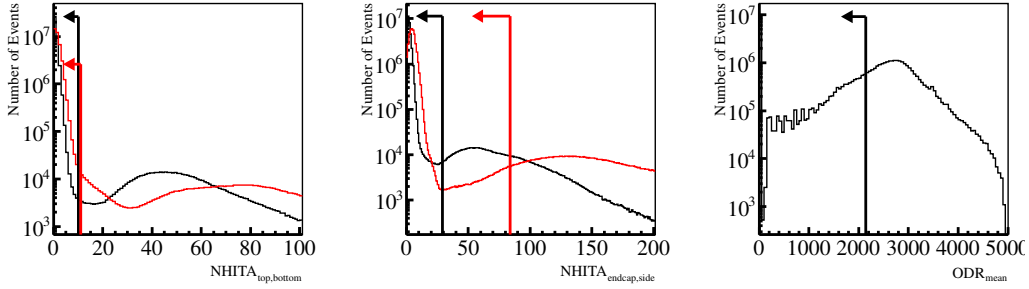


Figure 5.13: PC first reduction: NHITA (for top, bottom, endcap, and side) and ODR_{mean} distributions. The black (red) line of left panel corresponds to the $\text{NHITA}_{\text{top}}$ ($\text{NHITA}_{\text{bottom}}$). The black (red) line of center panel corresponds to the $\text{NHITA}_{\text{endcap}}$ ($\text{NHITA}_{\text{side}}$). The arrows mark the selected events. A typical 1-week dataset of the SK-IV phase was used.

5.2.2 Second Reduction

A clustering algorithm of OD hits is used to reject the through-going muons and the stopping muons. The ID and OD walls are divided into 21×21 and 11×11 patches. The charge observed in each patch is counted as shown in Figure 5.14. The clusters are formed by looking for the charge gradient to the neighboring patches.

For the SK-I, the following three clusters amounts are used to reject the events: the number of hits in the largest OD cluster (N_1^{outer}), the number of hits in the second-largest OD cluster (N_2^{outer}), and the smaller of the number of wall hits and the number of end-cap hits ($N_{\text{min}}^{\text{outer}}$). If either the N_2^{outer} or $N_{\text{min}}^{\text{outer}}$ is greater than 6, the events are rejected. Furthermore, when N_1^{outer} is greater than 6, and the number of the observed p.e. within 200 cm from the highest charge PMT in the ID hit cluster closest to the OD hit cluster (PE_{200}) is less than 1,000 p.e., the events are rejected.

For the SK-II, when the N_2^{outer} is greater than 6, the events are rejected as same as SK-I. When the $\text{NHITA}_{\text{endcap}}$ is greater than or equal to 20 and $\text{MAX}(\text{NHITA}_{\text{side}})$, the events are rejected. The definition of $\text{MAX}(\text{NHITA}_{\text{side}})$ is as follows:

$$\text{MAX}(\text{NHITA}_{\text{side}}) = \begin{cases} \exp(5.8 - 0.023 \times \text{NHITA}_{\text{side}}) & (\text{NHITA}_{\text{side}} < 75) \\ \exp(4.675 - 0.008 \times \text{NHITA}_{\text{side}}) & (\text{NHITA}_{\text{side}} \geq 75) \end{cases} \quad (5.5)$$

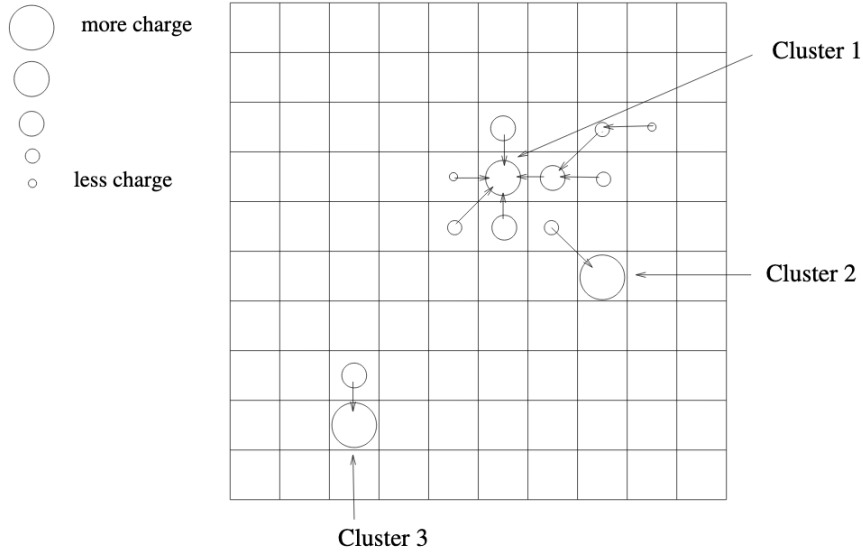


Figure 5.14: Algorithm for finding hit clusters in OD. The circles represent the charge observed at each patch. The size of the circle is proportional to the number of p.e.. The arrow represent the vector charge gradient, which points to highest charge among neighboring patches.

If N_1^{outer} and PE_{200} satisfy: $N_1^{\text{outer}} > 6$ and $N_1^{\text{outer}} \geq 12 + 0.085 \times PE_{200}$, the events are rejected.

For SK-III and SK-IV, because the first reduction using the OD segmentation is very efficient, the second reduction consists of two criteria for SK-II. First, when the N_2^{outer} is greater than 10, the events are rejected. Secondly, when the $NHITA_{\text{endcap}}$ is greater than or equal to 20 and $MAX(NHITA_{\text{side}})$, the events are rejected as shown in Figure 5.15.

5.2.3 Third Reduction

The flasher events are rejected in the same way as that of the FC third reduction, in which the broad timing distribution of the flasher events is used for the cut. For SK-I to SK-IV, when $NMIN_{100}$ is less than 15, the events are rejected as flasher events. Otherwise, when $NMIN_{100}$ is less than 10 and $NHIT$ is greater than or equal to 800 (400 for SK-II), the events are also rejected.

For the SK-I and SK-II, the stopping muons are also rejected by using the number of hit OD PMTs near the entrance point. The entrance position is estimated via backward extrapolation from the reconstructed vertex, which is fitted by point-fit. The events are rejected when the $NHITA_{\text{in}}$ is greater than 10 as shown in Figure 5.16. For SK-III and SK-IV, the stopping muon cut is applied at the PC fifth reduction stage.

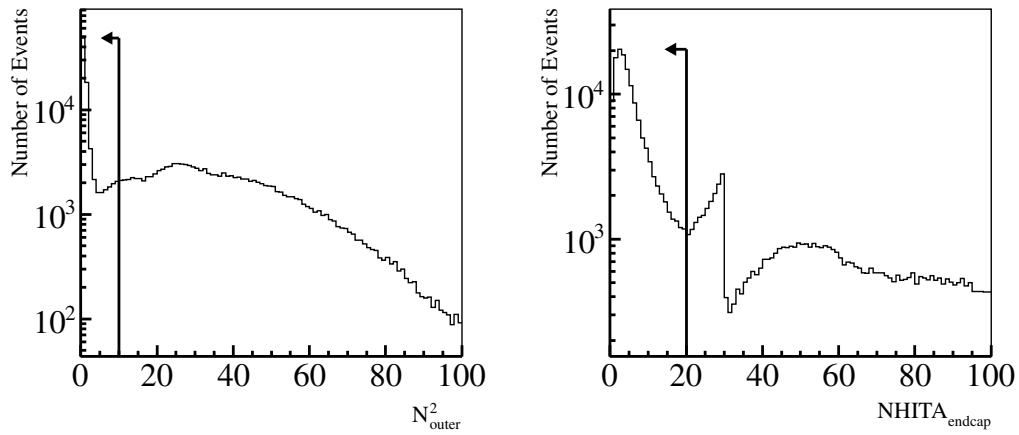


Figure 5.15: PC second reduction: N_{outer}^2 and $\text{NHITA}_{\text{endcap}}$ distributions. The arrows mark the selected events. A typical 1-week dataset of the SK-IV phase was used.

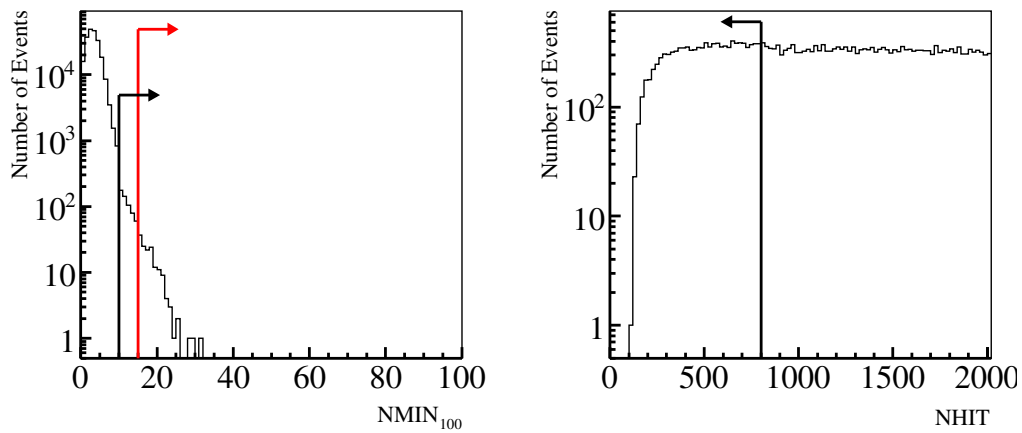


Figure 5.16: PC third reduction: NMIN_{100} and NHITA distributions. The two black arrows represent conditions having two parameters. The arrows mark the selected events. A typical 1-week dataset of the SK-IV phase was used.

5.2.4 Fourth Reduction

The fourth reduction was completely modified for SK-III and SK-IV because of the OD segmentation. Here, we describe two versions of the fourth reduction.

For SK-I and SK-II

To reject the CR muons, two types of event reconstruction tools are used: Point-fit and through-going muon fit. There are four criteria, and the event is rejected as a CR muon event if any of them is not satisfied.

First, the inner product of the reconstructed direction by the Point-fit (\vec{d}_{fit}), and the direction from the reconstructed vertex to the earliest saturated PMT (\vec{d}_{PMT}) should be greater than -0.8 . Second, the goodness of the through-going muon fit should be greater than 0.85 . Third, the track length of a muon (TLMU) estimated from the entrance and the exit points by the through-going muon fit should be greater than 30 m. Finally, the distance (DCORN) from the reconstructed vertex by the Point-fit to the nearest fringe of the ID should be greater than 150 cm.

The first criterion aims to reject the CR stopping muons that have an entrance point in the opposite direction to the reconstructed direction. The through-going muons which have a long track length are rejected by the second and third criteria. And the corner clipping muons are rejected by the final cut.

For SK-III and SK-IV

An event reconstruction tool is used to classify each event as a stopping muon, a through-going muon, or a corner clipping muon. For classification, there are five possible selection criteria based on the fitter as shown in Figure 5.17.

1. The angle (θ_{muon}) between the fitting direction and the vector between the fitted vertex and the center of the highest charge OD cluster is less than 90° .
2. The inner production of the fitting direction (\vec{d}_{muon}) and the vector (\vec{d}_{PMT}) between the fitted vertex and the earliest PMT is greater than -0.8 .
3. The goodness of the muon fitter ($\text{goodness}_{\text{muon}}$) is less than 0.52 .
4. The length (L_{muon}) of the fitted muon track is less than 17.5 m.
5. The distance ($\text{Corner}_{\text{muon}}$) between the fitted entrance point and the corner of the tank is less than or equal to 3 m.

The number of these criteria required to pass this reduction step depends on the classification of events from the fitter. If an event is classified as a PC through-going muon, it must pass four of the five criteria. Similarly, if an event is classified as a PC stopping muon, it must pass four of the five criteria, including the second criterion with additional requirements. The event must have the $\text{goodness}_{\text{muon}}$ less than 0.5 , or NHITA_{in} should be less than 10 . For the other classifications, two of the five criteria must be passed.

Finally, when the PE_{300} is less than $3,000$ p.e., the events are rejected to remove the low energy background. This threshold corresponds to a muon momentum of 500 MeV/c, which is safe for PC events, because exiting muons must have at least a momentum of 700 MeV/c to reach the OD.

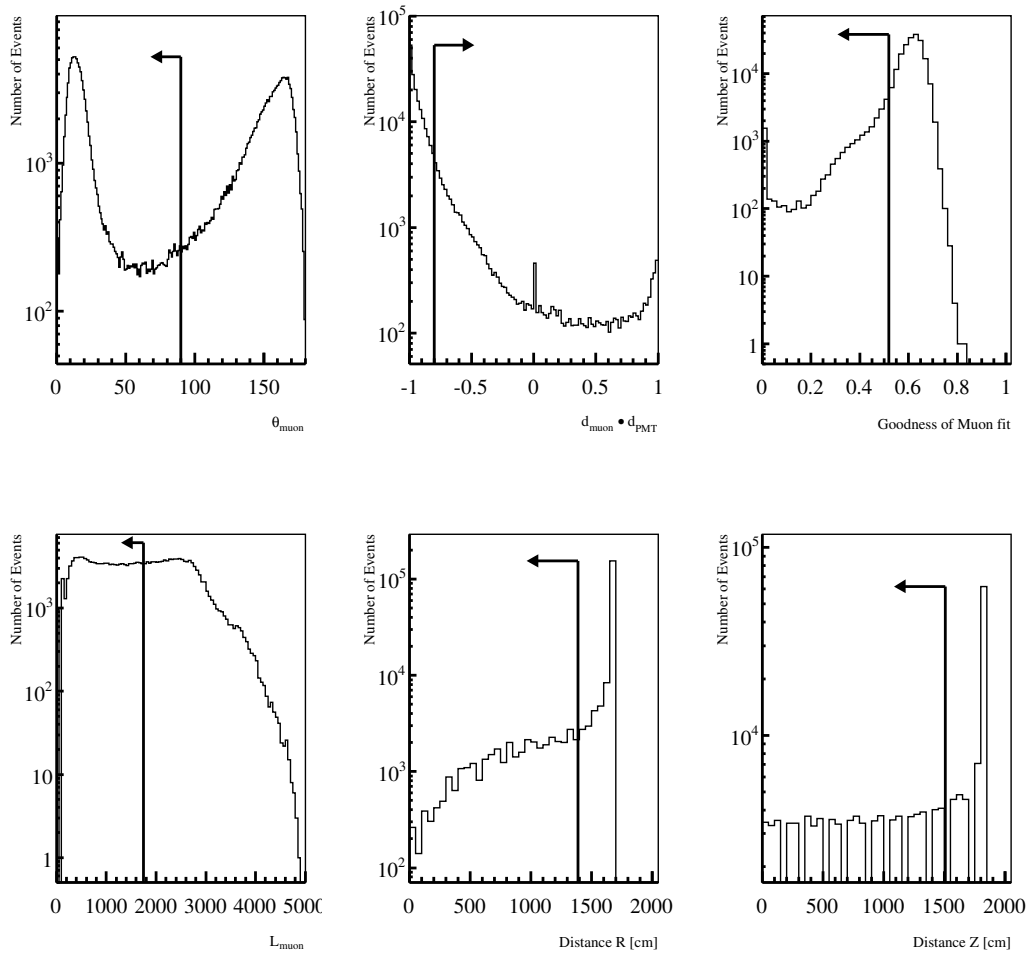


Figure 5.17: PC fourth reduction: These are distributions of the angle, the inner production, the goodness, the length, and the distance from the wall in order from the upper left. The arrows mark the selected events. A typical 1-week dataset of the SK-IV phase was used.

5.2.5 Fifth Reduction

The fifth reduction elaborate selection criteria, specialized for each background source, are applied. The selections for the SK-I to SK-II and SK-III to SK-IV phase are different. Here, we describe the criteria for using both versions of the fifth reduction. Two types of reduction are determined by a combination of these cuts.

Low energy event cut The remaining low energy background events are again rejected by using the PE_{300} . The PE_{300} should be greater than 3,000 p.e.. This will remove much of the low energy background.

Through-going muon cut (A) To remove the remaining through-going muons, OD hit cluster information obtained by the algorithm in the PC second reduction is used. There are three criteria: the distance ($\text{DIST}_{\text{cluster}}$) between the highest charge OD hit cluster and the second highest one is greater than 20 m; the number of p.e. (PEAC_2) detected in the second-highest charge OD hit cluster is greater than or equal to 10 p.e.; and the number of hits in third-largest OD cluster (N_3^{outer}) is greater than or equal to 2. When all of these criteria are satisfied, the events are rejected as through-going muon events.

Through-going muon cut (B) Some CR muons enter the detector from the edge atop the detector and exit from the edge at the bottom, and these events pass the prior reduction steps. The light collection efficiency around the edge of the OD is relatively poor, and the event reconstruction tools do not perform well at the detector boundaries.

An event that satisfies all of the following three criteria is rejected. First, the $\text{NHITA}_{\text{top}}$ and $\text{NHITA}_{\text{bottom}}$ are greater than or equal to 7. Second, the number of p.e. (PEA_{top} and $\text{PEA}_{\text{bottom}}$) in the OD detected in the same sphere as that for $\text{NHITA}_{\text{top}}$ and $\text{NHITA}_{\text{bottom}}$ are greater than or equal to 10. Finally, assuming that the detector tank height is 1, the distance the particle can pass in the time interval (TDIFFA) between the averaged hit timing of the top and bottom spheres are calculated. When the $\text{TDIFFA} \times c/40 \text{ m}$ is between 0.75 to 1.5, the event may be a through-going muon event, as shown in Figure 5.18.

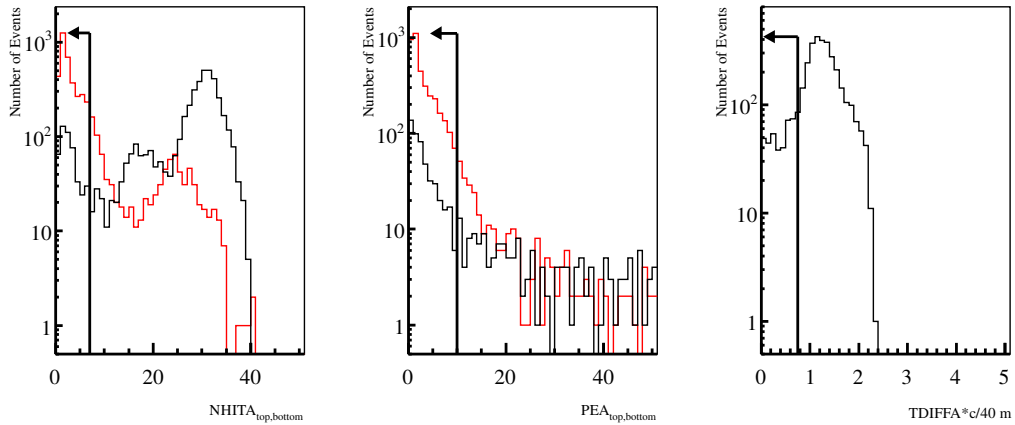


Figure 5.18: PC fifth reduction for through-going muon cut B: the distributions of the NHITA for top (black) and bottom (red), the PEA for top (black) and bottom (red), and the relative track length. The arrows mark the selected events. A typical 1-week dataset of the SK-IV phase was used.

Through-going muon cut (C) The through-going muons are removed per the number of hit OD PMTs near the entrance and the exit point. The vertex po-

sition and the direction of a particle are reconstructed with a precise fit using the Cherenkov ring pattern. The entrance and exit points are estimated by extrapolation.

An event that satisfies all of the following two criteria is rejected. First, NHITA_{in} is greater than or equal to 5, and $\text{NHITA}_{\text{out}}$ is greater than or equal to 7. Second, the same calculation used in the previous cut is performed, but the length of the track (TRACK) is used instead of the height of the tank. When the $0.75 < \text{TDIFFA} \times c/\text{TRACK} < 1.5$ is between 0.75 and 1.5, the event may be through-going muon event, as shown in Figure 5.19.

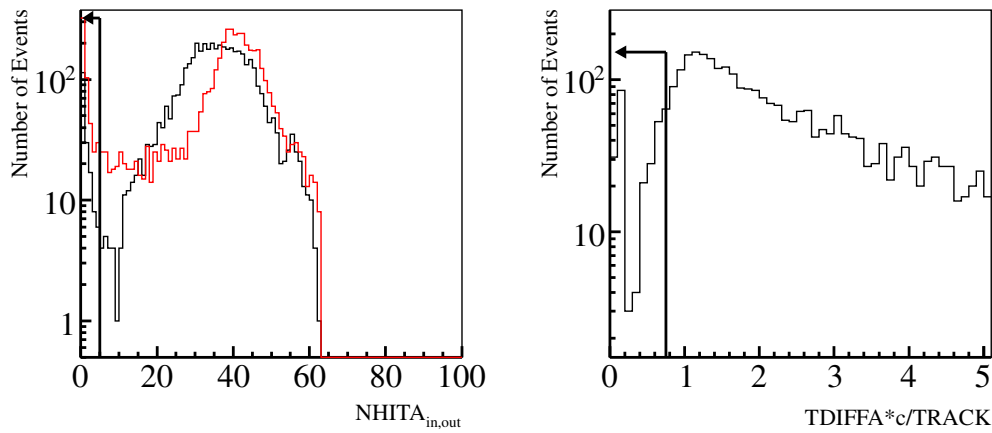


Figure 5.19: PC fifth reduction for through-going muon cut C: the distributions of the NHITA_{in} (black), the $\text{NHITA}_{\text{out}}$ (red), and the relative track length. The arrows mark the selected events. A typical 1-week dataset of the SK-IV phase was used.

Through-going muon cut (D) The remaining through-going muons are removed per the number of hit OD PMTs. The highest charge cluster (N_1^{outer}) and the second-highest charge cluster (N_2^{outer}) are used. These values are calculated the same way as the PC second reduction. When the N_1^{outer} is greater than 9, and N_2^{outer} is greater than 16, the events are rejected as a through-going muon event, as shown in Figure 5.20.

Stopping Muon Cut (A) The number of hit OD PMTs near the entrance position is counted for the stopping muon events. The entrance point of the stopping muons is estimated by reconstructing the vertex position and direction. When the NHITA_{in} is greater than or equal to 10, the event is rejected as a stopping muon, as shown in Figure 5.21.

Stopping muon cut (B) Although the stopping muon has a larger angle between the reconstructed direction and the OD hit cluster than a PC event, the

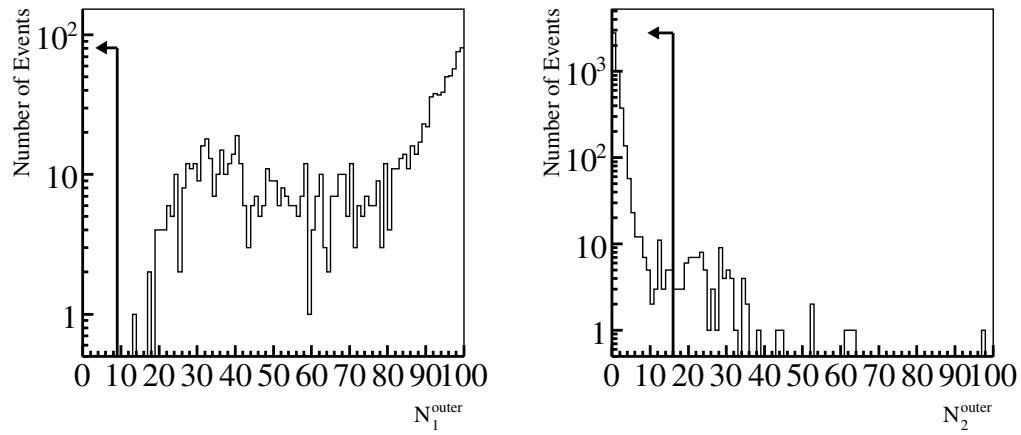


Figure 5.20: PC fifth reduction for through-going muon cut D: the distributions of the highest and the second-highest charge cluster. The arrows mark the selected events. A typical 1-week dataset of the SK-IV phase was used.

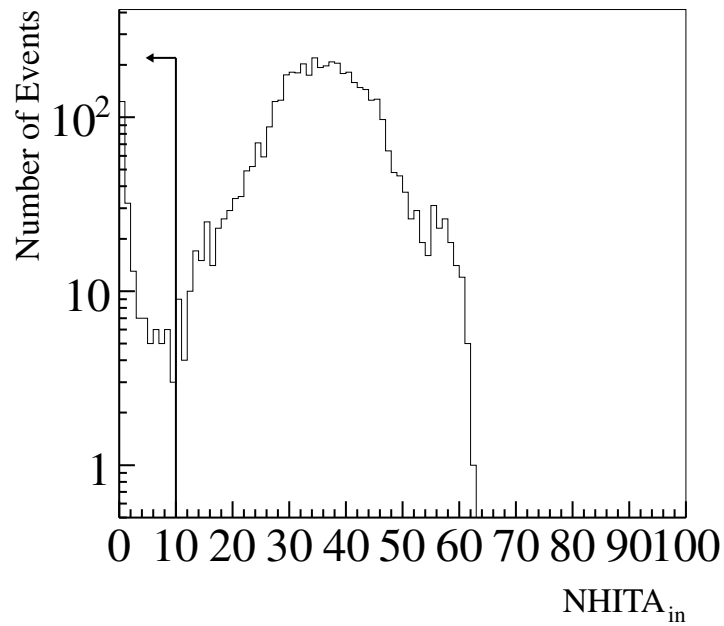


Figure 5.21: PC fifth reduction for stopping muon cut A; the NHITA_{in} distribution. The arrows mark the selected events. A typical 1-week dataset of the SK-IV phase was used.

angle is calculated using two different fitters. When the opening angle (θ_{TDCFit} or θ_{MSFit}) is greater than 90° , the event is rejected, as shown in Figure 5.22.

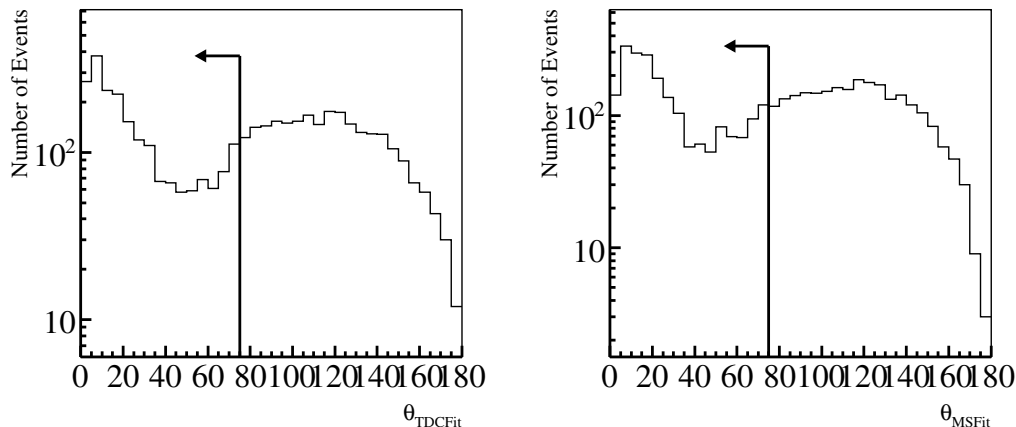


Figure 5.22: PC fifth reduction for stopping muon cut B; the distributions of opening angles calculated by TDC fitter and MS fitter. The arrows mark the selected events. A typical 1-week dataset of the SK-IV phase was used.

Stopping muon cut (C) The entrance position as the earliest hit cluster in the ID is estimated via stopping muon fitting. If the NHITA_{in} is less than or equal to 6, then the charge inside a 42° cone facing the entrance position is checked. When the ratio of charge inside (PE_{cone}) and outside (PE_{300}) the cone is less than 60%, the event is rejected as stopping muon event as shown in Figure 5.23.

Stopping Muon Cut (D) To reject stopping muon events, the number of hit OD PMTs within 8 m of the reconstructed entry point (NHITA_{in}) is used. This criterion was applied during the PC third reduction for SK-I and SK-II. For SK-III and SK-IV, the events with NHITA_{in} above 10 are required. Moreover, the entrance point is compared with two types of fitters: Point-fit ($\vec{P}_{\text{PointFit}}$) and MS-fit (\vec{P}_{MSFit}). The PC events require that the difference between $\vec{P}_{\text{PointFit}}$ and \vec{P}_{MSFit} be less than 15 m.

Stopping muon cut (E) The same criterion of θ_{muon} in PC fourth reduction is applied, because the cut was a loser for events that were classified as stopping or through-going muon events. When the θ_{muon} is greater than 90° , the events are rejected.

Corner clipping muon cut (A) Corner clipping muon events have a small hit cluster in the ID, and the vertex is sometimes mis-reconstructed in the ID. Therefore, we reject the mis-reconstructed edge clipping muon using the relation

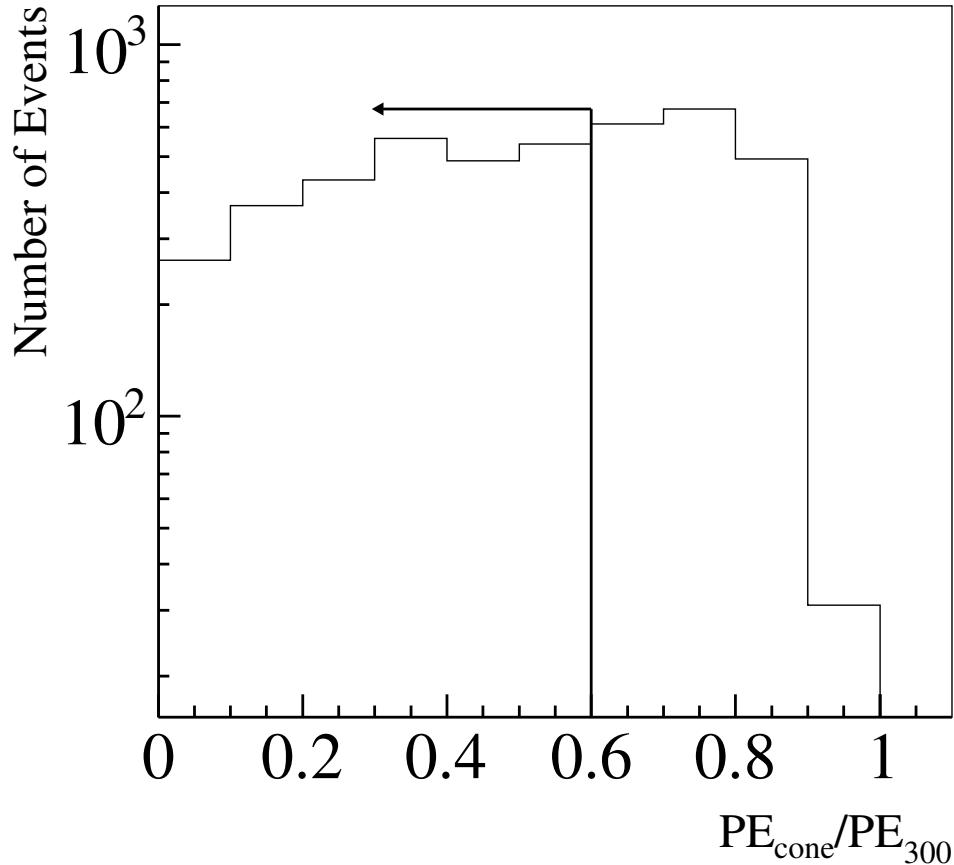


Figure 5.23: PC fifth reduction for stopping muon cut C: the distributions of the ratio of charge. The arrows mark the selected events. A typical 1-week dataset of the SK-IV phase was used.

between the energy loss and track length from vertex to OD exit position. When the estimated track length from the visible energy ($\text{TRACK}_{\text{vis}}$), assuming an energy loss of 2 MeV/cm minus TRACK is less than -15 m , the event is rejected as shown in Figure 5.24.

Corner clipping muon cut (B) This is the same criterion that was applied in the PC fourth reduction for the SK-I and SK-II. This cut avoids clipping muon events by requiring the edge to be not too close to the edge of the ID. When the DCORN is less than 150 cm , the events are rejected as shown in Figure 5.25.

Cable hole muon cut There are four veto scintillation counters placed over the cable holes atop of the detector. Because a PC event can activate those veto, two

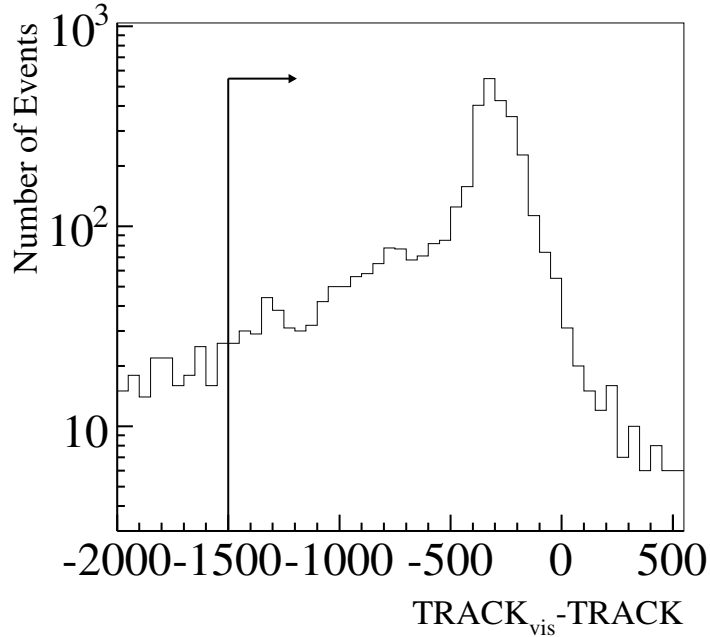


Figure 5.24: PC fifth reduction for corner clipping muon cut A: the distribution of the difference of track length. The arrows mark the selected events. A typical 1-week dataset of the SK-IV phase was used.

criteria are required. When one veto counter hits, the ring direction reconstructed by TDC-fit (\vec{d}_{ring}) and the direction from the hit veto counter to the reconstructed vertex ($\vec{d}_{\text{veto-vertex}}$) is calculated. When the inner production of \vec{d}_{ring} and $\vec{d}_{\text{veto-vertex}}$ is greater than -0.8 , the event is rejected.

Decay electron cut High energy neutrinos interact with nucleons in water mainly via DIS interaction to produce hadrons containing charged pions. Those pions decay into muons, and muons decay into electrons. When the number of tagged decay electrons (N_{decay}) is greater 1 and the visible energy (E_{vis}) is greater than 25 GeV, the events are rejected as the CR muons.

For SK-I and SK-II

The PC fifth reduction for SK-I and SK-II requires the following criteria. When all criteria are satisfied, the events will be saved as a PC sample.

1. Low energy cut
2. Through-going muon cut (A)
3. Through-going muon cut (B)

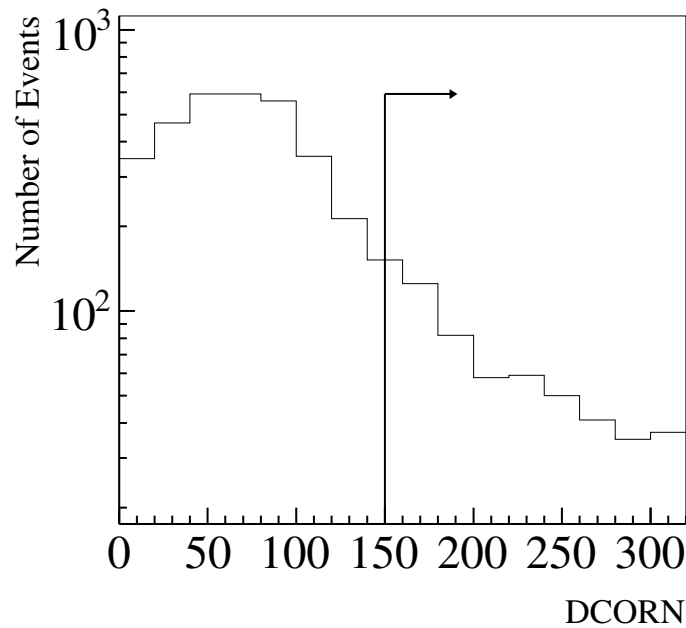


Figure 5.25: PC fifth reduction for corner clipping muon cut B: the DCORN distribution. The arrows mark the selected events. A typical 1-week dataset of the SK-IV phase was used.

4. Through-going muon cut (C)
5. Stopping muon cut (A)
6. Stopping muon cut (B)
7. Stopping muon cut (C)
8. Corner clipping (A)
9. Cable hole muon cut

For SK-III and SK-IV

There are two types of cuts: hard and soft for SK-III and SK-IV. PC reduction for SK-III and SK-IV is modified to keep efficiency as SK-I and SK-II. PC sample is required to pass all hard cuts and the events may fail soft cut just once. The hard cuts are:

1. Low energy cut
2. Through-going muon cut (A)
3. Through-going muon cut (B)

4. Stopping muon cut (B)
5. Corner clipping (B)
6. Cable hole muon cut

The soft cuts are:

1. Through-going muon cut (C)
2. Through-going muon cut (D)
3. Stopping muon cut (A)
4. Stopping muon cut (C)
5. Stopping muon cut (D)
6. Stopping muon cut (E)
7. Corner clipping (A)
8. Decay electron cut

5.2.6 Final PC Reduction

After five reduction steps, the neutrino events that satisfy the following three criteria are finally selected. First, the vertex of neutrino interactions should be inside the FV. Second, the NHITAC should be larger than 15 (9 for SK-I). Finally, the E_{vis} should be greater than 350 MeV, corresponding to the total observed charge in the ID greater than 3,000 p.e. (1,500 p.e. for SK-II).

5.2.7 Summary of PC Reduction

The detection efficiency after the PC reduction stage is estimated using the atmospheric neutrino MC at about 81%, 75%, 89%, and 86% for SK-I, SK-II, SK-III, and SK-IV, respectively. The background events in the final PC sample are mainly caused by CR muons. These background events are checked by eye scanning an event display. Most background events are removed by the FV cut. However, the presence of background events outside the FV can lead to some contamination. From the eye scanning and extrapolation of the background distribution outside the FV, the CR muon background contamination was estimated to be less than 2% during the SK-I to SK-IV phase.

The summary of PC reduction is posted at the end. The definition of variables is described above.

First Reduction

For SK-I & SK-II, an event is rejected if one of these criteria is satisfied:

1. $PE_{300} < 1,000$ p.e. (500 p.e. for SK-II)

2. TWIDA > 260 nsec (170 nsec for SK-II)
3. NCLSTA > 1 (only for SK-I)

For SK-III & SK-IV, an event is rejected if one of these criteria is satisfied:

1. PE₃₀₀ < 1,000 p.e.
2. NHITA_{top} < 11 or NHITA_{bottom} < 10
3. NHITA_{endcap} < 29 or NHITA_{side} < 84
4. ODR_{mean} ≥ 2,140 cm

Second Reduction

For SK-I, an event is rejected if one of these criteria is satisfied:

1. N₂^{outer} > 6
2. N_{min}^{outer} > 6
3. N₁^{outer} > 6 and PE₂₀₀ < 1,000 p.e.

For SK-II, an event is rejected if one of these criteria is satisfied:

1. N₂^{outer} > 6
2. NHITA_{endcap} ≥ 20 and NHITA_{endcap} ≥ MAX(NHITA_{side})
3. N₁^{outer} > 6 and N₁^{outer} ≥ 12 + 0.085 × PE₂₀₀

For SK-III & SK-IV, an event is rejected if one of these criteria is satisfied:

1. N₂^{outer} > 10
2. NHITA_{endcap} ≥ 20 and NHITA_{endcap} ≥ MAX(NHITA_{side})

Third Reduction

For SK-I & SK-II, an event is rejected if one of these criteria is satisfied:

1. NMIN₁₀₀ < 15
2. NMIN₁₀₀ < 10 and NHIT ≥ 800 (400 for SK-II)
3. NHITA_{in} ≤ 10

For SK-III & SK-IV, an event is rejected if one of these criteria is satisfied:

1. NMIN₁₀₀ < 15
2. NMIN₁₀₀ < 10 and NHIT ≥ 800

Fourth Reduction

For SK-I & SK-II, an event is rejected if one of these criteria is satisfied:

1. $\vec{d}_{\text{fit}} \cdot \vec{d}_{\text{PMT}} \leq -0.8$
2. goodness of through-going muon fit ≥ 0.85
3. TLMU ≥ 30 m

4. $\text{DCORN} \leq 150 \text{ cm}$

For SK-III & SK-IV, the classification of PC type is required following criteria based on the fitter results:

1. $\theta_{\text{muon}} < 90^\circ$
2. $\vec{d}_{\text{muon}} \cdot \vec{d}_{\text{PMT}} > -0.8$
3. $\text{goodness}_{\text{muon}} < 0.52$
4. $L_{\text{muon}} < 17.5 \text{ m}$
5. $\text{Corner}_{\text{muon}} < 3 \text{ m}$

An event that satisfies all of the following criteria is categorized as a PC through-going muon:

1. it should pass four of the above five criteria
2. $\text{PE}_{300} \geq 3,000 \text{ p.e.}$

An event that satisfies all of the following criteria is categorized as a PC stopping muon:

1. it should pass four of the above five criteria including the second criterion
2. $\text{goodness}_{\text{muon}} < 0.5$ or $\text{NHITA}_{\text{in}} < 10$
3. $\text{PE}_{300} \geq 3,000 \text{ p.e.}$

An event that satisfies all of the following criteria is categorized as another PC muon:

1. it should pass two of the above five criteria
2. $\text{PE}_{300} \geq 3,000 \text{ p.e.}$

Fifth Reduction

The combination of these criteria determines the conditions for each SK phase. The criteria is summarized below:

For low energy cut, PC events should be satisfied:

1. $\text{PE}_{300} > 3,000 \text{ p.e.}$

For through-going muon cut (A), all criteria should be satisfied to categorized as a PC event:

1. $\text{DIST}_{\text{cluster}} \geq 20 \text{ m}$
2. $\text{PEAC}_2 < 10 \text{ p.e.}$
3. $N_3^{\text{outer}} < 2$

For through-going muon cut (B), an event is rejected when all criteria are satisfied:

1. $\text{NHITA}_{\text{top}} \geq 7$

2. $\text{NHITA}_{\text{bottom}} \geq 7$
3. $\text{PEA}_{\text{top}} \geq 10 \text{ p.e.}$
4. $\text{PEA}_{\text{bottom}} \geq 10 \text{ p.e.}$
5. $0.75 < \text{TDIFFA} \times c/40 \text{ m} < 1.5$

For through-going muon cut (C), an event is rejected when all criteria are satisfied:

1. $\text{NHITA}_{\text{in}} \geq 5$
2. $\text{NHITA}_{\text{out}} \geq 7$ (5 for SK-III and SK-IV)
3. $0.75 < \text{TDIFFA} \times c/\text{TRACK} < 1.5$

For through-going muon cut (D), an event is rejected as through-going muon event when all criteria are satisfied:

1. $N_1^{\text{outer}} > 9$
2. $N_2^{\text{outer}} > 16$

For stopping muon cut (A), an event satisfying the following criterion is rejected:

1. $\text{NHITA}_{\text{in}} \geq 10$

For stopping muon cut (B), an event satisfying the following criterion is rejected:

1. $\theta_{\text{TDCFit}} > 90^\circ$ or $\theta_{\text{MSFit}} > 90^\circ$ (75° for SK-III and SK-IV)

For stopping muon cut (C), an event is rejected as stopping muon event when all criteria are satisfied:

1. goodness of stopping muon fit > 0
2. $\text{PE}_{\text{cone}}/\text{PE}_{300} \geq 0.6$
3. $\text{NHITA}_{\text{in}} > 6$

For stopping muon cut (D), The classification of PC type is required following criteria:

1. $\text{NHITA}_{\text{in}} > 10$
2. $\left| \vec{P}_{\text{PointFit}} - \vec{P}_{\text{MSFit}} \right| < 15 \text{ m}$

For stopping muon cut (E), The classification of PC type is required:

1. $\theta_{\text{muon}} < 90^\circ$

For corner clipping (A), The classification of PC type is required:

1. $\text{TRACK}_{\text{vis}} - \text{TRACK} \geq -15 \text{ m}$

For corner clipping (B), PC events are should be satisfied:

1. $\text{DCORN} \geq 150 \text{ cm}$

For cable hole muon cut, an event is rejected when all criteria are satisfied:

1. one veto counter hit
2. $\vec{d}_{\text{ring}} \cdot \vec{d}_{\text{veto-vertex}} > -0.8$

For decay electron cut, an event is rejected when all criteria are satisfied:

1. $N_{\text{decay}} \geq 1$
2. $E_{\text{vis}} > 25 \text{ GeV}$

Final Reduction

For the PC cut, an event that satisfies all of the following criteria is selected:

1. $\text{NHITAC} > 15$ (9 for SK-I)
2. $D_{\text{wall}} < 200 \text{ cm}$
3. $E_{\text{vis}} > 350 \text{ MeV}$

5.3 UPMU

The reduction for UPMU events is described in this section. The UPMU sample is divided into UPMU through-going and UPMU stopping subsamples for events that cross or stop within the ID, respectively.

5.3.1 First Reduction

Low energy and extremely high energy events are rejected in the reduction. For the UPMU sample, the PE_{300} is required between 6,000 to 1,750,000 p.e. (3,000 to 800,000 p.e. for SK-II). 6,000 p.e. corresponds to a muon momentum of 1 GeV/c and a track length of 3.5 m. The requirement for the final sample is a track length longer than 7 m. Thus, this criterion is a conservative cut. At a very high energy ID charge, the ID electronics are saturated and the muon fitters cannot work.

5.3.2 Second Reduction

To reject down-going CR muons, seven different fitters are used. The fitters are specialized to fit stopping muons, through-going muons, and muon events via Bremsstrahlung. The algorithms are as follows:

1. Muon fitter is applied to an event.
2. If the event is up-going and the goodness of fit is above the threshold (0.35), the event is saved.

3. If the event is down-going and the goodness of fit is above the threshold (0.35), the event is rejected.
4. If the event is traveling horizontally and the goodness of fit is above the threshold, or if the goodness of fit is below the threshold, the judgment is postponed.
5. The event is brought to the first step for the next muon fitter.

This sequence continues until the event passes through all fitters or is classified. The event is rejected if the fitter does not give a goodness above the threshold, but the event is saved if at least one fitter classifies the event as horizontal. A detailed description of the seven muon fitters and the definition of the goodness can be found in [74].

5.3.3 Third Reduction

To eliminate the remaining background, events are eye-scanned using a visual display. All events are checked one-by-one. About half of the events remaining after all the automated reduction steps are rejected.

5.3.4 Final UPMU Reduction

There are three criteria for UPMU stopping events. First, the fitter classification is a stopping event. Second, the fitted momentum is greater than or equal to 1.6 GeV/c, which corresponds to a track length of 7 m. Finally, the $\text{NHITA}_{\text{out}}$ is less than 10 (16 for SK-II).

The selection criteria for UPMU through-going events are similar to the stopping event. First, the fitter classification is a through-going event. Second, the distance from the ID entrance point to the ID exit point is greater than or equal to 7 m. Finally, the $\text{NHITA}_{\text{out}}$ is less than 10 (16 for SK-II).

The showering muon selection uses a chi-squared test based on the observed charge and the expected charge of the non-showering muons. The difference between the corrected observed charge and the expected charge of a non-showering muon is set as $\Delta(Q)$. The selection of the showering is as follows: When the χ^2 is greater than or equal to 50, the $\Delta(Q)$ should be greater than 0.5. Otherwise, when the χ^2 is less than 50, the $\Delta(Q)$ should be greater than $4.5 - 0.08\chi^2$.

5.3.5 Summary of UPMU Reduction

After all reductions, the remaining background events are most likely CR muons. Because there are multiple Coulomb scatterings of the muons or slight mis-reconstructions of near horizontally going muons, some CR muons are reconstructed as upward-going. Therefore, the background contamination is estimated by extrapolating the distribution of downward events. To estimate the uncertainty of the background, zenith angle distributions for nearly-horizontal CRs is compared between the two regions. The first region is reasonably well-insulated from CRs because of the thick

of rock around the SK. The second area is where the rocks are thin. From comparing the two regions, the uncertainty of contamination of horizontal muon to the UPMU sample is less than 25% during the SK-I to SK-IV phases.

The detection efficiency for the final samples is estimated to be over 97% during the SK-I to SK-IV phase. The final sample is made by subtracting the expected background events.

6 Event Reconstruction

Various event information can be derived by the reconstruction of the Cherenkov light cone detected by the PMT. With evidence gathered about the ring shape and the hit patterns, the Cherenkov angle, the number of rings, the vertex position, and the momentum of particles can be obtained. A detailed explanation of the reconstruction is found in Takenaga [215]. Here, FC samples are divided into two types. Events having visible energies below 1.33 GeV are classified as Sub-GeV, while events having visible energies above 1.33 GeV are classified as Multi-GeV.

6.1 Vertex Fitting

The vertex position is reconstructed using the timing information of hit PMTs in three steps. The initial estimation is the vertex position and ring direction assuming a point source. The opening angle of the ring and improved direction are then reconstructed. Further improvements of the position and direction, a line-source for the photons, and scattering are considered.

The first step, the Point-fit, is applied. A vertex is estimated assuming that all photons are emitted at the same time from a point source. After subtracting the TOF from a tested vertex, the PMT hit residual time distribution is constructed. The goodness of fit is defined as follows:

$$\text{goodness}_{\text{Point-fit}} = \frac{1}{N} \sum_i \exp\left(-\frac{(t_i - t_0)^2}{2(1.5 \times \sigma)^2}\right), \quad (6.1)$$

where N is the number of hit PMTs, t_i is the time residual of the i -th PMT, t_0 is a free parameter, and σ is the PMT timing resolution taken to be 2.5 nsec. The fitter searches for the vertex that gives the maximum value of goodness.

The direction and the outer edge of the dominant ring are measured in the second step. A pair consisting of direction the opening angle is tested by a parameter as follows:

$$Q(\theta_{\text{edge}}) = \frac{\int_0^{\theta_{\text{edge}}} \text{PE}(\theta) d\theta}{\sin(\theta_{\text{edge}})} \times \left(\frac{d\text{PE}(\theta)}{d\theta} \Big|_{\theta=\theta_{\text{edge}}} \right)^2 \times \exp\left(-\frac{(\theta_{\text{edge}} - \theta_{\text{exp}})^2}{2\sigma_\theta^2}\right), \quad (6.2)$$

where θ_{exp} and σ_θ are the Cherenkov opening angle expected from the charge within the cone and its resolution. $\text{PE}(\theta)$ is the angular distribution of the observed charge as a function of the opening angle θ from the particle direction. For the first factor, the numerator of the first element supports more of the charge in the ring and the denominator is enhanced against the narrower ring. The middle factor favors sharper rings and the last factor enhances the estimator if it is close to the expectation. The direction and the ring edge position are determined to maximize the estimator.

The vertex position is then determined using TDC-fit, wherein track length of charged particle and scattering are taken into account. The time residuals for PMTs inside and outside the Cherenkov ring are calculated, and the goodness of

fit is determined. The vertex is determined to be the position that maximizes the goodness parameter.

Finding the number of Cherenkov rings is described in the next section. However, if the event has a single-ring, a more precise fitter, called MC-fit, is used to determine the vertex. This can be improved by re-fitting the vertex position using the information of the ring pattern. The vertex position is adjusted parallel to the particle direction using TDC-fit and its timing information. This process is iterated until the changes in the vertex position and particle direction is less than 5 cm and 0.5° , respectively. Table 6.1 and Table 6.2 summarizes the vertex resolution and angular resolution. The vertex (angular) resolutions are the differences between the true vertex (lepton direction) and the reconstructed vertex (direction). Note that MS-fit is also used for UPMU reconstruction, assuming that the vertex locates at the ID surface.

Table 6.1: Vertex resolution of FC and PC for each SK phase. The resolution is defined as the width where 68% of the events are included.

Vertex Resolution [cm]		SK-I	SK-II	SK-III	SK-IV
FC : Sub-GeV					
Single-ring	e -like	31.3	35.4	30.9	31.2
	μ -like	24.0	30.9	24.0	23.3
Multi-ring	μ -like	38.5	41.7	45.0	51.3
FC : Multi-GeV					
Single-ring	e -like	35.9	36.8	35.9	34.0
	μ -like	25.0	27.0	25.0	23.8
Multi-ring	μ -like	68.4	111.2	74.2	87.8
PC					
Single-ring	μ -like	30.8	34.2	31.8	31.6
Multi-ring	μ -like	114.6	116.4	106.0	125.6

6.2 Ring Counting

When the vertex and the first Cherenkov ring are found, the ring count algorithm is applied to search for other such rings in the event. Other rings are searched using an algorithm with a Hough transformation [216] and the likelihood technique. Figure 6.1 shows the illustration of the method. The dashed line circles centered on each hit PMT are drawn with 42° half angles. The direction of the Cherenkov ring is identified as the intersection point of those dashed line circles.

By selecting the ring direction using this method, the second and subsequent ring candidates are searched. The likelihood method is used to determine whether a candidate ring is consistent with ring properties. When N rings are found for an

Table 6.2: Angular resolution of FC and PC for each SK phase. The resolution is defined as the width where 68% of the events are included.

Angular Resolution [°]		SK-I	SK-II	SK-III	SK-IV
FC : Sub-GeV					
Single-ring	<i>e</i> -like	3.2	3.4	3.2	3.2
	μ -like	1.9	2.2	1.9	1.9

FC : Multi-GeV					
Single-ring	<i>e</i> -like	1.3	1.4	1.3	1.2
	μ -like	0.9	1.0	0.8	0.8

PC					
Single-ring	μ -like	1.0	1.2	1.0	0.9

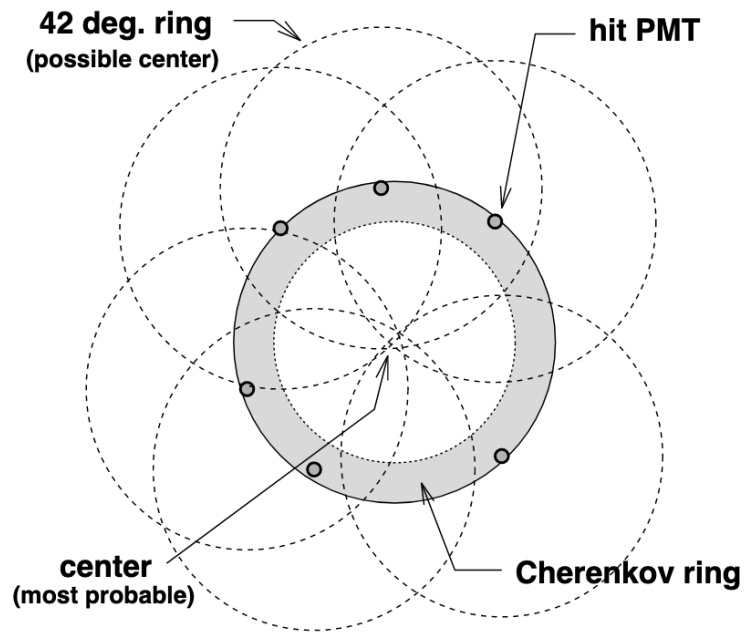


Figure 6.1: Basic idea of finding ring candidates is shown. The shaded circle represents the Cherenkov ring image, and the dashed circles are virtual Cherenkov rings centered on each PMT hit. The point of overlap is to be the center of the real Cherenkov ring.

event, we test whether the $(N + 1)$ -th ring candidate is true using the likelihood.

The likelihood function is defined as

$$\begin{aligned} \mathcal{L}_{N+1} &= \sum_i \log \left(\text{prob} \left(q_i^{\text{obs}}, \sum_{n=1}^{N+1} \alpha_n \cdot q_{i,n}^{\text{exp}} \right) \right), \quad (6.3) \\ \text{prob} \left(q^{\text{obs}}, q^{\text{exp}} \right) &= \begin{cases} \frac{1}{\sqrt{2}} \exp \left(-\frac{(q^{\text{obs}} - q^{\text{exp}})^2}{2\sigma} \right) & \text{for } q^{\text{exp}} > 20 \text{ p.e.} \\ \text{Single p.e. and Poisson convolution} & \text{for } q^{\text{exp}} < 20 \text{ p.e.} \end{cases} \quad (6.4) \end{aligned}$$

where hit PMTs inside $N + 1$ Cherenkov rings are summed. q_i^{obs} is the observed p.e. in the i -th PMT, $\alpha_n \cdot q_{i,n}^{\text{exp}}$ is the expected p.e. at the i -th PMT from the n -th ring, σ is the resolution for q^{exp} , and the probability function determines how well the expected charge reproduces the charge observed in the i -th PMT. The likelihood is maximized by varying the α_n factors with a lower momentum constraint. If it is determined that a second ring exists, we repeat the same procedure until a maximum of five other rings is found.

Figure 6.2 shows the ring-counting likelihood distributions comparing the data and MC. The difference between the data and MC is taken as the systematic uncertainty for ring counting. Among the reconstructed rings, rings having low momentum and overlapping with other energetic rings are discarded.

6.3 Particle Identification

The detected Cherenkov rings are identified as electron-like (e -like) or muon-like (μ -like) using particle identification (PID) programs. Electrons, positrons, or gamma-rays produce e -like rings owing to their electromagnetic shower via Bremsstrahlung, photon pair production, and multiple scattering. High-energy gamma-rays also generate electromagnetic showers, that are indistinguishable from electrons. Muons and heavy particles such as pions or kaons do not create showers, and their rings tend to have a very clear edge. Additionally, although the e -like ring has an opening angle of 42° , muons and other heavy particles can produce rings with slightly smaller opening angles if they are not highly relativistic.

To estimate the particle type, the likelihood is defined assuming a lepton. The definition of the likelihood for the n -th ring is expressed by

$$\mathcal{L}_n(\ell) = \prod_{\theta_i < 1.5\theta_c} \text{prob} \left(q_i^{\text{obs}}, q_{i,n}^{\text{exp}}(\ell) + \sum_{n' \neq n} q_{i,n'}^{\text{exp}}(\ell) \right), \quad (6.5)$$

where ℓ is the lepton flavor (electron or muon) and the probability function is the same as that defined by Equation 6.4. The product of the likelihood is taken over each PMT that is within 1.5 times the estimated Cherenkov opening angle for the n -th ring. The expected charge of the n -th ring is then calculated assuming a lepton type and by adding the charge from all the other rings.

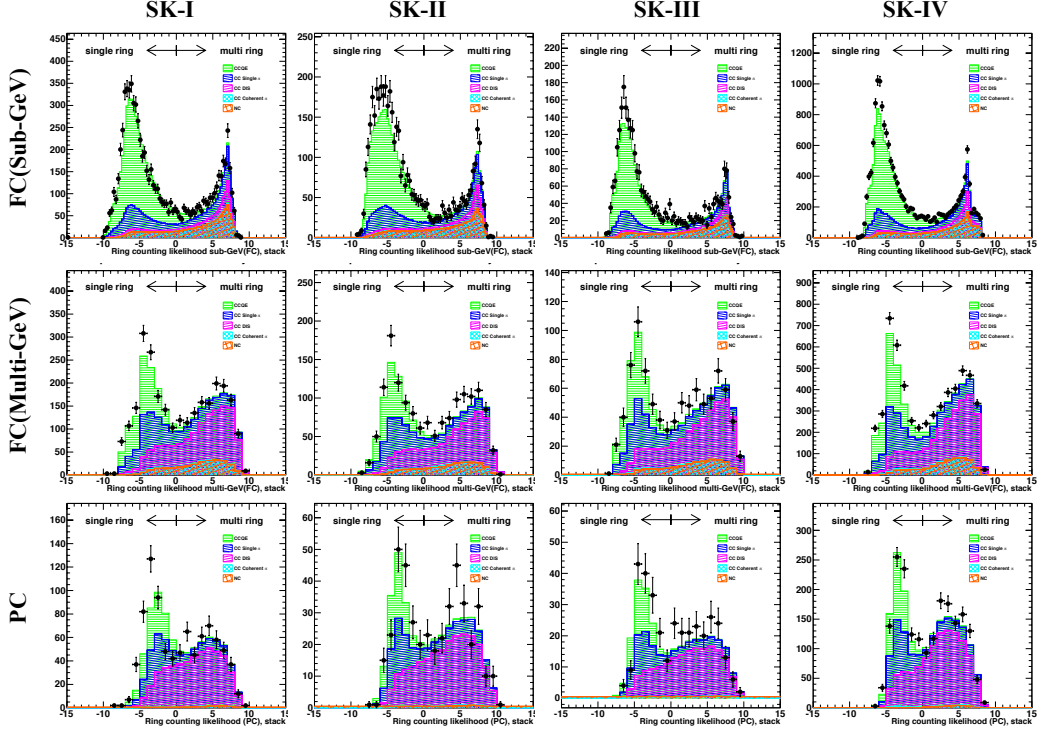


Figure 6.2: Ring-counting likelihood distributions ($L_2 - L_1$) for SK-I to SK-IV is shown. SK phases are shown in order from left to right. FC-Sub-GeV, FC-Multi-GeV, and PC are shown in order from the top. The experimental data (dots) are compared with MC (shaded) for various interaction modes with the two-flavor oscillation effect. The green-hatched region corresponds to CCQE, the blue is CC Single π , the magenta is CC DIS, the light blue is CC Coherent π , and the orange is NC interaction.

The probability of charge pattern and the opening angle of the ring are considered for PID. The likelihood is taken in the form of a χ^2 for the probability contribution from the charge distribution of the ring. Then, the pattern probability and opening angle probability are defined as:

$$P_n^{\text{pattern}}(\ell) = \exp\left(-\frac{1}{2} \frac{(\chi_n^2(\ell) - \min[\chi_n^2(e), \chi_n^2(\mu)])^2}{2\sigma_\chi^2}\right), \quad (6.6)$$

$$P_n^{\text{angle}}(\ell) = \exp\left(-\frac{1}{2} \frac{(\theta_c - \theta_n^{\text{exp}}(\ell))^2}{2(\delta\theta)^2}\right), \quad (6.7)$$

where $\chi_n^2(\ell) = -2 \log \mathcal{L}_n(\ell) + \text{constant}$. The resolution of the χ^2 distribution is approximated by $\sigma_\chi^2 = \sqrt{2N}$, where N is the number of PMTs used in the calcula-

tion. θ_n^{obs} is the reconstructed opening angle, $\delta\theta$ is the fitting error, and θ_n^{exp} is the expected opening angle of the n -th ring. The probability functions of the PID for single-ring events and multi-ring events are defined as:

$$P_{\text{single}}(\ell) = P^{\text{pattern}}(\ell) \times P^{\text{angle}}(\ell) \quad (6.8)$$

$$P_{\text{multi}}(\ell) = P^{\text{pattern}}(\ell) \quad (6.9)$$

$$P_{\text{PID}} \equiv \sqrt{-\log P(\mu)} - \sqrt{-\log P(e)} \quad (6.10)$$

The distribution of PID likelihood for single-ring events and multi-ring events is shown in Figure 6.3 and Figure 6.4. $P_{\text{PID}} < 0$ is e -like events and $P_{\text{PID}} > 0$ is μ -like events.

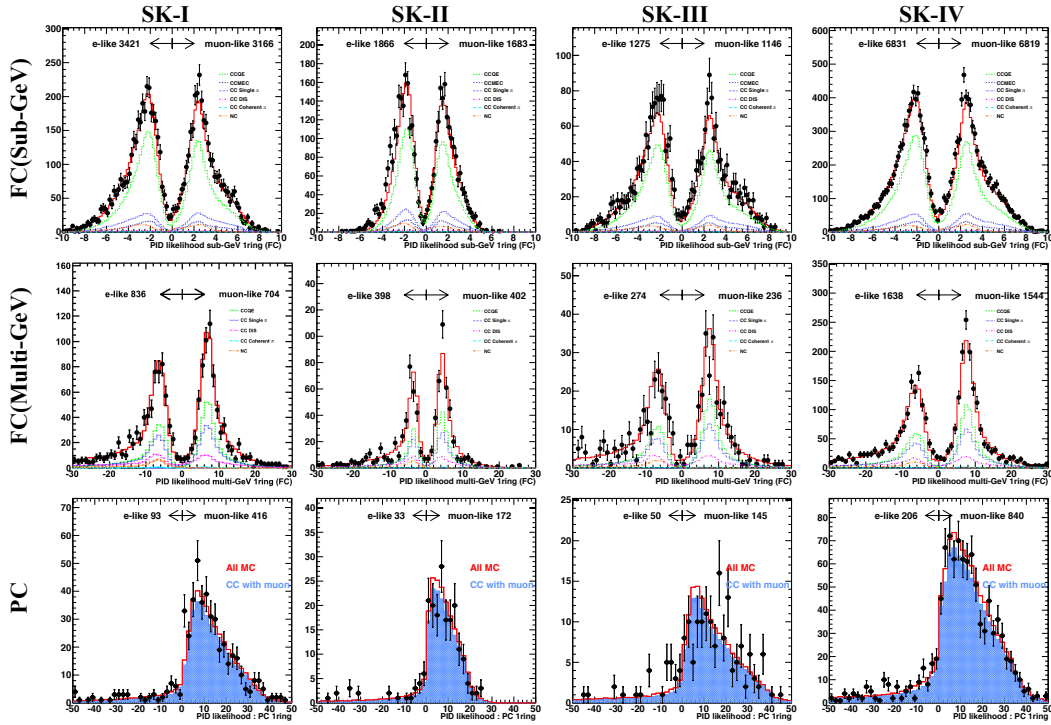


Figure 6.3: PID likelihood distributions of single-ring events for SK-I to SK-IV is shown. SK phases are shown in order from left to right. FC-Sub-GeV, FC-Multi-GeV, and PC are shown in order from the top. The experimental data (dots) is compared with MC (red line) for various interaction modes with the two-flavor oscillation effect. The MC lines correspond to CCQE (green dashed line), CCMEC (blue dashed line), CC Single π (blue dotted line), CC DIS (magenta long dashed-dotted line), CC Coherent π (light blue long dashed-dotted line), and NC (orange dashed line). For the PC samples, the blue hatched area represents the event owing to the muon CC reaction.

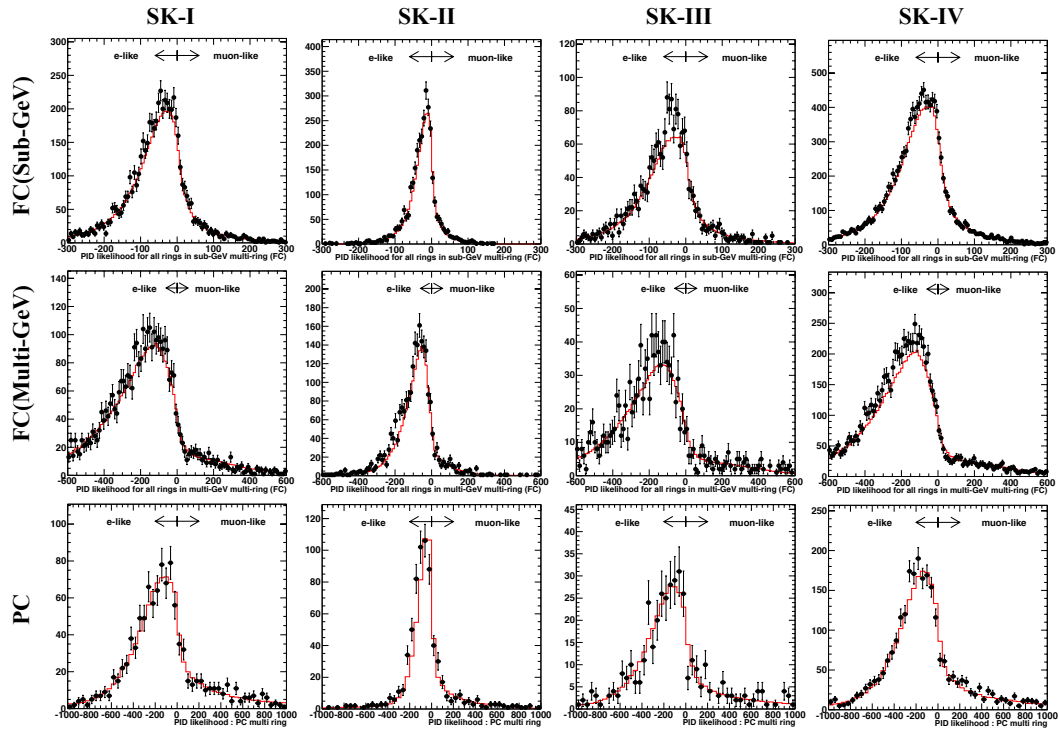


Figure 6.4: PID likelihood distributions of multi-ring events for SK-I to SK-IV is shown. SK phases are shown in order from left to right. FC-Sub-GeV, FC-Multi-GeV, and PC are shown in order from the top. The experimental data (dots) is compared with MC (red line) for various interaction modes with the two-flavor oscillation effect.

6.4 Momentum Determination

The momentum of each particle is estimated by the observed p.e. inside a cone having an opening angle of 70° . The observed p.e. in the hit PMT is separated into contributions from each ring to determine the momenta of the individual rings. The observed charge in the i -th PMT from the n -th ring is estimated as:

$$q_{i,n}^{\text{obs}} = q_i^{\text{obs}} \times \frac{q_{i,n}^{\text{exp}}}{\sum q_{i,n'}^{\text{exp}}} \quad (6.11)$$

where $q_{i,n}^{\text{obs}}$ is the fractional p.e. from the n -th ring in the i -th PMT, q_i^{obs} is the observed p.e. in the i -th PMT, and $q_{i,n}^{\text{exp}}$ is the expected p.e..

The charge in each PMT is corrected for the light attenuation in water and the acceptance of the PMT as follows:

$$\text{RTOT}_n = \frac{G_{\text{MC}}}{G_{\text{data}}} \left[\alpha \times \sum_{\theta_{i,n} < 70^\circ} \left(q_{i,n}^{\text{obs}} \times \exp\left(\frac{r_i}{L}\right) \times \frac{\cos \Theta_i}{f(\Theta_i)} \right) - \sum_{\theta_{i,n} < 70^\circ} S_i \right] \quad (6.12)$$

where G_{MC} and G_{data} are relative PMT gain parameters for data and MC, α is the normalization factor, r_i is the distance from the vertex position to the i -th PMT, L is the light attenuation length in water, Θ_i is the angle of photon arriving direction relative to the i -th PMT facing direction, $f(\Theta)$ is the correction function for the PMT acceptance, and S_i is the expected charge for the i -th PMT from scattered photons. The summation is restricted to be within the time window of -50 to 250 nsec around the peak of the TOF subtracted hit timing distribution.

RTOT_n is converted to momentum using the MC. As a result, the reconstructed momentum resolutions are estimated to be $0.6 + 2.6/\sqrt{P\text{GeV}/c}\%$ for single-ring electrons and $1.7 + 0.7/\sqrt{P\text{GeV}/c}\%$ for single-ring muons [217].

6.5 Improvements in Reconstruction

There are three checks used for better reconstruction: ring number correction, decay electron finding, and π^0 reconstruction. These are briefly described next.

6.5.1 Ring number Correction

Some of the rings are mis-fitted and have low momenta or are overlapped with other reconstructed rings. When comparing two rings, if one momentum is low and overlaps with a large momentum ring, or if one has a very low momentum, the ring is removed.

6.5.2 Decay electron Finding

Electrons are generated from the decay of the muon stopped in the detector. The information from decay electrons can help estimate the type of neutrino interaction. The decay electrons are classified to three types as follow.

primary-event type

Decay electron observed in primary event ($\Delta t < 900$ nsec)

sub-event type

Decay electron observed in separated event ($\Delta t > 900$ nsec)

split type

Decay electron observed around the border timing of event window. ($\Delta t \sim 900$ nsec)

Here, Δt is the timing difference between primary event and decay electron event.

The detection efficiency of decay electrons is 80% and 63% for μ^+ and μ^- , respectively. Because about 20% of μ^- is captured on ^{16}O nuclei [212], the efficiency is lower than μ^+ .

6.5.3 π^0 Reconstruction

FC Sub-GeV single-ring e -like events represent 9% of all NC events, and they mostly originated from an NC single π^0 production. A π^0 immediately decays into two gamma-rays and produces two e -like rings. If one of these rings is not detected because of low energy or overlapping rings, the event can be identified as a single-ring e -like event.

The π^0 fitter reconstructs the second gamma-ray on the assumption of the existence of two rings. Then the likelihood technique is used to determine their best-fit configuration.

6.6 Event Reconstruction for UPMU Sample

The UPMU event reconstruction algorithm differs from the FC and PC event algorithms. The reconstruction is based on an MS-fit assuming that the particle is a muon and that the vertex is on the ID surface. However, if the muon generates an electromagnetic shower, almost all ID PMTs will hit, or the Cherenkov ring cannot be observed. These events use the OD hit information to determine the direction of the particle. The same program is used for both observational data and atmospheric neutrino MC events that go through the data reduction process.

7 Search for Astronomical Neutrino from Blazar

IceCube detected a high-energy neutrino event from blazar TXS0506+056. The neutrino event, first discovered on 22 September 2017, was correlated with a gamma-ray flare and attracted a great deal of attention in the astroparticle field. Subsequently, the IceCube collaboration reported a possible neutrino event from the same blazar from older data between September 2014 and March 2015. However, no gamma-ray flare was found during that period.

Compared to the IceCube, the SK can observe neutrinos with lower energy and has continued to observe for a longer time. Therefore, it is strongly motivating to search for neutrinos in other energy ranges. The SK experiment has operated since April 1996, and its sensitive energy region is from several MeV to a few tens of TeV. In this analysis, neutrino data from SK-I to SK-IV until February 2018 are used for analysis. The livetime of each SK phase is 1,489.2, 798.6, 518.1, and 3,118.5 livetime days, and the total livetime is 5,924.4 livetime days.

To examine the neutrino from the point source, it is necessary to estimate the angular resolution for each event category. We search for a possible neutrino excess from the blazar by first counting the number of neutrinos in an angular region around the direction to the assumed source. Then, the number of events coming from an alternative direction is studied to check the consistency of the observation and background predictions. Finally, a simple statistical method is used to test for local increases in the event rate coming from the blazar direction.

The results of the SK are finally compared with the IceCube result in the form of an energy flux. This is the number of neutrinos per square centimeter per unit time and unit energy multiplied by the square of energy.

7.1 Angular Resolution

The arrival direction of neutrinos is determined via the reconstruction of Cherenkov rings in the ID. The reconstruction quality typically depends on the initial neutrino energy. It is important to use events having sufficient angular resolution for association with the blazar direction in this search. The angle between the true neutrino direction and the reconstructed direction is calculated by MC simulation. By studying the energy dependence of this angle, it gives the energy threshold for the angular resolution required for the analysis.

The searching area is 10° for FC and PC and 5° for UPMU, which is the same range as the point source search performed in SK in the past [218]. Figure 7.1 shows the angular resolution depending on the threshold of the observed energy at the SK calculated by MC. By applying an additional cut of 5.1 GeV for FC events and 1.8 GeV for PC events to the observed energy, we ensure that the angular deviation is within 10° for more than 68% of the events. Because UPMU events originate from neutrinos having higher energies than other categories, their arrival direction

is estimated with higher accuracy. Therefore, no additional restriction on the UPMU energy is used, because more than 77% of events are reconstructed within 5° of the true arrival direction.

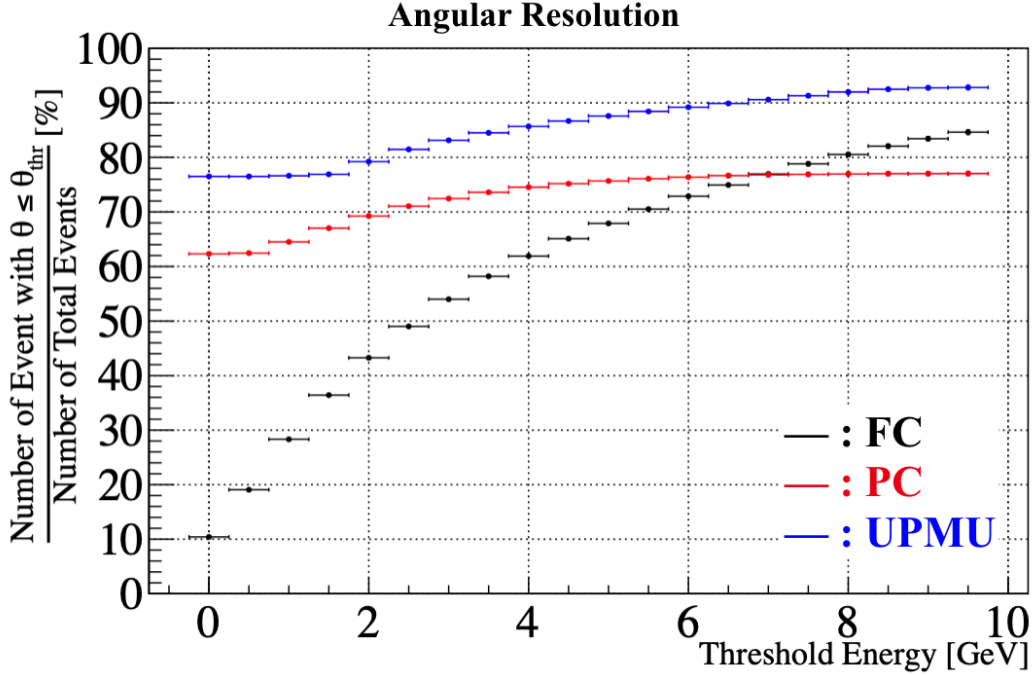


Figure 7.1: Percentage of events where the angle between reconstructed direction and true neutrino direction is within the threshold angle, 5° (10°) for FC and PC (UPMU). This percentage varies depending on the threshold of observed energy at the SK. The black, red, and blue points correspond to FC, PC, and UPMU samples, respectively.

Figure 7.2 shows a sky map of the reconstructed arrival direction of selected neutrino events around the blazar direction for all samples. There were 18 FC, 29 PC, and 20 UPMU events observed in these regions during SK-I to SK-IV. Note that neutrino events observed in the FC sample include both electron neutrino and muon neutrino interactions.

7.2 Expected Background

To quantitatively study possible event excesses above atmospheric neutrino backgrounds, MC is used to predict the event rate in the search region of each sample. The atmospheric neutrino event rate depends on the arrival direction, because the thickness of the atmosphere and the neutrino oscillation probability change with the zenith angle in detector coordinates. The thicker the atmosphere, the higher the probability that atmospheric neutrinos will be generated. For downward- or horizontally-produced neutrinos the path length to the detector is relatively short,

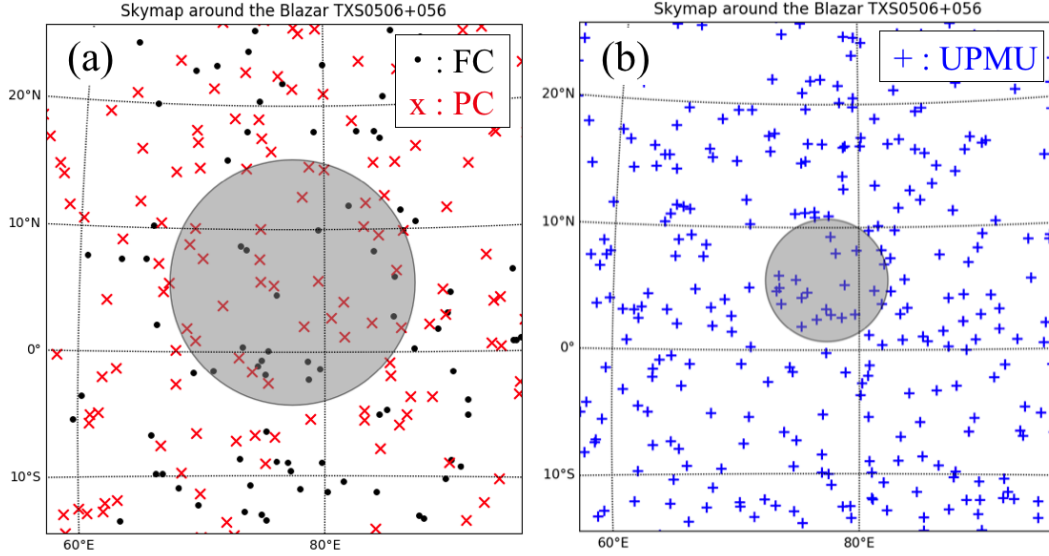


Figure 7.2: Reconstructed arrival directions of FC (black circle), PC (red x), and UPMU (blue +) events around the location of the blazar TXS0506+056 (α, β) = $(77.3582^\circ, +5.6931^\circ)$ in equatorial coordinates. The horizontal axis is the right ascension and the vertical axis is the declination. The shaded circle in the left (right) figure shows the 10 (5) degree search cone used in the analysis of FC and PC (UPMU) events.

and the effect of neutrino oscillations is reduced. Consequently, because the zenith angle is related to declination, the event rate also varies with declination. To simulate the effect of varying right ascension in the actual data, MC events are randomly assigned right ascension values under the assumption of flat local sidereal time.

The event rates in the search regions are calculated for each SK phase and combined with appropriate livetime normalization factors. The number of expected backgrounds at each declination, $N_{\text{bkg}}^{\text{Dec.}}$, are calculated as follows:

$$N_{\text{bkg}}^{\text{Dec.}} = \sum_i^{\text{in search cone}} W_i \times \frac{T_{\text{livetime}}}{500 \times 365} \times R_{\text{area}} \quad (7.1)$$

where W_i is the correction factor for the neutrino oscillation to reflect best-fit values of systematic error parameters from the analysis of Abe et al. [214]. Because the MC has the 500-year-equivalent dataset at each SK phase, it was normalized to livetime days. R_{area} is the area ratio of the spherical zone and search circle, and the schematic view of the area ratio is shown in Figure 7.3.

Figure 7.4 shows the observed data events in each fixed search cone superimposed on the MC taken over various declinations. Note that the FC and PC background events distribute across all declinations and show a slight increase at higher declinations, especially PC events, owing to the decrease of UPMU neutrinos lost to neutrino oscillations. The double-bump structure around -50° and 50° is caused

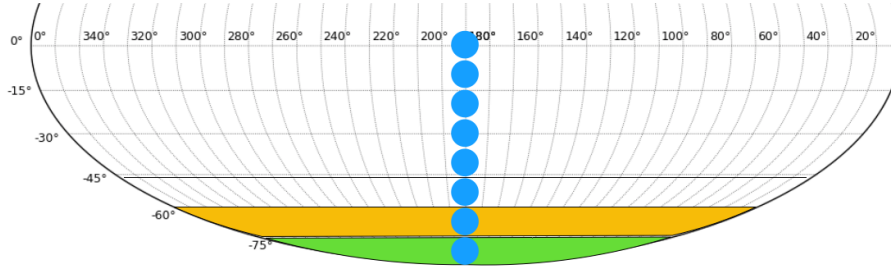


Figure 7.3: Area ratio (blue circle/green area and blue circle/yellow area). Because the area ratio of the spherical zone and search cone is depended on the declination, the ratio was calculated for each declination.

by the increased atmospheric neutrino flux coming from the near – horizon direction, where the effective atmospheric depth is deeper than other directions. Because UPMU events are required to come from below the horizon, their maximum declination is about 54° .

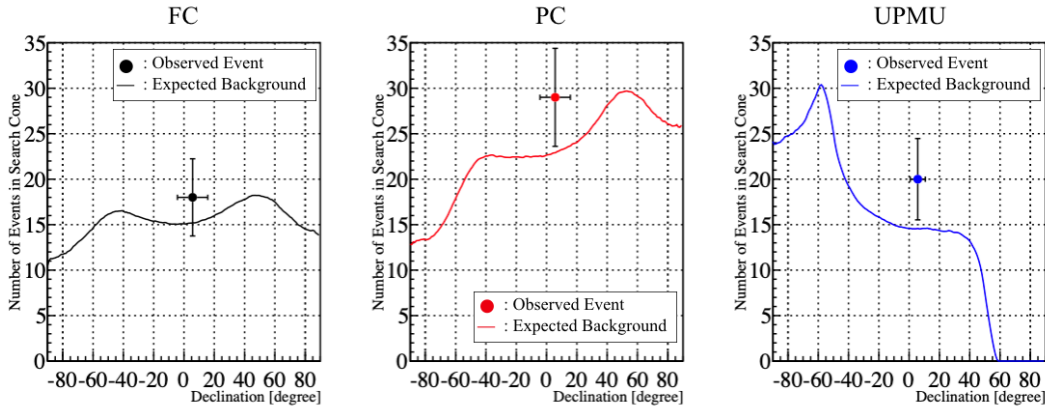


Figure 7.4: Number of detected events in each search region (points with error bar) and expected background (solid line) are shown with corresponding predictions for FC (black), PC (red), and UPMU (blue) samples. The error bar of the y-axis shows the statistical error, and the error bar of the x-axis shows the range of search cone.

The expected backgrounds at the direction of the blazar are 15.20, 22.91, and 14.57 for FC, PC, and UPMU samples, respectively. Therefore, the observed data agree with the expected background within 0.7σ for FC, 1.1σ for PC, and 1.2σ for UPMU events, considering statistical uncertainties alone.

7.3 On-source vs. Off-source

To further check the consistency of the observed event rates in the search cones, we further investigate by studying similarly sized angular regions taken at the same declination as the blazar TXS0506+056 but with different right ascension values.

These “off-source” regions are compared with the “on-source” region around the blazar.

Because the expected background does not change for the same declination, the number of on-source events is compared with the off-source. Figure 7.5 shows the number of observed events at on-source and off-source with the expected background. They are consistent within 0.7σ for FC, 1.5σ for PC, and 1.5σ for UPMU based on counting statistics only.

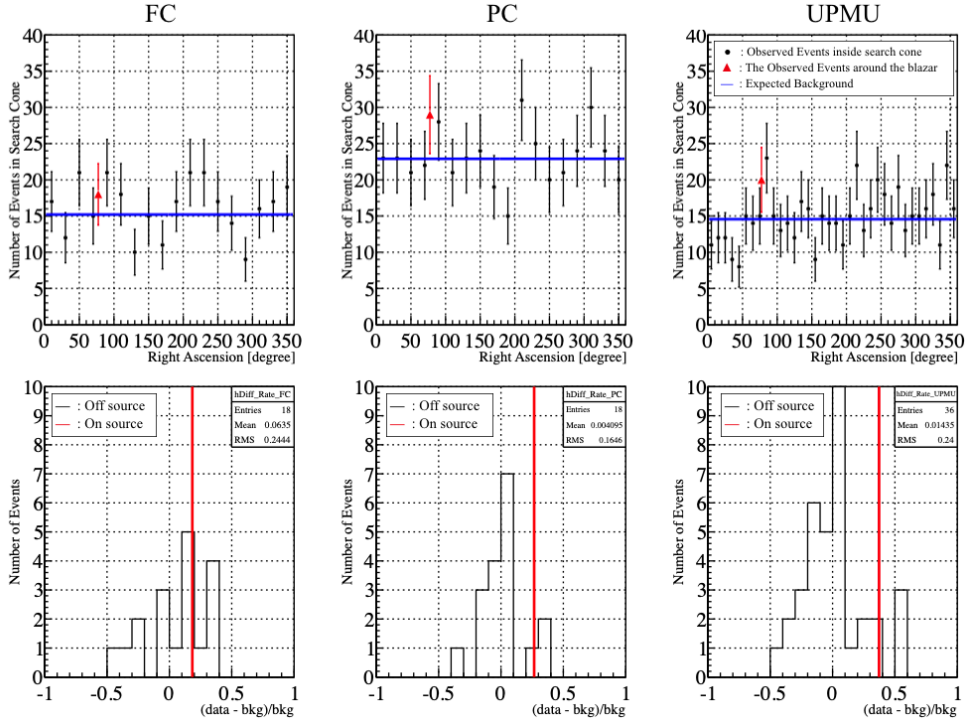


Figure 7.5: The upper figure shows the number of events in the search cone in on-source (red triangle) and off-source (black circle) with the expected background (blue line) for FC (left), PC (middle), and UPMU (right). The lower figure shows the relative difference, corresponding to the difference between the observation and the expectation. The relative difference distribution of off-source (black) is compared with the on-source (red) for FC (left), PC (middle), and UPMU (right).

The event rate, which is the ratio of the number of events in the search cone to the live days, is shown in Figure 7.6. The event rate in the on-source search cone is $(3.0 \pm 0.7) \times 10^{-3}$ for FC, $(4.9 \pm 0.9) \times 10^{-3}$ for PC, and $(3.4 \pm 0.8) \times 10^{-3}$ for UPMU events per livetime day. Averaging the off-source rates yields $(2.7 \pm 0.6) \times 10^{-3}$ for FC, $(3.9 \pm 0.6) \times 10^{-3}$ for PC, and $(2.5 \pm 0.6) \times 10^{-3}$ events per livetime day. The errors are calculated from the root mean square (RMS) of the off-source datasets.

From the comparison of on-source and off-source, no excess neutrino events from the blazar direction exists. The event rate was also no different between on-source and off-source. Therefore, on-source and off-source rates are consistent, indicating no excess of neutrino events in the direction of the blazar.

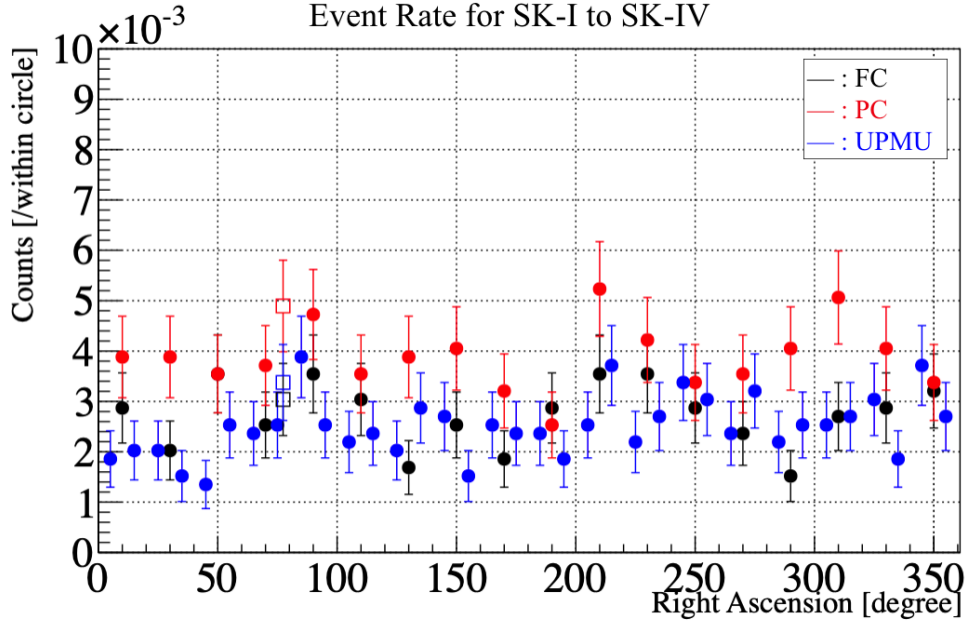


Figure 7.6: Event rate of the on-source (open square) and off-source (closed circle) of FC (black), PC (red), and UPMU (blue). The search range slid in the right ascension direction with a declination fixed in the direction of the blazar. The error bar shows the statistical error.

7.4 Kolmogorov–Smirnov (KS) Test

We searched for evidence of a local increase in the neutrino event rate in the period April 1996 to February 2018 range to test for possible correlation with gamma-ray flaring of the blazar. Because the atmospheric neutrino rate is known to be stable at each SK phase, the number of observed neutrino events is expected to increase linearly with increasing livetime if there is no neutrino emission from the blazar. On the other hand, the event rate would deviate from linearity if there were additional neutrinos from the gamma-ray flare.

To test for the presence of such a variation, we evaluated the probability (p -value) that the observed rate is consistent using a KS-test. The number of observed events in each SK phase is estimated from the atmospheric neutrino, MC, as summarized in Table 7.1.

Table 7.1: The number of expected events at each SK phase.

	SK-I	SK-II	SK-III	SK-IV
FC	3.7	2.1	1.3	8.1
PC	5.4	2.6	2.1	13.0
UPMU	3.8	1.9	1.0	7.9

Figure 7.7 compares the cumulative observed events with the expected events as a function of a livetime day. The maximum distance between the experimental data and the expectation is 0.13 for FC, 0.25 for PC, and 0.21 for UPMU.

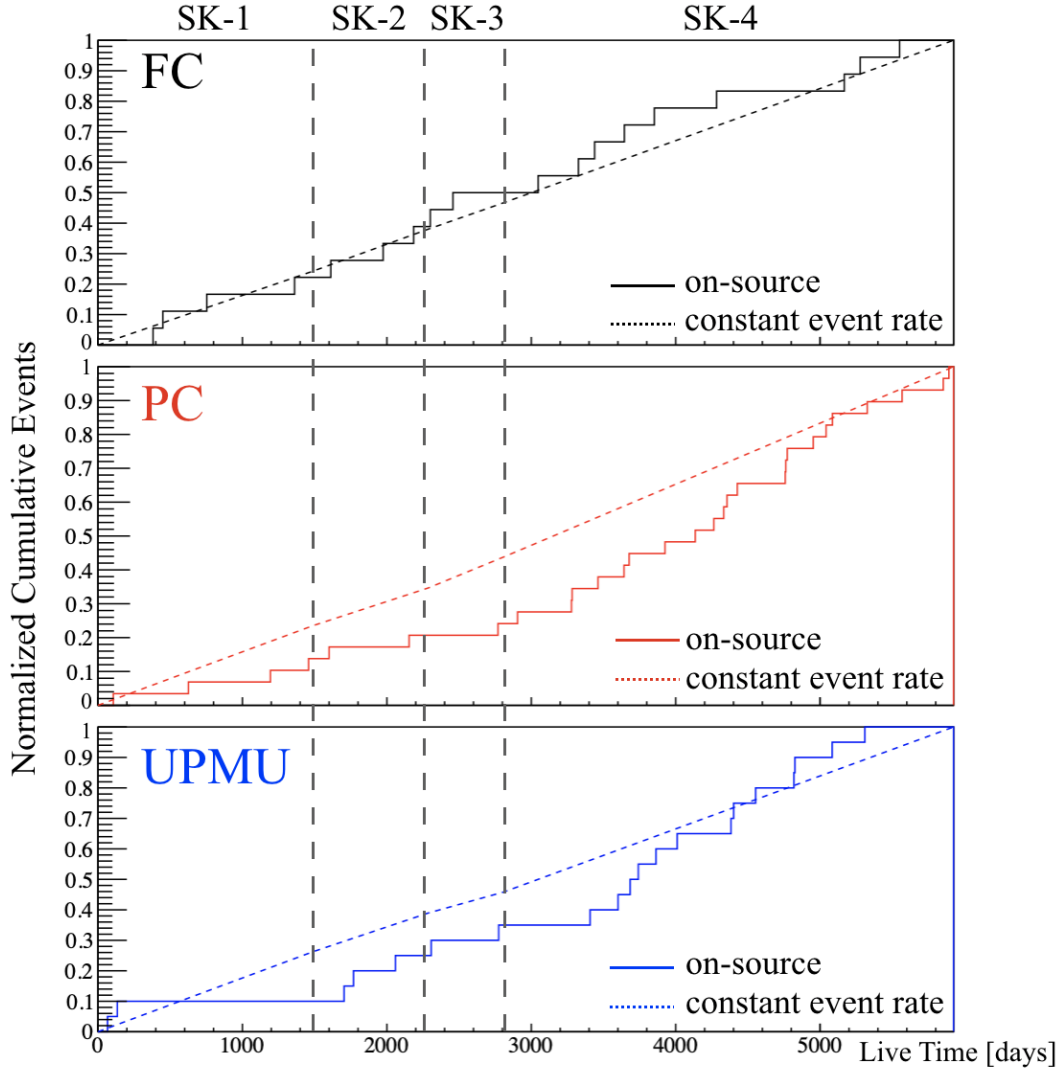


Figure 7.7: Normalized cumulative events as a function of livetime day for FC, PC, and UPMU. The solid lines are observed events from the on-source region and the dashed lines are estimated background events assuming a constant event rate for each SK phase. The ranges of each SK phase are shown as vertical dashed lines.

To calculate the p -value of the KS-test, a set of 10,000 pseudo experiments (toy-MC) were generated assuming the expected background from the MC in each SK phase. One toy-MC is calculated as follows:

- The total number of events in each SK phase is determined via Poisson distribution centered on the expected number (Table 7.1).

- The observed time of each event is randomly assigned assuming a constant rate in each SK phase.
- By calculating the maximum difference between the pseudo dataset and the expected events, the maximum distance is obtained.

The maximum distance is compared to that from the observed SK data to calculate a p -value (Figure 7.8). This represents the percentage of pseudo experiments having a maximum distance larger than the data. The estimated p -values are 91.74%, 12.26%, and 48.75% for FC, PC, and UPMU events, respectively, indicating consistency with a constant event rate. Accordingly, we conclude that no significant signal from the direction of the blazar TXS0506+056 exists in the SK data during the observation period considered.

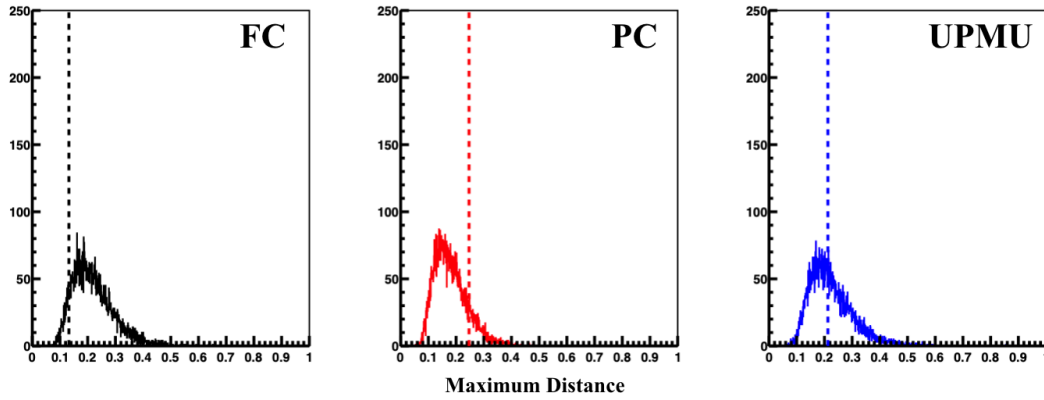


Figure 7.8: Distribution of maximum distance calculated by the toy-MC (solid line) with the result of experimental data (dashed line) shown for FC (left), PC (middle), and UPMU (right) samples. The percentage contained on the right side of the dashed line is calculated as the p -value.

7.5 Summary

In the above analyses, there was no significant signal. The results of these analyses are summarized in Table 7.2.

Table 7.2: Summary of analysis of neutrino search from the blazar TXS0506+056.

	FC	PC	UPMU
Search Criteria			
Threshold Energy [GeV]	5.1	1.8	1.6
Search Range [°]	10	10	5

Number of Events			
Observed Events	18.0 ± 4.2	29.0 ± 5.4	20.0 ± 4.5
Expected Events	15.2	22.9	14.5
Agreement	0.7σ	1.1σ	1.2σ

Relative Difference of On-source and Off-source			
On-source	0.18	0.27	0.37
Off-source Mean	0.064	0.0041	0.014
Off-source RMS	0.24	0.16	0.24
Agreement	0.7σ	1.5σ	1.5σ

Event Rate [/1,000 livetime day]			
On-source	3.0 ± 0.7	4.9 ± 0.9	3.4 ± 0.8
Off-source	2.7 ± 0.6	3.9 ± 0.6	2.5 ± 0.6
Agreement	not significant	not significant	not significant

Kolmogorov-Smirnov Test			
Maximum Distance	0.13	0.25	0.21
<i>p</i> -value	91.74%	12.26%	48.75%

8 Limit Calculation

Because no significant indications of a signal from the blazar are found in any of the tests of the previous chapter, we estimate fluence limits based on the expected background throughout the entire observation period. Neutrino-fluence is the number of neutrinos per square centimeter. The fluence is calculated to find out how many neutrinos arrived based on the number of neutrino observations at SK, according to Swanson et al. [219], Thrane et al. [220, 221].

8.1 90% Confidence Level (C.L.)

For the upper limit, the 90% C.L. limit on the number of neutrino events from the blazar direction is calculated as follows:

$$\int_{N_{\text{bkg}}}^{N_{90}} d\lambda \text{Poisson}(N_{\text{obs}}, \lambda) = 0.9 \int_{N_{\text{bkg}}}^{\infty} d\lambda \text{Poisson}(N_{\text{obs}}, \lambda) \quad (8.1)$$

$$\because \text{Poisson}(x, \lambda) = \frac{\lambda^x e^{-\lambda}}{x!} \quad (8.2)$$

where N_{bkg} is the number of expected background events, N_{obs} is the number of observed events, N_{90} is the 90% C.L. upper limit of observed events, and $\text{Poisson}(\lambda, x)$ is the Poisson probability.

The number of observed events and the expected background are estimated in the previous chapter. Figure 8.1 shows the Poisson distribution centered on the number of observations for FC, PC, and UPMU samples. The 90% C.L. upper limit of observed events is 10.2 for FC, 14.5 for PC, and 12.7 for UPMU samples.

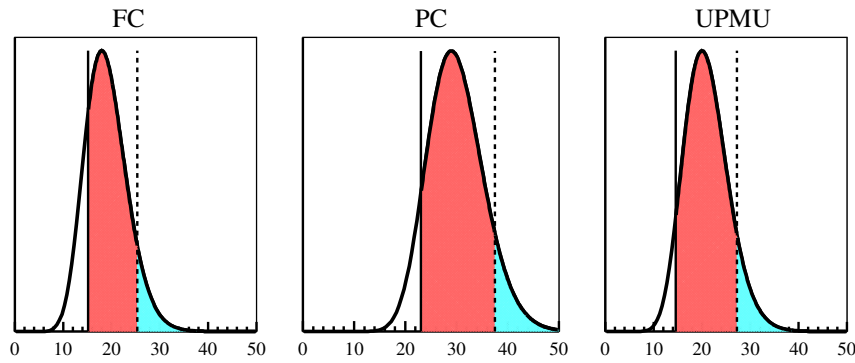


Figure 8.1: Poisson distribution centered on the number of observed events. The solid line corresponds to the number of expected background and the dashed line corresponds to the 90% C.L. upper limit. Of the area displayed in red and blue, the red area accounts for 90%.

8.2 FC and PC Fluence

The FC samples mix both electron and muon neutrino events. However, the PC samples are dominant muon neutrino events. This is because the mean free path of electrons in water is short and cannot pass through the structure between ID and OD.

For the FC and PC dataset, the neutrino fluence can be calculated as follows:

$$\Phi_{\text{FC}}^{\nu_x + \bar{\nu}_x} = \frac{N_{90}^{\text{FC}}}{N_T \int dE_\nu \left(\sigma^{\nu_x}(E_\nu) \varepsilon^{\nu_x}(E_\nu) + \sigma^{\bar{\nu}_x}(E_\nu) \varepsilon^{\bar{\nu}_x}(E_\nu) \right) \lambda(E_\nu^{-\gamma})}, \quad (8.3)$$

$$\Phi_{\text{PC}}^{\nu_\mu + \bar{\nu}_\mu} = \frac{N_{90}^{\text{PC}}}{N_T \int dE_\nu \left(\sigma^{\nu_\mu}(E_\nu) \varepsilon^{\nu_\mu}(E_\nu) + \sigma^{\bar{\nu}_\mu}(E_\nu) \varepsilon^{\bar{\nu}_\mu}(E_\nu) \right) \lambda(E_\nu^{-\gamma})}, \quad (8.4)$$

where ν_x is the electron type neutrino or muon type neutrino, σ is the total neutrino interaction cross-section, ε is the neutrino detection efficiency, and λ is the number density distribution from the blazar direction. Finally, N_T is the number of nucleons in the 22.5 kilotons FV of the detector. It expresses as $N_T = 2.25 \times 10^{10} \times N_A$, where N_A is the Avogadro constant.

Figure 8.2 shows the cross-section for all interactions combined in the range of 0.01 to 100 GeV. The cross-sections are calculated by NEUT version 5.3.5 [121].

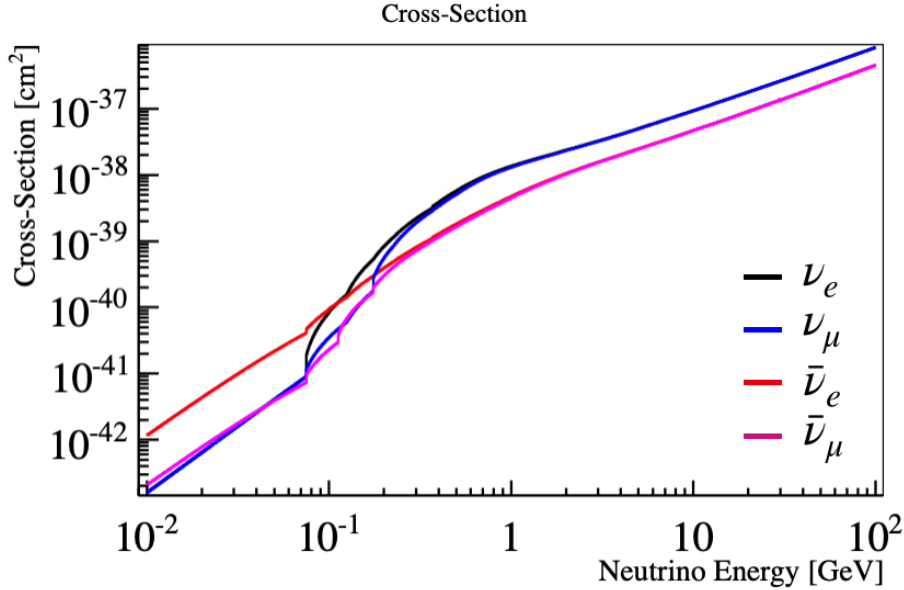


Figure 8.2: Neutrino-nucleon interaction cross-section. The black line corresponds to the electron neutrino, blue is the muon neutrino, red is the electron anti-neutrino, and purple is the muon anti-neutrino. Because it is inferred that the model changes around 100 MeV, it has a large fluctuation.

Figure 8.3 shows the detection efficiency of FC and PC for each neutrino flavors. The detection efficiency is defined as the ratio of the number of detected neutrino events to the total number of neutrinos reacting within the FV.

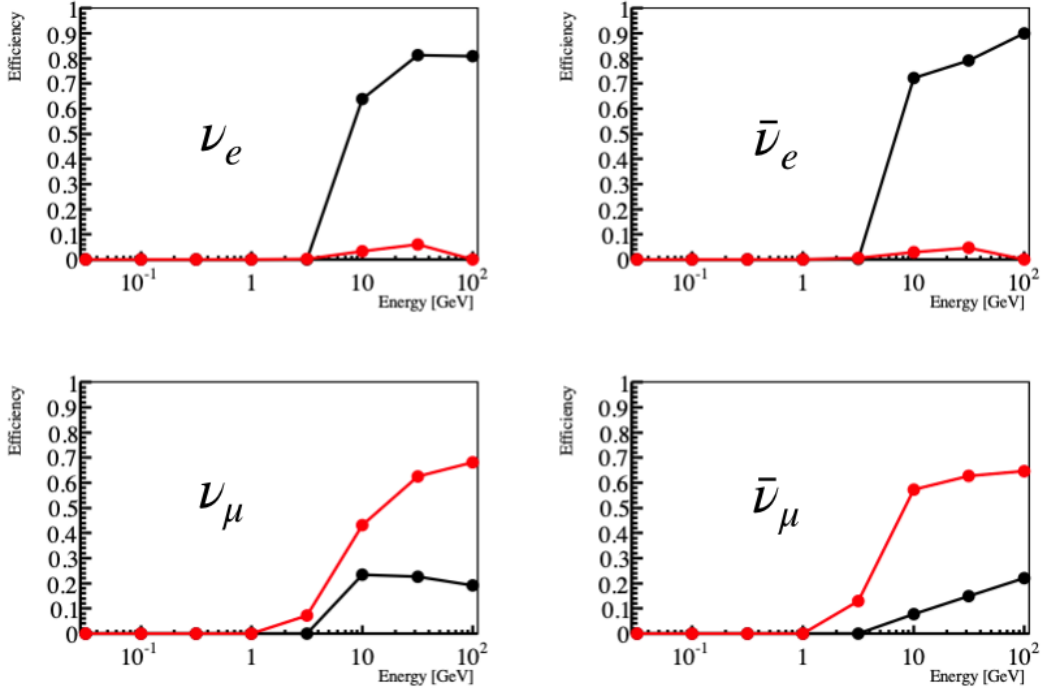


Figure 8.3: Detection efficiency for FC (black) and PC (red) as a function of neutrino energy. Because the Cherenkov threshold for the muon is 160.3 MeV, there is no sensitivity for ν_μ and $\bar{\nu}_\mu$ below the threshold. Furthermore, more energetic neutrinos are usually needed to produce PC events. Thus, the sensitivity is near 0 below 1 GeV.

8.3 UPMU Fluence

Because the neutrinos of the UPMU sample penetrate the Earth and interact with the nucleus of the rock surrounding the detector, the method of calculation for neutrino fluence is the difference from the FC and PC samples. For the UPMU samples, the neutrino fluence can be calculated as follows:

$$\Phi_{\text{UPMU}}^{\nu_\mu + \bar{\nu}_\mu} = \frac{N_{90}^{\text{UPMU}}}{A_{\text{eff}}(z) \int dE_\nu \left(P^{\nu_\mu}(E_\nu) S^{\nu_\mu}(z, E_\nu) + P^{\bar{\nu}_\mu}(E_\nu) S^{\bar{\nu}_\mu}(z, E_\nu) \right) \lambda(E_\nu^{-\gamma})} \quad (8.5)$$

where z is the zenith angle, A_{eff} is the effective area, $P(E_\nu)$ is the probability that a neutrino with energy E_ν creates a muon with energy greater than E_μ^{min} , $S(z, E_\nu)$

is the shadowing of the neutrinos caused by interactions in the Earth depending on zenith angle, and λ is the number density distribution from the blazar direction. In this calculation, the fluence limit is calculated using the average zenith angle to the source taken over the detector observation period.

8.3.1 Effective Area

The effective area is the required area to get enough information for UPMU which has a given direction. The sensitivity depends on azimuth and zenith angles of muon path. Because a track length longer than 7 m is required for UPMU, the area longer than the track length in the detector is called the effective area. The schematic of the effective area is shown in Figure 8.5.

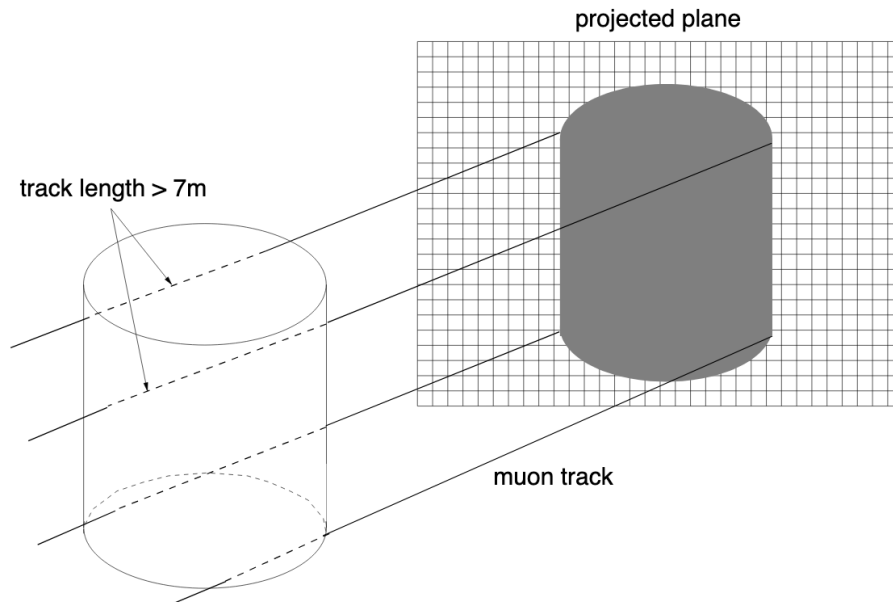


Figure 8.4: Effective area. The figure was taken from Saji [222].

The effective area is calculated as follows.

- A large plane enough to be projected is taken.
- 2D grid points at every 10 cm step are plotted.
- A vertical line on the defined plane is drawn from each grid point to the detector.
- If the length of the line crossing the detector is longer than 7 m, the corresponding grid point is counted as part of the effective area.
- The calculation is performed for every zenith angle of the area divided into 10 directions.

The result of the effective area is shown in Figure 8.5.

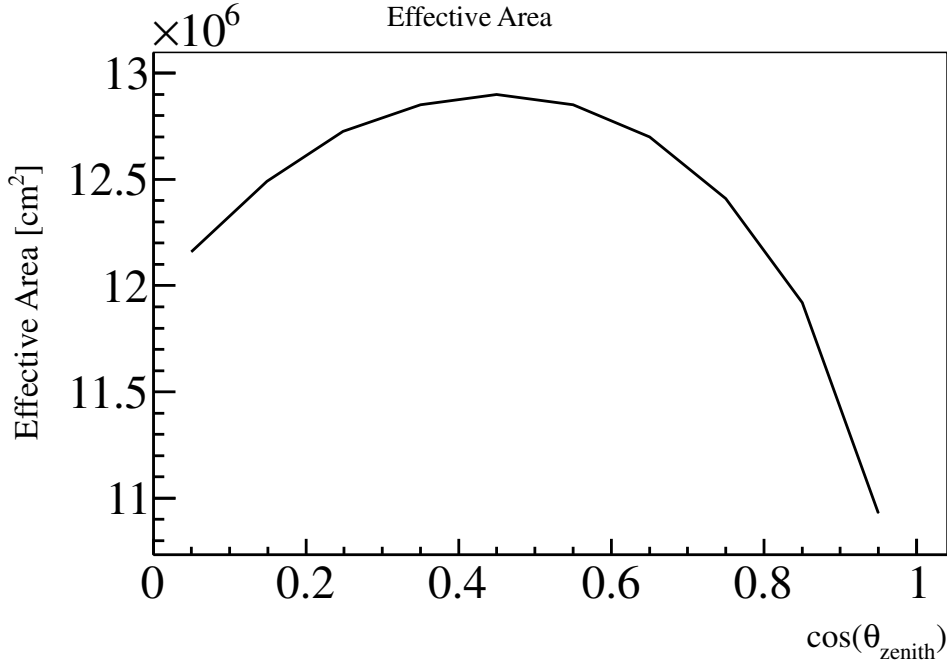


Figure 8.5: Effective area as a function of zenith angle. $\cos = 0$ represents the horizontal direction, and $\cos = 1$ represents the vertical direction.

8.3.2 Probability of a Neutrino Creating a Muon

The probability, $P(E_\nu, E_\mu^{\min})$, that a neutrino having energy E_ν creates a muon with energy greater than E_μ^{\min} can be expressed as follows:

$$P(E_\nu, E_\mu^{\min}) = \int_0^\infty N_A dX \int_0^{E_\nu} \frac{d\sigma_{CC}}{dE_\mu} \times g(X, E_\mu, E_{\text{thr}}), \quad (8.6)$$

where N_A is the Avogadro constant. Because the NC interactions do not produce muons, σ_{CC} is the CC component of the neutrino-nucleon cross-section [223]. Furthermore, the probability that a muon having enough energy, E_μ , to survives with an energy larger than E_{thr} coming into detector after the traveling the thickness X [g/cm^3] in the rock is defined as $g(X, E_\mu, E_{\text{thr}})$. The function, g , can be written as:

$$g(X, E_\mu, E_{\text{thr}}) = \Theta(R(E_\mu, E_{\text{thr}}) - X), \quad (8.7)$$

where $R(E_\mu, E_{\text{thr}})$ is a range that the muon travels while its energy decreases from E_μ to E_{thr} [224]. Θ is the step function as follows:

$$\Theta(x) = \begin{cases} 1 & (x \geq 0) \\ 0 & (x < 0) \end{cases} \quad (8.8)$$

Therefore, Equation 8.6 is replaced as follows:

$$P(E_\nu, E_\mu^{\min}) = N_A \int_0^{E_\nu} \frac{d\sigma_{\text{CC}}}{dE_\mu} \times R(E_\mu, E_{\text{thr}}) \quad (8.9)$$

Figure 8.6 shows the result of the calculation of probability. The UPMU samples includes only muon neutrino or anti-neutrino events.

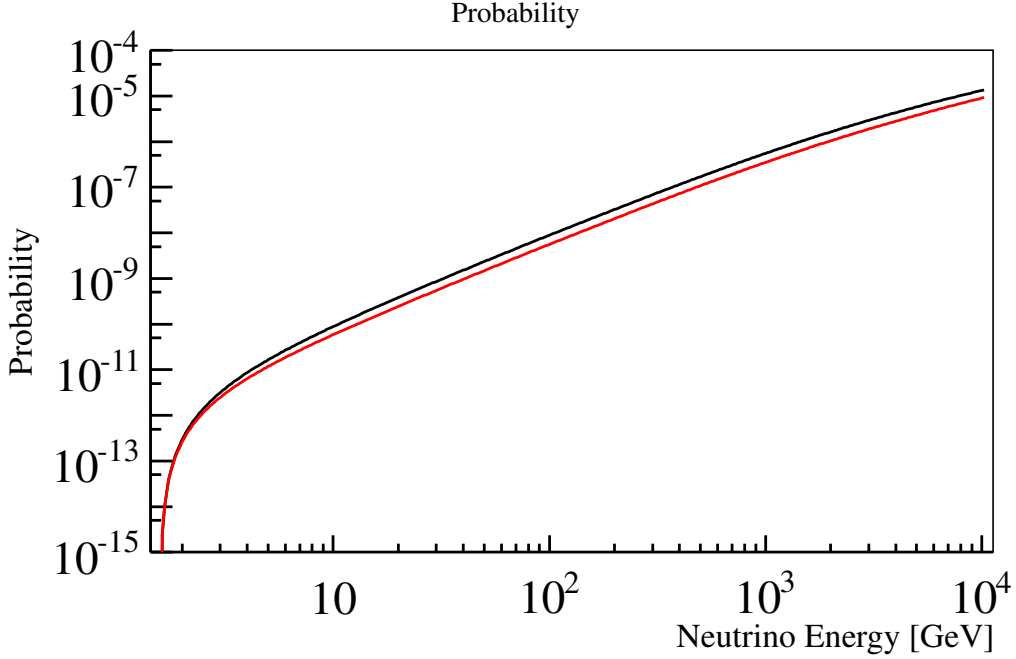


Figure 8.6: Probability that a neutrino creates a muon via neutrino interaction and that the muons reach the detector. The black line corresponds to muon neutrino and the red line corresponds to muon anti-neutrino.

8.3.3 Shadow Effect

Some of the high energy neutrinos are absorbed by the Earth. For energies above 1 TeV, neutrino flux is increasingly suppressed by a shadow factor that is a function of both energy and zenith angle. The Earth's shadow effect is defined as follows [225, 226]:

$$S(z, E_\nu) = \exp(-\ell_{\text{col}}(z)\sigma(E_\nu)N_A), \quad (8.10)$$

where ℓ_{col} is the Earth's column depth measured in centimeters water equivalent calculated using the "Preliminary Earth Model" [225], σ is CC and NC neutrino-nucleon cross-section, and N_A is the Avogadro number.

Figure 8.7 displays the Earth's shadow effect. This effect is negligibly small for neutrinos coming from near the horizontal direction or with low energy. However, it

cannot be ignored for high energy neutrinos or neutrinos passing through the center of the Earth. For $\cos(z) = 1$, the shadow factor is 0.94 (0.97) for muon neutrino (anti-neutrino) at 1 TeV and 0.68 (0.78) for a muon neutrino (anti-neutrino) at 10 TeV.

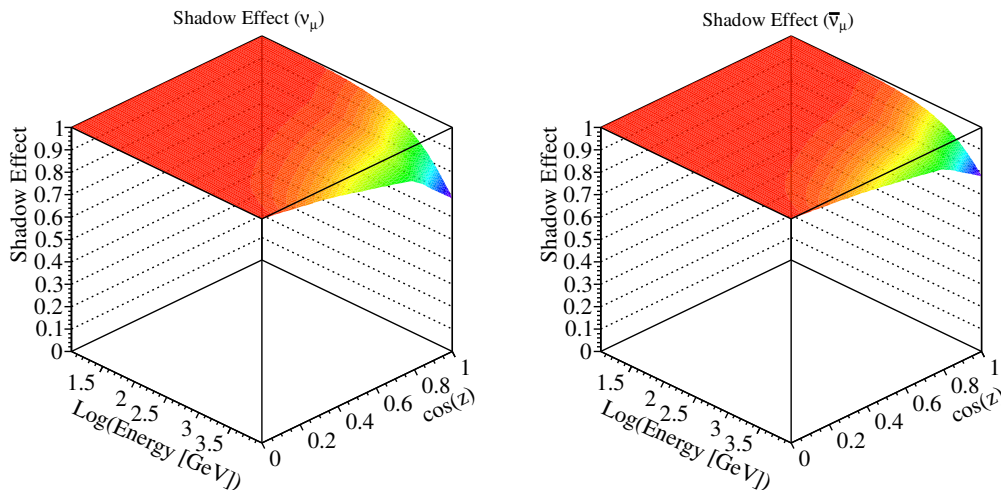


Figure 8.7: Earth's shadow effect for muon neutrino (left) and muon antineutrino (right) as a function of neutrino energy and zenith angle. The neutrino energy is shown in log form, and the zenith angle is shown as the cosine value. $\cos(z) = 0$ corresponds to the horizontal direction seen from SK.

8.4 Results

Above, the calculation method of the upper limit of each sample is described. To calculate the fluence upper limit, Equation 8.3, 8.4, and 8.5 are used. It is necessary to define the energy ranges in the integrals, the treatment of the upper limit of the observed event at 90% C.L., and the number density of neutrino from the blazar. Here, the final result is shown using specific numerical values.

Energy range

The energy ranges used in the equations are 5.1 to 10 GeV (FC), 1.8 to 100 GeV (PC), and 1.6 GeV to 10 TeV (UPMU). These ranges represent the MC neutrino energies populating each sample (see Figure 5.2). For the calculation of the upper limit, FC is divided into one bin, PC is divided into two bins, and UPMU is divided into four bins.

90% C.L.

Upper limits are calculated for both electron and muon neutrinos using FC events, because this sample is sensitive to both. Only that of muon neutrino fluence limits are estimated for the other samples. For the FC sample, we conservatively make no

distinction between electron and muon neutrinos when calculating observed events at the 90% C.L. upper limit. The FC sample is populated almost entirely by events having energies less than 10 GeV. Thus, our limit for electron neutrinos spans a single bin. Note that tau neutrinos are present in the SK data but they represent negligible contributions to the current dataset.

For the PC and UPMU samples, the same observed event value at 90% C.L. is used to calculate the upper limit in each energy bin. The neutrino energy cannot be reconstructed for UPMU events, because they are produced by neutrinos interacting in the rock surrounding the detector. The PC sample also cannot reconstruct the neutrino energy, because the charged particles generated by the neutrino interaction exit the detector.

Figure 8.8 shows the relationship between the reconstructed momentum of the charged particle produced by neutrino interactions and true neutrino energy calculated by atmospheric MC. It can be seen that there is no correlation between charged particle momentum and neutrino energy and that the neutrino energy cannot be reconstructed.

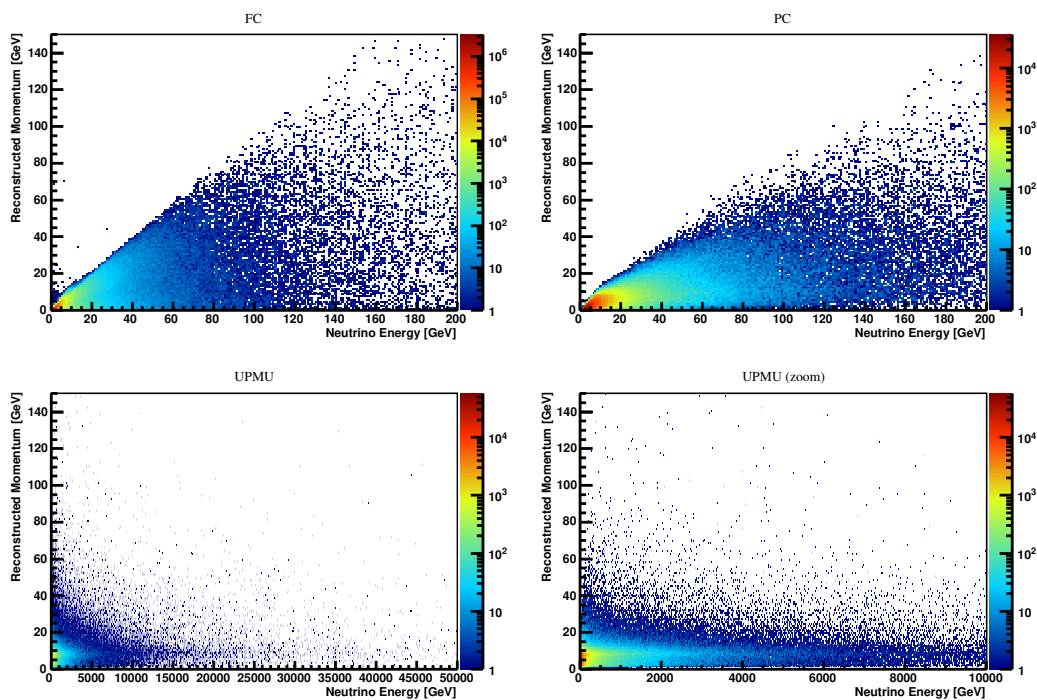


Figure 8.8: Relationship between the reconstructed momentum of charged particles produced by neutrino interactions and neutrino energy. There are FC (upper left), PC (upper right), UPMU (lower left), and UPMU enlarged views of the x-axis (lower right). The colors correspond to the number of events.

Energy spectrum of neutrino

Because the gamma rays associated with neutrino production can cascade down to lower energies, the neutrino flux is likely to be correlated with the gamma-ray energy flux [227]. Therefore, the following spectral analysis is performed.

The third Fermi Large Area Telescope (Fermi-LAT) source catalog (3FGL) [228] models the gamma-ray spectrum of TXS0506+056 as a power function:

$$\frac{dN}{dE} \propto E^{-\gamma} \quad (8.11)$$

The IceCube collaboration assumes an energy spectrum of $\gamma = 2$ [19] for the high-energy neutrino event, IceCube-170922A. Furthermore, for the analysis of the neutrino flare from 2014 to 2015 (IceCube-14/15), the IceCube collaboration performed time-dependent analysis. The results of the best-fitting parameter are given by $\gamma = 2.1 \pm 0.2$ for the Gaussian time window and by $\gamma = 2.2 \pm 0.2$ for the box-shaped time window [56].

The Fermi-LAT, the All-Sky Automated Survey for Supernovae (ASAS-SN), and IceCube collaboration analyzed 9.6 years of Fermi-LAT data in the TXS0506+056 region ($10^\circ \times 10^\circ$) using the source-finding algorithm. As a result, an alternative spectral model (log-parabolic function) was obtained, having additional free parameters compared to a simple power-law:

$$\frac{dN}{dE} \propto \left(\frac{E}{E_0} \right)^{-\alpha - \beta \log(E/E_0)}, \quad (8.12)$$

where $E_0 = 1.44 \text{ GeV}$ is given from Massaro et al. [229]. The parameters of the best-fit are $\alpha = 2.03 \pm 0.02$ and $\beta = 0.05 \pm 0.01$, respectively [227].

From Equation 8.12, we prepare four parameter sets of the energy spectrum for the limit calculation. The parameters are summarized in Table 8.1. These values are used in the next section.

Table 8.1: Parameters of the neutrino spectrum using Equation 8.12.

	Parameter1 ^a	Parameter2 ^b	Parameter3 ^b	Parameter4 ^c
E_0	1	1	1	1440
α	2	2.1	2.2	2.03
β	0	0	0	0.05

^a see reference Aartsen et al. [19]

^b see reference Aartsen et al. [56]

^c see reference Garrappa et al. [227]

8.4.1 Fluence Limit

The fluence limit is calculated for electron-neutrinos as 1 to 10 GeV in one bin. For muon-neutrinos, the energy range (1.6 GeV to 10 TeV) is divided into four bins, and the fluence limit is calculated for each. For the first bin and the second bin of the muon-neutrino limit, the limit is calculated using the total observation and expectation as follows;

$$\Phi^{\nu_\mu + \bar{\nu}_\mu} = \frac{N_{90}^{\text{FC}} + N_{90}^{\text{PC}} + N_{90}^{\text{UPMU}}}{N_{90}^{\text{FC}}/\Phi_{\text{FC}}^{\nu_\mu + \bar{\nu}_\mu} + N_{90}^{\text{PC}}/\Phi_{\text{PC}}^{\nu_\mu + \bar{\nu}_\mu} + N_{90}^{\text{UPMU}}/\Phi_{\text{UPMU}}^{\nu_\mu + \bar{\nu}_\mu}}. \quad (8.13)$$

Figure 8.9 shows the upper limits at 90% C.L. on the neutrino fluence for electron-neutrinos ($\nu_e + \bar{\nu}_e$) and muon-neutrinos ($\nu_\mu + \bar{\nu}_\mu$) by SK observations. The limits are calculated using the four parameters described above. Each difference is expressed as an error bar, and the specific numbers are summarized in the appendix of this paper.

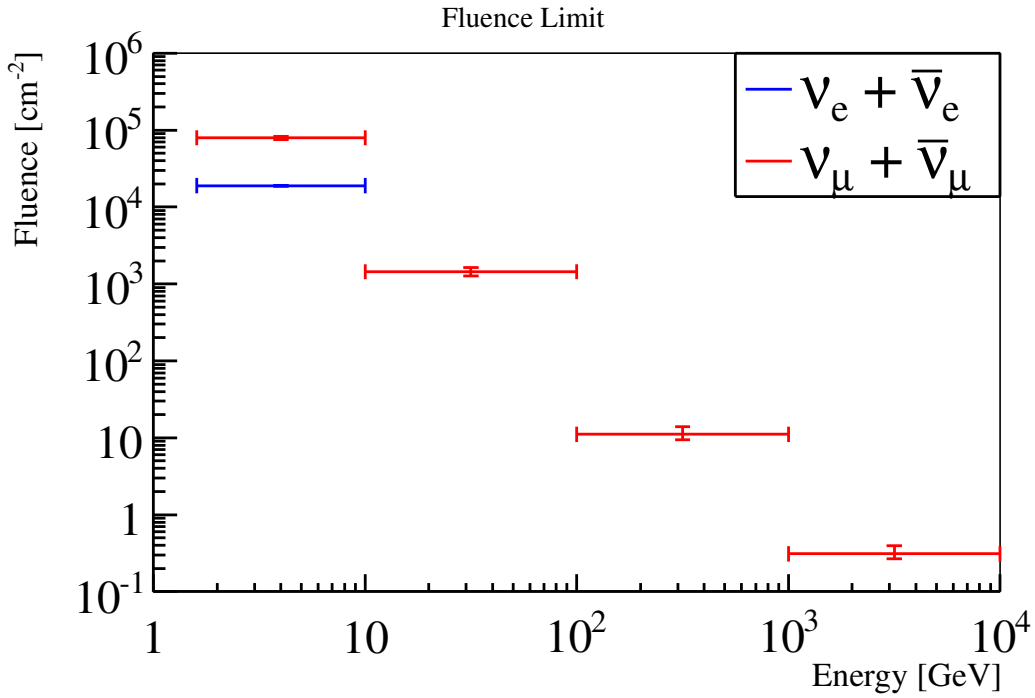


Figure 8.9: Fluence upper limits at 90% C.L. for electron-neutrino (blue) and muon-neutrino (red). The error bars of the x-axis represent the energy range of the integral. The error bars of the y-axis represent differences when calculated with Parameter 1 to 4.

8.4.2 Energy-flux Limit

To compare the results of the IceCube, the energy-flux is calculated. The definition of the energy-flux is as follows;

$$E^2 \frac{dN}{dE} = E^2 \times \frac{\Phi}{T_L(E_{\max} - E_{\min})} \times C \quad [\text{erg cm}^{-2} \text{sec}^{-1}], \quad (8.14)$$

where T_L is 5,924.35 days, which is the sum of SK livetimes for all periods, E_{\max} (E_{\min}) is maximum (minimum) energy of the integration range, and E is the energy at the center of the bin. The unit of energy is converted from MeV to erg by the constant value, $C = 1.60218 \times 10^{-6}$.

The IceCube collaboration considers two neutrino emission periods to calculate the flux limit. In the first scenario, neutrinos are assumed to be emitted only during the about 6 month period corresponding to the duration of the gamma-ray flare. Alternatively, neutrinos emitted over the whole observation of IceCube (7.5 years) are considered. The results of these two benchmark cases correspond to $1.8 \times 10^{-10} \text{ erg cm}^{-2} \text{ s}^{-1}$ and $1.2 \times 10^{-11} \text{ erg cm}^{-2} \text{ s}^{-1}$.

We note that the IceCube group observed evidence of the neutrino event excess between 2014 and 2015 from the direction of the blazar whose best fit the energy spectrum was $E^{-2.2}$ and whose flux was $2.6_{-1.0}^{+1.1} \times 10^{-11} \text{ erg cm}^{-2} \text{ sec}^{-1}$ at 100 TeV [56]. This corresponds to a flux of 1.9×10^{-10} , 1.3×10^{-10} , 8.1×10^{-11} , and $5.1 \times 10^{-11} \text{ erg cm}^{-2} \text{ sec}^{-1}$ at 4.0, 3.2×10^1 , 3.2×10^2 , and $3.2 \times 10^3 \text{ GeV}$, respectively. These represent the values at the center of the bin of the SK results.

The comparison between the results of SK observations and the IceCube events (IceCube-170922A and IceCube-14/15) are shown in Figure 8.10.

Figure 8.11 shows the result of the gamma-ray spectrum analysis for TXS0506+056 using Fermi-LAT data of the whole 9.6 years time range, compared with our result. To reproduce the result of the energy-flux of the gamma-ray, we calculated using the Equation 8.12;

$$E^2 \frac{dN}{dE} = E^2 \times N_0 \left(\frac{E}{E_0} \right)^{-\alpha - \beta \log(E/E_0)}, \quad (8.15)$$

where E is the energy of the gamma-ray and $N_0 = 4.16 \times 10^{-12} \text{ cm}^{-2} \text{ s}^{-1} \text{ MeV}^{-1}$ is the intensity of the gamma-ray spectrum [227].

The specific values of fluence and flux calculated for each parameter are summarized in the Appendix A.

8.4.3 Luminosity Limit

We finally calculate the upper limit of the neutrino luminosity using the luminosity distance. The relationship between the energy-flux and the luminosity is expressed as follows:

$$L = E^2 \frac{dN}{dE} \times 4\pi D_L^2 \quad [\text{erg sec}^{-1}]. \quad (8.16)$$

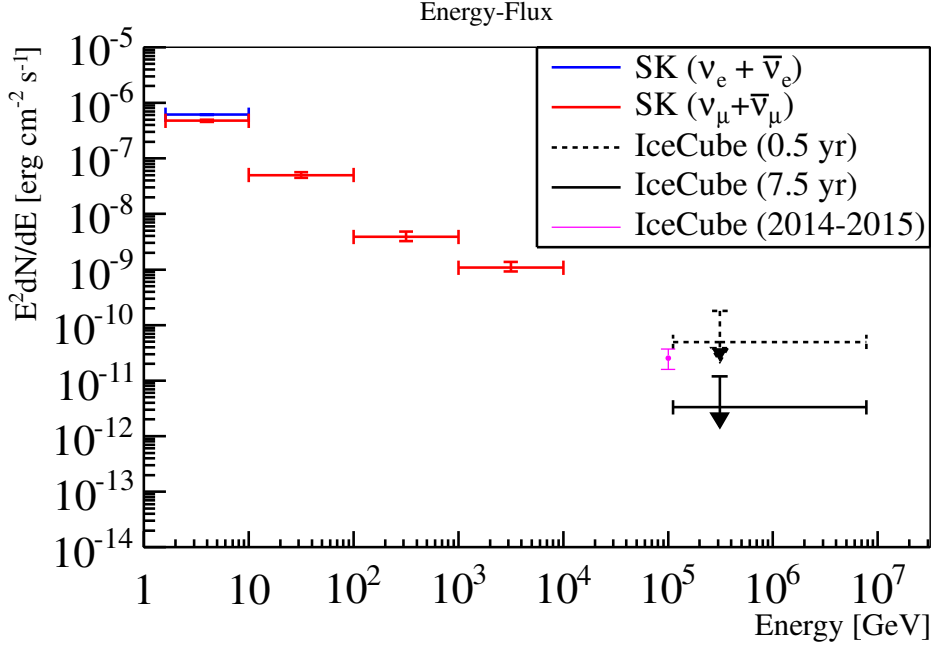


Figure 8.10: 90% C.L. energy-flux upper limit in the direction of the blazar TXS0506+056 by SK electron neutrino (blue) and muon neutrino (red) compared with IceCube events (IceCube-170922A and IceCube-14/15). For the IceCube-170922A event, the upper limit of typical muon neutrino flux that produces, on average, one detection similar to IceCube-170922A over a period of 0.5 years (dashed black line) and 7.5 years (solid black line), are shown. They assume a spectrum of $dN/dE \propto E^{-2}$ at the most probable neutrino energy (311 TeV). The IceCube-14/15 event (purple) is deduced from the optimal result of a box-shaped time window using the $E^{-2.2}$ energy spectrum.

where L is the luminosity, and D_L is the luminosity distance. D_L represents the distance to an object calculated based on the observed luminosity in the absence of any unanticipated attenuation.

The luminosity distance is expressed as follows [230];

$$D_L = (1+z) \frac{c}{H_0} \int_0^z dz' \frac{1}{\sqrt{\Omega_M(1+z')^3 + \Omega_k(1+z')^2 + \Omega_\Lambda}} \quad (8.17)$$

where z is the redshift, H_0 is the Hubble constant, Ω_M is the matter density, Ω_k is the spatial curvature density, and Ω_Λ is the vacuum density. Because we assume a flat Universe, $\Omega_k = 0$ and $\Omega_M + \Omega_\Lambda = 1$. The value of the cosmological parameters, $H_0 = 67.3 \pm 1.2$ and $\Omega_M = 0.315 \pm 0.017$, are obtained from the results of the Planck Collaboration [231]. Therefore, the luminosity distance of the TXS0506+056 located at redshift $z = 0.336$ is 1,835.0 Mpc.⁸

⁸<http://www.astro.ucla.edu/~wright/CosmoCalc.html>.

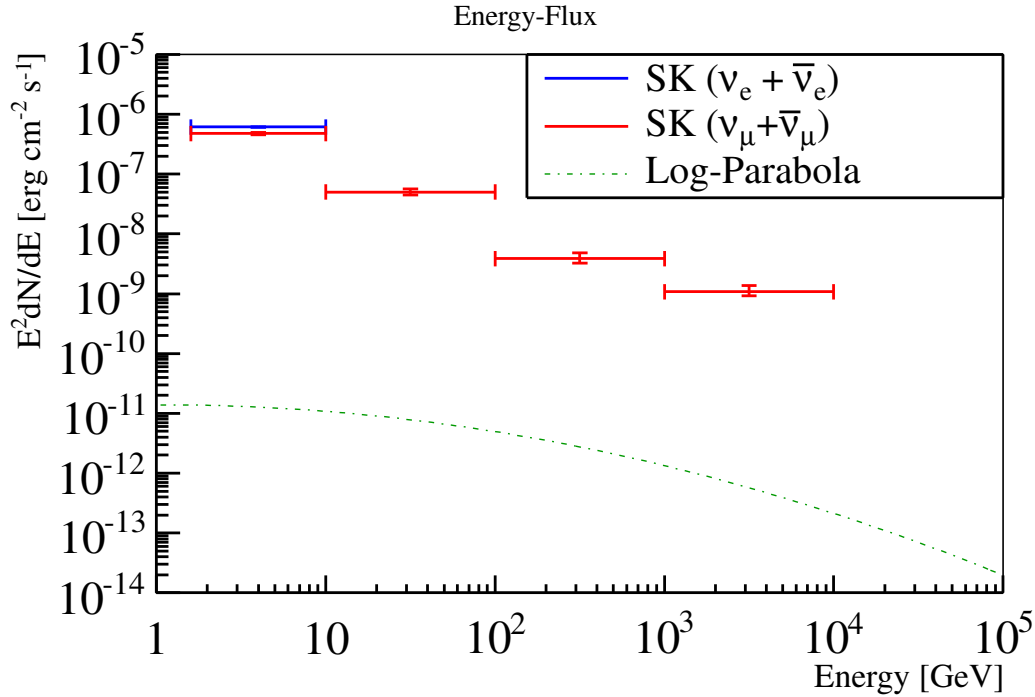


Figure 8.11: Energy-flux upper limit at 90% C.L. of the electron neutrino (blue) and the muon neutrino (red) at SK are compared with the gamma-ray spectrum [227]. The green dashed-dotted line corresponds to the log-parabola model.

As a result of luminosity calculation, the upper limit of the luminosity observed at SK is summarized in Table 8.2. These limits are one to five orders of magnitude higher than the IceCube result [19]. However, this leads to the first limit calculation of this energy region.

Table 8.2: Summary of upper limits (90% C.L.) of luminosity. The unit of luminosity is erg sec⁻¹.

Energy [GeV]	4.0	3.2×10^1	3.2×10^2	3.2×10^3
$\nu_e + \bar{\nu}_e$	2.5×10^{50}	–	–	–
$\nu_\mu + \bar{\nu}_\mu$	1.9×10^{50}	2.0×10^{49}	1.6×10^{48}	4.3×10^{47}

8.5 Discussion

AGNs are expected to emit high-energy hadrons, gamma-rays, and neutrinos. Because the high-energy hadrons repeatedly interact with various materials to reach our galaxy, information about the origin of the CR emission is lost. The information inside the jet of the AGN cannot be obtained from gamma-rays because of absorp-

tion and scattering by interstellar gas. Neutrinos have a very small cross-section, but they can provide us with information about when they are generated.

Gamma-rays having various wavelengths from blazars have been observed by several researchers. These gamma-rays are presumed to have been produced by protons and electrons accelerated by the jet. In the high-energy hadron processes, the neutrinos and gamma-rays are also generated in parallel via pion decay. Various theoretical models of neutrinos and gamma-rays emissions have been verified using IceCube results [232–237]. The comparisons of the energy-flux of neutrino events observed by IceCube using gamma-ray data from telescopes placed restrictions on various model parameters. However, there is no model that completely describes both.

For example, the results of the 2014/2015 neutrino flare event and gamma-ray multi-wavelength observations were tested by Rodrigues et al. [237] using a numerical model [238]. They demonstrated that the models compatible with the gamma-ray spectral energy distribution produce too few neutrinos (Figure 8.12: left). On the other hand, a compatible neutrino flux level implies a gamma-ray spectral energy distribution in tension with observations (Figure 8.12: right). In both cases, the neutrino flux in the GeV to TeV region is very small, because it is parameterized to have a peak in the several hundred TeV region. The neutrino energy-flux is about 10^{-11} to 10^{-13} [erg cm⁻²sec⁻¹] at about 1 TeV and about 10^{-12} to 10^{-14} [erg cm⁻²sec⁻¹] at about 1 GeV. These energy-fluxes are about three to eight orders of magnitude lower than our limits.

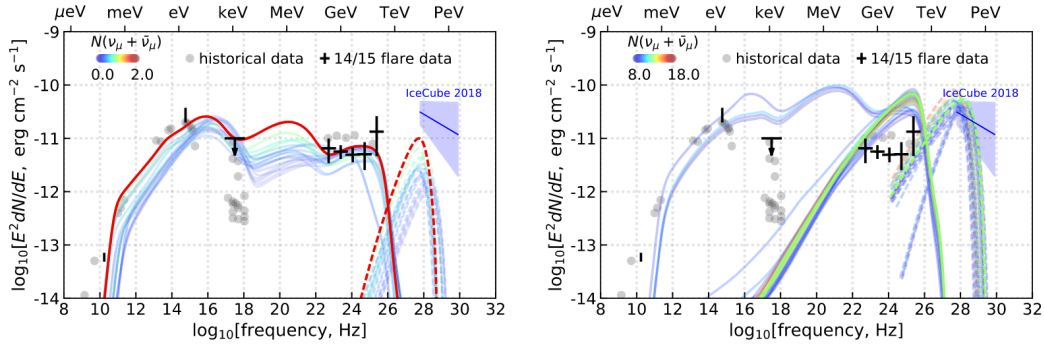


Figure 8.12: Spectral energy distributions and muon neutrino fluxes are shown. The black points with the error bar reflect the gamma-ray energy-flux observed between October 2014 and March 2015. The gray points are archival data taken during the year prior to 2017. The colors represent the results of changing the parameters of the numerical calculation. On the left, a set of parameters optimized to describe the gamma-ray spectral energy distribution consistent with observations by IceCube is shown. They fail to explain neutrino emission. On the right, the parameters are set to account for neutrino flare of IceCube-14/15. They overshoot the multi-wavelength emission. The figures are taken from Rodrigues et al. [237].

Some models have high neutrino flux in the GeV energy region, which is based on inverse Compton scattering of soft target photons by highly relativistic electrons

in the jets [239–242]. In these models, the electron acceleration process must be very fast to compete efficiently with radiation losses at high energies. It is considered, therefore, that high energy electrons are generated by the interaction of primary high-energy hadrons.

The AGN jet was modeled by Pohl and Schlickeiser [243] as a plasma consisting of electrons and protons. A typical primary particle is a proton having a Lorentz factor γ of the order of 100, which is distributed in the jet isotropically, moving with a bulk Lorentz factor⁹, Γ , of the order of 100. The neutrinos produced from the decays of pions and subsequent muon decay was calculated by Schuster C. et al. [244] using the MC model: DTUNUC [245–248].

Of the two calculated examples of resulting proton distributions, the first considers that the radius of the plasma disk, $R = 10^{14}$ cm, the thickness of the disk, $d = 3 \times 10^{13}$ cm, the initial Lorentz factor, $\Gamma_0 = 300$, the plasma density, $n_b = 5 \times 10^8 \text{ cm}^{-3}$, the interstellar medium density, $n_i = 0.2 \text{ cm}^{-3}$, and the viewing angle, $\theta = 0.1^\circ$. The parameters of second example are $R = 2 \times 10^{15}$ cm, $d = 10^{14}$ cm, $\Gamma_0 = 300$, $n_b = 10^8 \text{ cm}^{-3}$, $n_i = 1.5 \text{ cm}^{-3}$, and $\theta = 2^\circ$. Figure 8.13 shows two examples of the spectral evolution of total muon-neutrino emissions and gamma-rays created from neutral pions. The difference between the initial values in the first and second examples changes the cooling rate of the particles. In the first example, the swept-up particles cool down faster than the jet decelerates, whereas in the second example, the cooling is slow compared with the deceleration of the jet.

In the first example, the neutrino flux has a peak around 10^3 to 10^4 GeV. The highest energy-flux is about $5 \times 10^{-6} \text{ GeV cm}^{-2} \text{ sec}^{-1}$ ($= 8 \times 10^{-9} \text{ erg cm}^{-2} \text{ sec}^{-1}$), which appears to be above our calculated limit. Therefore, TXS0506+056 might be a blazar that does not match the parameters of the first example. On the other hand, in the second example, the peak position is around 10^1 to 10^2 GeV, and the highest energy-flux is about $2 \times 10^{-8} \text{ GeV cm}^{-2} \text{ sec}^{-1}$ ($= 3 \times 10^{-11} \text{ erg cm}^{-2} \text{ sec}^{-1}$). The second example flux is predicted to be lower than our calculated limit.

Depending on the theoretical model and the direction of the jet, the neutrino signal from blazar can possibly be detected by SK. Because the neutrino energy-flux changes sensitively depending on the parameters of the AGN jet model, neutrino observations in the GeV to TeV region are important for determining these parameters. By limiting these parameters, the origin of high-energy CRs and the mechanism of acceleration of CRs are elucidated.

⁹A bulk Lorentz factor is the Lorentz factor of the plasma. The particles in the plasma have their own individual velocities.

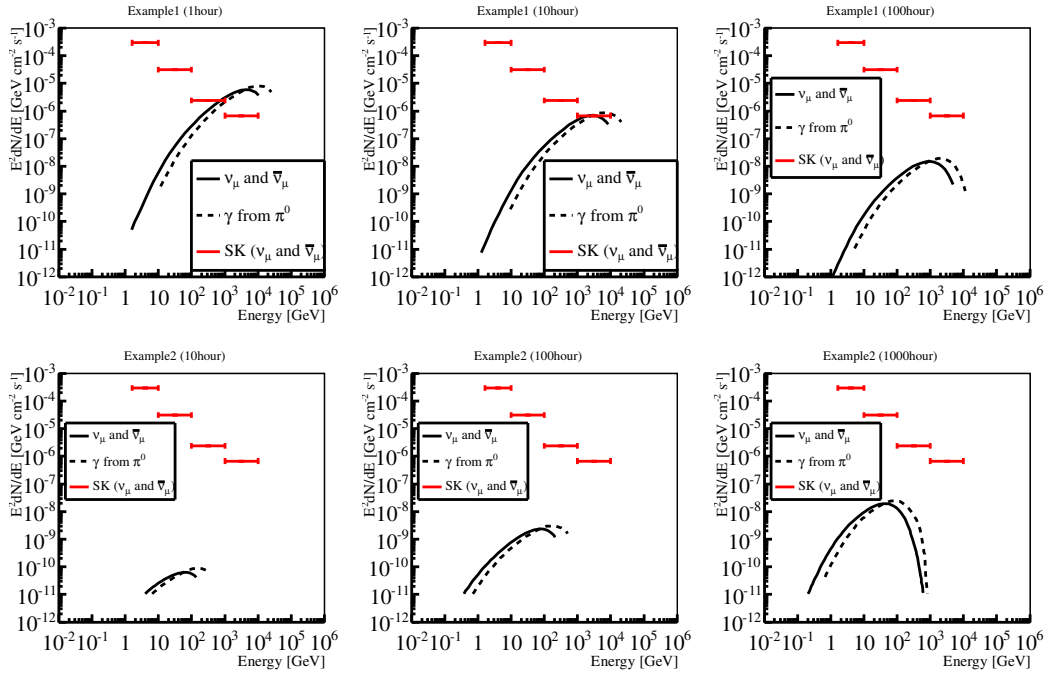


Figure 8.13: Time evolution of the muon neutrino emission from the jet of AGN. The solid line (dashed line) represents the energy-flux of the muon neutrino (gamma-ray from pion decay). The top figures show the condition of first example, and the bottom figures represent the second example. Those two examples assume that the redshift of the AGN is $z = 0.5$. The data are taken from Schuster C. et al. [244]. The red line represents the upper limit of energy-flux at SK, as calculated by our study.

A Table of the Upper Limit

For the calculation of the upper limit, the energy spectrum was calculated with four different parameter sets. The upper limit when each energy spectrum is used is summarized in a tables. The parameterized equation is expressed as;

$$\frac{dN}{dE} \propto \left(\frac{E}{E_0} \right)^{-\alpha - \beta \log(E/E_0)} . \quad (\text{A.1})$$

Table A.1: Parameter1 ; $E_0 = 1$, $\alpha = 2.0$, $\beta = 0$

		Energy Range [GeV]	Fluence [/cm ²]	dFlux/dE [/cm ² /sec/MeV]	E2dFlux/dE [erg/cm ² /sec]
FC	$\nu_e + \bar{\nu}_e$	5.1–10	1.9×10^4	7.4×10^{-9}	6.0×10^{-7}
	$\nu_\mu + \bar{\nu}_\mu$		6.9×10^4	2.7×10^{-8}	2.2×10^{-6}
PC	$\nu_\mu + \bar{\nu}_\mu$	1.8–10	1.1×10^5	2.5×10^{-8}	7.1×10^{-7}
		10–100	5.4×10^3	1.2×10^{-10}	1.9×10^{-7}
UPMU	$\nu_\mu + \bar{\nu}_\mu$	1.6–10	6.1×10^5	1.4×10^{-8}	3.6×10^{-7}
		10–100	6.8×10^2	1.5×10^{-11}	2.4×10^{-8}
		100–10 ³	9.4	2.0×10^{-14}	3.3×10^{-9}
		10 ³ –10 ⁴	2.7×10^{-1}	5.8×10^{-17}	9.3×10^{-10}

Table A.2: Parameter2 ; $E_0 = 1$, $\alpha = 2.1$, $\beta = 0$

		Energy Range [GeV]	Fluence [cm^2]	dFlux/dE [$\text{cm}^2/\text{sec}/\text{MeV}$]	E2dFlux/dE [$\text{erg}/\text{cm}^2/\text{sec}$]
FC	$\nu_e + \bar{\nu}_e$	5.1–10	1.9×10^4	7.5×10^{-9}	6.1×10^{-7}
	$\nu_\mu + \bar{\nu}_\mu$		7.0×10^4	2.8×10^{-8}	2.2×10^{-6}
PC	$\nu_\mu + \bar{\nu}_\mu$	1.8–10	1.1×10^5	2.6×10^{-8}	7.5×10^{-7}
		10–100	5.6×10^3	1.2×10^{-10}	1.9×10^{-7}
UPMU	$\nu_\mu + \bar{\nu}_\mu$	1.6–10	6.5×10^4	1.5×10^{-8}	3.9×10^{-7}
		10–100	7.4×10^2	1.6×10^{-11}	2.6×10^{-8}
		100– 10^3	1.0×10^1	2.2×10^{-14}	3.5×10^{-9}
		10^3 – 10^4	2.8×10^{-1}	6.1×10^{-17}	9.8×10^{-10}

Table A.3: Parameter3 ; $E_0 = 1$, $\alpha = 2.2$, $\beta = 0$

		Energy Range [GeV]	Fluence [cm^2]	dFlux/dE [$\text{cm}^2/\text{sec}/\text{MeV}$]	E2dFlux/dE [$\text{erg}/\text{cm}^2/\text{sec}$]
FC	$\nu_e + \bar{\nu}_e$	5.1–10	1.9×10^4	7.6×10^{-9}	6.2×10^{-7}
	$\nu_\mu + \bar{\nu}_\mu$		7.1×10^4	2.8×10^{-8}	2.3×10^{-6}
PC	$\nu_\mu + \bar{\nu}_\mu$	1.8–10	1.2×10^5	2.8×10^{-8}	8.0×10^{-7}
		10–100	5.9×10^3	1.3×10^{-10}	2.0×10^{-7}
UPMU	$\nu_\mu + \bar{\nu}_\mu$	1.6–10	7.0×10^4	1.6×10^{-8}	4.2×10^{-7}
		10–100	8.0×10^2	1.7×10^{-11}	2.8×10^{-8}
		100– 10^3	1.1×10^1	2.4×10^{-14}	3.8×10^{-9}
		10^3 – 10^4	3.0×10^{-1}	6.4×10^{-17}	1.0×10^{-9}

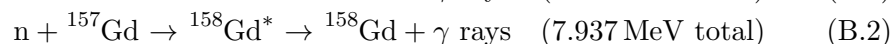
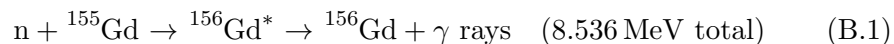
Table A.4: Parameter4 ; $E_0 = 1440$, $\alpha = 2.03$, $\beta = 0.05$

		Energy Range [GeV]	Fluence [cm^2]	dFlux/dE [$\text{cm}^2/\text{sec}/\text{MeV}$]	E2dFlux/dE [$\text{erg}/\text{cm}^2/\text{sec}$]
FC	$\nu_e + \bar{\nu}_e$	5.1–10	1.9×10^4	7.6×10^{-9}	6.2×10^{-7}
	$\nu_\mu + \bar{\nu}_\mu$		7.1×10^4	2.8×10^{-8}	2.3×10^{-6}
PC	$\nu_\mu + \bar{\nu}_\mu$	1.8–10	1.1×10^5	2.7×10^{-8}	7.7×10^{-7}
		10–100	6.2×10^3	1.3×10^{-10}	2.2×10^{-7}
UPMU	$\nu_\mu + \bar{\nu}_\mu$	1.6–10	6.7×10^4	1.5×10^{-8}	4.0×10^{-7}
		10–100	8.9×10^2	1.9×10^{-11}	3.1×10^{-8}
		100– 10^3	1.4×10^1	3.0×10^{-14}	4.9×10^{-9}
		10^3 – 10^4	4.0×10^{-1}	8.6×10^{-17}	1.4×10^{-9}

B Gamma-ray Spectrum from Gadolinium

The SK will start new phase, SK-Gd, that dissolves Gd in ultra-pure water. The natural composition of Gd includes isotopes with the atomic mass numbers $A=152$, 154 - 158 , and 160 . Gd has the largest capture cross-section for thermal neutrons among all stable elements due to the contributions of the isotopes ^{155}Gd and ^{157}Gd (60,900 b and 254,000 b respectively) [249]. Natural Gd plays a role in the identification of the electron anti-neutrino interactions by tagging neutrons emitted from inverse beta decay reaction. Modeling of the behavior of gamma rays from Gd for proper simulation was created.

To create a high accurate gamma-ray emission model (ANNRI-Gd model¹⁰ [204–206]), the gamma-rays energy spectrum from the thermal neutron capture on an enriched ^{157}Gd and ^{155}Gd targets were measured using the Accurate Neutron-Nucleus Reaction measurement Instrument (ANNRI) germanium spectrometer [250–254]. The neutron capture reaction is expected to produce about four gamma-rays, which have total energy of about 8 MeV.



Experimental Data

The incident neutron beam from the Japan Spallation Neutron Source (JSNS) at the Material and Life Science Experimental Facility (MLF) of the Japan Proton Accelerator Research Complex (J-PARC) [255]. In order to study the gamma-ray spectrum from thermal neutron capture, the events from neutrons in the kinetic energy range 4 to 100 meV were selected. The ANNRI spectrometer has two Ge cluster detectors, one of which consists of seven Ge crystals with a hexagonal front from the target's point of view. Two Ge clusters provide a total solid angle coverage of about 15% with respect to the target.

We assigned a multiplicity value M and a hit value H to each recorded event using the information of 14 Ge crystals. The multiplicity was defined as the combined number of isolated sub-clusters of hit Ge crystals at the upper and lower clusters. The hit value describes the total number of Ge crystals hit in the event. Figure B.1 shows that the energy spectra of the experimental results for each multiplicity and hit value.

About 90% of all events are classified as ($M=1, H=1$) and ($M=1, H=2$) events, and the ($M=2, H=2$) events are about 7% of the total. At low energy, the spectra are slightly distorted by the effect of Compton scattering.

¹⁰You can see also the homepage of ANNRI-Gd; http://www.physics.okayama-u.ac.jp/~sakuda/ANNRI-Gd_ver1.html, the date of the last access is 29 December 2019

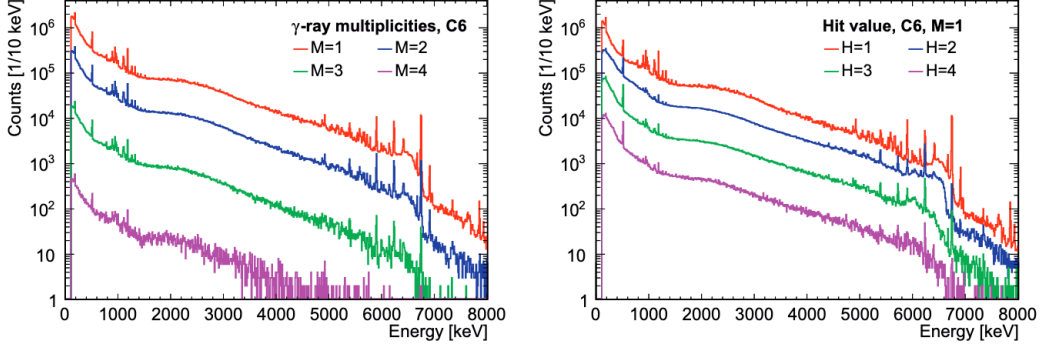


Figure B.1: The energy spectrum from $^{157}\text{Gd}(n, \gamma)$ reaction with different multiplicity values, M , and hit values, H , that were observed by the Ge detector No.6 which is the center of the upper cluster in ANNRI. The figures are taken from Hagiwara et al. [206].

Simulation Model

The ANNRI-Gd model is composed of two parts; discrete prompt gamma-rays and continuum spectrum. The discrete gamma-ray emission in the range from 5 to 8 MeV is expected to arise mostly from the first transition. Their photo-peak energies and the relative intensities were estimated from our data. For modeling the continuum part, the transition probability was computed from the number of transmission coefficient and level density. The transition probability $P(E_a, E_b)$ from the initial energy level E_a to the final energy level E_b , emitting the gamma-ray energy $E_\gamma (= E_a - E_b)$, is expressed as follow.

$$P(E_a, E_b) = \frac{\rho(E_b)T(E_\gamma)}{\int_0^{E_a} \rho(E'_b)T(E'_\gamma) dE'_b} \delta E, \quad (\text{B.3})$$

$$E'_\gamma = E_a - E'_b,$$

$$T(E_\gamma) = 2\pi E_\gamma^3 f^{\text{SLO}}(E_\gamma),$$

$$f^{\text{SLO}}(E_\gamma) = \frac{1}{3\pi(\hbar c)^2} \sum_i \frac{\sigma_i E_\gamma \Gamma_i^2}{(E_\gamma^2 - E_i^2)^2 + E_\gamma^2 \Gamma_i^2},$$

where δE is a finite energy step in our computation, $T(E_\gamma)$ is transmission coefficient, and ρ is the number of level density. The transmission coefficient refers to the photon strength function, $f(E_\gamma)$, depending on cross section (σ_i), the width (Γ_i), and the energy (E_i) of the resonances. There are four resonances for ^{155}Gd and two resonances for ^{157}Gd [256]. Note that we used the simplest model for the photon strength function named Standard Lorentzian model [257].

For ^{155}Gd , the fraction of the discrete part in the total number of events to be $2.78 \pm 0.02\%$ and remaining part, $97.22 \pm 0.02\%$, contributes to the continuum part of the gamma-ray spectrum. On the other hand, for ^{157}Gd , the contribution of discrete part is $6.94 \pm 0.01\%$ and continuum part is $93.0 \pm 0.01\%$.

Comparison between Data and Model

Figure B.2 shows a comparison between the ANNRI-Gd model and the GLG4Sim package¹¹, which is Geant4-based MC developed by KamLAND group. The shape of the energy spectrum in our data is significantly better reproduced by our model, the mean deviation from the mean ratio is about 17% for the spectrum with 200 keV binning. Figure B.3 shows the ratio of experimental data divided by ANNRI-Gd model in bins of 200 keV for ^{155}Gd , ^{157}Gd , and $^{\text{natural}}\text{Gd}$. The mean deviation of the single ratios from the mean ratio is also about 17% for each of spectra.

A more detailed discussion is described in Hagiwara et al. [206].

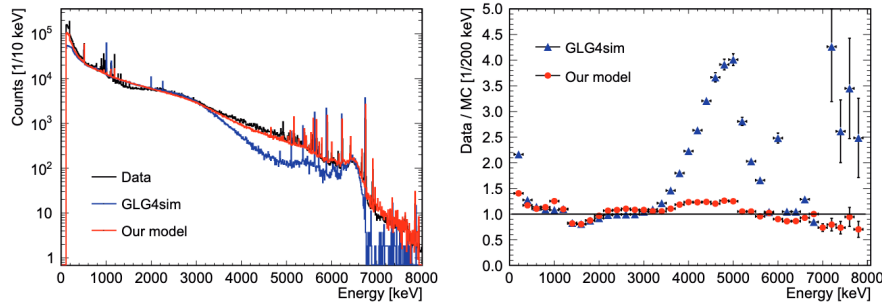


Figure B.2: Left: The energy spectrum of single gamma-rays ($M=1$, $H=1$) from $^{157}\text{Gd}(n, \gamma)$ reaction; our measurement data (black), the simulation with ANNRI-Gd model (red), and the simulation with GLG4Sim package (blue). Right: The ratio between data and MC per 200 keV of observed energy. The figures are taken from Hagiwara et al. [206].

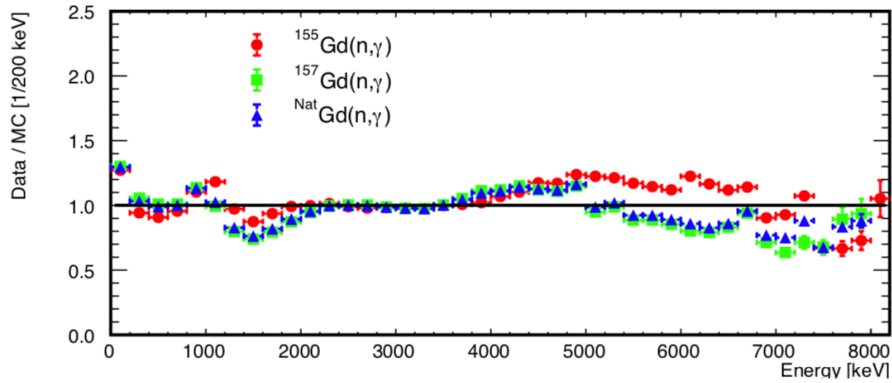


Figure B.3: The Ratio of data by MC for the single gamma-ray ($M=1$, $H=1$ and $M=1$, $H=2$) from $^{155}\text{Gd}(n, \gamma)$, $^{157}\text{Gd}(n, \gamma)$, and $^{\text{natural}}\text{Gd}(n, \gamma)$ reaction.

¹¹available at <https://www.phys.ksu.edu/personal/gahs/GLG4sim/>, the date of the last access is 29 December 2019.

References

- [1] W. Pauli, “Dear radioactive ladies and gentlemen”, *Physics Today*, **31N9**, pp.27, (1978).
- [2] F. Reines, & C. L. Cowan, “Detection of the Free Neutrino”, *Physical Review*, **92**, pp.830, (1953).
- [3] F. Reines, & C. L. Cowan, “The Neutrino”, *Nature*, **178**(4531), pp.446, (1956).
- [4] G. Danby, J.-M. Gaillard, K. Goulianos, *et al.*, “Observation of High-Energy Neutrino Reactions and the Existence of Two Kinds of Neutrinos”, *Physical Review Letters*, **9**, pp.36, (1962).
- [5] K. Kodama, N. Ushida, C. Andreopoulos, *et al.*, (DONUT Collaboration), “Observation of tau neutrino interactions”, *Physics Letters B*, **504**(3), pp.218, (2001).
- [6] R. Davis, D. S. Harmer, & K. C. Hoffman, “Search for Neutrinos from the Sun”, *Physical Review Letters*, **20**, pp.1205, (1968).
- [7] B. T. Cleveland, T. Daily, J. Raymond Davis, *et al.*, “Measurement of the Solar Electron Neutrino Flux with the Homestake Chlorine Detector”, *The Astrophysical Journal*, **496**(1), pp.505, (1998).
- [8] K. S. Hirata, T. Kajita, T. Kifune, *et al.*, “Observation of ^8B solar neutrinos in the Kamiokande-II detector”, *Physical Review Letters*, **63**, pp.16, (1989).
- [9] Q. R. Ahmad, R. C. Allen, T. C. Andersen, *et al.*, (SNO Collaboration), “Measurement of the Rate of $\nu_e + d \rightarrow p + p + e^-$ Interactions Produced by ^8B Solar Neutrinos at the Sudbury Neutrino Observatory”, *Physical Review Letters*, **87**, pp.071301, (2001).
- [10] K. Hirata, T. Kajita, M. Koshiba, *et al.*, “Experimental study of the atmospheric neutrino flux”, *Physics Letters B*, **205**(2), pp.416, (1988).
- [11] R. Becker-Szendy, C. B. Bratton, D. Casper, *et al.*, “Electron- and muon-neutrino content of the atmospheric flux”, *Physical Review D*, **46**, pp.3720, (1992).
- [12] Y. Fukuda, T. Hayakawa, E. Ichihara, *et al.*, (Super Kamiokande Collaboration), “Evidence for Oscillation of Atmospheric Neutrinos”, *Physical Review Letters*, **81**, pp.1562, (1998).
- [13] S. Fukuda, Y. Fukuda, M. Ishitsuka, *et al.*, (Super Kamiokande Collaboration), “Solar ^8B and hep Neutrino Measurements from 1258 Days of Super-Kamiokande Data”, *Physical Review Letters*, **86**, pp.5651, (2001).

-
- [14] Q. R. Ahmad, R. C. Allen, T. C. Andersen, *et al.*, (SNO Collaboration), “Direct Evidence for Neutrino Flavor Transformation from Neutral-Current Interactions in the Sudbury Neutrino Observatory”, *Physical Review Letters*, **89**, pp.011301, (2002).
- [15] K. Hirata, *et al.*, “Observation of a Neutrino Burst from the Supernova SN 1987a”, *Physical Review Letters*, **58**, pp.1490, (1987).
- [16] R. M. Bionta, G. Blewitt, C. B. Bratton, *et al.*, “Observation of a neutrino burst in coincidence with supernova 1987A in the Large Magellanic Cloud”, *Physical Review Letters*, **58**, pp.1494, (1987).
- [17] E. N. Alekseev, L. N. Alekseeva, V. I. Volchenko, & I. V. Krivosheina, “Possible Detection of a Neutrino Signal on 23 February 1987 at the Baksan Underground Scintillation Telescope of the Institute of Nuclear Research”, *JETP Letters*, **45**, pp.589, (1987).
- [18] K. Scholberg, “Supernova Neutrino Detection”, *Annual Review of Nuclear and Particle Science*, **62**(1), pp.81, (2012).
- [19] M. Aartsen, M. Ackermann, J. Adams, *et al.*, (IceCube Collaboration), “Multi-messenger observations of a flaring blazar coincident with high-energy neutrino IceCube-170922A”, *Science*, **361**(eaat1378), (2018).
- [20] B. Pontecorvo, “Mesonium and anti-mesonium”, *Soviet Physics JETP*, **6**, pp.429, (1957).
- [21] B. Pontecorvo, “Inverse beta processes and nonconservation of lepton charge”, *Soviet Physics JETP*, **7**, pp.172, (1958).
- [22] Z. Maki, M. Nakagawa, & S. Sakata, “Remarks on the Unified Model of Elementary Particles”, *Progress of Theoretical Physics*, **28**(5), pp.870, (1962).
- [23] B. Pontecorvo, “Neutrino Experiments and the Problem of Conservation of Leptonic Charge”, *Soviet Physics JETP*, **26**, pp.984, (1968).
- [24] L. Wolfenstein, “Neutrino oscillations in matter”, *Physical Review D*, **17**, pp.2369, (1978).
- [25] L. Wolfenstein, “Neutrino oscillations and stellar collapse”, *Physical Review D*, **20**, pp.2634, (1979).
- [26] S. P. Mikheyev, & A. Yu. Smirnov, “Resonance Amplification of Oscillations in Matter and Spectroscopy of Solar Neutrinos”, *Soviet Journal of Nuclear Physics*, **42**, pp.913, (1985).
- [27] K. Abe, Y. Hayato, T. Iida, *et al.*, (Super Kamiokande Collaboration), “Solar neutrino results in Super-Kamiokande-III”, *Physical Review D*, **83**, pp.052010, (2011).

- [28] B. Aharmim, S. N. Ahmed, A. E. Anthony, *et al.*, (SNO Collaboration), “Electron energy spectra, fluxes, and day-night asymmetries of ^8B solar neutrinos from measurements with NaCl dissolved in the heavy-water detector at the Sudbury Neutrino Observatory”, *Physical Review C*, **72**, pp.055502, (2005).
- [29] S. Abe, T. Ebihara, S. Enomoto, *et al.*, (KamLAND Collaboration), “Precision Measurement of Neutrino Oscillation Parameters with KamLAND”, *Physical Review Letters*, **100**, pp.221803, (2008).
- [30] Y. Ashie, J. Hosaka, K. Ishihara, *et al.*, (Super Kamiokande Collaboration), “Evidence for an Oscillatory Signature in Atmospheric Neutrino Oscillations”, *Physical Review Letters*, **93**, pp.101801, (2004).
- [31] M. H. Ahn, E. Aliu, S. Andringa, *et al.*, (K2K Collaboration), “Measurement of neutrino oscillation by the K2K experiment”, *Physical Review D*, **74**, pp.072003, (2006).
- [32] P. Adamson, C. Andreopoulos, R. Armstrong, *et al.*, (MINOS Collaboration), “Measurement of the Neutrino Mass Splitting and Flavor Mixing by MINOS”, *Physical Review Letters*, **106**, pp.181801, (2011).
- [33] K. Abe, J. Adam, H. Aihara, *et al.*, (T2K Collaboration), “Measurement of Neutrino Oscillation Parameters from Muon Neutrino Disappearance with an Off-Axis Beam”, *Physical Review Letters*, **111**, pp.211803, (2013).
- [34] F. P. An, A. B. Balantekin, H. R. Band, *et al.*, (Daya Bay Collaboration), “Spectral Measurement of Electron Antineutrino Oscillation Amplitude and Frequency at Daya Bay”, *Physical Review Letters*, **112**, pp.061801, (2014).
- [35] J. K. Ahn, S. Chebotaryov, J. H. Choi, *et al.*, (RENO Collaboration), “Observation of Reactor Electron Antineutrinos Disappearance in the RENO Experiment”, *Physical Review Letters*, **108**, pp.191802, (2012).
- [36] Y. Abe, C. Aberle, J. C. d. Anjos, *et al.*, (Double Chooz Collaboration), “Reactor $\bar{\nu}_e$ disappearance in the Double Chooz experiment”, *Physical Review D*, **86**, pp.052008, (2012).
- [37] K. Abe, J. Adam, H. Aihara, *et al.*, (T2K Collaboration), “Observation of Electron Neutrino Appearance in a Muon Neutrino Beam”, *Physical Review Letters*, **112**, pp.061802, (2014).
- [38] K. Abe, J. Amey, C. Andreopoulos, *et al.*, (T2K Collaboration), “Combined Analysis of Neutrino and Antineutrino Oscillations at T2K”, *Physical Review Letters*, **118**, pp.151801, (2017).
- [39] P. Adamson, L. Aliaga, D. Ambrose, *et al.*, (NOvA Collaboration), “Constraints on Oscillation Parameters from ν_e Appearance and ν_μ Disappearance in NOvA”, *Physical Review Letters*, **118**, pp.231801, (2017).

- [40] F. Capozzi, E. Lisi, A. Marrone, D. Montanino, & A. Palazzo, “Neutrino masses and mixings: Status of known and unknown 3 ν parameters”, *Nuclear Physics B*, **908**, pp.218 , (2016).
- [41] A. D. Panov, “Electrons and Positrons in Cosmic Rays”, *Journal of Physics: Conference Series*, **409**, pp.012004, (2013).
- [42] K. Greisen, “End to the Cosmic-Ray Spectrum?”, *Physical Review Letters*, **16**, pp.748, (1966).
- [43] G. T. Zatsepin, & V. A. Kuz'min, “Upper Limit of the Spectrum of Cosmic Rays”, *Soviet Journal of Experimental and Theoretical Physics Letters*, **4**, pp.78, (1966).
- [44] C. Patrignani, *et al.*, (Particle Data Group), “Review of Particle Physics”, *Chinese Physics C*, **40**(10), pp.100001, (2016).
- [45] L. I. MIROSHNICHENKO, & J. A. PEREZ-PERAZA, “ASTROPHYSICAL ASPECTS IN THE STUDIES OF SOLAR COSMIC RAYS”, *International Journal of Modern Physics A*, **23**(01), pp.1, (2008).
- [46] E. Fermi, “On the Origin of the Cosmic Radiation”, *Physical Review*, **75**, pp.1169, (1949).
- [47] A. M. Hillas, “The Origin of Ultra-High-Energy Cosmic Rays”, *Annual Review of Astronomy and Astrophysics*, **22**(1), pp.425, (1984).
- [48] D. J. Mortlock, S. J. Warren, B. P. Venemans, *et al.*, “A luminous quasar at a redshift of $z = 7.085$ ”, *Nature*, **474**(7353), pp.616, (2011).
- [49] C. M. Urry, & P. Padovani, “Unified Schemes for Radio-Loud Active Galactic Nuclei”, *Publications of the Astronomical Society of the Pacific*, **107**, pp.803, (1995).
- [50] P. Padovani, & P. Giommi, “The Connection between X-Ray- and Radio-selected BL Lacertae Objects”, *The Astrophysical Journal*, **444**, pp.567, (1995).
- [51] A. A. Abdo, M. Ackermann, I. Agudo, *et al.*, “The Spectral Energy Distribution of Fermi Bright Blazars”, *The Astrophysical Journal*, **716**(1), pp.30, (2010).
- [52] S.-S. Lee, K. Wajima, J.-C. Algaba, *et al.*, “Interferometric Monitoring of Gamma-Ray Bright AGNs. I. The Results of Single-epoch Multifrequency Observations”, *The Astrophysical Journal*, **227**(1):8, (2016).
- [53] A. A. Abdo, M. Ackermann, M. Ajello, *et al.*, “Fermi Large Area Telescope Observations of Markarian 421: The Missing Piece of its Spectral Energy Distribution”, *The Astrophysical Journal*, **736**(2):131, (2011).

- [54] A. Franceschini, G. Rodighiero, & M. Vaccari, “Extragalactic optical-infrared background radiation, its time evolution and the cosmic photon-photon opacity”, *Astronomy & Astrophysics*, **487**(3), pp.837, (2008).
- [55] M. Aartsen, M. Ackermann, J. Adams, *et al.*, (IceCube Collaboration), “The IceCube Neutrino Observatory: instrumentation and online systems”, *Journal of Instrumentation*, **12**(03), pp.P03012, (2017).
- [56] M. Aartsen, M. Ackermann, J. Adams, *et al.*, (IceCube Collaboration), “Neutrino emission from the direction of the blazar TXS 0506+056 prior to the IceCube-170922A alert”, *Science*, **361**(6398), pp.147, (2018).
- [57] S. Paiano, R. Falomo, A. Treves, & R. Scarpa, “The Redshift of the BL Lac Object TXS 0506+056”, *The Astrophysical Journal*, **854**(2), pp.L32, (2018).
- [58] E. Massaro, A. Maselli, C. Leto, *et al.*, “The 5th edition of the Roma-BZCAT. A short presentation”, *Astrophysics and Space Science*, **357**(1), pp.75, (2015).
- [59] S. Abdollahi, M. Ackermann, M. Ajello, *et al.*, “The Second Catalog of Flaring Gamma-Ray Sources from the Fermi All-sky Variability Analysis”, *The Astrophysical Journal*, **846**(1), pp.34, (2017).
- [60] Y. T. Tanaka, S. Buson, & D. Kocevski, “Fermi-LAT detection of increased gamma-ray activity of TXS 0506+056, located inside the IceCube-170922A error region.”, *The Astronomer’s Telegram*, **10791**, (2017).
- [61] J. Chiang, J. Carson, & W. Focke, “Automated Science Processing for GLAST LAT Data”, *Proceedings of the AIP Conference*, **921**, pp.544, (2007).
- [62] S. Fukuda, Y. Fukuda, T. Hayakawa, *et al.*, (Super Kamiokande Collaboration), “The Super-Kamiokande detector”, *Nuclear Instruments and Methods in Physics Research Section A: Accelerators, Spectrometers, Detectors and Associated Equipment*, **501**(2), pp.418, (2003).
- [63] K. Abe, N. Abgrall, H. Aihara, *et al.*, (T2K Collaboration), “The T2K experiment”, *Nuclear Instruments and Methods in Physics Research Section A: Accelerators, Spectrometers, Detectors and Associated Equipment*, **659**(1), pp.106, (2011).
- [64] P. A. Cherenkov, “Visible luminescence of pure liquids under the influence of γ -radiation”, *Doklady Akademii Nauk SSSR*, **2**(8), pp.451, (1934).
- [65] I. M. Frank, & I. E. Tamm, “Coherent visible radiation of fast electrons passing through matter”, *Physical Institute of the Academy of Sciences of the USSR Moscow*, **14**(3), pp.109, (1937).
- [66] J. Jackson, “Classical Electrodynamics”. John Wiley & Sons Inc., ISBN 978-0-471-30932-1, (1990).

- [67] M. Koshiba, “KAMIOKA nucleon decay experiment”, *Il Nuovo Cimento C*, **9** (2), pp.141, (1986).
- [68] Y. Fukuda, T. Hayakawa, E. Ichihara, *et al.*, (Super Kamiokande Collaboration), “Evidence for Oscillation of Atmospheric Neutrinos”, *Physical Review Letters*, **81**(8), pp.1562, (1998).
- [69] M. H. Ahn, S. Aoki, H. Bhang, *et al.*, “Indications of Neutrino Oscillation in a 250 km Long-Baseline Experiment”, *Physical Review Letters*, **90**, pp.041801, (2003).
- [70] E. Aliu, S. Andringa, S. Aoki, *et al.*, “Evidence for Muon Neutrino Oscillation in an Accelerator-Based Experiment”, *Physical Review Letters*, **94**, pp.081802, (2005).
- [71] J. F. Beacom, & M. R. Vagins, “Antineutrino Spectroscopy with Large Water Čerenkov Detectors”, *Physical Review Letters*, **93**(17), (2004).
- [72] H. Kume, S. Sawaki, M. Ito, *et al.*, “20 inch diameter photomultiplier”, *Nuclear Instruments and Methods in Physics Research*, **205**(3), pp.443 , (1983).
- [73] A. Suzuki, M. Mori, K. Kaneyuki, *et al.*, “Improvement of 20 in. diameter photomultiplier tubes”, *Nuclear Instruments and Methods in Physics Research Section A: Accelerators, Spectrometers, Detectors and Associated Equipment*, **329**(1), pp.299 , (1993).
- [74] S. Desai, “High energy neutrino astrophysics with Super-Kamiokande”, PhD thesis, Boston University, (2004). URL http://lss.fnal.gov/cgi-bin/find_paper.pl?other/thesis/desai-s.pdf.
- [75] R. Becker-Szendy, R. Bionta, C. Bratton, *et al.*, “IMB-3: a large water Cherenkov detector for nucleon decay and neutrino interactions”, *Nuclear Instruments and Methods in Physics Research Section A: Accelerators, Spectrometers, Detectors and Associated Equipment*, **324**(1), pp.363 , (1993).
- [76] Z. Conner, “A Study of Solar Neutrinos Using the Super-Kamiokande Detector”, PhD thesis, University of Maryland, (1997). URL <http://www-sk.icrr.u-tokyo.ac.jp/doc/sk/pub/icrc97.pdf>.
- [77] T. Tanimori, H. Ikeda, M. Mori, *et al.*, “Design and performance of semi-custom analog IC including two TACs and two current integrators for “Super-Kamiokande””, *IEEE Transactions on Nuclear Science*, **36**(1), pp.497, (1989).
- [78] H. Ikeda, M. Mori, T. Tanimori, *et al.*, “Front-end hybrid circuit for super-KAMIOKANDE”, *Nuclear Instruments and Methods in Physics Research Section A: Accelerators, Spectrometers, Detectors and Associated Equipment*, **320** (1), pp.310 , (1992).

- [79] S. Yamada, K. Awai, Y. Hayato, *et al.*, “Commissioning of the new electronics and online system for the Super-Kamiokande experiment”, *IEEE Transactions on Nuclear Science*, **57**(2 PART 1), pp.428, (2010).
- [80] Y. Koshio, “Study of Solar Neutrinos at Super-Kamiokande”, PhD thesis, University of Tokyo, (1998). URL <http://www-sk.icrr.u-tokyo.ac.jp/~koshio/dthesis.html>.
- [81] K. Nitta, “Neutrino oscillation analysis of upward through-going and stopping muons in Super-Kamiokande”, PhD thesis, Osaka University, (2003). URL <http://www-sk.icrr.u-tokyo.ac.jp/sk/pub/index.html#dthesis>.
- [82] A. L. Stachyra, “A Search for astrophysical point sources of neutrinos with Super-Kamiokande”, PhD thesis, University of Washington, (2002). URL <https://search.proquest.com/docview/305496752>.
- [83] H. Nishino, K. Awai, Y. Hayato, *et al.*, “Development of New Front-End Electronics for Super-Kamiokande”, *Proceedings of the 15th IEEE-NPSS Real-Time Conference*, (2007).
- [84] H. Nishino, K. Awai, Y. Hayato, *et al.*, (Super Kamiokande Collaboration), “High-speed charge-to-time converter ASIC for the Super-Kamiokande detector”, *Nuclear Instruments and Methods in Physics Research Section A: Accelerators, Spectrometers, Detectors and Associated Equipment*, **610**(3), pp.710 , (2009).
- [85] M. Honda, T. Kajita, K. Kasahara, & S. Midorikawa, “Calculation of the flux of atmospheric neutrinos”, *Physical Review D*, **52**, pp.4985, (1995).
- [86] M. Honda, T. Kajita, K. Kasahara, & S. Midorikawa, “Comparison of 3-dimensional and 1-dimensional schemes in the calculation of atmospheric neutrinos”, *Physical Review D*, **64**, pp.053011, (2001).
- [87] M. Honda, T. Kajita, K. Kasahara, & S. Midorikawa, “New calculation of the atmospheric neutrino flux in a three-dimensional scheme”, *Physical Review D*, **70**, pp.043008, (2004).
- [88] M. Honda, T. Kajita, K. Kasahara, S. Midorikawa, & T. Sanuki, “Calculation of atmospheric neutrino flux using the interaction model calibrated with atmospheric muon data”, *Physical Review D*, **75**, pp.043006, (2007).
- [89] M. Honda, T. Kajita, K. Kasahara, & S. Midorikawa, “Improvement of low energy atmospheric neutrino flux calculation using the JAM nuclear interaction model”, *Physical Review D*, **83**, pp.123001, (2011).
- [90] T. Sanuki, M. Motoki, H. Matsumoto, *et al.*, (BESS Collaboration), “Precise Measurement of Cosmic- Ray Proton and Helium Spectra with the BESS Spectrometer”, *The Astrophysical Journal*, **545**(2), pp.1135, (2000).

-
- [91] S. Haino, T. Sanuki, K. Abe, *et al.*, (BESS Collaboration), “Measurements of primary and atmospheric cosmic-ray spectra with the BESS-TeV spectrometer”, *Physics Letters B*, **594**(1), pp.35 , (2004).
- [92] J. Alcaraz, B. Alpat, G. Ambrosi, *et al.*, (AMS Collaboration), “Cosmic protons”, *Physics Letters B*, **490**(1), pp.27 , (2000).
- [93] T. K. Gaisser, M. Honda, P. Lipari, & T. Stanev, “Primary spectrum to 1 TeV and beyond”, *Proceedings of the 27th International Cosmic Ray Conference*, **5**, pp.1643, (2001).
- [94] T. K. Gaisser, & M. Honda, “FLUX OF ATMOSPHERIC NEUTRINOS”, *Annual Review of Nuclear and Particle Science*, **52**(1), pp.153, (2002).
- [95] W. R. Webber, R. L. Golden, & S. A. Stephens, “Cosmic ray proton and helium spectra from 5 - 200 GV measured with a magnetic spectrometer.”, *Proceedings of the 20th International Cosmic Ray Conference*, **1**, pp.325, (1987).
- [96] P. Papini, C. Grimani, G. Basini, *et al.*, (MASS Collaboration), “Observations of Proton and Helium Spectra Near Solar Maximum”, *Proceedings of the 23rd International Cosmic Ray Conference*, **1**, pp.579, (1993).
- [97] E. S. Seo, J. F. Ormes, R. E. Streitmatter, *et al.*, (LEAP Collaboration), “Measurement of cosmic-ray proton and helium spectra during the 1987 solar minimum”, *The Astrophysical Journal*, **378**, pp.763, (1991).
- [98] W. Menn, M. Hof, O. Reimer, *et al.*, (IMAX Collaboration), “The Absolute Flux of Protons and Helium at the Top of the Atmosphere Using IMAX”, *The Astrophysical Journal*, **533**(1), pp.281, (2000).
- [99] M. Boezio, P. Carlson, T. Francke, *et al.*, (CAPRICE Collaboration), “The Cosmic- Ray Proton and Helium Spectra between 0.4 and 200 GV”, *The Astrophysical Journal*, **518**(1), pp.457, (1999).
- [100] M. J. Ryan, J. F. Ormes, & V. K. Balasubrahmanyam, “Cosmic-Ray Proton and Helium Spectra above 50 GeV”, *Physical Review Letters*, **28**, pp.985, (1972).
- [101] K. Asakimori, T. H. Burnett, M. L. Cherry, *et al.*, (JACEE Collaboration), “Cosmic- Ray Proton and Helium Spectra: Results from the JACEE Experiment”, *The Astrophysical Journal*, **502**(1), pp.278, (1998).
- [102] A. Apanasenko, V. Sukhadolskaya, V. Derbina, *et al.*, (RUNJOB Collaboration), “Composition and energy spectra of cosmic-ray primaries in the energy range 1013–1015 eV/particle observed by Japanese–Russian joint balloon experiment”, *Astroparticle Physics*, **16**(1), pp.13 , (2001).
- [103] I. P. Ivanenko, L. A. Khein, D. M. Podoroznyi, *et al.*, “Apparatus ‘AYAKS’ for Study of Cosmic Rays Nuclei at Energies 0.1 - 500 TeV”, *Proceedings of the 23rd International Cosmic Ray Conference*, **2**, pp.484, (1993).

- [104] Y. Kawamura, H. Matsutani, H. Nanjyo, *et al.*, “Quasidirect observations of cosmic-ray primaries in the energy region 10^{12} - 10^{14} eV”, *Physical Review D*, **40**, pp.729, (1989).
- [105] T. Mclachlan Fukuei, “Study of the Oscillation of Neutrinos and Anti-Neutrinos and of Non-Standard Neutrino Interactions with the Atmospheric Data in Super-Kamiokande”, PhD thesis, University of Tokyo, (2015-04-01). URL <http://www-sk.icrr.u-tokyo.ac.jp/sk/publications/index-e.html>.
- [106] Y. Nara, N. Otuka, A. Ohnishi, K. Niita, & S. Chiba, “Relativistic nuclear collisions at 10A GeV energies from $p + \text{Be}$ to $\text{Au}+\text{Au}$ with the hadronic cascade model”, *Physical Review C*, **61**, pp.024901, (1999).
- [107] S. Roesler, R. Engel, & J. Ranft, “The Monte Carlo Event Generator DPMJET-III”, *Advanced Monte Carlo for Radiation Physics, Particle Transport Simulation and Applications*, pages 1033–1038, (2001).
- [108] K. Niita, T. Sato, H. Iwase, *et al.*, “PHITS—a particle and heavy ion transport code system”, *Radiation Measurements*, **41**(9), pp.1080 , (2006).
- [109] A. Capella, U. Sukhatme, C.-I. Tan, & J. T. T. Van, “Dual parton model”, *Physics Reports*, **236**(4), pp.225 , (1994).
- [110] M. Catanesi, E. Radicioni, R. Edgecock, *et al.*, (HARP Collaboration), “Measurement of the production cross-sections of $\pi \pm$ in $p\text{-C}$ and $\pi \pm\text{-C}$ interactions at $12\text{GeV}/c$ ”, *Astroparticle Physics*, **29**(4), pp.257 , (2008).
- [111] M. Catanesi, E. Radicioni, R. Edgecock, *et al.*, (HARP Collaboration), “Forward $\pi \pm$ production in $p\text{-O}2$ and $p\text{-N}2$ interactions at $12\text{GeV}/c$ ”, *Astroparticle Physics*, **30**(3), pp.124 , (2008).
- [112] T. Sanuki, M. Fujikawa, K. Abe, *et al.*, (BESS Collaboration), “Measurements of atmospheric muon spectra at mountain altitude”, *Physics Letters B*, **541** (3-4), pp.234, (2002).
- [113] P. Achard, O. Adriani, M. Aguilar-Benitez, *et al.*, (L3 Collaboration), “Measurement of the atmospheric muon spectrum from 20 to 3000 GeV”, *Physics Letters B*, **598**(1-2), pp.15, (2004).
- [114] O. Allkofer, G. Bella, W. Dau, *et al.*, “Cosmic ray muon spectra at sea-level up to 10 TeV”, *Nuclear Physics B*, **259**(1), pp.1 , (1985).
- [115] S. Matsuno, F. Kajino, Y. Kawashima, *et al.*, “Cosmic-ray muon spectrum up to 20 TeV at 89° zenith angle”, *Physical Review D*, **29**, pp.1, (1984).
- [116] T. Sanuki, M. Honda, T. Kajita, K. Kasahara, & S. Midorikawa, “Study of cosmic ray interaction model based on atmospheric muons for the neutrino flux calculation”, *Physical Review D*, **75**, pp.043005, (2007).

-
- [117] K. Kasahara, “Introduction to Cosmos and some Relevance to Ultra High Energy Cosmic Ray Air Showers”, *Proceedings of the 24th International Cosmic Ray Conference*, **1**, pp.399, (1995).
- [118] G. Battistoni, A. Ferrari, T. Montaruli, & P. Sala, “The FLUKA atmospheric neutrino flux calculation”, *Astroparticle Physics*, **19**(2), pp.269, (2003).
- [119] G. D. Barr, T. K. Gaisser, P. Lipari, S. Robbins, & T. Stanev, “Three-dimensional calculation of atmospheric neutrinos”, *Physical Review D*, **70**, pp.023006, (2004).
- [120] Y. Hayato, “Neut”, *Nuclear Physics B Proceedings Supplements*, **112**, pp.171, (2002).
- [121] Y. Hayato, “A neutrino interaction simulation program library NEUT”, *Acta Physica Polonica B*, **40**, pp.2477, (2009).
- [122] S. Jadach, Z. Was, R. Decker, & J. Kuhn, “The τ decay library TAUOLA, version 2.4”, *Computer Physics Communications*, **76**(3), pp.361, (1993).
- [123] C. H. Llewellyn Smith, “Neutrino reactions at accelerator energies”, *Physics Reports*, **3**, pp.261, (1972).
- [124] R. Gran, E. J. Jeon, E. Aliu, *et al.*, (K2K Collaboration), “Measurement of the quasielastic axial vector mass in neutrino interactions on oxygen”, *Physical Review D*, **74**, pp.052002, (2006).
- [125] A. A. Aguilar-Arevalo, A. O. Bazarko, S. J. Brice, *et al.*, (MiniBooNE Collaboration), “Measurement of Muon Neutrino Quasielastic Scattering on Carbon”, *Physical Review Letters*, **100**, pp.032301, (2008).
- [126] J. Reich, H. Abele, M. A. Hoffmann, *et al.*, “A measurement of the beta asymmetry in neutron decay with PERKEO II”, *Nuclear Instruments and Methods in Physics Research Section A: Accelerators, Spectrometers, Detectors and Associated Equipment*, **440**, pp.535, (2000).
- [127] H. Abele, “The standard model and the neutron beta-decay”, *Nuclear Instruments and Methods in Physics Research Section A: Accelerators, Spectrometers, Detectors and Associated Equipment*, **440**, pp.499, (2000).
- [128] D. Groom, M. Aguilar-Benitez, C. Amsler, *et al.*, “Review of particle physics”, *European Physical Journal C*, **15**(1-4), pp.1, (2000).
- [129] P. E. Bosted, “Empirical fit to the nucleon electromagnetic form factors”, *Physical Review C*, **51**, pp.409, (1995).
- [130] E. J. Brash, A. Kozlov, S. Li, & G. M. Huber, “New empirical fits to the proton electromagnetic form factors”, *Physical Review C*, **65**, pp.051001, (2002).

- [131] A. Bodek, S. Avvakumov, R. Bradford, & H. S. Budd, “Modeling Atmospheric Neutrino Interactions: Duality Constrained Parameterization of Vector and Axial Nucleon Form Factors”, *Proceedings of the 30th International Cosmic Ray Conference*, (2007).
- [132] G. Mitsuka, “Study of Non-Standard Neutrino Interactions with Atmospheric Neutrino Data in Super-Kamiokande”, PhD thesis, University of Tokyo, (2009). URL http://www-sk.icrr.u-tokyo.ac.jp/sk/pub/dthesis_feb9-mitsuka.pdf.
- [133] R. Smith, & E. Moniz, “Neutrino reactions on nuclear targets”, *Nuclear Physics B*, **43**, pp.605 , (1972).
- [134] J. Nieves, J. E. Amaro, & M. Valverde, “Inclusive quasielastic charged-current neutrino-nucleus reactions”, *Physical Review C*, **70**, pp.055503, (2004).
- [135] H. Nakamura, & R. Seki, “Quasi-elastic neutrino-nucleus scattering and spectral function”, *Nuclear Physics B Proceedings Supplements*, **112**(1), pp.197 , (2002).
- [136] S. J. Barish, J. Campbell, G. Charlton, *et al.*, “Study of neutrino interactions in hydrogen and deuterium: Description of the experiment and study of the reaction $\nu + d \rightarrow \mu^- + p + p_s$ ”, *Physical Review D*, **16**, pp.3103, (1977).
- [137] A. I. Mukhin, V. F. Pereygin, K. E. Shestermanov, *et al.*, “Energy Dependence of Total Cross-sections for Neutrino and Anti-neutrino Interactions at Energies Below 35-GeV”, *Soviet Journal of Nuclear Physics*, **30**, pp.528, (1979).
- [138] S. Bonetti, G. Carnesecchi, D. Cavalli, *et al.*, “Study of Quasielastic Reactions of Neutrino and anti-neutrino in Gargamelle”, *Il Nuovo Cimento A*, **38**, pp.260, (1977).
- [139] M. Pohl, M. Dewit, D. Haidt, *et al.*, “Experimental study of the reaction $N n \rightarrow M-p$ ”, *Lettere Al Nuovo Cimento Series 2*, **26**(11), pp.332, (1979).
- [140] N. Armenise, *et al.*, “CHARGED CURRENT ELASTIC ANTI-NEUTRINO INTERACTIONS IN PROPANE”, *Nuclear Physics B*, **152**, pp.365, (1979).
- [141] S. V. Belikov, A. P. Bygorsky, L. A. Klimenko, *et al.*, “Quasielastic neutrino and antineutrino scattering total cross-sections, axial-vector form-factor”, *Zeitschrift für Physik A Atoms and Nuclei*, **320**(4), pp.625, (1985).
- [142] J. Brunner, *et al.*, (SKAT Collaboration), “Quasielastic Nucleon and Hyperon Production by Neutrinos and Anti-neutrinos With Energies Below 30-GeV”, *Zeitschrift für Physik C Particles and Fields*, **45**, pp.551, (1990).
- [143] C. H. Albright, C. Quigg, R. E. Shrock, & J. Smith, “Neutrino - Proton Elastic Scattering: Implications for Weak Interaction Models”, *Physical Review D*, **14**, pp.1780, (1976).

-
- [144] K. Abe, L. A. Ahrens, K. Amako, *et al.*, “Precise Determination of $\sin^2\theta_W$ from Measurements of the Differential Cross Sections for $\nu_\mu p \rightarrow \nu_\mu p$ and $\bar{\nu}_\mu p \rightarrow \bar{\nu}_\mu p$ ”, *Physical Review Letters*, **56**, pp.1107, (1986).
- [145] A. A. Aguilar-Arevalo, C. E. Anderson, A. O. Bazarko, *et al.*, (Mini-BooNE Collaboration), “First measurement of the muon neutrino charged current quasielastic double differential cross section”, *Physical Review D*, **81**, pp.092005, (2010).
- [146] J. Nieves, I. R. Simo, & M. J. V. Vacas, “Inclusive charged-current neutrino-nucleus reactions”, *Physical Review C*, **83**, pp.045501, (2011).
- [147] D. Rein, & L. M. Sehgal, “Neutrino Excitation of Baryon Resonances and Single Pion Production”, *Annals of Physics*, **133**, pp.79, (1981).
- [148] D. Rein, “Angular distribution in neutrino-induced single pion production processes”, *Zeitschrift für Physik C Particles and Fields*, **35**(1), pp.43, (1987).
- [149] R. P. Feynman, M. Kislinger, & F. Ravndal, “Current Matrix Elements from a Relativistic Quark Model”, *Physical Review D*, **3**, pp.2706, (1971).
- [150] G. Breit, & E. Wigner, “Capture of Slow Neutrons”, *Physical Review*, **49**, pp.519, (1936).
- [151] K. S. Kuzmin, V. V. Lyubushkin, & V. A. Naumov, “Lepton polarization in neutrino nucleon interactions”, *Modern Physics Letters A*, **19**, pp.2815, (2004).
- [152] C. Berger, & L. M. Sehgal, “Lepton mass effects in single pion production by neutrinos”, *Physical Review D*, **76**, pp.113004, (2007).
- [153] M. Glück, E. Reya, & A. Vogt, “Dynamical parton distributions revisited”, *The European Physical Journal C*, **5**(3), pp.461, (1998).
- [154] A. Bodek, & U. K. Yang, “Modeling neutrino and electron scattering inelastic cross-sections in the few GeV region with effective LO PDFs TV Leading Order”, *Proceedings of the 2nd International Workshop on Neutrino-Nucleus Interactions in the Few GeV Region*, (2003).
- [155] P. Musset, & J.-P. Vialle, “Neutrino physics with gargamelle”, *Physics Reports*, **39**(1), pp.1, (1978).
- [156] J. E. Kim, P. Langacker, M. Levine, & H. H. Williams, “A theoretical and experimental review of the weak neutral current: a determination of its structure and limits on deviations from the minimal $SU(2)_L \times U(1)$ electroweak theory”, *Reviews of Modern Physics*, **53**, pp.211, (1981).
- [157] M. Derrick, P. Gregory, L. G. Hyman, *et al.*, “Properties of the hadronic system resulting from $\bar{\nu}_\mu p$ interactions”, *Physical Review D*, **17**, pp.1, (1978).
- [158] Z. Koba, H. Nielsen, & P. Olesen, “Scaling of multiplicity distributions in high energy hadron collisions”, *Nuclear Physics B*, **40**, pp.317, (1972).

-
- [159] S. Barlag, P. Dam, E. Wolf, *et al.*, “Charged hadron multiplicities in high energy $\bar{\nu}_\mu n$ and $\bar{\nu}_\mu p$ interactions”, *Zeitschrift für Physik C Particles and Fields*, **11**(4), pp.283, (1982).
- [160] T. Sjostrand, “PYTHIA 5.7 and JETSET 7.4: Physics and manual”, *CERN Program Library Long writeups*, (1994).
- [161] P. S. Auchincloss, R. Blair, C. Haber, *et al.*, “Measurement of the inclusive charged-current cross section for neutrino and antineutrino scattering on isoscalar nucleons”, *Zeitschrift für Physik C Particles and Fields*, **48**(3), pp.411, (1990).
- [162] P. Berge, A. Blondel, P. Böckmann, *et al.*, “Total neutrino and antineutrino charged current cross section measurements in 100, 160, and 200 GeV narrow band beams”, *Zeitschrift für Physik C Particles and Fields*, **35**(4), pp.443, (1987).
- [163] S. Ciampolillo, B. Degrange, M. Dewit, *et al.*, “Total cross section for neutrino charged current interactions at 3 GeV and 9 GeV”, *Physics Letters B*, **84**(2), pp.281, (1979).
- [164] J. V. Allaby, U. Amaldi, G. Barbiellini, *et al.*, “Total cross sections of charged-current neutrino and antineutrino interactions on isoscalar nuclei”, *Zeitschrift für Physik C Particles and Fields*, **38**(3), pp.403, (1988).
- [165] N. J. Baker, P. L. Connolly, S. A. Kahn, *et al.*, “Total cross sections for $\nu_\mu n$ and $\nu_\mu p$ charged-current interactions in the 7-foot bubble chamber”, *Physical Review D*, **25**, pp.617, (1982).
- [166] C. Baltay, H. French, M. Hibbs, *et al.*, “Cross Sections and Scaling-Variable Distributions of Neutral- and Charged- Current Neutrino-Nucleon Interactions from a Low-Energy Narrow Band Beam”, *Physical Review Letters*, **44**, pp.916, (1980).
- [167] D. C. Colley, G. T. Jones, S. O’Neale, *et al.*, “Cross sections for charged current ν and $\bar{\nu}$ interactions in the energy range 10 to 50 GeV”, *Zeitschrift für Physik C Particles and Fields*, **2**(3), pp.187, (1979).
- [168] V. B. Anikeev, S. V. Belikov, A. A. Borisov, *et al.*, “Total cross section measurements for $\nu_m u$, $\bar{\nu}_\mu$ charged current interactions in 3–30 GeV energy range with IHEP-JINR neutrino detector”, *Zeitschrift für Physik C: Particles and Fields*, **70**(1), pp.39, (1996).
- [169] D. B. MacFarlane, M. V. Purohit, R. L. Messner, *et al.*, “Nucleon structure functions from high energy neutrino interactions with iron and QCD results”, *Zeitschrift für Physik C Particles and Fields*, **26**(1), pp.1, (1984).

- [170] D. Baranov, A. Bugorsky, A. Ivanilov, *et al.*, “Measurement of the $\nu \mu N$ total cross section at 2–30 GeV in a skat neutrino experiment”, *Physics Letters B*, **81**(2), pp.255 , (1979).
- [171] D. Rein, & L. M. Sehgal, “Coherent π^0 production in neutrino reactions”, *Nuclear Physics B*, **223**(1), pp.29 , (1983).
- [172] M. Hasegawa, E. Aliu, S. Andringa, *et al.*, (K2K Collaboration), “Search for Coherent Charged Pion Production in Neutrino-Carbon Interactions”, *Physical Review Letters*, **95**, pp.252301, (2005).
- [173] D. Rein, & L. Sehgal, “PCAC and the deficit of forward muons in π^+ production by neutrinos”, *Physics Letters B*, **657**(4), pp.207 , (2007).
- [174] A. Kartavtsev, E. A. Paschos, & G. J. Gounaris, “Coherent pion production by neutrino scattering off nuclei”, *Physical Review D*, **74**, pp.054007, (2006).
- [175] L. Alvarez-Ruso, L. S. Geng, S. Hirenzaki, & M. J. V. Vacas, “Charged current neutrino-induced coherent pion production”, *Physical Review C*, **75**, pp.055501, (2007).
- [176] K. Hiraide, J. L. Alcaraz-Aunion, S. J. Brice, *et al.*, (SciBooNE Collaboration), “Search for charged current coherent pion production on carbon in a few-GeV neutrino beam”, *Physical Review D*, **78**, pp.112004, (2008).
- [177] J. L. Raaf, “A Measurement of the Neutrino Neutral Current π^0 Cross Section at MiniBooNE”, PhD thesis, University of Cincinnati, (2005). URL http://lss.fnal.gov/cgi-bin/find_paper.pl?thesis-2005-20.
- [178] H. Faissner, E. Frenzel, M. Grimm, *et al.*, “Observation of neutrino and antineutrino induced coherent neutral pion production off Al²⁷”, *Physics Letters B*, **125**(2), pp.230 , (1983).
- [179] E. Isiksal, D. Rein, & J. G. Morfín, “Evidence for Neutrino- and Antineutrino-Induced Coherent π^0 Production”, *Physical Review Letters*, **52**, pp.1096, (1984).
- [180] R. D. Woods, & D. S. Saxon, “Diffuse Surface Optical Model for Nucleon-Nuclei Scattering”, *Physical Review*, **95**, pp.577, (1954).
- [181] C. D. Jager, H. D. Vries, & C. D. Vries, “Nuclear charge- and magnetization-density-distribution parameters from elastic electron scattering”, *Atomic Data and Nuclear Data Tables*, **14**(5), pp.479 , (1974).
- [182] L. Salcedo, E. Oset, M. Vicente-Vacas, & C. Garcia-Recio, “Computer simulation of inclusive pion nuclear reactions”, *Nuclear Physics A*, **484**(3), pp.557 , (1988).
- [183] G. Rowe, M. Salomon, & R. H. Landau, “Energy-dependent phase shift analysis of pion-nucleon scattering below 400 MeV”, *Physical Review C*, **18**, pp.584, (1978).

- [184] R. Seki, & K. Masutani, “Unified analysis of pionic atoms and low-energy pion-nucleus scattering: Phenomenological analysis”, *Physical Review C*, **27**, pp.2799, (1983).
- [185] D. Ashery, I. Navon, G. Azuelos, *et al.*, “True absorption and scattering of pions on nuclei”, *Physical Review C*, **23**, pp.2173, (1981).
- [186] C. H. Q. Ingram, P. A. M. Gram, J. Jansen, *et al.*, “Quasielastic scattering of pions from ^{16}O at energies around the $\Delta(1232)$ resonance”, *Physical Review C*, **27**, pp.1578, (1983).
- [187] B. Martin, & M. Pidcock, “KN interactions in the resonance region: (I). Analysis of data”, *Nuclear Physics B*, **126**(2), pp.266, (1977).
- [188] B. Martin, & M. Pidcock, “KN interactions in the resonance region: (II). Amplitudes”, *Nuclear Physics B*, **126**(2), pp.285, (1977).
- [189] J. S. Hyslop, R. A. Arndt, L. D. Roper, & R. L. Workman, “Partial-wave analysis of K^+ -nucleon scattering”, *Physical Review D*, **46**, pp.961, (1992).
- [190] D. A. Sparrow, “Effects of the nuclear medium on the observation of baryon number violation”, *Proceedings of the AIP Conference*, (1984).
- [191] H. W. Bertini, “Nonelastic Interactions of Nucleons and π Mesons with Complex Nuclei at Energies Below 3 GeV”, *Physical Review C*, **6**, pp.631, (1972).
- [192] S. J. Lindenbaum, & R. M. Sternheimer, “Isobaric Nucleon Model for Pion Production in Nucleon-Nucleon Collisions”, *Physical Review*, **105**, pp.1874, (1957).
- [193] R. Brun, F. Bruyant, M. Maire, A. C. McPherson, & P. Zancarini, “GEANT 3: user’s guide Geant 3.10, Geant 3.11; rev. version”. CERN, Geneva, (1987).
- [194] R. Brun, F. Bruyant, F. Carminati, *et al.*, “GEANT Detector Description and Simulation Tool”, *CERN Program Library*, (1993).
- [195] C. Zeitnitz, & T. Gabriel, “The GEANT-CALOR interface and benchmark calculations of ZEUS test calorimeters”, *Nuclear Instruments and Methods in Physics Research Section A: Accelerators, Spectrometers, Detectors and Associated Equipment*, **349**(1), pp.106, (1994).
- [196] M. Nakahata, K. Arisaka, T. Kajita, *et al.*, “Atmospheric Neutrino Background and Pion Nuclear Effect for KAMIOKA Nucleon Decay Experiment”, *Journal of the Physical Society of Japan*, **55**(11), pp.3786, (1986).
- [197] E. Bracci, J. P. Droulez, V. Flaminio, J. D. Hansen, & D. R. O. Morrison, “Compilation of cross-sections”, *CERN-HERA-72-01*, (1972).
- [198] A. S. Carroll, I. H. Chiang, C. B. Dover, *et al.*, “Pion-nucleus total cross sections in the (3,3) resonance region”, *Physical Review C*, **14**, pp.635, (1976).

- [199] S. Agostinelli, J. Allison, K. Amako, *et al.*, “Geant4—a simulation toolkit”, *Nuclear Instruments and Methods in Physics Research Section A: Accelerators, Spectrometers, Detectors and Associated Equipment*, **506**(3), pp.250 , (2003).
- [200] J. Allison, K. Amako, J. Apostolakis, *et al.*, “Geant4 developments and applications”, *IEEE Transactions on Nuclear Science*, **53**(1), pp.270, (2006).
- [201] J. Allison, K. Amako, J. Apostolakis, *et al.*, “Recent developments in Geant4”, *Nuclear Instruments and Methods in Physics Research Section A: Accelerators, Spectrometers, Detectors and Associated Equipment*, **835**, pp.186 , (2016).
- [202] M. Harada, Y. Koshio, & K. Hagiwara, “Development of Geant4 based simulation for Super-Kamiokande”, *Proceedings of The 4th KMI International Symposium*, (2019).
- [203] M. Harada, “Development of Super-Kamiokande detector simulation based on Geant4”, *Proceedings of the 36th International Cosmic Ray Conference*, **1**, (2019).
- [204] P. K. Das, K. Hagiwara, T. Tanaka, *et al.*, “Measurement of Relative Intensity of the discrete γ rays from the thermal neutron capture reaction $^{155,157}\text{Gd}(n, \gamma)$ using ANNRI detector (JPARC)”, *Proceedings of The 3rd International Symposium on Quest for the Origin of Particles and the Universe*, (2017).
- [205] K. Hagiwara, T. Tanaka, P. K. Das, *et al.*, “Comparison of γ production from thermal neutron capture of gadolinium with the MonteCarlo simulation”, *Proceedings of the 3rd International Symposium on Quest for the Origin of Particles and the Universe*, (2017).
- [206] K. Hagiwara, T. Yano, T. Tanaka, *et al.*, “Gamma-ray spectrum from thermal neutron capture on gadolinium-157”, *Progress of Theoretical and Experimental Physics*, **2019**(2), (2019).
- [207] J. Apostolakis, S. Giani, M. Maire, *et al.*, “GEANT4 low energy electromagnetic models for electrons and photons”, (CERN-OPEN-99-034), (1999).
- [208] K. Abe, Y. Hayato, T. Iida, *et al.*, (Super Kamiokande Collaboration), “Calibration of the Super-Kamiokande detector”, *Nuclear Instruments and Methods in Physics Research Section A: Accelerators, Spectrometers, Detectors and Associated Equipment*, **737**, pp.253 , (2014).
- [209] J. Hosaka, K. Ishihara, J. Kameda, *et al.*, (Super Kamiokande Collaboration), “Solar neutrino measurements in Super-Kamiokande-I”, *Physical Review D*, **73**, pp.112001, (2006).
- [210] D. Motta, & S. Schonert, “Optical properties of Bialkali photocathodes”, *Nuclear Instruments and Methods in Physics Research Section A: Accelerators, Spectrometers, Detectors and Associated Equipment*, **539**, pp.217, (2005).

- [211] A. Filevich, P. Bauleo, H. Bianchi, J. R. Martino, & G. Torlasco, “Spectral-directional reflectivity of Tyvek immersed in water”, *Nuclear Instruments and Methods in Physics Research Section A: Accelerators, Spectrometers, Detectors and Associated Equipment*, **423**(1), pp.108 , (1999).
- [212] P. Hänggi, R. Viollier, U. Raff, & K. Alder, “Muon decay in orbit”, *Physics Letters B*, **51**(2), pp.119 , (1974).
- [213] M. Yamada, K. Miyano, H. Miyata, *et al.*, “Measurements of the charge ratio and polarization of 1.2-TeV/c cosmic-ray muons with the Kamiokande II detector”, *Physical Review D*, **44**, pp.617, (1991).
- [214] K. Abe, C. Bronner, Y. Haga, *et al.*, (Super Kamiokande Collaboration), “Atmospheric neutrino oscillation analysis with external constraints in Super-Kamiokande I-IV”, *Physical Review D*, **97**, pp.072001, (2018).
- [215] Y. Takenaga, “Atmospheric neutrino oscillation analysis with solar terms in Super-Kamiokande”, PhD thesis, University of Tokyo, (2008). URL <http://www-sk.icrr.u-tokyo.ac.jp/sk/pub/index.html#dthesis>.
- [216] E. R. Davies, “Machine Vision: Theory, Algorithms, Practicalities”. Morgan Kaufman Publishers Inc., ISBN 0122060938, (2004).
- [217] Y. Ashie, J. Hosaka, K. Ishihara, *et al.*, (Super Kamiokande Collaboration), “Measurement of atmospheric neutrino oscillation parameters by Super-Kamiokande I”, *Physical Review D*, **71**(11), pp.112005, (2005).
- [218] K. Abe, C. Bronner, G. Pronost, *et al.*, (Super Kamiokande Collaboration), “Search for an Excess of Events in the Super-Kamiokande Detector in the Directions of the Astrophysical Neutrinos Reported by the IceCube Collaboration”, *The Astrophysical Journal*, **850**(2), pp.166, (2017).
- [219] M. E. C. Swanson, K. Abe, J. Hosaka, *et al.*, (Super Kamiokande Collaboration), “Search for Diffuse Astrophysical Neutrino Flux Using Ultra-High-Energy Upward- going Muons in Super- Kamiokande I”, *The Astrophysical Journal*, **652**(1), pp.206, (2006).
- [220] E. Thrane, K. Abe, Y. Hayato, *et al.*, (Super Kamiokande Collaboration), “SEARCH FOR ASTROPHYSICAL NEUTRINO POINT SOURCES AT SUPER-KAMIOKANDE”, *The Astrophysical Journal*, **704**(1), pp.503, (2009).
- [221] E. Thrane, K. Abe, Y. Hayato, *et al.*, (Super Kamiokande Collaboration), “Search for Neutrinos from GRB 080319B at Super-Kamiokande”, *The Astrophysical Journal*, **697**, pp.730, (2009).
- [222] C. Saji, “Study of upward-going muons in Super-Kamiokande”, PhD thesis, Niigata University, (2002). URL <http://www-sk.icrr.u-tokyo.ac.jp/sk/pub/index.html#dthesis>.

- [223] M. Glück, E. Reya, & A. Vogt, “Dynamical parton distributions of the proton and small-x physics”, *Zeitschrift für Physik C Particles and Fields*, **67**(3), pp.433, (1995).
- [224] P. Lipari, & T. Stanev, “Propagation of multi-TeV muons”, *Physical Review D*, **44**(11), pp.3543, (1991).
- [225] R. Gandhi, C. Quigg, M. Hall Reno, & I. Sarcevic, “Ultrahigh-energy neutrino interactions”, *Astroparticle Physics*, **5**(2), pp.81, (1996).
- [226] R. Gandhi, C. Quigg, M. H. Reno, & I. Sarcevic, “Neutrino interactions at ultrahigh energies”, *Physical Review D*, **58**, pp.093009, (1998).
- [227] S. Garrappa, S. Buson, A. Franckowiak, *et al.*, (Fermi-LAT, ASAS-SN and IceCube Collaborations), “Investigation of Two Fermi-LAT Gamma-Ray Blazars Coincident with High-energy Neutrinos Detected by IceCube”, *The Astrophysical Journal*, **880**(2), pp.103, (2019).
- [228] F. Acero, M. Ackermann, M. Ajello, *et al.*, “FERMILARGE AREA TELESCOPE THIRD SOURCE CATALOG”, *The Astrophysical Journal Supplement Series*, **218**(2), pp.23, (2015).
- [229] E. Massaro, M. Perri, P. Giommi, & R. Nesci, “Log-parabolic spectra and particle acceleration in the BL Lac object Mkn 421: Spectral analysis of the complete BeppoSAX wide band X-ray data set”, *Astronomy & Astrophysics*, **413**, pp.489, (2004).
- [230] S. Weinberg, “Gravitation and Cosmology: Principles and Applications of the General Theory of Relativity”. John Wiley & Sons Inc., (1972).
- [231] P. A. R. Ade, N. Aghanim, M. Arnaud, *et al.*, (Planck Collaboration), “Planck2015 results”, *Astronomy & Astrophysics*, **594**, pp.A13, (2016).
- [232] S. Ansoldi, L. A. Antonelli, C. Arcaro, *et al.*, “The Blazar TXS 0506+056 Associated with a High-energy Neutrino: Insights into Extragalactic Jets and Cosmic-Ray Acceleration”, *The Astrophysical Journal Letters*, **863**(1):L10, (2018).
- [233] A. Keivani, K. Murase, M. Petropoulou, *et al.*, “A Multimessenger Picture of the Flaring Blazar TXS 0506+056: Implications for High-energy Neutrino Emission and Cosmic-Ray Acceleration”, *The Astrophysical Journal*, **864**(1), pp.84, (2018).
- [234] M. Cerruti, A. Zech, C. Boisson, *et al.*, “Leptohadronic single-zone models for the electromagnetic and neutrino emission of TXS0506+056”, *Monthly Notices of the Royal Astronomical Society: Letters*, **483**(1), pp.L12, (2018).
- [235] S. Gao, A. Fedynitch, W. Winter, & M. Pohl, “Modelling the coincident observation of a high-energy neutrino and a bright blazar flare”, *Nature Astronomy*, **3**(1), pp.88, (2018).

- [236] R. Xue, R.-Y. Liu, M. Petropoulou, *et al.*, “A Two-zone Model for Blazar Emission: Implications for TXS 0506+056 and the Neutrino Event IceCube-170922A”, *The Astrophysical Journal*, **886**(1), pp.23, (2019).
- [237] X. Rodrigues, S. Gao, A. Fedynitch, A. Palladino, & W. Winter, “Lepto-hadronic Blazar Models Applied to the 2014–2015 Flare of TXS 0506+056”, *The Astrophysical Journal*, **874**(2), pp.L29, (2019).
- [238] S. Gao, M. Pohl, & W. Winter, “On the Direct Correlation between Gamma-Rays and PeV Neutrinos from Blazars”, *The Astrophysical Journal*, **843**(2), pp.109, (2017).
- [239] C. D. Dermer, R. Schlickeiser, & A. Mastichiadis, “High-energy gamma radiation from extragalactic radio sources.”, *Astronomy & Astrophysics*, **256**, pp.L27, (1992).
- [240] C. D. Dermer, & R. Schlickeiser, “Model for the High-Energy Emission from Blazars”, *The Astrophysical Journal*, **416**, pp.458, (1993).
- [241] M. Sikora, M. C. Begelman, & M. J. Rees, “Comptonization of Diffuse Ambient Radiation by a Relativistic Jet: The Source of Gamma Rays from Blazars?”, *The Astrophysical Journal*, **421**, pp.153, (1994).
- [242] S. D. Bloom, & A. P. Marscher, “An Analysis of the Synchrotron Self-Compton Model for the Multi-Wave Band Spectra of Blazars”, *The Astrophysical Journal*, **461**, pp.657, (1996).
- [243] M. Pohl, & R. Schlickeiser, “On the conversion of blast wave energy into radiation in active galactic nuclei and gamma-ray bursts”, *Astronomy & Astrophysics*, **354**, pp.395, (2000).
- [244] Schuster C., Pohl M., & Schlickeiser R., “Neutrinos from active galactic nuclei as a diagnostic tool”, *Astronomy & Astrophysics*, **382**(3), pp.829, (2002).
- [245] H. J. Möhring, & J. Ranft, “Dual parton model with complete formation zone intranuclear cascade for the description of particle production in hadron-nucleus and nucleus-nucleus interactions”, *Zeitschrift für Physik C Particles and Fields*, **52**(4), pp.643, (1991).
- [246] J. Ranft, & S. Roesler, “Single diffractive hadron-nucleus interactions within the dual parton model”, *Zeitschrift für Physik C Particles and Fields*, **62**(2), pp.329, (1994).
- [247] A. Ferrari, J. Ranft, S. Roesler, & P. Sala, “Cascade particles, nuclear evaporation, and residual nuclei in high energy hadron-nucleus interactions”, *Zeitschrift für Physik C Particles and Fields*, **70**(3), pp.413, (1996).
- [248] R. Engel, J. Ranft, & S. Roesler, “Photoproduction off nuclei and pointlike photon interactions. I. Cross sections and nuclear shadowing”, *Physical Review D*, **55**, pp.6957, (1997).

- [249] S. Mughabghab, “Atlas of Neutron Resonances, Fifth Edition: Resonance Parameters and Thermal Cross Sections, Z=1-100”. Elsevier Science, (2006).
- [250] M. Igashira, Y. Kiyonagi, & M. Oshima, “Nuclear data study at J-PARC BL04”, *Nuclear Instruments and Methods in Physics Research Section A: Accelerators, Spectrometers, Detectors and Associated Equipment*, **600**(1), pp.332 , (2009).
- [251] T. Kin, K. Furutaka, S. Goko, *et al.*, “The 4π Ge Spectrometer for Measurements of Neutron Capture Cross Sections by the TOF Method at the J-PARC/MLF/ANNRI”, *Journal of the Korean Physical Society*, **59**(2(3)), pp.1769, (2011).
- [252] K. Kino, M. Furusaka, F. Hiraga, *et al.*, “Measurement of energy spectra and spatial distributions of neutron beams provided by the ANNRI beamline for capture cross-section measurements at the J-PARC/MLF”, *Nuclear Instruments and Methods in Physics Research Section A: Accelerators, Spectrometers, Detectors and Associated Equipment*, **626-627**, pp.58 , (2011).
- [253] A. Kimura, T. Fujii, S. Fukutani, *et al.*, “Neutron-capture cross-sections of ^{244}Cm and ^{246}Cm measured with an array of large germanium detectors in the ANNRI at J-PARC/MLF”, *Journal of Nuclear Science and Technology*, **49**(7), pp.708, (2012).
- [254] K. Kino, M. Furusaka, F. Hiraga, *et al.*, “Energy resolution of pulsed neutron beam provided by the ANNRI beamline at the J-PARC/MLF”, *Nuclear Instruments and Methods in Physics Research Section A: Accelerators, Spectrometers, Detectors and Associated Equipment*, **736**, pp.66 , (2014).
- [255] S. Nagamiya, “Introduction to J-PARC”, *Progress of Theoretical and Experimental Physics*, **2012**(1), (2012).
- [256] K. SHIBATA, O. IWAMOTO, T. NAKAGAWA, *et al.*, “JENDL-4.0: A New Library for Nuclear Science and Engineering”, *Journal of Nuclear Science and Technology*, **48**(1), pp.1, (2011).
- [257] R. Capote, M. Herman, P. Obložinský, *et al.*, “RIPL – Reference Input Parameter Library for Calculation of Nuclear Reactions and Nuclear Data Evaluations”, *Nuclear Data Sheets*, **110**(12), pp.3107 , (2009).